Hydrogen oxydation electrocatalysts in the presence of pollutants – Application for hydrogen purification/compression

Marine Tregaro

THÈSE

Pour obtenir le grade de

DOCTEUR DE L'UNIVERSITE GRENOBLE ALPES

Spécialité : **Matériaux, Mécanique, Génie Civil, Electrochimie**

Arrêté ministériel : 25 mai 2016

Présentée par

Marine TREGARO

Thèse dirigée par **Marian CHATENET, Professeur, Grenoble-INP**, et codirigée par **Christophe GEANTET, Directeur de recherche, IRCELYON**

préparée au sein du **Laboratoire d'Electrochimie et de Physicochimie des Matériaux et des Interfaces (LEPMI)**
dans **l'École Doctorale Ingénierie- Matériaux, Mécanique, Energétique, Environnement, Procédés, Production (I-MEP²)**

Électrocatalyseurs de l'oxydation de l'hydrogène en présence de polluants

Application à la purification/compression de l'hydrogène

Hydrogen oxidation electrocatalysts in the presence of pollutants

Application for hydrogen purification/compression

Thèse soutenue publiquement le **16 juillet 2021** devant le jury composé de :

M. Gaël MARANZANA
Professeur, Université de Lorraine (Président du jury)

Mme Sophie DIDIERJEAN
Professeur, Université de Lorraine (Rapportrice)

M. Pierre MILLET
Professeur, Université Paris-Sud (Rapporteur)

Mme Laetitia DUBAU
Chargée de recherche, CNRS (Examinatrice)

M. Christophe GEANTET
Directeur de recherche, CNRS (co-Directeur de thèse)

M. Marian CHATENET
Professeur, Université Grenoble Alpes (Directeur de thèse)

Remerciements

J'aimerai dédier cette page à toutes les personnes, qui, par leur implication, leur savoir-faire ou juste leur présence, ont fait de cette thèse un magnifique moment d'apprentissage, de rire et de recherche.

Je souhaiterai tout d'abord remercier les membres de mon jury de thèse, Mesdames Sophie Didierjean et Laetitia Dubau et Messieurs Pierre Millet et Gaël Maranzana, pour avoir accepté de relire et juger mon travail, et pour la qualité et la bienveillance des discussions partagées lors de la soutenance.

Il y a une personne sans qui cette thèse ne serait pas, et c'est toi Marian. Merci de m'avoir fait confiance en me proposant de participer à ce projet. Tu as été un directeur de thèse exceptionnel, tant au niveau des discussions et conseils scientifiques, qu'au niveau humain. Tu m'as laissé une grande liberté, sans jamais me laisser seule pour autant. Merci Marian, pour tout ce que tu m'as apporté.

Christophe, tu étais certes plus éloigné, tant en ville qu'en discipline, et pourtant tu as toujours pris part à ce projet de bon cœur. Merci pour le partage de ta passion, ton regard extérieur, et pour m'avoir souvent rappelé qu'il existe un monde autour de l'électrocatalyse.

Je me dois également de remercier la Région Auvergne Rhône-Alpes, pour avoir financé ma thèse dans le cadre du projet Elo PussHy (Et oui, j'ai fini par m'y faire… ^^).

I also would like to warmly thank professor Matthias Arenz and his team, for kindly receiving me in your lab, teaching me about the GDE, and even lending me one ! It's thanks to people like you that science can move further. Special thanks to Johanna and Shima, for your kindness and all the precious discussions.

And for the same reason, I would like to thank professor Kucernak and his team, for receiving me in your lab and teaching me about the Floating electrode. I did not work on it in the end, but I learned a lot thanks to you all.

Mon nom a beau figurer en couverture de ce manuscrit, je ne suis pas la seule à avoir travaillé sur les données présentées. C'est pourquoi j'aimerais remercier tous ceux qui m'ont aidé dans les mesures, les analyses présentées le long de ces pages : Stéphane et Thierry, du CMTC, pour les analyses XRD ; Mimoun pour les très magnifiques (mais tout aussi difficiles à réaliser) images E-TEM ; Karine et Muriel, pour m'avoir sauvée avec l'ATG, ou le potentiostat ; et le trio de masters, Léa, Patricia et Marie, pour avoir testé les cata d'oxydes métalliques, malgré toutes les difficultés (j'espère au moins que vous vous êtes amusées ^^). Dans le laboratoire, je ne peux évidemment pas oublier Vincent Martin, sans qui cette thèse, et de nombreuses autres au LEPMI, ne seraient pas aussi riches. Que ce soit le DEMS, le réseau de gaz, l'ICP et j'en passe, tu es essentiel. Et surtout un sacré paparazzi d'étudiant !

Plus généralement, j'adresse mes plus sincères remerciements à tous les permanents de l'équipe EIP, Jonathan, Frédéric, Laeticia, Eric, Eric, (et Laure !), et tous les autres pour votre bienveillance, le partage de vos connaissances, et vous être organisés pour nous permettre de maniper durant cette dernière année. Je ne peux pas non plus oublier notre chère directrice de labo, Fannie, qui a

si bien géré cette année de crise au labo, et a toujours tout fait pour nous permettre d'expérimenter dans les meilleures conditions. Dans les essentielles du labo, j'aimerai également remercier Claire, Yasmine, Claire et Corine, sans qui nous serions tous bien perdus au milieu de toute cette administration. Merci à vous ! ☺

J'aimerai maintenant remercier les personnes grâce à qui mon aventure au LEPMI a été si riche, colorée et agréable : mes collègues, et bien souvent, amis. Nous avons la chance d'avoir une atmosphère si conviviale au LEPMI. Entre entraide, discussions scientifiques et sorties en tout genre, j'ai passé trois années merveilleuses avec vous. Des week-end ski aux cueillettes de champignons, des raclettes/fondues en folies aux anniversaires piégés :P, des escape games géniaux aux superbes canyonings, en passant par les régulières sorties au bar, on ne risquait pas de s'ennuyer.

Alors Merci à tous ☺. Clémence, pour d'avoir été une géniale voisine de bureau, et m'avoir tant inspirée, tant au niveau de l'organisation que du courage nécessaire pour la mettre en œuvre. Fabien, pour avoir partagé tes passions avec moi, et pour avoir été le plus impitoyable Enigme Master qui soit. Maha, ma super partenaire de sujet, ces moments discussions ont illuminé mes journées. Guillaume, pour les parties de président (presque) maraboutées et le superbe zoo d'origamis qu'est devenu notre bureau. Vivien, pour ta diplomatie et ton ouverture d'esprit rafraichissante. Marie, pour ta douceur et ta gentillesse. Eris pour ta joie de vivre et ta maîtrise des selfies. Delphine, pour ton sourire capable d'illuminer nos journées. François, pour ces discussions (et recommandations !) sur l'héroïc fantasy. Estelle, pour ta combativité à toute épreuve (il n'y aura qu'une seule présidente au final ! :P). Killian, mon seul soutien breton quand il faut défendre le beurre (salé !). Raph, pour le partage de la recette magique du polyol. Kavita (et Ugo ;)) pour le trafic de boîtes de jeux. Matthieu, pour ce magnifique schéma de cellule (et bon courage avec la GDE !). Camilla, tu nous auras quitté bien trop vite, mais ta gentillesse restera dans mes souvenirs. Abdennour, Arnaud, pour votre expertise sur ce micro-ondes de l'enfer. Parfait, ne fait pas de bêtises dans la salle H_2 :P. Sedik, pour les randos et l'expertise photo. Sans oublier beaucoup d'heureuses rencontres comme Marion, Ricardo, Sofyane, Huong, Tristan et bien d'autres… Enfin, parmi toutes ces merveilleuses rencontres, la tienne est certainement la plus lumineuse, Raphaël. Merci pour ces longs moments de complicité partagés à rigoler, bricoler ou rivaliser ;) Et Merci pour ton soutien indéfectible, surtout pendant mon infernale rédaction.

En dehors du labo, je ne peux pas oublier mes géniales amies qui bien que loin physiquement, prenaient toujours le temps de prendre de mes nouvelles quand je me laissais déborder, Emilie, Pauline, c'est à vous que je pense. Et surtout toi Maeva, pour nos skypes hebdomadaires. Pour les rires et les larmes partagés, Merci.

Cela peut paraitre étrange, mais à ce stade j'aimerais… me remercier. Enfin, la Marine du passé. Merci de n'avoir rien lâché, même lorsque c'était difficile. Ça en valait largement le coup.

Et enfin, parce que vous étiez toujours à mes côtés dans mon cœur, parce que je vous dois qui je suis aujourd'hui, merci Yoann, Papa, Maman. Je vous aime de tout mon cœur, et je suis fière de pouvoir être votre fille, ta sœur. Si j'en lui là aujourd'hui, je vous le dois en grande partie. Merci.

Table of content

List of abbreviations and symbols

Symbols

[X]	Concentration of the species X in the electrolyte (mol L^{-1})
A	Absorbance
A_X	Mass normalized surface area of a X species nanoparticle (m^2 g^{-1})
D	Diffusion coefficient (cm^2 s^{-1})
d_{hkl}	Nanoparticle diameter measured by XRD (nm)
d_n	Mathematical particle diameter (nm)
d_s	Diameter relative to the surface area of particles (nm)
d_V	Diameter relative to the volume of particles (nm)
E	Potential (V vs RHE)
$\mathcal{F}$	Faraday constant
J	Current density (A cm^{-2})
j_0	Exchange current density (A cm^{-2})
j_{ECSA}	Current density normalized by the ECSA (A cm^{-2})
j_{geo}	Current density normalized by the geometric surface (A cm^{-2})
J_{lim}	Current density limit given by the Levich law (A cm^{-2})
K	Absorption coefficient of a photon (mol^{-1} L cm^{-1})
l	Optical distance in an AAS atomizer (cm)
m_X	Mass of a X species nanoparticle (g)
N_0	Number of excited atoms in the volume (mol L^{-1})
P	Pressure (Pa)
$P_{H2,\ anode}$	Partial pressure of hydrogen at the anode (bar)
$P_{H2,\ anode}$	Partial pressure of hydrogen at the cathode (bar)
$Q_{CO,\ Ox}$	Coulombic charge related to CO oxidation (C)
R	Gas constant
R	Ratio
r_{Pr}	Radius of a Pt nanoparticle (nm)
S_{metal}	Metallic apparent surface (cm^2)

T	Temperature (K)
T_{amb}	Ambient temperature (K)
T_{cell}	Temperature of the cell (K)
$U_{compressor}$	Tension of the electrochemical hydrogen compressor (V)
U_{ohmic}	Tension related to the ohmic drop losses (V)
U_{onset}	Potential of the CO oxidation onset (V vs RHE)
U_{peak}	Potential of the main CO-stripping peak (V vs RHE)
$U_{\text{transport}}$	Tension related to the mass transport limitations (V)
β	Width of the XRD peak
ΔH	Free enthalpy (kJ mol^{-1})
η	Overvoltage (V)
θ_{CO}	CO coverage on an electrocatalyst
λ	Wavelength (Å)
υ	Viscosity of the electrolyte (cm^2 s^{-1})
ρ_{Pt}	Density of Pt (g cm^{-3})
ω	Rotating speed of the RDE (rpm: *round per minute*)

Abbreviations

AAS	Atomic Adsorption Spectroscopy
AFC	Alkaline Fuel Cell
at.%	Atomic Percentage
CA	Chronoamperometry
CCUS	Carbon Capture Utilization And Storage
CV	Cyclic Voltammetry
DEFC	Direct Ethanol Fuel Cell
DEMS	Differential Electrochemical Mass Spectrometry
DMFC	Direct Methanol Fuel Cell
ECSA	Electrochemical Surface Area
EHC	Electrochemical Hydrogen Compressor
ETEM	Environmental Transmission Electronic Microscope
fcc	Face-Centred Cubic

FFT	Fast Fourier Transform
GDE	Gas Diffusion Electrode
GDL	Gas Diffusion Layer
HAADF	High Angular Dark Field Mode
HER	Hydrogen Evolution Reaction
HOR	Hydrogen Oxidation Reaction
HR-TEM	High Resolution Transmission Electron Microscopy
H_{UPD}	Hydrogen Underpotential Deposition
ICP-MS	Inductively Coupled Plasma Mass Spectrometry
IPA	Isopropanol
MCFC	Molten Carbonate Fuel Cell
MEA	Membrane Electrode Assembly
ORR	Oxygen Reduction Reaction
PAFC	Phosphoric Acid Fuel Cell
PEMFC	Proton Exchange Membrane Fuel Cell
PEMWE	Proton Exchange Membrane Water Electrolyzer
PSA	Pressure Swing Adsorption
PTFE	Polytetrafluoroethylene
PZTC	Point Of Zero Total Charge
RDE	Rotating Disk Electrode
RHE	Reversible Hydrogen Electrode
RWGS	Reverse Water Gas Shift Reaction
SMR	Steam Methane Reforming
SOFC	Solid Exchange Fuel Cell
STEM	Scanning Transmission Electron Microscopy
TEM	Transmission Electron Microscope
TGA	Thermogravimetric Analysis
TSA	Temperature Swing Adsorption
wt.%	Weigh Percentage
X-EDS	X-Ray Energy Dispersive Spectroscopy
XPS	X-Ray Photoelectron Spectroscopy
XRD	X-Ray Diffraction

General Introduction

Hydrogen, or dihydrogen to be precise. That's the name of the energy vector that could become central in our future economy, and change the world for the better. The hydrogen molecule could be the energy carrier between renewable, intermittent energy sources and our cars, trucks, boats, planes, trains, bikes, mobile phones… Through its use in fuel cells, *e.g.* the proton exchange membrane fuel cell (PEMFC), hydrogen can produce electricity… and water. That's all.

Of course, as for any technology, the production, handling and transportation costs, both environmental and energetic, of hydrogen (and hydrogen technologies/materials) should be taken into account. As of today, hydrogen is far from being a clean and cheap energy vector. This is why many researchers are working on the production of hydrogen, and on the numerous processes this molecule requires to be safely used. The electrochemical hydrogen compressor, EHC, is a technology that works on the concepts of PEMFC and PEM water electrolyzers (PEMWE) to purify and compress hydrogen at a much lower estimated cost than in presently-used systems. It also presents the interesting advantages of working soundlessly, without adverse generation of by-products, and can be implanted at a local scale, such as in a network of hydrogen refilling stations, for example.

The EHC technology however faces one main challenge in order to combine both the purification and oxidation steps: it necessitates the use of an electrocatalyst that is both very active towards the hydrogen oxidation reaction (HOR), and tolerant to high concentration of impurities, such as 1% CO. Platinum, known to be very active for the HOR, is also very vulnerable to poisoning. The state-of-the-art CO-tolerant material presented by the literature, PtRu alloy, does not have an activity high enough to sustain the 2 A cm^{-2} required for this technology to be energetically competitive.

This thesis project was created from the desire to find an electrocatalyst responding to these ambitious criteria. It was funded by the Auvergne-Rhône-Alpes Region in France, which, with its plans for a "Zero Emission Valley", wishes to develop the hydrogen economy at a local scale.

The first step of this work was to synthetize and compare two types of electrocatalysts, chosen for their promising CO-tolerance from the literature. Pt+Ru/C, a composite of both Pt and Ru nanoparticles supported on carbon, could ally both the HOR activity of the Pt, and the CO-tolerance of the Pt alloys. Pt nanoparticles supported on tungsten oxide, Pt/WO_3, is known to oxidize CO at very low potential, but with poor durability. A novel morphology was synthetized, with the aim to render the material more robust in operation.

Both families of materials were then extensively tested towards the CO and hydrogen oxidation reactions, firstly in a classical setup in electrochemistry: the rotating disk electrode (RDE). This setup enabled to unveil some of the properties of these materials and to propose a first ranking of the electrocatalysts in view of their application in an EHC anode. However, the RDE, although commonly used in electrocatalysis, is impeded by high mass-transport limitations when the reactants at stake are gaseous (here H_2), preventing any operation at high current densities, a clear drawback for the targeted application.

To counter the inherent drawbacks of the RDE, the last step if this work consisted in comparing each electrocatalyst towards the HOR (and the HOR in presence of CO), in a more realistic and righteous manner. To that goal, the gas diffusion electrode (GDE) setup was employed; after some technological development of the technique, the electrocatalysts could be compared at current densities approaching those required in an EHC.

CHAPTER I

General context and State-of-the-art on EHC technology

Chapter I General context and state-of-the-art on the EHC technology

I.1. From climate change to fuel cells

I.1.1. Global warming and pollution

Today's world is the place of many challenges and questioning. Since the beginning of the industrial area, mid-19th century, the world has undergone so many changes and developments that it is impossible to compare this period to any other period. Globalization, life quality improvement, lifespan improvement, development of transport, communications, energy sources… No area is left behind.

Of course, such a development comes with a price, though it was only recently discovered [1]. In many places around the world, the climate is changing, shifting. This process is unequal, affecting some regions more (notably the poles and temperate areas) than others, but nonetheless present.

The increase of temperatures was measured in many countries in the recent years [2,3]. In fact, 2020 and 2016 were graded the warmest years ever measured, since record-tracking began in 1880 [4]. In 2019, the GIEC estimated the global warming since the pre-industrial area of 1.5°C [5] Figure I.1. The climate however, is a vast and complex system with many interactions, with often an escalating impact through a chain of consequences. Such a fast and global temperature increase then leads to more frequent and more intense natural disasters, resulting in local floods, droughts, forest fire, etc., but also to chronic and large-scale desertification or ice melting.

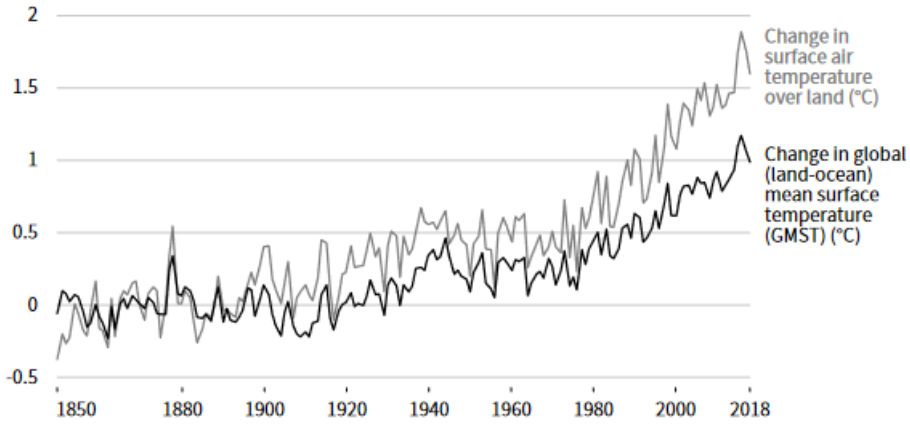

Figure I.1: Evolution in air and global (land-ocean) temperatures, relative to the mean temperature between 1850 and 1900 [6].

At the north pole, ice melting is accelerating. Specialists calculated its possible complete disappearance in summers as soon as 2035 [7]. And this comes with many consequences: ocean level rising, endangered species natural habitat disappearance, melting of Permatfrost (a type of land that stays frozen for more than 2 years) [8]. The latter could provoke the liberation of a large quantity of greenhouse gases, as well as ancient biogic agents, some of them related to lethal diseases (pest, spanish flu, etc.), which cannot leave us stoic in these times of pandemic.

Meteorologists and scientists of the whole World now agree on the reality of global warming. Though many climate changes happened before in Earth's history, the current one was declared too fast and too consequent to be due only to natural causes [9,10], especially when its exact beginning can be traced back to the industrial revolution period, when coal industries were massively implanted.

The increase of greenhouse gases in particular, has been closely monitored since that period. The greenhouse effect is a natural phenomenon which permits the presence of life on earth. It is provoked by the accumulation of several gases in the atmosphere: mainly carbon dioxide (74%), methane (17%) and nitrous oxide (6%) [11]. All of them have a different impact, that can be normalized as CO_2-equivalent. Their concentration is directly linked to the global surface temperature of Earth. An increase in the concentration of those gases, especially CO_2, was measured over the recent years. Figure I.2 represents the amount of CO_2 emissions by year by countries. Since 1950, our global CO_2 emissions has been multiplied by 7.

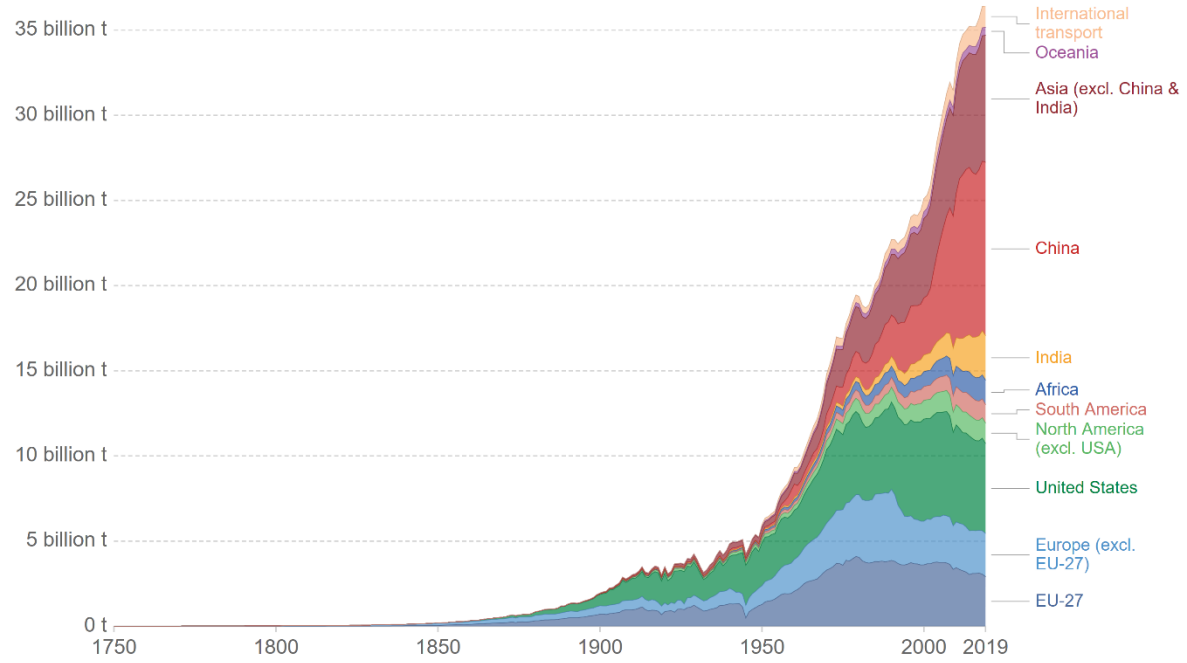

Figure I.2: Annual CO_2 emissions by world regions from fossil fuels and cement production (land use change is not included), based on the Global Carbon Project [12].

The major actors of this increase are the developed countries, with China and United States in the lead, and the groups of European and Asian countries close behind. Those emissions come from many different sources (Figure I.3). In first position, the energy sector makes 72% of these overall emissions, electricity and heat generation being the main causes. Then comes transportation and manufacturing domains, and agriculture.

As a consequence, a global consensus is that the global energetic mix needs to be changed. All around the world organisations and countries are moving ahead to try and decrease if not stop the phenomena.

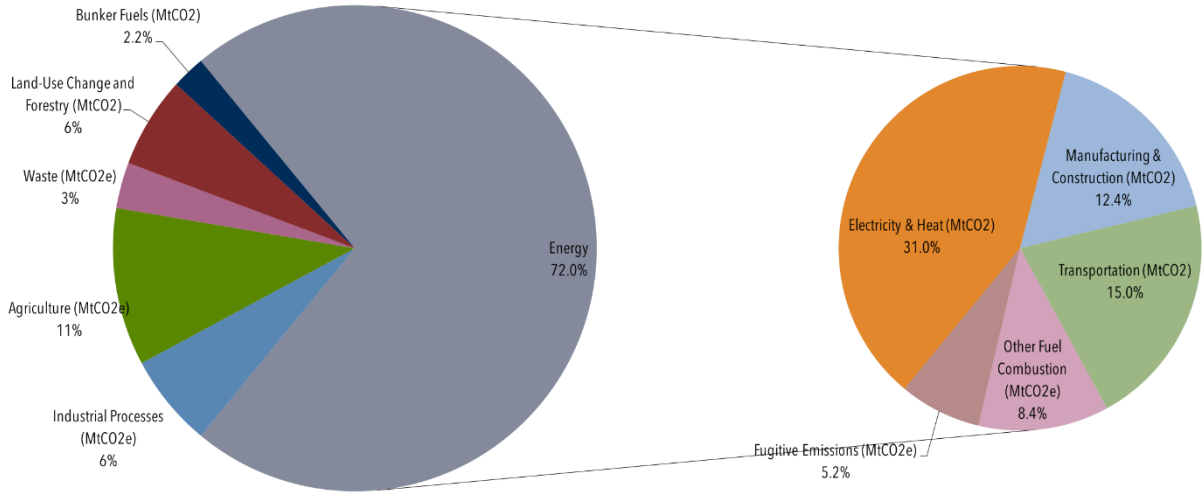

Figure I.3: Global manmade greenhouse gas emissions by sector, 2013 [13]

In 1997, The Kyoto protocol, with today 192 signing countries [10], aimed to limit the total amount of CO_2 emission per country. More recently, in 2015, the Paris Agreements were signed by 175 nations (now 182), which engaged to take all actions to limit the temperature increase below 2°C [14]. Following that , the European commission as well as Japan exposed their wish to respect these agreement and attain a objective of zero emission in 2050 [15,16]

For that, there are different possibilities: one of them is to reduce CO_2 emissions.

I.1.2. Towards a new energetic mix

The energetic mix is the repartition of the sources for the energy production in the world. Figure I.4 presents the global energetic mix in 2018. This mix was dominated by coal, oil and natural gas, three fuels qualified as “fossil” based on their consumption of a limited material formed by geologic processes over time. These fuels all contain carbon, and their usage rejects a large amount of CO_2. The portion of renewable sources (which are carbon-neutral) is of 14%, biofuels in first position, which is by far insufficient if one wants to reach the ambitious goals mentioned above.

The idea is then to reduce the part of polluting sources such as coal industries to replace them by greener energies. Renewable energies are obvious candidates. They harvest energies from natural, non-limited sources (solar light, wind, …) and can be used at the local scale. However, their production process must also be taken into account. Off shore wind turbine for example, contains around 400 kg of neodymium. As a rare earth material, this element is only located in some specific places in the world (mostly China, India and …) and its extraction process is very polluting, not speaking from the safety of the extraction/processing/use of the ore [18,19].

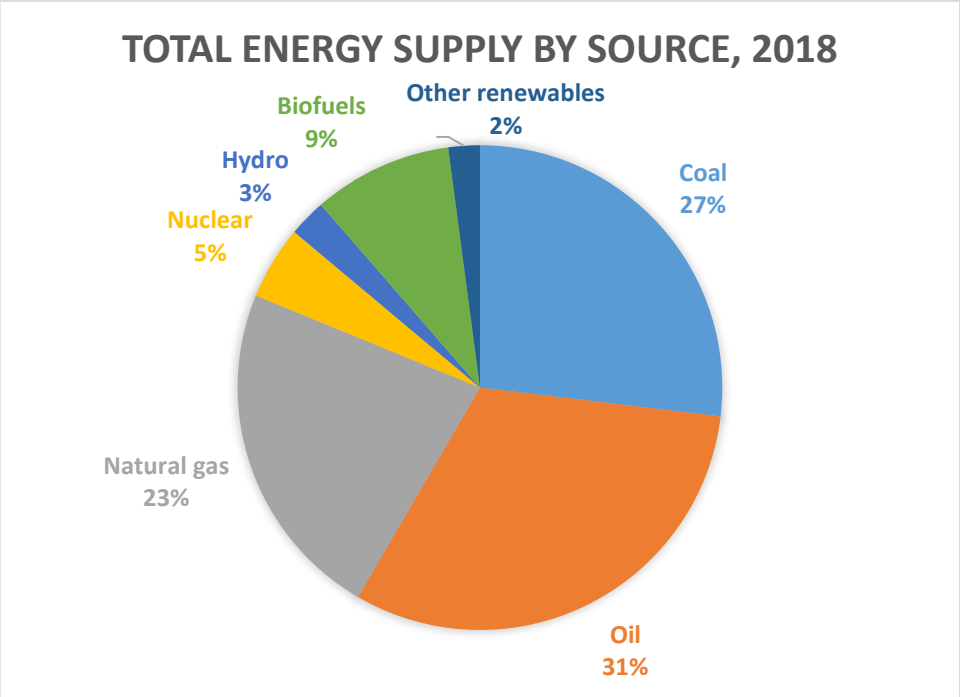

Figure I.4: Total primary energy supply by source, for the world in 2018 [17].

Renewable energies are still at their development, though, and still have a wide margin for improvement, notably for their choice of key materials, their efficiency and their usage (smart grid, …). One of their specificity, compared to coal and nuclear based industries, lies in their inherent intermittency for electricity production. Solar panels mostly produce electricity during the day and in summer, the production of wind turbines also scaling with the wind force, that also depends on daylight; so, in order to keep the electricity for later consumption (both on daily and seasonal scales), electricity storage is mandatory.

There are several possibilities to store electricity. One of them are batteries, that already exist in our everyday life: from mobile devices to transport, to stationary storage. However, it seems hardly feasible to deploy them at the large scale (because they are based on critical materials [20], and for long-term seasonal storage (because they self-discharge) [21]. Reversible dams are also popular, but most sites where it can be implemented are already saturated (at least in developed countries), not speaking from their non-negligible environmental impact. Another very actual solution consists of power-to-gas and notably in power-to-hydrogen. Hydrogen is the first element of the periodic table and, despite being very abundant on the planet, dihydrogen (H_2, it will be referred in this manuscript as simply “hydrogen”) is only merely present naturally on Earth. H_2 can however be produced from water and energy, stored in multiple ways, and then reused to produce electricity in a fuel cell. It is wise to say that these multiple means complement each other, and all have their own advantages and drawbacks, depending on when and for what they are implemented.

I.1.3. Hydrogen in industry and as an energy vector

A virtuous hydrogen economy works around one main technology, capable of converting hydrogen and oxygen into electricity, with only water as an outlet: the fuel cell. In the reverse reaction, hydrogen can be produced by providing electricity (from renewable energies for example) and water. This promising concept brought the attention as one of the solutions to attain carbon neutrality.

This leads to a global enthusiasm towards the possible use of hydrogen as an energy vector. France recently voted a budget of 7 billion euros or the next 10 years [22] to support research and development on the hydrogen vector. Globally, the European commission estimates a cumulative investment for hydrogen (production and usage) up 470 billion euros until 2050 [15,23], so as to develop the hydrogen grid, and encourage both research and applications.

Many of such application are concentrated in the transport sector, second sector in terms of CO_2 emissions behind electricity production [24], but also in H_2 for the industry (fertilizer, metallurgy, etc.).

The first hydrogen vehicle commercialized was the Toyota Mirai, in 2014. After 3000 vehicles sold each year, the new version, the Mirai 2, is very promising [25,26]. With its stored capacity of 5.6 kg of Hydrogen, the new model can drive for 650 km with a refill of only 3 minutes [27]. Honda and Hyundai now also have their own hydrogen model. In France, Symbio [28] adds an hydrogen tank to commercial electric vehicle to increase its autonomy (range extender). Buses [29], trucks [25] or even garbage trucks fleets (HECTOR European Project) [30] now have an hydrogen version, taking profit from their fixed journey to efficiently recharge them.

Road vehicles are not the only ones being converted to fuel cells. In 2018, Alstom lunched its ILint Coradia, the first hydrogen train [31,32]. In aeronautics, the European Group Airbus announced its ambition to commercialize the first non-emission aircraft (based on hydrogen technology) by 2035. Several boats also work with a fuel cell device, as the Energy Observer for example [33].

I.1.4. Fuel Cells

The first fuel cell was first experimented by Sir William Grove and Christian F. Schoenbein in 1838. They measured a voltage between two platinum plates, each associated to either a hydrogen or oxygen-containing tube and separated by acidified water [34]. It had to wait nearly a century, before Francis Thomas Bacon made it into a full stack prototype, in 1932 [35]

During the 60's 70's, an alkaline type of fuel cell was used for both Gemini and Apollo mission, preferred to batteries for their light weight and convenient water cycle.

Since that period, the fuel cell concept of oxidizing a fuel at the anode while reducing an oxidant (often oxygen) at the cathode, has been applied to several systems. The major ones are detailed in Table I.1 [35–38]. There are in fact many types of fuel cells, depending on the nature of the fuel, the electrolyte and the operating temperature. Instead of hydrogen, the direct ethanol fuel cells (DEFC) and direct methanol fuel cells (DMFC) use ethanol and methanol as a fuel, respectively,

which eases the fuel handling and storing and makes them suited for portable applications, but their performances are severely hampered by the too complex, hence sluggish fuel oxidation reaction. High temperature fuel cells such as solid oxide fuel cells (SOFC), or molten carbonate fuel cells (MCFC) are more adapted to stationary power plant, and present the advantage of possible direct use of reformate gas. Their operational durability is however not granted.

Table I.1: Common features of different fuel cell types

Type of Fuel Cell	Fuel	Ionic conductor	Operating Temperature (°C)	Electrical Efficiency (%)	Qualified Power (kW)	Application
Alkaline (AFC)	H_2	KOH	70-100	60-70	10-100	Mobile
Direct Methanol (DMFC)	CH_3OH	proton conducting polymer	90-120	20-30	100-1000	Mobile
Direct Ethanol (DEFC)	C_2H_5OH	proton conducting polymer	90-120	20-30	100-1000	Mobile
Proton Exchange Membrane (PEMFC)	H_2	proton conducting polymer	80-100	30-50	0.1-500	Mobile / Stationnary
Phosphoric acid (PAFC)	H_2	H_3PO_4	150-220	40-55	5-10000	Stationnary
Molten Carbonate (MCFC)	H_2	immobilized alkaline solution	650-700	50-60	100-300	Stationnary
Solid-Oxide Fuel Cell (SOFC)	H_2	ZrO_2-Y_2O_3	800-1000	50-60	0.5-100	Stationnary

PEMFC is the technology mostly used in transports today. Because a unit cell only operates at a voltage of ca. 1 V, PEMFC systems usually consists of stacks of several unit cells, each cell containing 4 main components:

The **ionic membrane** is made of a proton conducting polymer. It enables proton conductivity and electrode separation (both electrical and in terms of reactants).

The **catalyst layers**, on both sides of the membrane, are made of carbon, proton conducting ionomer, and electrocatalyst. Their role is to provide triple contact regions between gas, electrons and ions, a prerequisite for the reactions to take place.

The **gas diffusion layers (GDL)**, on both sides of those catalyst layers, are porous carbon matrices, enabling both gas distribution, product draining and electronic/thermal conductivity.

These three components (and (sub)gaskets) constitute the membrane-electrodes assembly (MEA).

The **bipolar plates** maintain the MEA under compressive strain (hence gas tightness) and are in charge of electronic conductivity, gas distribution and single cell separation. They bring oxygen on one side, and hydrogen to the other side of each MEA.

Figure I.5 gives a schematic representation of the functioning of a PEMFC. The anode is furnished with hydrogen, that will be oxidized into protons in the catalyst layer. The electrons flow into the electronic circuit to reach the cathode side, thus creating an electrical current. The protons cross the polymer membrane, and participate in oxygen reduction. Pure water is produced at the cathode.

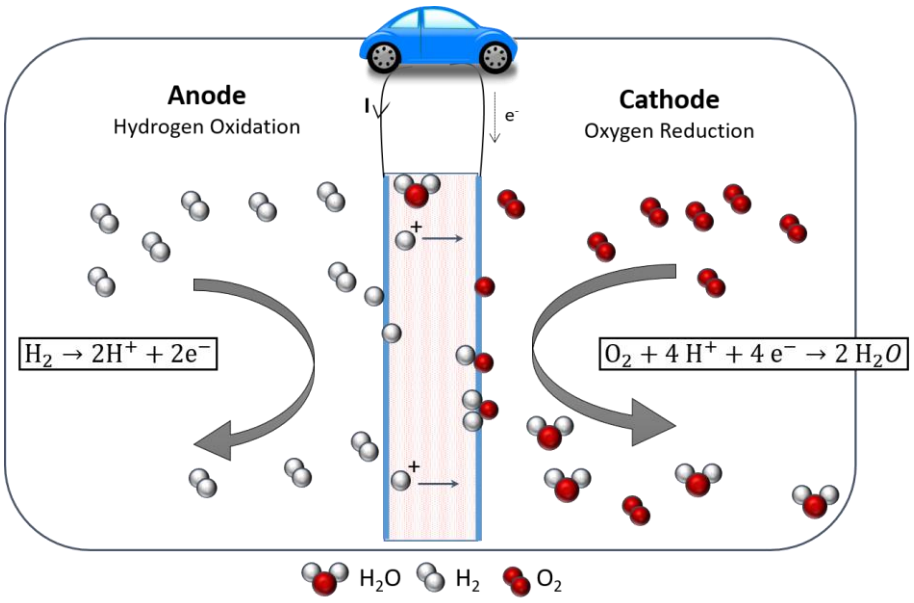

Figure I.5: Schematic representation of a PEMFC

I.1.5. Hydrogen Production

As of today, 99% of the world's hydrogen is produced by "Grey Hydrogen" (Hydrogen production routes are often referred to with a colour code, connoting their ecological value) : mostly steam methane reforming (SMR) and coal gasification [39]. Both techniques are known to produce carbon dioxide as well as hydrogen. The maturity of those techniques permits the production of hydrogen at the lowest cost today: it sold less than 2 USD/kg_{H2} (~1.5 euros) [25,40].

When Carbon Capture, Utilization and Storage (CCUS) is used to prevent CO_2 from reaching the atmosphere, the hydrogen produced by those process is called "Blue Hydrogen". CO_2 emissions per mass of hydrogen can be reduced by four with such a technique, as shown on Figure I.6. Only 0.5% of SMR Hydrogen was produced this way in 2018 [40].

For the hydrogen economy to be completely viable and ecological, it is not only the technology, but also the fuel source that has to be low-carbon emission [37,41,42]. "Green Hydrogen" qualifies the hydrogen produced with electricity from renewable sources, e.g. via water electrolysis powered by renewable electricity. It is the endeavour of the hydrogen strategies, but its cost is

still high compared to grey hydrogen, and needs to be reduced by decreasing the cost of renewable electricity and of water electrolyzers, and by increasing their efficiency. Today, less than 2% of H_2 is made this way [39]. The null carbon impact present in Figure I.6 has to be nuanced however, since renewable energies can also responsible for CO_2 rejection, especially during their conception.

Hydrogen made with electrolysis with other electricity sources does not have a defined colour, and it is wise to say that, depending on the electricity grid of each country, the carbon impact will vastly differ. For instance in China (Figure I.6) electricity is mostly produced from coal, which explains the high carbon emission of electrolysis from the electricity grid.

The case of biomass is also an ambiguous one, as it depends on the source of fuel. Biomass gasification is the process used to produce syngas, a mixture of hydrogen and carbon monoxide. The latter can be used to produce more hydrogen through the water gas shift reaction. When properly filtered at the outlet with CCUS (to prevent carbon and nitrogen oxides to go into the atmosphere), it becomes a negative carbon-emission, hence green, process [43–45].

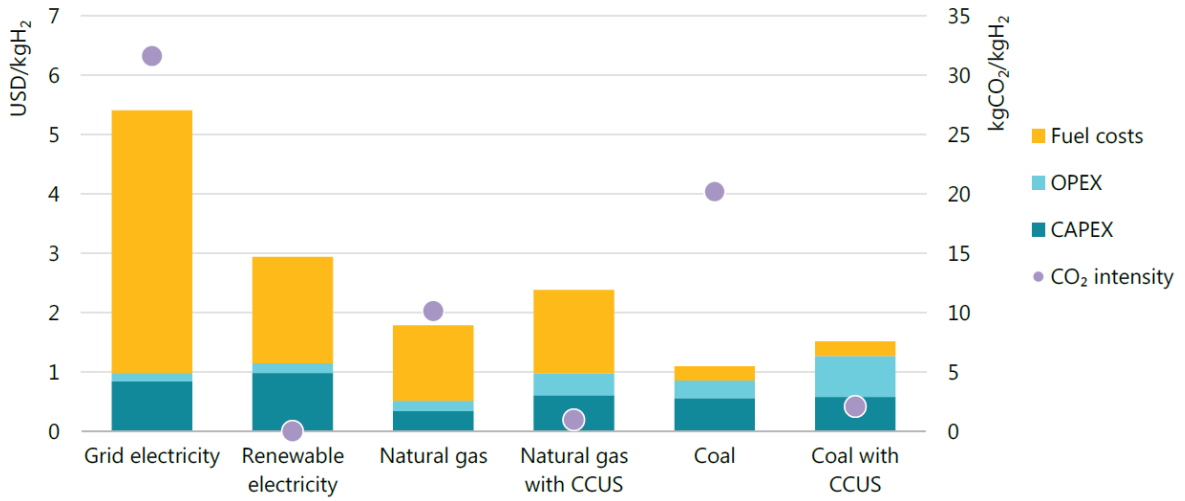

Figure I.6: Hydrogen production costs and carbon emissions per source in China in 2019 [40]. *CAPEX= Capital expenditure, OPEX= Operating expenditure; respectively representing the investment cost and the operating cost.*

Very recently, researchers found that the existence of natural hydrogen was not as rare as it was previously thought. It appears that hydrogen is produced underground, mostly in areas were ultramafic rocks (containing Fe and/or Mg) and water [46–52]. Those conditions are gathered offshore, on the oceanic ridge, but also onshore (around 4-10 10^6 kg_{H2}/year/km_{ridge} [51]), as hydrogen vents were found in Mali, Brazil, Russia, France, etc. In Mali, this source is already used since 5 years without any pressure loss. In this production, the hydrogen cost is even lower than for STM: less than 1 €/kg_{H2}.

As of today, hydrogen cost is still higher than for other fuels. At Paris for example, one can buy 1 kg of H_2 for 10-15 €, or 1 L of petrol for ca. 1.6 €. This means that for an equivalent powered car, the user will pay between 8.6-13 € for 100 km in a hydrogen powered car (here calculated for a Mirai II), against 9.5 for a petrol powered car (with an estimation of 5.9 L/100 km). This cost comes from the hydrogen production chain before its use in fuel cell, from production to purification and compression. To reduce that price, the cost of production has to be reduced (renewable energies

and electrolysis cost for example), but also the cost of all processes needed upstream its final use in fuel cell. Obviously, compression and purification of hydrogen, must be considered.

I.2. Compression and Purification of Hydrogen

Most of the contents presented here are inspired from a set of two review articles written in collaboration with Maha Rhandi:

M. Rhandi, M. Trégaro, F. Druart, J. Deseure, M. Chatenet, « Electrochemical hydrogen compression and purification versus competing technologies: Part I. Pros and cons », Chinese J. Catal. **2020**, 41, 756–769.

M. Trégaro, M. Rhandi, F. Druart, J. Deseure, M. Chatenet, « Electrochemical hydrogen compression and purification versus competing technologies: Part II. Challenges in electrocatalysis », Chinese J. Catal. **2020**, 41, 770–782.

I.2.1. Main compression/purification technologies of today

Contrary to electrolysis, where hydrogen purity reaches 99.999% excluding water vapour [53,54], most of hydrogen production routes may include large amounts of impurity in the hydrogen outlet flow. A purification step is hence required prior any use in a fuel cell setup. The hydrogen purity benchmark is detailed in section I.2.3.8 for each impurity [55,56]. Meeting this purity is essential to ensure proper fuel cell functioning and lifespan. Furthermore, hydrogen volumetric energetic content is very small at room pressure, making it mandatory to compress it to high pressures to compete with usual fuels [57].

This part will present each technology used for either compression and purification, before presenting the electrochemical separation/purification and compression processes.

I.2.1.1 Separation/purification processes

The most widely used hydrogen purification method today for petrochemical and chemical industries is Pressure Swing Adsorption (PSA), commonly associated to steam methane reforming production plants [58]. This process uses the adsorption capacity of some solid surfaces (zeolite, activated carbon, …) under high pressure to capture selected gases from a mix at high pressure, to then free them under low pressure. With its high energetic cost (especially from compression unit) [59] PSA is more adapted to high scale units and to gross separation more than to high-purity applications.

Temperature Swing Adsorption (TSA) is also widely used. It follows a similar principal with PSA and presents the same main drawback: its very high energy consumption makes TSA more adapted to large scale units [60].

Cryogenic processes operate at very low operating temperatures (-253°C); as the two previous technologies, they are highly energy-consuming, making their use in high scale units preferable (thus not relevant to dispersed hydrogen station network). They however present the benefits of liquid hydrogen storage, lowering the H_2 storage footprint [61].

Membrane separation works with a high pressure gradient between the gas inlet and outlet, thus pushing the gas through a selective membrane. Porous membranes, dense and protonic membranes can be used for that application [62]. It permits high values of hydrogen purity (higher than PSA and cryogenic). This technology is currently limited to small scale units.

The electrochemical hydrogen compressor (EHC) will be detailed in section I.2.2.

A comparison of those technologies is presented on Figure I.7. Five markers were chosen for the comparison: gas recovery (1% to 20% purge-to-feed ratios), operating temperature convenience (1 for 25 < *T* < 200°C, 0.5 for 200 < *T* <500°C and 0.2 for *T* < 0°C or *T* > 500°C), compatibility of the system with continuous operation (regenerative to external regenerative methods), energetic cost of the process (with the use of Agrawal *et al.* classification [63]) and gas purity that can be reached with the system. More details are given in the related publication [64].

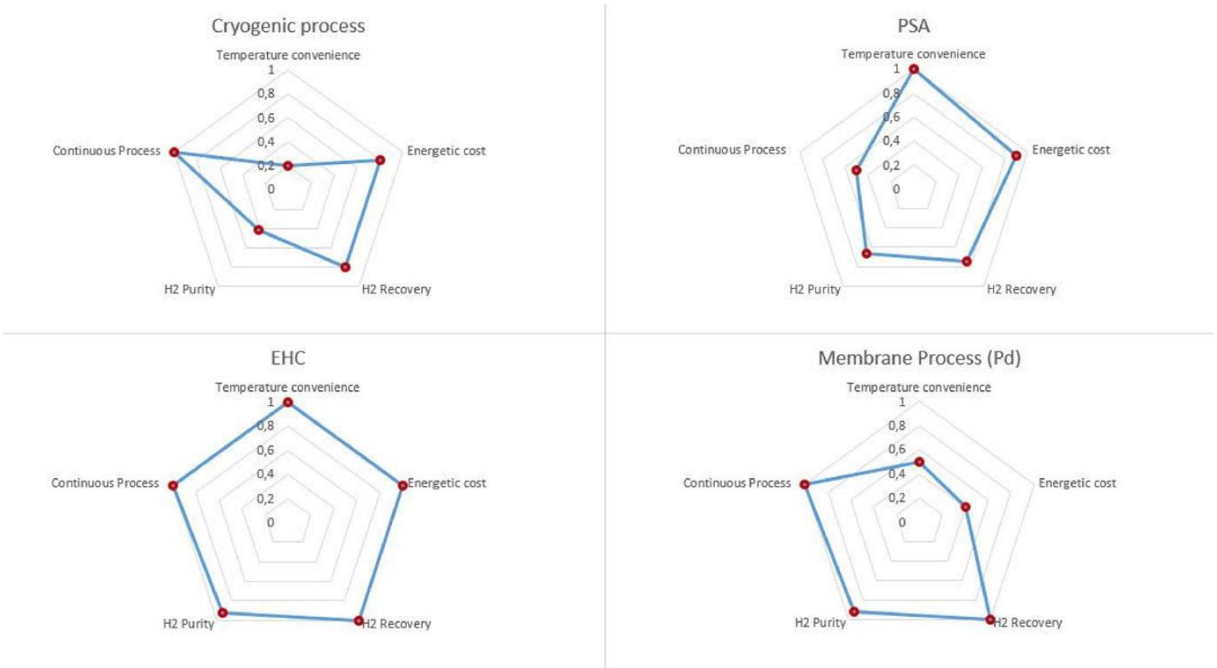

Figure I.7: Comparative diagram of the performances of different hydrogen purification methods [64]

I.2.1.2 Compression processes

As of today, most of the industrial compression is done with the mechanical compressor technology. As the name states, it uses mechanical force to reduce the volume of a gas, and thus increase its pressure. The used energy can be for pneumatic or electrical, the later requiring lower

energy [65,66]. Because of its very low adiabatic coefficient, hydrogen demands nine times more energy than methane to be compressed, and fifteen times more than air. The energy consumption of hydrogen compression can therefore not be considered negligible, by far. There are several types of compressors, as detailed hereafter.

Linear mechanical compressors lower the cost of compression by decreasing the amount of rotating components. Operation in absence of lubricants in the system is possible, thus increasing the outlet hydrogen purity. It is mainly used in small domestic refrigeration and cryogenic systems [67,68].

Ionic liquid compressors present high compression ratio with a very high efficiency for hydrogen. Ionic liquids present many useful advantages due to their low vapour pressure, their great lubrication characteristics and high thermal stability [69]. However, cavitation issues can occur, as well as leaks of (usually very corrosive) liquids [70].

Thermal hydrogen compression by metal hydrides relies on the reversible insertion/de-insertion process of hydrogen in a hydride-forming metal [71]. This technique appears to be one the most promising for hydrogen compression. System operating costs can be greatly decreased with the use of heat wastes produced by the industry. The process is also simple and safe, a great advantage for the application. It however necessitates some costly and specific material that are very sensitive to impurities (e.g. O_2 or H_2O). Their coupling to a purification system upstream is therefore essential [72,73].

Another compressor system is the hydrogen electrochemical compressor. It will be described below.

I.2.2. Hydrogen electrochemical compressor (EHC)

Most industrial techniques of hydrogen post-treatment after production use separate steps for the purification and compression processes. Despite its name, the EHC enables both the purification and compression of hydrogen in the same step. It is based on a membrane electrode assembly (MEA) very similar to those used in PEMFC or PEM water electrolyzers, with two gas-diffusion electrodes, a solid (usually polymer-based) electrolyte located in between the electrodes. Its core, the MEA, comprises two catalysts layers, on each side of the polymer electrolyte.

This system consumes electrical energy to oxidize hydrogen at the anode and reduces it at the cathode. Provided the protonic conducting membrane is selective to protons and impermeable to gases, protons are the only species crossing the membrane from the anode to the cathode (Figure I.8) and the cathode reaction must be the hydrogen evolution reaction, producing pure H_2 (if necessary under pressure – provided the operating conditions are appropriate). The mechanism driving this application can be summarized by the two electrochemical reactions for the hydrogen oxidation reaction (HOR) (Equation (I.1)) and hydrogen evolution reaction (HER) (Equation (I.2)):

$$H_2 \rightarrow 2\,H^+ + 2\,e^- \quad \text{(I.1)}$$

$$2\,H^+ + 2\,e^- \rightarrow H_2 \quad \text{(I.2)}$$

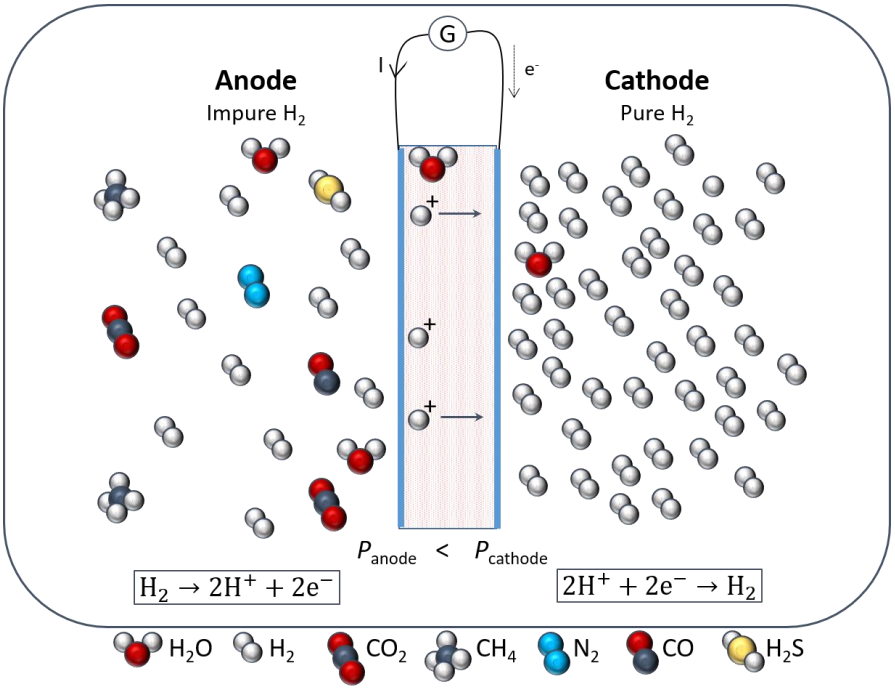

Figure I.8: Operation principle of an electrochemical hydrogen compressor

The electrochemical compression process obeys the Nernst equation, involving hydrogen partial pressures at the inlet $P_{H2,\,anode}$ and at the outlet $P_{H2,\,cathode}$. It also involves other processes such as the ohmic drop U_{ohmic} present at the MEA, mostly dependent of the protonic conductivity and thickness of the membrane, $U_{transport}$ related to mass transport limitations, as well as the overpotential related to charge transfer resistance on the electrocatalysts η for the HOR and HER. Considering fast kinetics for these two reactions on a Pt-based catalyst, this value should however be very small. The cell voltage $U_{compressor}$ is then given by equation (I.3):

$$U_{\text{compressor}} = \eta + U_{\text{ohmic}} + U_{\text{transport}} + \frac{RT}{2\mathcal{F}} \ln\left(\frac{P_{\text{H}_2,\text{cathode}}}{P_{\text{H}_2,\text{anode}}}\right) \quad \text{(I.3)}$$

where R is the gas constant, T the temperature, $\mathcal{F}$ the Faraday constant. This equation shows that by increasing the cell voltage, it is possible to increase the ratio between $P_{H2,\,anode}$ and $P_{H2,\,cathode}$, thus increasing the pressure at the cathode side [74]. This pressure gradient is only limited by the intrinsic mechanical and separation properties of the membrane, meaning that very high pressure gradient can be achieved in principle [75,76]. The Dutch company HyET, effectively performed a 1000 bar of compression using a single stage electrochemical compressor, an outstanding performance (obtained for a small demonstration cell: 1 cm² geometric area) [77].

Nevertheless, without going as far as 1000 bar, only increasing hydrogen pressure from room pressure to 30-100 bars would be enough to lower in a significant manner the cost of H_2 compression, usual compressor implying a large operation cost from 1 to ca. 30-50 bars.

EHC present both advantages of a high efficiency and its compatibility with pure H_2 grades, because the systems operates lubricant-free, owing to the absence of moving part (often present in other compression applications); EHC are also compatible with confined or urban operation,

because they do not generate noises [78]. Their isothermal operation, thus necessitating no outside temperature regulator, can be done in one or several stages. For the EHC to reach performances of the best purification system presented in I.2.1.1, a geometric current density of at least j = 2 A cm^{-2} is however necessary.

Whereas reaching so high current density at reasonable cell voltage is viable for an EHC that only compresses hydrogen (pure H_2 at both the anode and cathode), it is far more critical if one wants to combine the compression and purification steps into a single EHC chamber, the real endeavour. Indeed, this would require fast oxidation of hydrogen at the anode, even in presence of non-negligible amounts of impurities; the common HOR material (Pt/C) is actually hardly capable of this, as critical impurities (e.g. CO or H_2S) strongly affect its HOR capabilities. This issue will be addressed in details in I.3.3.

I.2.3. Effect of impurities on common PEMFC anode catalysts

One of the main goals of the EHC is precisely the production of compressed hydrogen gas, pure enough to serve as a PEMFC fuel, starting from impure hydrogen produced from reformates, biomass or natural hydrogen harvesting for example. Table I.2 presents the hydrogen content range for the most common hydrogen sources. This will be, hypothetically, the gas inlet for the EHC, meaning the anode will have to maintain HOR current around 2 A cm^{-2} with the presence of impurities; for some of them, such as CO, CO_2, H_2S, CH_4, NH_3, … this is a very ambitious goal.

Table I.2: Hydrogen composition depending on its production source [47,49,50,79]

	Natural hydrogen	**Steam reforming**	**Coal gasification**
H_2 (%)	27-97.4	94.3	87.8
N2 (%)	3-68	0.2	5
CO_2 (%)	0-45	2.5	3.9
CH_4 (%)	0-69	2.9	0
Ar (%)	0-9	0	0.9
CO (ppm)	0-1000	1000	26 k
H_2S (ppm)	0-20 k		

As of today, no articles have been published on the EHC tolerance to such gas mixtures. This is however not the case for the PEMFC, for which the behaviour in presence of H_2 reformates at the anode has been vastly studied. As a matter of fact, PEMFC and EHC present very similar environments at their anode: their operating temperature is in a range of 25 to 80°C and their anode potential has to be as low as possible. Most studies focus on platinum and platinum-based electrocatalysts.

The limit of this comparison has to be kept in mind however: (i) EHC does not have air at the cathode, only pure hydrogen (hence no produced humidity by the oxygen reduction reaction, ORR), (ii) Hydrogen evolution reaction (HER) at the cathode is not limiting contrary to the ORR, and (iii) a high pressure gradient is present between the two electrodes. Despite those discrepancies, PEMFC studies present a picture similar enough to rely on so as to determine the respective effect of each impurity, especially towards platinum, and their possible countermeasures.

Effects associated to each reformate impurities will be presented in the following sections.

I.2.3.1 Inert gases

In Hydrogen reformates or in natural gases, argon and nitrogen can be expected in small proportions. In PEMFC, those gases are referred to as “inert gases”, and thus, should not impact the catalyst layer. However, a well-known starvation phenomenon often occurs in PEMFC anodes used in a dead-end mode, where the hydrogen content is locally decreased because of nitrogen crossover from the cathode side. Because of that, both performances and durability are negatively impacted, especially at the cathode side [80,81].

Um *et al.* proposed a model to calculate the consequences of such hydrogen dilution [82]. It appears that in a stoichiometry of 2.8 at T = 80°C with a current density of j = 2 A.cm^{-2}, there is no effect on the cell performance if the hydrogen percentage is kept above 50% (Figure I.9) [82]. In the case of a content lower than 50%, the potential starts to decrease, especially for high current densities, hinting to possibly induced mass transport limitations.

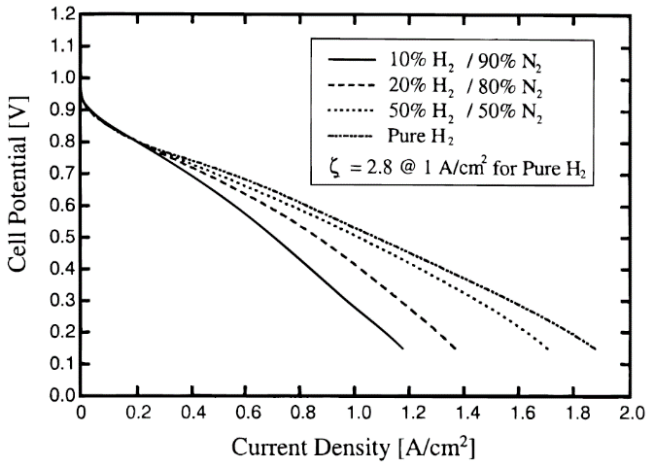

Figure I.9: Effect of molecular hydrogen fraction inlet in cell polarization curves with dry cathode – PEMFC mode [82]

These results were confirmed by several PEMFC studies for nitrogen concentrations higher than 50-60% [83–85]. The EHC operating at very high current densities, it could be severely impacted by such fuel starvation. A recommended maximum limit content of 6% of inert gases seems wiser. In the case of dead-end or multi-stage EHC, more significant performances effects will occur, hence necessitating appropriate measures [86].

In PEMFC, dilution issues seem to be the sole problem related to inert gases. In the case of EHC however, recent advances show that the high pressure gradient stimulates the reduction of N_2 (at the cathode) into NH_3, thus creating severe pollution of the membrane (see part on NH_3 for more information) [87].

I.2.3.2 CH_4

Depending on the hydrogen source, methane presence can be found from 3% to 90-95% [79] (the latter value makes sense if ones uses natural gas pipelines to transport H_2). The literature is however quite poor on the subject of CH_4 effect in EHC or even PEMFC. A study from 2007 focuses on the electrochemical separation of hydrogen from natural gas and its efficiency [88]: from a H_2/ CH_4 feed, more than 80% H_2 recovery was performed, without any dependence on the inlet flow. Changing the temperature from -30°C up to 45°C, only 20 mA cm^{-2} of difference between the current limits was measured, under the same feed. For an 8% hydrogen content in either CH_4 or Ar gas, similar current densities were reached. Working at 140°C, Chen measured no difference between N_2 and CH_4 dilutions as well.

From these informations, methane appears to mainly dilute hydrogen on Pt-based electrocatalysts, and should have similar effects to those described for argon in the previous section. As such, no real issues are anticipated with CH_4 impurities for the operation of an EHC anode.

I.2.3.3 CO_2

Because of its high content in hydrogen reformate, where it is the main by-product, carbon dioxide received a lot of attention from the PEMFC community. Its behaviour towards Pt-based electrocatalysts is also quite ambiguous: are its effects more similar to those of inert gases, or does it poison the catalyst surface? In 1963, Giner [89] studied the influence of carbon dioxide towards PEMFC, and the related mechanisms. It appeared that CO_2 had more effect than just hydrogen dilution. Later, Gu *et al.* compared the respective effects of hydrogen dilution in nitrogen or carbon dioxide [90]. Their results, shown in Figure I.10, agrees with Giner's data: a non-negligible difference of performance is noted between operation under CO_2 or an inert gaz. This experience is totally relevant for the present EHC study, since they used the hydrogen pump configuration (cathode filled with hydrogen).

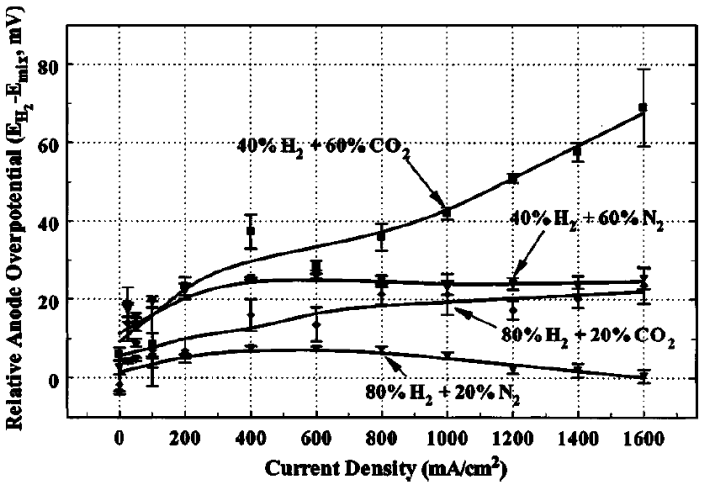

Figure I.10: Comparison of cell performances with N_2/ H_2 and CO_2/ H_2 anode inlets in similar proportions [90]

According to the studies that thoroughly investigated this phenomenon [85,89,91,92], a reverse water gas shift reaction (RWGS) seems to be the cause of such a difference. This reaction is believed to occur in two regions. Firstly, in the gas phase, when both gases are already in contact, following reaction (I.4). In order to reach the equilibrium, an amount of 10 to 100 ppm of CO can be produced. More precisely, for a gas made of 99% H_2 and 1% CO_2, at a temperature of 70°C, Gu *et al.* calculated a formation of 10 ppm CO.

$$CO_2 + H_2 \rightarrow CO + H_2O \quad (I.4)$$

Secondly, the RWGS can also be enhanced in presence of platinum (electro)catalyst, with CO_2 reacting with adsorbed proton (H_{ad}, reaction (I.5)) to produce CO groups (reaction (I.6), well-known for their easy Pt-poisoning (detailed in section I.2.3.5).

A mechanism was suggested by Giner *et al.* [89] to describe that process:

$$2\ Pt + H_2 \rightarrow 2\ Pt\text{-}H_{ad} \quad (I.5)$$

$$CO_2 + 2\ Pt\text{-}H_{ad} \rightarrow Pt\text{-}CO + H_2O + Pt \quad (I.6)$$

Diaz *et al.* found that the carbon dioxide effect gets worse with its increasing content in the hydrogen feed [93], in agreement with Figure I.10. With a current density of j = 600 mA cm^{-2}, 10% CO_2 leads to an overpotential of η = 43 mV, against η = 62 mV for 25% CO_2.

However, CO adsorption on Pt being very strong, the available Pt sites will decrease with time, thus decreasing that same CO production [94]: this will minor CO production (an advantage), but also decrease the anode performance (a clear drawback). Several groups verified the CO adsorption on the electrocatalyst surface in this case, mainly with cyclic voltammetry experiments [95,96]. With a CO_2 content as low as 5%, they found the common CO-oxidation peak. Some reservation has to be expressed, on the exact nature of those adsorbates: Papageorgopoulos *et al.* found similar peaks with presence of COOH and CH_3OH instead in the electrolyte [95].

The CO_2 effects on PEMFC performances are also related to the cell parameters. The temperature effect was studied by Diaz *et al.* with a 25% CO_2/ H_2 inlet. They measured an overpotential increase from η = 50 mV at T = 40°C to η = 60 mV at T = 60°C. It is possible that even though CO oxidation kinetics are increased at high temperatures (which is favourable), CO production through the RWGS reaction increases as well (which is highly detrimental): with a free enthalpy of ΔH = –41.1 kJ mol^{-1}, the RWGS reaction is endothermic, which means it is faster at high temperatures [97,98].

The influence of humidity was also demonstrated in presence of CO_2 [99], possibly due to the improvement of CO oxidation, here again. The huge influence of water on common PEMFC parameters such as ion conductivity or anode flooding is however difficult to distinguish from its real effect on CO_2 “poisoning”.

Very high current densities are required for the EHC application. Karimi *et al.* fuelled a 25% CO_2/ H_2 mixture to a stack, and measured a loss of potential of 0.5% at 0.1 A cm^{-2}. This loss was increased to 12% with a current density of j = 1 A cm^{-2} [100]. Such a voltage penalty for high current densities would certainly non-negligibly detrimentally affect the EHC efficiency. One notes this will probably be the case with each type of poison.

I.2.3.4 NH_3

As preciously exposed in section I.2.3.1, ammonia can be produced from high temperature processes involving N_2 and H_2. It can be found between 30 and 90 ppm in reformates [79], and sometimes up to 150 ppm, according to Zamel *et al.* [97]. Its presence in the hydrogen inlet drastically decreases the cell potential: only 44 ppm is necessary to lose 12% [101]. At concentration as low as 1 ppm though, they found no effective loss, when Halseid et al., on the other hand, found non-negligible effects [102].

Possible effect on the catalyst layer were studied through cyclic voltammetry, with no witnessed difference whatever the NH_3 concentration [103,104]. This surprising observation suggests that the overpotential increase was mostly due to an increase of the ohmic drop, due to "damages" to the Nafion® membrane or ionomer. The membrane resistance of a PEMFC was measured by Halseid *et al.* in presence of NH_3 [96,102]: a significant decrease of the membrane conductivity with the NH_3 content was measured.

It appears that according to the thermodynamics, NH_3 is very soluble in H_2O, especially in acidic environment, and that ammonium cation NH_4^+ are easily formed. Those cations could replace protons on the sulfonic site of the Nafion membrane, thus reducing the general membrane conductivity (in particular the protonic conductivity).

This ohmic drop however does not completely explain the overvoltage measured in these studies, and until now, no precise explanation has been provided to account for the other contributions.

In their work of 2011, Imamura *et al.* characterized the outlet gas of a fuel cell, using 50 ppm of ammonia in addiction of hydrogen as the anode inlet [105]. At the anode exhaust, nearly no ammonia was detected, while the cathode exhaust displayed the presence of ammonia as well as other nitrogen compounds. This experiment is shown on Figure I.11. Since ammonia oxidation initiates at E = 0.7 V vs RHE on Pt [106], part of that gas could have crossed through the membrane (possibly in the form of NH_4^+), and then been oxidized at the PEMFC cathode, thus degrading the cathode performances.

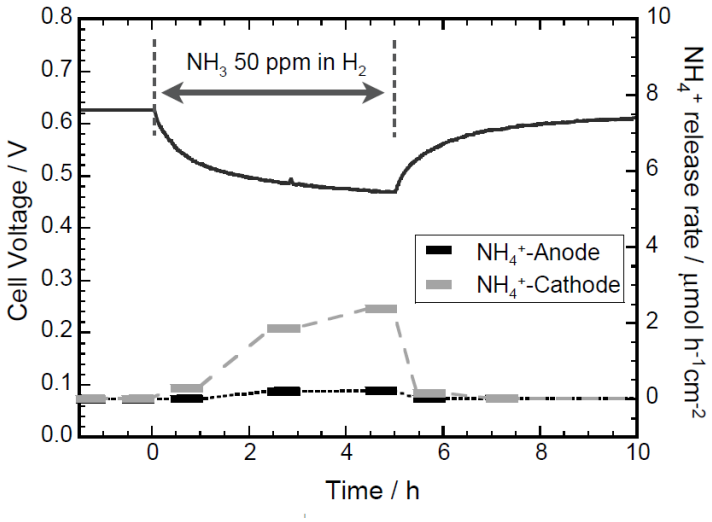

Figure I.11 : Cell voltage variations and NH_3 content in the exhausts gas of a cell fuel with 50 ppm NH_3, with a current density of j = 1 A cm^{-2}, at T = 80°C [105]

In the studies where the anode feed is switched back to pure hydrogen after NH_3 poisoning, the performance recovery does not depend on the ammonia amount, but on the duration of the supply. A short-term exposition (*ca.* 3 h) to ammonia, with amounts as high as 5 ppm can be recovered. For long term poisoning (*ca.* 80 h) on the other end, even a previous exposition to only 5 ppm of ammonia cannot be entirely recovered [103,107]. Gomez *et al.* suggested that after a certain amount of time, the contact between the ionomer and platinum nanoparticles is lost, hence provoking an irreversible loss of active surface area [107].

I.2.3.5 CO

One of the most common impurities in hydrogen reformates, also known for its critical impact on platinum performances, is carbon monoxide. Its effects on PEMFC have been widely studied and modelled [108], along with the influence of many parameters on the cell performances. CO is a molecule that adsorbs very strongly on platinum, effectively blocking the electrocatalyst sites for other reactions such as hydrogen dissociation and oxidation [79,83,98,101,109,110]. This adsorption and oxidation mechanism follows a Langmuir-Hinshelwood mechanism described in equations (I.7) to (I.9) [99,109] :

$$CO + Pt \rightarrow Pt\text{-}CO \quad (I.7)$$

$$Pt + H_2O \rightarrow Pt\text{-}OH + H^+ + e^- \quad (I.8)$$

$$Pt\text{-}OH + Pt\text{-}CO \rightarrow 2\,Pt + CO_2 + H^+ + e^- \quad (I.9)$$

Usually, PEMFC CO-tolerances studies survey the amount of CO impurities from units to several hundreds of ppm. For the EHC application, CO proportions as high as 2%, *i.e.* 20 000 ppm (Table I.2) can be expected, a much higher proportion. Murthy *et al.* studied CO concentrations as high as 1%, both at T = 70°C and 90°C (Figure I.12) [110]. With a current density j = 2 A cm^{-2}, there is nearly 0.5 V of difference between pure hydrogen and 1% CO/H_2 on a Pt-based electrocatalyst. Since CO oxidation kinetics are increased with temperature, operation at a higher temperature could reduce CO poisoning effect. Such a solution however is very detrimental for the electrocatalyst durability; and its practical effect questionable [111]. Pressure on the other hand, seems to induce only a slight improvement on the poisoning. Murthy *et al.* [110] and Cheng *et al.* [83] also found that at a higher current density, the cell potential decreased much faster.

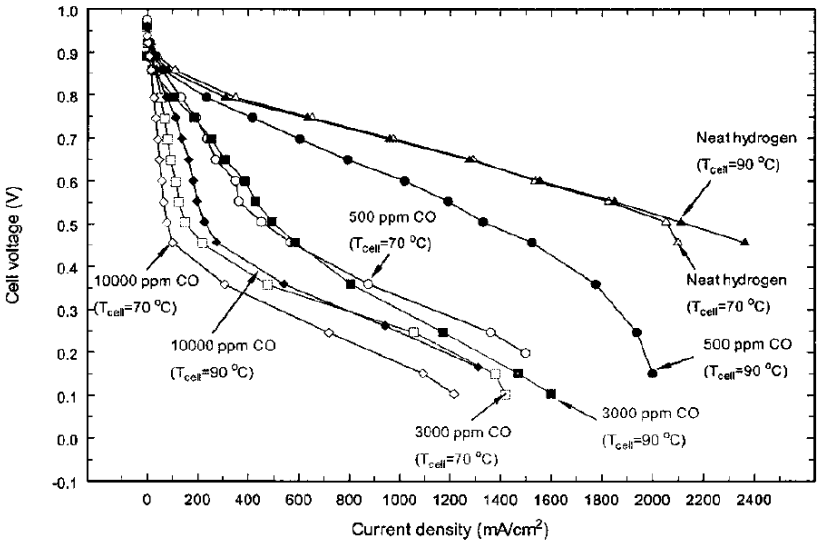

Figure I.12: Effect of temperature and CO inlet content at 202 kPa. Open symbols correspond to 70°C, filled symbols to 90°C [110]

Numerous techniques and materials have been studied to counter the effects of CO poisoning. They will be developed in section I.3 of this chapter.

I.2.3.6 H_2S

Hydrogen sulphide can be found is proportions up to 10 ppm in natural gas (and even 6% is some cases, as the Lacq deposit, in France) [112]. As CO, it can strongly adsorb on Pt surface and thus block active sites [113], which depletes anode performances and cell voltage. Two types of platinum-sulphur bonds were found by Jayaram *et al.* [114]: two-sites adsorption bond are the most present at low-coverage, while high-coverage solely presents one-site adsorption bonds [115,116]. Several groups suggested the formation of platinum sulphides from those adsorbates, through the mechanism presented in equation (I.10), (I.11) and (I.12) [117,118] :

$$H_2S + Pt \rightarrow Pt\text{-}H_2S \quad (I.10)$$

$$Pt\text{-}H_2S \rightarrow Pt\text{-}S_{ad} + 2\,H^+ + 2\,e^- \quad (I.11)$$

$$2\,Pt\text{-}S_{ad} \rightarrow Pt + PtS_2 \quad (I.12)$$

The effective active surface area loss was brought to evidence by impedance spectroscopy, with increase of the charge transfer resistance [119], and by cyclic voltammetry [120].

Recovery is actually partially possible through the oxidation of sulphur adsorbates on Pt surfaces at potentials higher than E = 0.8 V vs RHE [121].This de-poisoning, forming sulphates, is however partial as only a portion of the surface can be recovered; besides, the oxidation reaction consumes water from the membrane, which could reduce its ionic conductivity, especially for the EHC, where water is produced from cell reactions.

Several groups studied the H_2S concentration effect on the cell potential of a PEMFC [101,122]. Benesch *et al.* measurements on H_2S concentration influence are shown Figure I.13. As the poison

amount increases, the overvoltage does the same: 30 hours with 2 ppm of H_2S lead to a drop of 0.4 V.

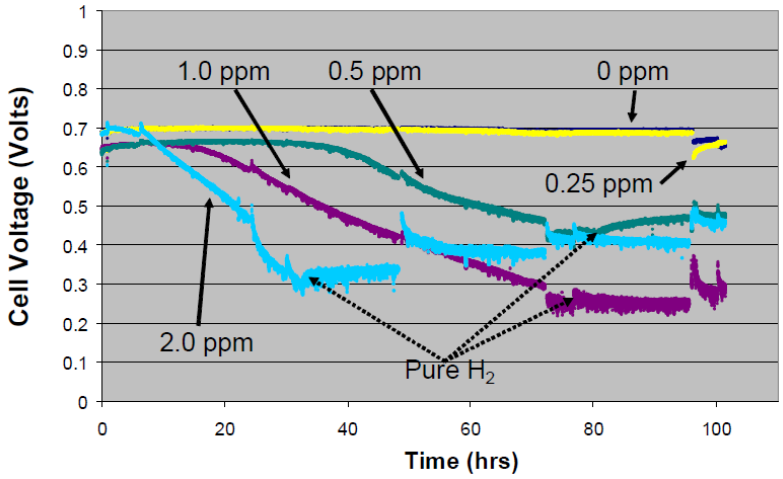

Figure I.13: Impact of the H_2S content in the anode inlet flow on the fuel cell potential [101]

This poisoning phenomenon is also influenced by the cell temperature: the platinum-sulphide bond seems to weaken at elevated temperature (a positive effect), but its formation kinetics also increase (a negative effect) [123]. Urdampilleta *et al.* measured a 69% increase in the rate of the poisoning when the temperature is increased from 50 to 90°C, with 5 ppm H_2S [122]. This enables to demonstrate that the latter effect is predominant.

I.2.3.7 Multiple gas

The previous sections highlight the individual effects of several impurities present in hydrogen reformates on the HOR performances of a Pt-based electrocatalyst. In real conditions however, all previously presented gases are present in the feed at the same time. To phrase it differently, the catalyst layer will have to bear multiple effects from CO, H_2S, NH_3 and the possible dilution of H_2 by these species and the possible presence of inert gases. Some groups focused on the study of the influence of several gas mixtures, in order to investigate an eventual synergetic effect due to their simultaneous presence.

Bhatia *et al.* exposed a diluted hydrogen to the 10-100 ppm of CO, bringing to evidence Pt surface vulnerability in such a case [124]. Decreasing the hydrogen partial pressure appears to worsen CO poisoning effects, since the effect of site inhibition by the poisons is amplified and reduces even more the surface coverage of free Pt-sites for the HOR. The entire mechanism was modelled and confirmed by experimental results [108,124,125].

In 2004, Janssen *et al.* also calculated the effects of replacing 20% N_2 by 20% CO_2 in a 10 ppm CO/40% H_2/40% N_2 feed: the current density loss was similar in both cases, whether CO_2 was present or not [125]. This agrees with the hypothesis that CO_2 effects are close to CO adsorption effects on the Pt surface, related to the RWGS equilibrium (see section I.2.3.3).

Shi *et al.* exposed a PEMFC to the two most poisoning gases for Pt, CO and H_2S ; they measured severe loss of performances, related to simultaneous absorption of CO and sulphur on the active

surface area [119]. The general overpotential tendency is however slightly different from the simple sum of both contributions: both molecules are in competition for adsorption the same Pt sites, as shown Figure I.14.

Finally, Wang *et al.* synthetized a gas reformate mixture by addition of several minor compounds that could be found in natural gas: CO, H_2S, formic acid, benzene, ammonia [127]. After 200 h of operation, those impurities barely had any effect on the PEMFC performances when present only at trace levels (4 ppb for H_2S and 2 ppm for formic acid). When those values when multiplied by five however, the potential loss increased straight to 66 mV for the same amount of time, and was noted partially irreversible.

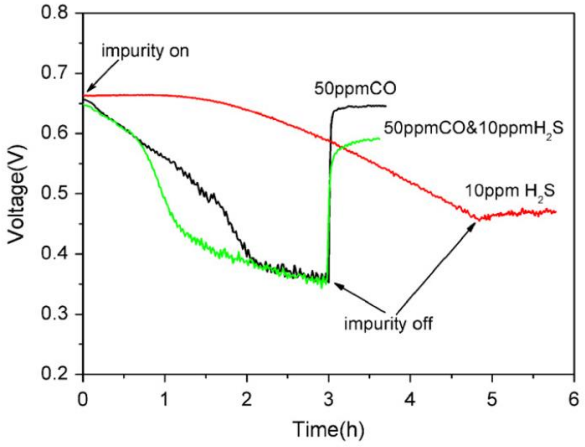

Figure I.14: Comparison of the effects of 50 ppm CO, 10 ppm H_2S, and the gas mixture (50 ppm CO and 10 ppm H_2S) on the performances of a PEMFC. j = 600 mA cm^{-2}, T_{cell} = 60°C, operating pressure: P = 0.1 MPa, humidification temperatures of the anode and cathode: T = 25 and 60°C, respectively [126].

I.2.3.8 Countering impurities effect

Previous sections brought to evidence the different effects of hydrogen reformate impurities, those highly detrimental to PEMFC performances. Several recommendations concerning the maximum level of each impurity in the H_2 feed of a PEMFC were already made for the common Pt electrocatalyst. They are presented in Table I.3.

Table I.3 Recommendations for a PEMFC hydrogen inlet, according to the DYNAMIS project [79]

Impurity	Concentration (ppm)
Total gases	500
He, N_2, Ar	Sum:500
CO_2	2
CO	0.5
Total sulphur compounds	0.01
NH3	0.1
O_2	5
CH_4	100
Total other hydrocarbons (C2 +)	2
Water	5

The EHC however, requires a high current density to be competitive towards other compression/purification technologies. Such a current density, much higher than for of PEMFC, is expected to impact even more EHC devices from the presence of these impurities (possibly present in a larger proportion than in a PEMFC feed). In order to keep the HOR activity of the catalyst layer and reach current densities of more than 2 A cm^{-2}, it is mandatory to find materials and/or technical solutions to recover of even keep that current density at a reasonable anode potential (and EHC cell voltage). From the study of these impurities and their effects until today, numerous solutions were investigated and tested in various environments. Most of those solutions were dedicated to CO poisoning, but some of them can also be applied to other impurities. Two main alternatives can be distinguished: either recovering the initial state of components through a technical method, or enhancing the materials tolerance towards poisons. The following sections will describe these two strategies.

I.3. Countering strategies for impurities presence

I.3.1. Recovery techniques

The most widespread recovery method, used in almost each impurities study, is to switch the impurity containing feed to a pure hydrogen feed (in practice this strategy will not always be possible). It is also used to determine the possible reversibility of the poisoned state of the electrocatalyst. After CO contamination, changing the feed to a pure H_2 inlet seems to free most of the platinum surface [93,119]. After more than 3 h with 9 ppm CO, Benesch *et al.* measured the recovery of 95% of the initial cell voltage with 5.5 h with a pure H_2 feed at the anode. It is not known if this recovery happens also under longer operation or larger CO contents.

In the case of sulphur-contaminated surfaces though, such a recovery was not achieved [122]. Applied after a H_2/CO/ H_2S gas mix, this method only permitted the recovery of the surface lost with CO, emphasizing the irreversibility of H_2S poisoning. Shi *et al.* results on that matter are presented on Figure I.14. Imamura *et al.* [128] and Urdampilleta *et al.* [122] tried to apply a fixed potential during the pure H_2 feed, getting the initial current back even with 2 ppm H_2S. It is possible that this recovery was made related to partial sulphur oxidation at the cathode, after crossover. However, this cannot be applied to the EHC case, considering the absence of oxygen at the cathode, and the pressure gradient between both electrodes should prevent any crossover from the impurities (fortunately, as it is the basis of the purification targeted using an EHC). Concerning ammonia contamination, recovery by a pure H_2 feed depends on the duration of the previous NH_3 feed, as explained in section I.2.3.4

"Air bleeding" or "O_2 bleeding" is another technique that enables to counter CO contamination effects. A small amount of oxygen (or air) is injected into the anode feed, so that oxygen adsorbs on Pt to support CO oxidation [85,93,97,98,100,129,130]. Equations (I.13), (I.14) and (I.15) describe the occurring mechanism.

$$O_2 + 2\ Pt \rightarrow 2\ Pt\text{-}O \quad (I.13)$$

$$Pt\text{-}O + Pt\text{-}CO \rightarrow 2\ Pt + CO_2 \quad (I.14)$$

$$Pt\text{-}O + 2\ Pt\text{-}H \rightarrow 3\ Pt + H_2O \quad (I.15)$$

Karimi *et al.* achieved significant decontamination with only 0.5 to 4% of oxygen, after a 25% CO_2/ H_2 feed [100]. To go further, Adcock *et al.* created a reconfigured anode with that process in mind, adding a catalyst layer upstream of the electrocatalyst layer to directly oxidize carbon monoxide with cheap material before it reaches the Pt nanoparticles, in a heterogeneous catalysis process [131]. This overall minimized the effects on the Pt based electrode. At high current densities however, introducing oxygen does not have that much efficiency. At j = 2 A cm^{-2} with a 0.3% CO/ H_2 feed, a 15% air bleed was not enough to protect/recover the active surface area [110,132]. Some dioxygen molecules can also react with dihydrogen, thus depleting the overall system efficiency by decreasing the hydrogen amount. This "air bleeding" technique was also applied with H_2S and NH_3, with no positive effect in these cases [107,133].

To recover the initial active surface area, Garder *et al.* suggested the method of applying periodic pulses to the cell [134]. They applied 10 A pulses every 0.8 s to cell fuelled with a $H_2/CO_2/CO$ inlet. The overpotential decreased but was not supressed. Shi *et al.* tried to apply pulses in potential instead to a H_2S -poisoned cell, effectively recovering 97% of the initial current. It was later found that those oxidation peaks can however damage the electrocatalyst layer and magnify the dissolution of some of its components [135]. Cyclic voltametries, based on the same idea, lead to a similar issue. This undeniable sensitivity of Pt-based electrocatalysts to fast potential changes is now well documented in the literature, both in acidic [136–140], and alkaline [138,141,142] media. This confirms the very damaging and somewhat irreversible effect of H_2S on Pt-based electrocatalysts.

As a consequence, it is essential to limit the presence of H_2S impurities in the hydrogenous fuel of a EHC (and a PEMFC). A common method is to mix ZnO with inert substances, such as SiO_2 to create hydrogen sulphide scavenging module [143]. Numerous adsorbents [144,145] are proposed for this operation: most processes are based on TSA method, and decrease the overall gas separation process productivity [146]. H_2S capturing at room temperature remains a great scientific challenge [147] though, which is beyond the topic of this thesis.

I.3.2. Tolerant materials

The most convenient way to prevent or limit the damage of impurities on a given catalyst layer is still to adapt it to tolerate such impurities. Apart from ammonia contamination, all poisons affect the Pt-based electrocatalyst, which then need to be strengthened. Numerous materials and additives were studied to reduce the CO poisoning effect on platinum, and one could go further by saying that if an electrocatalyst is tolerant towards CO, it will also be tolerant towards CO_2 (the reverse case being untrue). H_2S tolerance however, was only scarcely studied.

Focusing on the CO oxidation mechanism, it appears that the limiting step is not the one of CO oxidation, but the one of hydroxyl groups adsorption, essential to strip the CO adsorbates (see equations (I.8) and (I.9). Anderson *et al.* calculated that even if the activation energy of reaction (I.8) increases with potential, the overall activation energy will decrease [148]. This is due to the high-potential adsorption of hydroxyl groups on platinum, starting only at 0.6 V vs RHE. The first

strategy to enhance the CO-tolerance for Pt-based electrocatalysts lies in the addition if a co-catalyst able to adsorb those hydroxyl groups at much lower potential, hence favouring easier CO oxidation. The second strategy is based on the weakening the Pt-CO bond, in order to facilitate its oxidation or even prevent its initial adsorption [149]. Increasing the platinum nanoparticles size has a positive effect on this strategy, as well as the creation of nanoparticles agglomerates [150,151]. The later increases the amount of concave platinum sites, which have a weak CO-bond. Changing the structure and morphology of the electrocatalyst can enhance its activity towards a reaction, or in particular its tolerance to CO [151].

I.3.2.1 Pt-based alloys

The use of an alloy of Pt with a less noble catalyst can help achieve both strategies and has been widely studied in the fields of reformate-fed PEMFC and direct alcohol fuel cells (in which CO is poisoning the anode catalysts after the initial dehydrogenation steps of the fuel). Changing the electronic structure of platinum weakens the Pt-CO bond, and components adsorbed on less noble metal sites can diffuse towards Pt sites. Multiple PtM alloys were tested, with M= Ru, Ir, V, Rh, Cr, Co, Ni, Fe, Os, Mn, Pd, W, Mo, Sn, Au [152–155]. Almost all studies concluded that PtRu is the best material, as shown on Figure I.15 from Iwase's work [153]. PtRu has been studied for long time now [128,156–160], and in a wide range of conditions. With an optimum atomic ratio of (1:1), it oxidizes CO as low as E = 0.59 V vs RHE in cyclic voltammetry at ambient temperature with a 20 mV s^{-1} scan rate. Papageorgopoulos *et al.* found that under a CO_2 contaminated feed, PtRu/C lost only 15% of its sites while Pt/C lost as much as 78% in the same conditions [95]. Dubau *et al.* [161] and Maillard *et al*. [162] even found that alloying was not mandatory: Pt-Ru composites supported on carbon also demonstrated enhanced CO-oxidation activity, or more precisely, of methanol (admitting that methanol rapid dehydrogenation at the electrocatalyst surfaces leaves CO_{ad} [163]), which means that the electronic effect is not the only one that can enable to mitigate CO-poisoning; for the unalloyed catalyst materials, it is the bifunctional effect (the M element, less noble than Pt, is able to generate OH_{ad} species at lower potential than Pt, which can diffuse to the Pt atoms) that promotes the Langmuir-Hinshelwood reactions (8) and (9) and oxidation of CO into CO_2, hence decontaminate the catalyst surface.

Concerning H_2S however, PtRu showed no difference with a common Pt/C electrocatalyst [164]. As of today, PtRu alloy (or composite) stays the main reference concerning CO tolerance (and tolerance to small hydrocarbon molecules). It is even used in commercial applications. Its main drawbacks might be its poor stability and the associated ruthenium dissolution problems [165].

Amongst the other studied alloys, Pt_3Sn was chosen for the absence of CO affinity for Sn sites, thus freeing the surface for hydroxyl groups adsorption [158,166,167]. This decreased the onset oxidation potential to E = 0.3 V vs RHE. This alloy however, presents very poor PEMFC performance, probably related to a reduced activity towards the HOR compared to Pt. Its poor stability makes it hard for Sn to be used alone or in composites.

Pt-Mo also presented interesting results towards its activity for CO oxidation [168–172]. Its optimum ratio seems to be (3:1), according to Mukerjee *et al.* [173] no clear data could however

be found on it activity towards HOR, and the results of Nepel *et al.* [172] showed a small performance loss in a PEMFC.

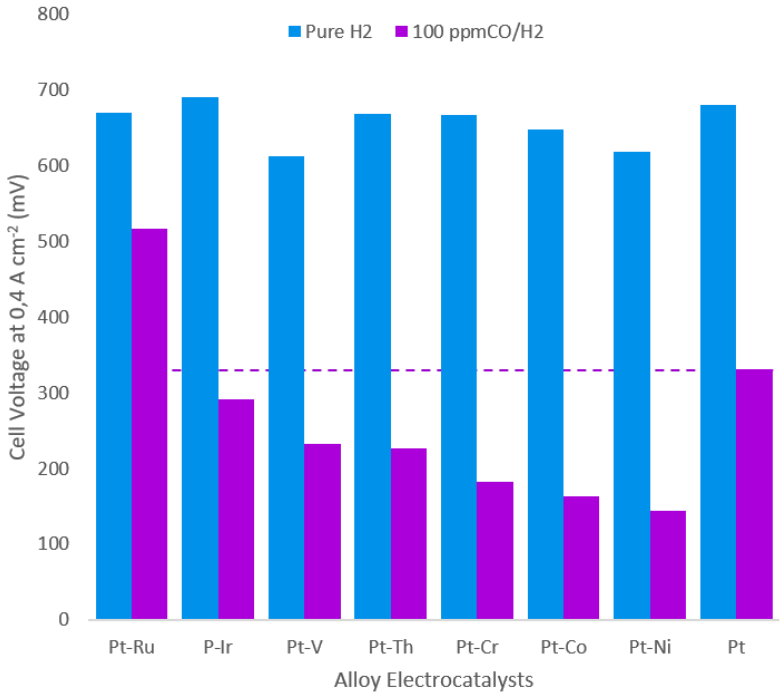

Figure I.15 : Cell voltages of Pt-based alloy electrocatalysts with pure hydrogen feed or 100 ppm CO/H_2 feed at the PEMFC anode. All electrocatalysts are made with 20 wt. % alloy/C (Vulcan XC72R) with Pt loading rate of 0.4 mg_{Pt}. Cathode electrocatalysts are made with 20 wt. % Pt/C [153]

Sometimes the studied alloy is even composed of a third or even fourth element, in order to improve its activity and/or its stability [135,174,175]. Hassan *et al.* added Ru or Fe to in PtMo, fruitfully increasing its activity towards HOR [174]. A Pt atomic layer was also added on top of an alloy in some experiments, thus increasing the CO tolerance. The long-term stability of these complex materials is however hardly demonstrated.

I.3.2.2 Supported platinum and additives

Enhancing the CO oxidation kinetics of Pt-based catalysts is also possible by replacing its support material instead. Changing the common carbon black for metal oxides such as RuO_x, WO_x, SnO_x, MoO_x, or FeO_x, has also been a used strategy to create a new family of electrocatalyst with performances towards CO oxidation sometimes better than PtRu [176–181].

Pt/WO_3 for instance, proved to free a portion of Pt active sites at a potential as low as E = 0.1 V vs RHE, an outstanding performance that will be more described in chapter IV [182,183]. It presented however very poor stability. Sugimoto *et al.* synthetized Ru and RuO_2 nanosheets, effectively increasing PtRu CO-tolerance in a 300 ppm CO/H_2 inlet (Figure I.16). This electrocatalyst behaviour towards the very high CO concentration to be experienced by the EHC however remains unknown. Despite their interesting CO activity, all these oxide supports present two major drawbacks that have to be taken into account: their low electronic conductivity and their poor durability.

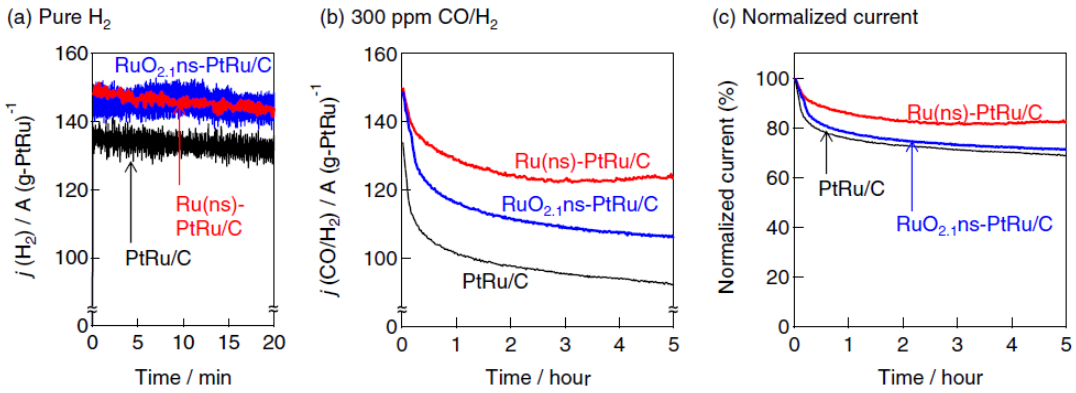

Figure I.16: Comparison of the CO tolerance of PtRu/C, RuO_2 (ns)-PtRu/C and Ru(ns)-PtRu/C [180]

The addition of components to Pt nanoparticles was also experienced under CO-poisoning conditions. Polymorphins for instance, do not participate in the HOR activity, but upon addition in the optimal amount, they increased CO-oxidation on Pt at a potential as low as E = 0.08 V vs RHE, a remarkable performance [184,185]. There is no mention, however, of the effect of that association on the intrinsic HOR activity of Pt.

Numerous electrocatalysts have been optimized towards the CO (or methanol) oxidation or tolerance at a PEMFC anode. Modifying platinum properties or its environment proved to be an efficient solution to achieve low-potential oxidation of carbon monoxide. These modified shapes and compositions do however not always present a good stability under working conditions, or even present a short lifespan. Furthermore, the vast majority of these studies were performed under a small CO-feed, well below that could be present in a EHC inlet. Besides, research was often focused on the CO impurity only, with no precise HOR measurements. Such HOR activity assessment still needs to be done for all these promising new electrocatalysts, in order to compare them in the conditions of the EHC application, where very large HOR current densities need to be employed.

I.3.3. HOR electrocatalysts materials and relevant kinetics study

For the EHC to be competitive towards other purification /compression technologies, it needs to operate at current densities (much) higher than j = 2 A cm^{-2}. The HOR activity, for which Pt is known to be the best electrocatalyst, is then essential to meet this requirement. Amongst the studies dealing with the CO-tolerance of Pt-based electrocatalysts, (very) few of them also addressed the HOR activity. This is certainly mostly due to the PEMFC setup, where in front of the slow ORR kinetics, vastly studied, HOR is (almost) never a limiting reaction.

A couple of studies used the hydrogen-pump configuration, by filling their cathode with hydrogen during the anode study, to properly analyse the anode electrocatalysts and their behaviour under poisoned-containing hydrogen feed. Table I.4 gathers the measured overpotential values. The reading of these data must however be done with caution, since many differences exist between the experiments, especially in terms of operating conditions. One can also notice that the impurities tested in these studies are not the most critical ones. More studies will need to be done in these conditions, with strong poisons like CO and H_2S.

Table I.4: Measured overpotential values at a PEMFC anode in hydrogen pump configuration (H_2 inlet at the cathode)

Electrocatalyst	Loading (mg cm^{-2})	Gas inlet	Overpotential at 1 A cm^{-2}	Ref.
Pt	0.4	80% H_2 + 20% N_2	7 mV	[90]
Pt	0.4	80% H_2 + 20% CO_2	15 mV	[90]
PtRu	0.45	100% H_2	13 mV	[96]
PtRu	0.45	75% H_2 + 25% N_2	14 mV	[96]
PtRu	0.45	75% H_2 + 25% CO_2	30 mV	[96]

The electrocatalyst activity for the HOR can also be studied through the use of complementary methods.

The rotating-disk electrode is often used to measure kinetics and/or study reactions mechanisms. The 3-electrode setup allows a precise control over the reaction, and its facile use permits a fast study of a wide range of electrocatalysts. In a RDE setup, all reactions occur in the liquid electrolyte, de-oxygenated or saturated with gases when needed. However, diffusion of gases in water is extremely slow compared to the gas phase and their solubility is small, leading to severe mass-transport limitations. For the ORR, a reaction of slow charge transfer kinetics, a correction can be applied [186], but that is not the case for the HOR, which exhibits much-faster charge transfer kinetics; as such, the HOR is always limited by mass-transport kinetics when characterized in RDE configuration, thereby preventing any proper study of the HOR kinetics in this configuration [187,188].

The floating electrode technique is a novel configuration developed by Zalitis *et al*., with the aim to overcome RDE mass-transport limitations [188–190]. Its setup is quite similar to that of a RDE, with a 3-electrodes setup and a liquid electrolyte. The working electrode is made of a porous and hydrophobic material that floats onto the electrolyte surface, thus creating a direct contact between the gas and liquid phases at the electrocatalyst surface. Very low loading of electrocatalysts are employed (0.1-10 µg cm^{-2}_{Pt}) which helps reaching the charge transfer limits of the HOR kinetics. This methodology can thus lead to HOR kinetics determination, providing a proper technique to compare different electrocatalysts materials. This technique does not seem to have been used in presence of impurities yet.

The gas diffusion electrode (GDE), a very ancient technique in electrocatalysis [191,192], was recently brought back to life by Inaba *et al.* for PEMFC application (the concept also existed for the phosphoric acid studies) [193]. This setup provides an equivalent precise control other a small loading of electrocatalyst, while providing reacting in the gas flow, similar to what happens in a PEMFC setup. This setup will be presented in more details in the Chapter V of this thesis, where it will be used to compare several electrocatalysts for their HOR properties.

A last method consists of using a complete PEMFC setup, while monitoring the potential difference between both electrodes under a hydrogen pump configuration [139,187,194,195]. This is the most realistic method to access HOR kinetics, especially with the non-limited gas-transport and the realistic water content. A proper study of the anode side however could be difficult because of the occasional cathodes limitations and possible crossover. Furthermore, the characterization of the reaction mechanism, necessary for electrocatalyst improvement, could be prevented or impacted by this two electrodes setup (one or two electrodes could be limiting at the same time).

I.4. Conclusion and Thesis objectives

The last century increasingly fast human development, both in technologies and population, lead to a major disequilibrium with our environment. To face that situation, fossil fuels will have to be replaced from the global energetic mix, possibly by the growing renewable energies. To that goal, hydrogen was presented a solution for a new and clean energy carrier.

This so called "hydrogen economy" relies on the reversible fuel cell process, producing only water vapour and electricity from hydrogen and oxygen. However, the hydrogen cost is still very high compared to that of other common fuels, mainly due to its production but also the purifications and compression steps that are unavoidable to its transportation, storage and use.

A new possible device, combining both the purification and compression steps has been proposed: the electrochemical hydrogen (purificator) compressor (EHC). An EHC relies on the well-known PEMFC and PEMWE setup; nevertheless, this similarity is limited considering the extreme conditions under which the EHC will be operated. Both side of its electrodes are filled with hydrogen, performing two reactions with some of the fastest known charge-transfer kinetics. The anode side, in particular, will be fed with an impure hydrogen flow, with impurities contents, especially in the CO case, much higher than what was previously studied for the PEMFC. Despite that, its current density has to be higher than 2 A cm^{-2} to be competitive with regards to alternative processes of compression/purification. This current density is a realistic value considering the HOR fast kinetics on platinum if performed in pure hydrogen conditions. However, when the HOR shall proceed with an impure fuel, the trick is much harder, and scarce literature could be found with dealing with impure HOR at such high current density values.

Thus, the aim of this thesis consists of preparing, characterising and improving electrocatalysts for the EHC application. Such materials will have to sustain high HOR activity, under the presence of poisoning impurities. To face this challenge, we selected two electrocatalysts for their promising behaviour: Pt+Ru/C composites, found to present good CO-tolerance even without alloying, and tungsten-supported platinum and platinum-ruthenium, which exhibit outstanding results at very low potential. It was chosen to limit the study of impurity tolerance to the most critical and common gas: carbon monoxide.

This thesis will be divided in five chapters. This **Chapter I** already introduced the context that led to research on the EHC, and a state-of-the-art on impurities and their countermeasures. Characterization techniques will be presented and described in **Chapter II,** along with the electrocatalysts synthesis methods. **Chapter III** will focus on the Pt+Ru composites electrocatalysts, from their physical and chemical characterizations to their electrochemical characterizations in RDE configuration. The same methodology will be followed for tungsten oxide-supported electrocatalysts in **Chapter IV**. Lastly, the best electrocatalysts of each family will be characterized in a gas diffusion electrode setup in **Chapter V**, enabling proper HOR kinetics measurement and comparison both in pure and CO-containing gas feeds.

CHAPTER II

Experimental Procedures

Chapter II Experimental Procedures

This chapter is dedicated to the introduction of the multiple techniques and protocols used in in this work. If not specified otherwise, the experiments were performed at the LEPMI Laboratory (Grenoble). The synthesis protocol of the electrocatalysts is introduced in the first part. It will then be followed by the description of the techniques related to the physico-chemical characterization of the materials. The electrochemical characterizations are then presented in a last part.

II.1. Cleaning protocol

In order to avoid irreproducibility in the results or alteration of experiments, it is mandatory to use highly cleaned equipment and tools.

For this reason, all glassware cited in the following experiments were cleaned by at least overnight soaking in Caro acid (1/3 H_2O_2 30 wt.% and 2/3 H_2SO_4 98 wt.%, Roth®), a very strong oxidant, to remove organic pollution. Before usage, the soaked glassware is then thoroughly rinsed four times with ultrapure water (18.2 MΩ cm, < 3 ppb Total Organic Carbon, TOC) using a Millipore Elix + MilliQ gradient apparatus. Whenever relevant, PolyTetraFluoroEthylene (PTFE) pieces (see DEMS, GDE sections), were also boiled for half an hour in ultrapure water to desorb all sulphur compounds that could originate from the Caro acid (e.g. sulphate anions).

In the case of the synthesis glassware, an overnight soaking in fresh aqua regia (1/3 85% nitric acid and 2/3 37% hydrochloric acid, Roth®) was also necessary to remove any metal pollution.

II.2. Synthesis of electrocatalysts

II.2.1. Polyol synthesis

All homemade electrocatalysts were synthetized using the polyol process, which was sometimes slightly improved depending on the targeted material. Hereafter, the protocol is described for the synthesis of the most common electrocatalyst: Pt nanoparticles supported on a high surface area carbon substrate.

The so-called polyol synthesis process consists in elaborating nanoparticles in suspension, and then immobilizing them on the chosen substrate. First described by Fievet et al. in his article concerning particle precipitation in liquid polyol [196], this process was further improved by Oh et al., who introduced a fine manner to tailor the synthesis by tight pH control of the polyol solution in the course of the synthesis [197].

To that goal, a platinum precursor solution is firstly prepared by dissolving several milligrams of a platinum salt, here H_2PtCl_6, (99.9%, Alfa Aesar®) in 250 mL of a 1:2 pure water-ethylene glycol mix. The solution's platinum concentration is adjusted to 0.33 g L^{-1}. The solution is set in a 3-neck round bottom glass flask designed to be maintained at controlled temperature and atmosphere.

To prepare the nanoparticle reduction, drops of 0.5 M NaOH are added until the pH reaches around 11-12. This solution is mechanically stirred during one hour under Argon bubbling, in order to purge away all traces of oxygen.

The flask is then placed on a heating stirring place, a condenser placed on the top neck of the flask, and heated at 120°C during 3 hours. During that time, platinum metal clusters nucleate, by reduction of the Pt salt with the ethylene glycol, and form Pt (nano)colloids. The size and shape of the colloids depend on the synthesis parameters. The system is afterwards cooled down under Argon bubbling until it reaches room temperature, to avoid re-oxidation of the nanoparticles. The flask is then re-opened to air.

Once cooled down, that solution is mixed with the carbon support, here Vulcan XC72 (Cabot®). Following Oh's suggestion [197], the pH is adjusted around 2-3 with 0.5 M H_2SO_4, and the solution is left to stirring overnight at ambient temperature. At this pH, the interaction between the positively-charged Pt nanoparticles and the negatively-charged carbon support forces adhesion, as shown Figure II.1.

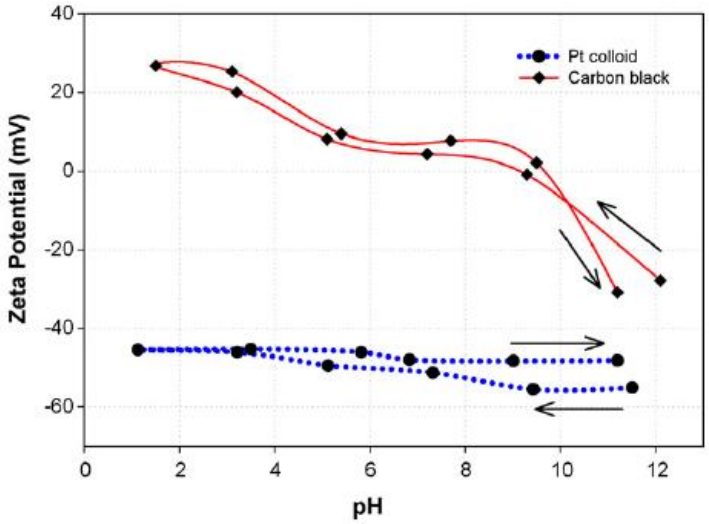

Figure II.1: Zeta potential of both Pt colloids and carbon black, as a function of pH [197]

For the filtration, a 100 kPa Laboport N 820 (KNF®) vacuum pump is used, along with a 0.22 µm filter. All carbon particles (that now support all the Pt nanoparticles), are kept by the filter, and the filtrate is completely clear. That filter is rinsed thoroughly with pure water in order to clear it from all ethylene glycol remains. It is then dried 45 minutes at 110°C, and finally kept in a vial, until further experiments with the so-obtained electrocatalysts.

For other syntheses, the procedure is modified according to the composition of the metal nanoparticles chosen and/or the nature of the substrate at which they are immobilized. They will be detailed in the corresponding chapter (see Chapter 3, and Chapter 4 of this manuscript).

II.3. Physical and chemical characterizations.

In this section will be described all processes and experiments that were used in order to characterize the synthesized materials.

II.3.1. Electronic Microscopy

The morphology of the electrocatalyst nanoparticles is investigated using a JEOL 2100 transmission electron microscope (TEM), with a point to point resolution of 0.23 nm operating at 200 kV. Electrons are generated from a LaB_6 single crystal-based filament (in this case), accelerated through a potential field focused with electromagnetic lenses before interacting with the sample. The latter has to be thin enough (below 100 nm) to permit transmission. Electrons and X-rays emitted by the interactions between the electron beam and the material provides information on the size and shape of particles, their dispersion on the support and their chemistry at local scale.

Through the detection and analysis of the energy of X-rays, the nature and chemical composition of the sample can be analysed. This was done punctually on the TEM through the X-Ray energy dispersive spectroscopy (X-EDS), or while scanning a large surface (10x10 µm maximum) with the scanning transmission electron microscope (STEM) with a probe size between 0.2 and 1.5 nm, dedicated to chemical mapping.

The sample are prepared on specially-designed copper TEM grids, 200 mesh from Eloïse company. The grid is firstly rinsed by several dipping steps into ethanol, then left to dry on a Fisherbrand® standard filter paper. Afterwards, dipping the grid twice into the electrocatalyst powder is enough to immobilize nanoparticles on it. If the sample is an ink, a droplet is dropped onto the grid instead, and left to dry for ten minutes.

A unique process was used for all samples, unless otherwise stated. For statistical relevance, four randomly-chosen areas are studied for each grid at 50 kX magnification, and four 200 kX images are then acquired in each region (this guaranteeing that the sample is homogeneous). X-EDS was also performed in order to verify the local chemical composition in these several regions. As a rule, the samples were usually indeed homogeneous and did not require more complex TEM procedure. Microscopy imaging was performed by Marian Chatenet, and micrographs were then fully analysed by the author.

Nanoparticles size distribution histograms of the various studied electrocatalysts were determined by counting ca. three hundred isolated metal particles on 200 kX magnification images with the ImageJ freeware, and presented as a distribution of particle size (diameter). Normal, surface and volume mean particle size were calculated for each particle distributions as presented in equations (II.1),(II.2) and (II.3).

$$d_n = \frac{\Sigma_{i=1}^{N} n_i d_i}{\Sigma_{i=1}^{N} n_i} \quad \text{(II.1)}$$

$$d_s = \frac{\Sigma_{i=1}^{N} n_i d_i^3}{\Sigma_{i=1}^{N} n_i d_i^2} \quad \text{(II.2)}$$

$$d_v = \frac{\Sigma_{i=1}^{N} n_i d_i^4}{\Sigma_{i=1}^{N} n_i d_i^3} \quad \text{(II.3)}$$

d_n is the mathematical particle diameter of the particles. d_s is the diameter relative the surface area of particles and is thus comparable to the electrochemical active surface (ECSA) measured by electrochemistry. d_v is the diameter relative the volume surface area, and can be compared to the particle diameter measured in X-ray diffraction (XRD).

II.3.2. STEM

For some electrocatalysts, several metal elements are present on the same carbon. It is the case for the Pt+Ru/C electrocatalyst for example. Because it is difficult to differentiate Pt and Ru particles on TEM images simply by their thickness contrast, another microscope, a FEG JEOL 2100F, operated in scanning transmission EM with a high angular dark-field mode (STEM-HAADF) and enabling X-EDS mapping at the nanometer scale was used to acquire chemical cartographies of the surface [198]; those enable probing the distribution of each metal component at the nanometer scale, hence to verify the chemical homogeneity of the sample. Samples were analysed by Laeticia Dubau.

II.3.3. Environmental transmission electron microscopy (ETEM)

In the frame of a collaboration with IRCELYON, some of the samples could be observed with a FEI TITAN ETEM G2 microscope, an aberration-corrected environmental TEM with atomic resolution (0.1 nm point to point resolution) operating at 300 kV. Such a microscope also permits the observation of sample under a low-pressure atmosphere (up to 20 mbar) of gas such as Ar, N_2, O_2 or H_2. The temperature can also be increased up to 1000°C.

Samples were prepared and analysed by Mimoun Aouine.

II.3.4. X-ray diffraction

X-ray diffraction (XRD) is a non-destructive technique commonly used to study the crystallinity of a material, the lattice parameter if it is crystalline, the presence of alloys and their chemical composition, the size of crystallites…

X-rays are sent from a monochromic source (here Cu Kα1, λ=0.5406 Å) the sample from a wide range of specific angles and received by sensors placed all around. The resulting diffraction is dependent on the crystallinity of the sample, the atom size (the element present) and the coherent size of the crystallites. To analyse it, results are plotted on an intensity *vs* angle (2θ) graph, and compared to the database relevant to the material in presence. The crystallinity type and lattice parameter can be measured this way. The crystallite sizes d_{hkl} in one specific orientation are measured by the use of the Scherrer formula:

$$d_{hkl} = \frac{0.9\,\lambda}{\Delta(2\theta)\ \cos\theta} \qquad \text{(II.4)}$$

where 2θ is the abscissa of the studied peak, Δ(2θ) is the width of the related diffraction line at mid-height and λ the source wavelength [199]. Another formula can be used in case of irregularities in the peak, as it takes the integrated mean width of the peak β, instead [199]:

$$d_{hkl} = \frac{\lambda}{\beta \cos\theta} \quad \text{(II.5)}$$

When Pt is alloyed with Ru, its angle of diffraction is shifted towards higher angles. The percentage of presence of each material (in a binary alloy) is given by the Vegard's law, which states that the lattice parameter *a* of a cubic alloy varies linearly between the value of one component and that of the other.

$$a^{\mathrm{R}}_{\mathrm{A_xB_{1-x}}} = x\, a^{\mathrm{R}}_{\mathrm{A}} + (1-x)\, a^{\mathrm{R}}_{\mathrm{B}} \quad \text{(II.6)}$$

II.3.5. X-ray photoelectron spectroscopy

X-ray photon spectroscopy (XPS) is a non-destructive technique that permits the study of surface composition. X-rays are sent to the sample surface, and the resulting emitted photoelectron kinetic energies are plotted as a spectrum. The binding energies deduced from the kinetic energies give information on the oxidation state of surface elements (5-10 nm depth), as well as their concentration.

Electrocatalysts were studied in their powder form, deposited on an adhesive carbon tape. For this experiment, a K-alpha ThermoScientific spectrometer was used, with an Al X-ray source (hv = 1486.6 eV) of 400 µm spot size diameter. The chosen energy limits are given for the survey spectra and element spectra in Table II.1. All data were analysed using the ThermoScientific Advantage software, and the background was fitted using the Smart algorithm.

Table II.1: Survey spectra and element spectra limits for XPS analysis

	End scan (eV)	Scan start (eV)
Survey spectra	1100.58	0.58
C1s	298.38	239.38
Ru3d	288.38	276.38
W4f	48.38	28.38
Pt4f	87.38	64.38
Ru3p	510.38	440.38

II.3.6. Thermogravimetric analysis

In order to properly characterize the amount of metal present in the electrocatalyst (and by subtraction of the amount of carbon), the thermogravimetric analysis (TGA) is performed on all electrocatalysts. A TGA device monitors mass variations of a small amount of powder (here ~10 mg) under controlled gas flow with a piezo electric scale, in function of the temperature applied

and/or time [200]. In this case, a STA 409 PC system (Netzsch ®) was used, with a mix of N_2 and O_2 as the gas, with the temperature set from 25 to 1000°C at a 5°C min^{-1} rate. As the carbon support of the electrocatalysts nanoparticles is oxidized around 400°C (in presence of Pt and oxygen), only the metal is left on the device at 1000°C, which gives us the precise ratio between metal and carbon of the initial sample. An empty crucible was measured under similar conditions, to isolate mass gain unrelated to catalysts (gas viscosity gain for example) [200]. Its results were subtracted to all catalysts mass measurements.

It is not possible however to differentiate between metals such as Pt, Ru and W, since they evaporate/sublimate (possibly in the form of oxides) at much higher temperature (above 1500°C).

Although this method was used with Ru-containing electrocatalysts, it has to be kept in mind that Ru can form RuO_4, a volatile compound above 108°C [201] , and thus create an additional mass loss.

II.3.7. AAS and ICPMS elemental analysis

As well as the metal/carbon ratio, it is also important to determine the exact chemical composition of the electrocatalyst nanoparticles in the overall powder. To that goal, atomic adsorption spectroscopy (AAS) and inductively coupled plasma mass spectrometry (ICP-MS) are used.

II.3.7.1 Digestion protocols

(1) Simple digestion

A simple (and commonly-used) technique was firstly employed to prepare samples for Pt-containing powders for AAS analysis. Each electrocatalyst is sampled, weighed and mixed with aqua regia (*cf* section I.A.) in a proportion of 5 mg powder for 1 mL solution. The obtained suspension is kept under fumehood and stirred overnight at 60°C in order to maximize the dissolution. Because part of the liquid evaporates during the night, the volume has to be adjusted back to 5 mL (or 10 mL) by ultrapure water addition. It is then centrifuged at 10,000 rpm for 10 min (with a Hettich®, Universal 320 R centrifugation device). The top 1 mL is pipetted and then diluted again in another clean vial, with ultrapure water. The dilution is set so that we reach the domain of appropriate AAS analysis: 1-50 ppm of Pt.

This digestion process however, proved to be non-efficient towards Ru and W, both resistant to such conditions. Also, the AAS needing ppm level of concentration, only few dilutions could be made: leading to a chloride concentration sometimes too high, which could damage the spectrometer. Next part will introduce a similar digestion assisted by a microwave oven.

(2) Microwave-assisted digestion

As its name makes it clear, the microwave-assisted digestion protocol differs from the simple digestion protocol by the fact that the suspension is heated in a microwave oven for an enhanced digestion. Temperature and pressures are both increased through microwave irradiation, which enhances both heavy metal solubility in solution and dissolution kinetics.

Around 10 mg of electrocatalyst is weighed in a PTFE vial designed for microwave heating; 10 mL of fresh aqua regia are then added (using it to also rinse the weighing support). The vial is then properly enveloped in its vessel and then put into the microwave oven (Mars 6, CEM®) at 150°C for 1 hour with a temperature ramp of 20 minutes. The temperature is monitored through a sensor, present in one standard-vial: filled with aqua regia only. After the dilution process is complete and the temperature is back below 60°C, all solutions are centrifuged, and then diluted by 10 for AAS analysis, and then again by 10k for ICP-MS analysis.

II.3.7.2 AAS principle

The AAS methodology consists in fully dissolving the metal fraction in a proper solvent, and then, possibly after pH adjustment and/or dilution, analysing the obtained digestion solutions in dedicated spectrometer. The latter will atomize a volume of the solution, and light it up with a monochromatic light, whose wavelength corresponds to the energy necessary to excite the atoms of a specific element.

The resulting absorption *A*, is proportional with number of excited atoms in the volume, N_0. It is given by a Beer-Lambert-type law [202]:

$$A = K\, l\, N_0 \tag{II.7}$$

where K is absorption coefficient of a photon, and l, the optical distance in the atomizer.

A set of five standards of gradient concentrations (1, 2, 5, 10, 25, 50 ppm) are prepared with a commercial standard solution (1000 mg L^{-1} Pt, Roth®). This range was chosen upon the detection accuracy for Pt in those concentrations.

Then, the analysis of the unknown sample is compared to the linear calibration plot of the AAS for the Pt element, and the unknown concentration interpolated.

A PinAAcle 900P atomic absorption spectrometer (PerkinElmer®) was used here.

Despite the use of brand new UV lamp and standard solution for ruthenium, no proper signal was detected. Henceforth, only the Pt element was measured via this method.

II.3.7.3 ICP-MS principle

Contrary to AAS, ICP measurements require a much lower element concentration (around the ppb level). Along with dissolved elements, it can also detect very small particles, which will really help in the case of elements hard to dissolve, such as Ir, or Ru and W in the present case.

It consists in heating and ionizing the dissolved solution into an induced plasma made of a rare gas (here Ar), and then analysing the resulting ions with a mass spectrometer. A benchmarked curve is realised with standard solutions from 1-50 ppb of Pt (and similar values for the other elements analysed) and used for interpolation with unknown solutions results.

A NexIon 2000 (PerkinElmer®) ICPMs was used here. Analysis were made by Vincent Martin.

This method was preferred for Ru and W quantifications, and was also used to check Pt values previously measured through AAS. Table II.2 shows Pt content obtained from a single microwave dissolution of two commercial Pt/C electrocatalysts (ETEK, Johnson Matthew), first measured with AAS, then diluted again for ICP measurements. It comes at a surprise, that even with such a sophisticated dissolution process, theoretical values are still far from reach, especially from the alloy. But what can also be noticed, is that ICP values present in each case 3% more of Pt than AAS values. One hypothesis is that the dissolution is not entirely complete, and that some nanoparticles are left in the solution. Contrary to AAS, ICP can detect such nanoparticles, which could explain that difference in the measurements.

Table II.2: Pt content in commercial catalysts, measured by AAS and ICP after microwave assisted dissolution

Catalyst	Theory	AAS	ICP
PtRu/C 40% ETEK	27%	17.9%	20.8%
Pt/C 30% ETEK	30%	26.9%	29.1%

II.4. Electrochemical characterizations

II.4.1. Electrochemical setup

II.4.1.1 Ink and electrode preparation

Each electrocatalyst powder is first prepared into an ink, that would be deposited on a polished glassy carbon rod to test model electrodes (so-called thin films [203,204]) of the corresponding material. The inks are made of four components: the electrocatalyst powder, the Nafion® ionomer in solution, and a 1:2 mix of isopropanol (IPA) and ultrapure water. The volume of ionomer is calculated so that the mass ratio between Nafion® and carbon is 0.3. The volume of IPA and water are calculated so that the platinum concentration of the ink is 0.59 g L^{-1}; so deposition of 10 µL of the ink on the glassy carbon electrode tip (of 0.196 cm^2 geometric surface area) gives a loading of platinum of 25 μg_{Pt} cm^{-2}.

All components for the ink preparation are manipulated under a laminar-flow nano hood (Safetech), to prevent nanoparticles dissemination into the laboratory. The vials containing the ink are then properly closed and sonicated in an ultrasonic bath for 15 minutes to mix all components. Depending on the electrocatalyst material at stake, the ink has to be used right away, or be stored for a day prior any experiments. Usually, an ink can be used up to one month after its preparation without reproducibility issues.

The working electrode consists of a glassy carbon rod inserted in Teflon. The surface is mirror-polished beforehand, using 6 µm, 3 µm and then 1 µm diamond paste. The electrode has to be cleaned with acetone in ultrasonic bath between each step to prevent contamination, and after polishing in acetone for 5 minutes, in an ethanol/water mix for another 5 minutes and finally in pure water for 10 minutes. The electrodes are then cleaned in Caro acid for at least one night. Prior to the experiment, they are thoroughly rinsed with ultrapure water and left to dry in the oven at 110°C immediately before the thin-film deposition of the electrocatalyst ink.

The deposition setup consists of an upside-down rotating disk electrode (RDE), and a hair-drier as shown on Figure II.2. The hot electrode is screwed on the RDE motor and put in rotation (around 400 rpm); 10 µL of the ink, sonicated 5 minutes beforehand, are deposited on the glassy carbon rod, then dried under the hair drier flux of air. This spin-coating technique was essentially derived from the work of Garsany et al [205]. The fresh electrode is always used the day of its deposition.

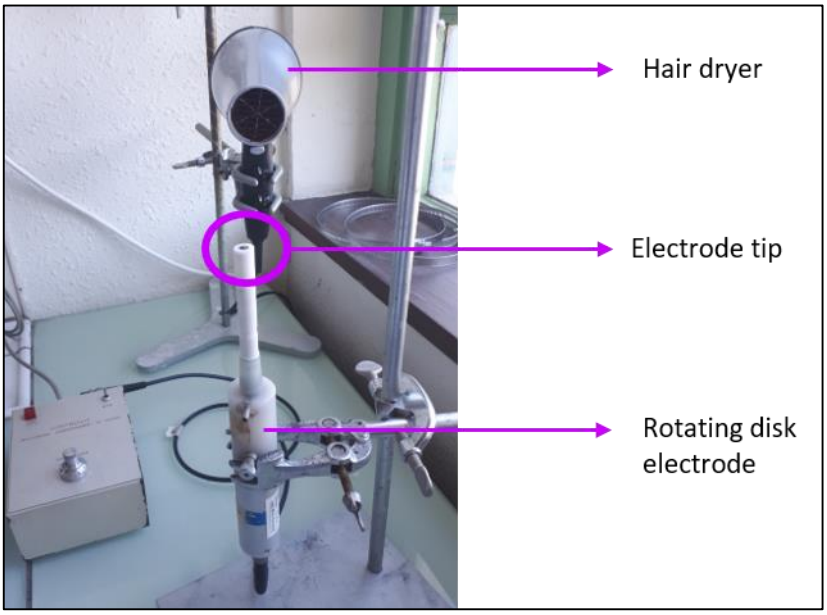

Figure II.2: Ink deposition setup

II.4.1.2 Four electrode setup

In order to increase the reproducibility and the viability of the results, electrochemical experiments were performed with the same setup, using same chemicals, and same protocol.

All electrochemical tests are performed in a homemade cell, made of PYREX glass, with 5 necks and one gas outlet (Figure II.3). The working electrode potential and current are monitored with a Biologic VMP3 potentiostat. All experiments were made at 25°C, using a cryothermostat (Thermo Scientific).

The working electrode is made of a 5 mm diameter mirror-polished glassy carbon rod encapsulated into Teflon. It is then screwed at the tip of the RDE (OrigaTrod, Origalys). The rotation speed is adjusted and monitored to enable known mass-transport rate.

The counter electrode is made of a long platinum wire, shaped as a spring at the tip to increase its surface area.

The reference electrode is a freshly-prepared reversible hydrogen reference (RHE). The RHE is renewed every 4 hours, to ensure its stability.

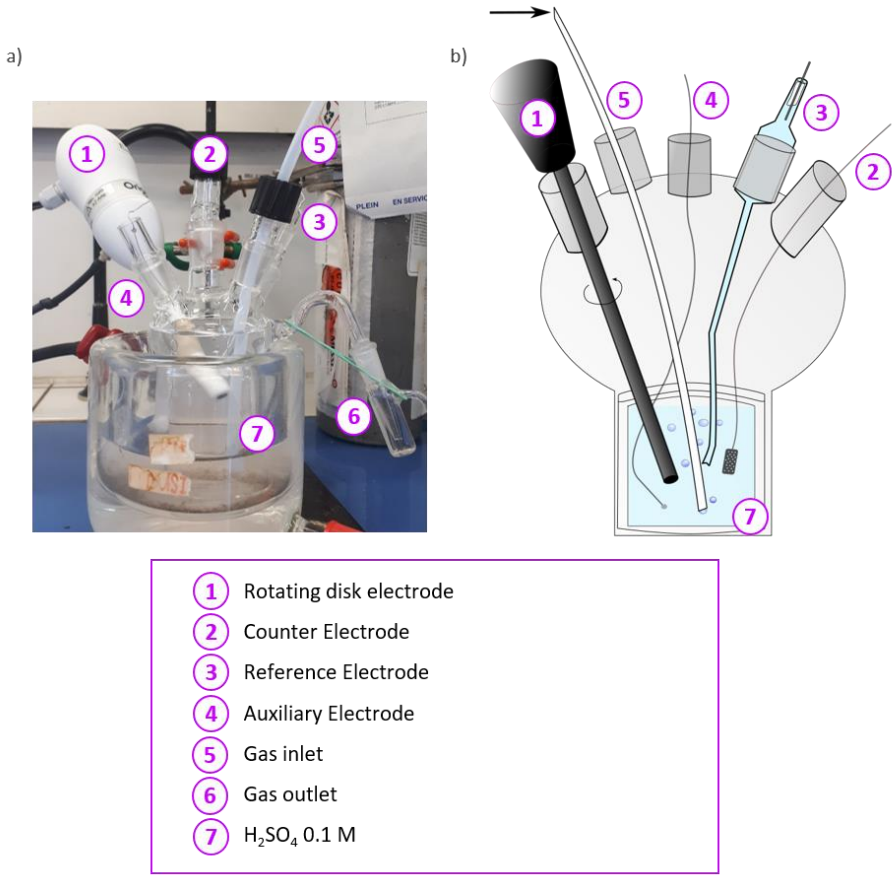

Figure II.3: a) Photography and b) schematic representation of a four-electrode electrochemical cell (Drawing by Matthieu Tempelaere).

The auxiliary electrode (fourth electrode) is used to reduce the noise coming from surrounding electronic instruments. It is made of a simple Pt wire, linked to the reference electrode through a capacitor bridge, playing the role of a low-pass filter [206].

The gas inlet: A glass tube is used to purge the electrolyte and cell with either Ar (> 99.999%, Messer), or H_2 (>99.999%, Messer), depending on the experiment. The gas is directly bubbled into the electrolyte during purging times, and above the electrolyte during recording times, to avoid noise.

The electrolyte: it was chosen to work in 0.1 M H_2SO_4 (Suprapur®, Merck), to enable comparison with previous studies about CO poisoning and/or resistance. The electrolyte was prepared each morning before experiments.

II.4.2. Basic Electrochemical protocol

For each electrocatalyst, the following protocol was used in order to ensure proper comparison from one material to the other. To check the reproducibility of the results, at least 2 electrodes of the same ink were studied each time (more if reproducibility was insufficient). All potentials are referred to the RHE scale and will be simply noted V. Before inserting the working electrode in the

cell, the cell is de-oxygenized by bubbling argon into the electrolyte for 30 min. The following procedure is then applied.

1- Cyclic Voltammetry

A cyclic voltammetry (CV) is first made to clean the electrocatalyst surface and establish its electrochemical signature. The potential is set to 0.1 V for 10 s, then cycled between 0.05 and 1.23 V three times at 20 mV s^{-1}. A classic cyclic voltammogram is shown Figure II.4. At high potential values, the Pt surface is partially-oxidized at the anodic scan (light blue region in Figure II.4), then reduced during the cathodic one (dark blue region in Figure II.4). At low potential values, protons are adsorbed on the Pt surface in the so-called hydrogen underpotential deposition (H_{UPD}, cathodic scan – dark green region in Figure II.4), and then desorbed in the anodic scan (light green region in Figure II.4). Protons forming a one-one Pt-H bond [207], the related desorption charge gives the Pt surface, considering the polycrystalline platinum surface charge exchange for 1 electron: 210 µC cm^{-2} applies for nanostructured electrocatalysts (which is a widely-accepted hypothesis). The blank area is the double capacitive layer, which depends, mostly, on the carbon surface area.

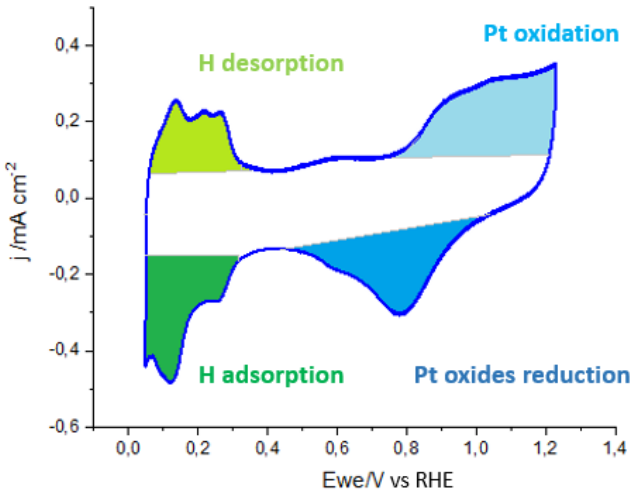

Figure II.4: Classic cyclic voltammetry of a Pt/C electrocatalyst, under Ar, at 20 mV s^{-1}

2- Hydrogen Evolution Reaction (HER)

A cyclic voltammetry at low potential is made in order to witness the activity towards the hydrogen evolution reaction. Since the hydrogen oxidation reaction (HOR) is limited by mass transport in liquid acidic electrolyte, the kinetics of the reaction on a given electrocatalyst cannot be directly determined. However, if an electrocatalyst presents good activity towards one hydrogen reaction, it usually also presents a good one towards the other [208]. The HER activity was therefore used as a marker of the electrocatalyst activity towards HOR, at least in liquid electrolyte conditions. For this characterization, the potential is cycled three times between 0.4 and -0.1 V at 20 mV s^{-1}. The hydrogen evolution current at both -20 mV and -100 mV are used as markers to compare the different electrocatalysts in terms of HER/HOR activity.

3- CO stripping

A CO stripping voltammetry is then performed in order to determine both the electrochemically active surface area and the CO oxidation behaviour on the electrocatalyst.

The potential is held at 0.1 V for 35 minutes. During this time, carbon monoxide is purged into the cell for 5 minutes and then flushed out with argon for the remaining 30 minutes, a necessary time to ensure that no traces of CO remain in the electrolyte. The potential is afterwards cycled between 0.05 and 1.23 V three times, at 20 mV s^{-1}.

Carbon monoxide being a strong poison to platinum, it strongly adsorbs on its surface, until it is completely covered (blocked). When the CO coverage (θ_{CO}) reaches its maximum value on the electrocatalyst surface, CO is mostly bonded to Pt atoms through a linear bond (equation (II.8)) [209]. This is complete in 5 minutes for the present experiments. Ruthenium also strongly adsorbs CO at that potential. Then, the Ar purge chases all the remaining CO molecules away from the electrolyte, so that only the adsorbed CO monolayer remains on the Pt (or PtRu) surface.

Upon potential increase from that state, the current firstly essentially stays null because of the CO poisoning (only the carbon surface is accessible, hence possibly active, at that stage). Then at a given potential (that depends on the electrocatalyst), OH^- groups start to adsorb in the few remaining spots (sometimes freed because of a weak Pt-CO bond) [210] (equation (II.9)). The monolayer of CO is then gradually oxidized on the first cycle, following the well-known Langmuir-Hinshelwood mechanism (equation (II.10)). On the second cycle, the cyclic voltammetry regains its original shape, with the capacitive behaviour in supporting electrolyte of Figure II.4.

$$CO + Pt \rightarrow CO_{ad} \quad \text{(II.8)}$$

$$H_2O + Pt \rightarrow OH_{ad} + H^+ + e^- \quad \text{(II.9)}$$

$$CO_{ad} + OH_{ad} \rightarrow CO_2 + H^+ + e^- \quad \text{(II.10)}$$

This method is often used in electrochemistry to determine ECSA of Pt, being admitted that the stoichiometry of CO_{ad} to surface atoms is known with precision (this method also applies, with limitations, for Ru). The CO oxidation charge, that can be approximately given by subtraction of the second anodic cycle to the first one, and then integration of the result, is strongly related to the metal surface. The ratio $Q_{CO,ox}/S_{metal}$ was calculated for polycrystalline platinum, taking into account the atom density on its surface. For a 2-electron exchange oxidation of a full-covering monolayer, the surface coulombic charge is 420 µC cm^{-2} [207] (red area in Figure II.5). Known values for other materials, that were used in this work, are shown in Table II.3. The inconsistency of values for different sources in the case of Ru and PtRu, however, must be pointed out. It was chosen to use those values anyways, but was kept in mind that the error factor is superior to that of pure Pt ECSA calculation, broadly studied.

Another way to calculate the ECSA would be to use the H_{UPD} area on the cyclic voltammogram, with the subtraction between second and first cycles. This method however, proved to be quite irrelevant since it does not only take into account the hydrogen under potential deposition, but also the capacitive current. Whereas this is often made and relevant for pure Pt electrocatalysts,

for Ru or W-containing electrocatalysts it leads to non-negligible (or even overwhelming) errors [209], these metals leading to strong pseudocapacitive behaviours (e.g. bronze formation in W-oxides [183,211]). It was chosen not to use it.

Table II.3: Surface charge values for studied materials

Metal	Q_{CO}/S (µC cm^{-2})	Reference
Pt	420	[207]
Ru	550	[157]
PtRu	385	[157]
Pt+Ru	485	Mean between Pt and Ru in 1:1 proportion

The CO stripping technique also permits to determine the CO resistance and/or CO oxidation performance of an electrocatalyst. As shown Figure II.5, two values are mainly used here:

The CO oxidation onset potential. It is the potential at which the first electroactive sites are recovered. It can be read either from the curve, at the moment the current starts increasing above the baseline; practically speaking, it was determined from the crossing point between the first and second cycles of a CO stripping CV, when the oxidation current reaches that of the capacitive current given by the support.

The CO oxidation peak. It is the potential at which the maximum oxidation current can be read. It is not a mean for CO oxidation, but can however help identify good CO-resistant electrocatalyst.

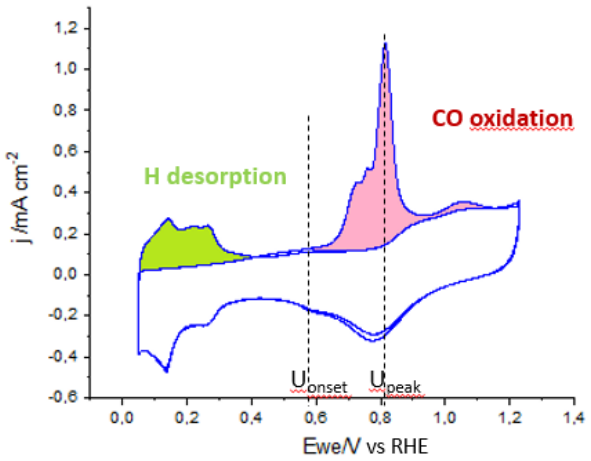

Figure II.5 : Example of a CO-stripping performed on Pt nanoparticles, under Ar flux, at 20 mV s^{-1}

4- CO stripping under H_2

This method consists in performing a CO stripping technique, but uses molecular hydrogen to purge the electrolyte instead of argon. As for the "classical" CO stripping technique, the potential is firstly held at 0.1 V for 35 minutes. For the first 5 minutes, CO is bubbled into the electrolyte. Then, for 15 minutes, argon is used to purged the cell (hydrogen being too light compared to CO, it is much more difficult to chase the CO away), and in the end, hydrogen is purged into the cell for another 15 minutes. A cyclic voltammetry is then performed by cycling the potential between

0.05 and 0.9 V, at 20 mV s^{-1}, while keeping a slow hydrogen bubbling into the cell. During this experiment, the RDE is set at 1000 rpm, a value high enough to ensure a fixed mass transport flux.

The difference with the "classical" CO stripping technique relies on the hydrogen saturation of the electrolyte and the very high activity of Pt for the hydrogen oxidation reaction. As soon as CO desorbs/is oxidized from Pt sites, those sites can now adsorb and oxidize H_2 (HOR). This leads to a fast increase in the oxidation current, until the mass-transport limit is reached. It was calculated that only 5% Pt sites being freed is enough to reach 90% of the current transport limit [212], meaning that CO oxidation beginning is much more visible with such a method.

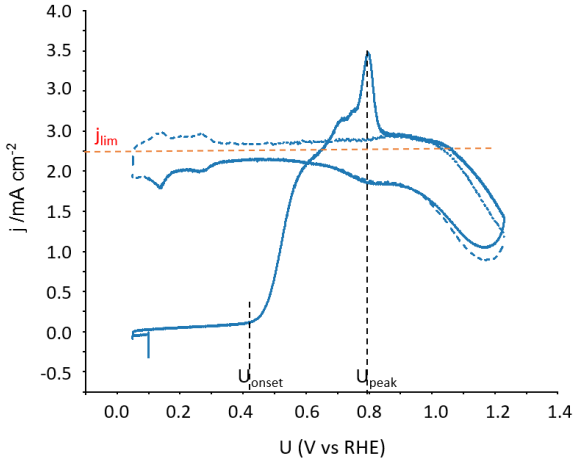

Figure II.6: CO stripping under H_2 performed on a Pt/C electrode, at 2 0mV s^{-1}, at 1000 rpm.

As shown on Figure II.6, several values can be extracted on such a graph. The current plateau, j_{lim}, can be compared to the Levich current limit (see equation (II.11))., expressed with n the number of exchanged electrons, the Faradic constant F, the diffusion coefficient *D*, the electrolyte viscosity υ, the hydrogen concentration in the electrolyte [H_2], and the rotating speed ω .

$$j_{lim} = 0.620nFD^{\frac{2}{3}}\omega^{\frac{1}{2}}\upsilon^{-\frac{1}{6}}[H_2] \quad \text{(II.11)}$$

The potential peak U_{peak}, can be compared to the one obtained during the "classical" CO-stripping; the onset potential U_{onset}, is read at 5% of j_{lim}, it gives the potential at which the CO oxidation is starting on the studied material.

5- HER in argon

The low potential cyclic voltammetry of step 2 is performed again after switching back the cell into argon atmosphere, in order to witness any change in the hydrogen evolution/oxidation reaction activity.

II.4.3. Differential electrochemical mass spectrometry

Electrochemical experiments are not always enough to properly understand all reaction mechanisms at stake on an electrode surface. The use of a coupled technique is sometimes required to unveil concomitant phenomena and be capable to fully-describe a cyclic

voltammogram, and the proposed explanations for the observed currents in terms of competing reactions.

The differential electrochemical mass spectrometry (DEMS) couples a mass spectrometer with electrochemistry. It permits to follow continuously the consumption and/or production of gaseous or volatile species at the working electrode. Figure II.7 gives a schematic representation of the setup. The setup is made of an electrochemical cell with several necks for (i) the purge by the relevant gas (Ar, H_2 or CO), (ii) the counter electrode (Pt wire), and (iii) the reference electrode (homemade RHE). The working electrode is situated at the bottom of the cell, at the junction between the liquid electrolyte and the vacuum chamber. It is necessarily porous, to enable both contact with the electrolyte (above the electrode) and the vacuum (below it). This cell is controlled with a VMP300 potentiostat (Biologic).

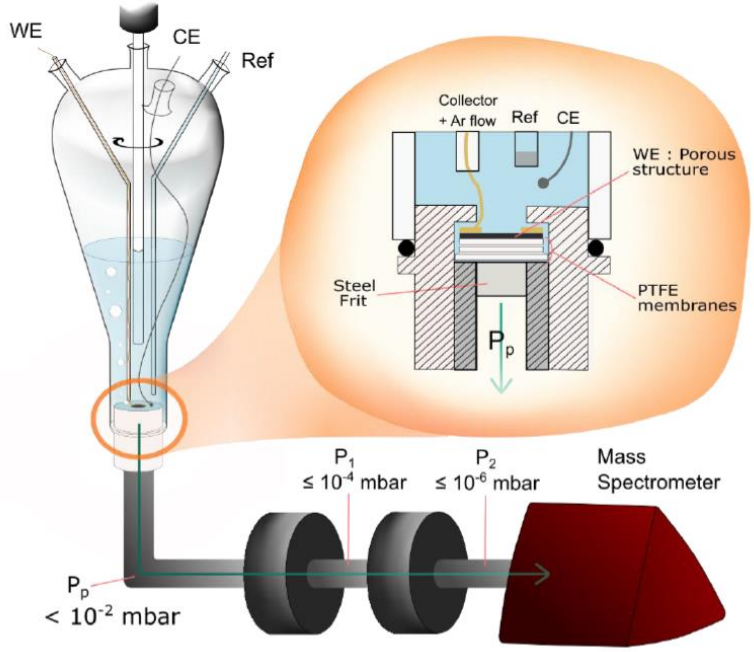

Figure II.7: Schematic representation of a differential electrochemical mass spectrometer cell, along with the vacuum system (from Guillaume Braesch's Thesis) [213].

The bottom of the cell is screwed to a vacuum tube, first purged until 10^{-2} mbar with a primary pump (PFEIFFER®). When the vacuum is good enough, this primary chamber is opened to the high vacuum line, associated with two turbomolecular pumps (PFEIFFER®) present in two successive chambers separated by a small diaphragm, ensuring a cascade of vacuum to the mass spectrometer. The vacuum reaches 10^{-7} mbar at the mass spectrometer (PRISMA PLUS QMG 220 M1, heated 1 hour before experiment); this pressure gradient enables a ballistic trajectory of the gases presents at the working electrode to the mass spectrometer, enabling on-time detection (with a lag time below 1 s).

For this to work, the junction between the vacuum chamber and the electrochemical cell, besides being porous for gases to pass, needs to be hydrophobic, to prevent liquid water from entering the vacuum line (which would be seriously damaging to both the mass spectrometer and the pumps). It is made of three layers of porous PTFE (thickness = 20 µm, pore size = 20 nm, porous fraction = 50%), known for its hydrophobicity, on top of a fritted steel that ensures the mechanical

resistance of the support. The last PTFE layer is covered with a porous layer of sputtered gold (ca. 50 nm thick), enabling electronic conductivity on the whole surface, hence efficient current collection to the working electrode. The latter is made by depositing the ink (same as for RDE experiments) at the middle of that last layer, in 4 depositions of 2.5 µL. The Pt loading goal is, as for RDE experiments, of 25 $\mu g_{Pt}\ cm^{-2}$. The connexion of the working electrode is ensured by a gold flat ring linked to a gold wire, leading it to the top of the cell and then the potentiostat.

II.4.4. Gas diffusion electrode

The gas diffusion electrode is a type of electrochemical cell which permits to feed the working electrode with gas phase reactants, while controlling its potential with a reference and a counter electrode. Thanks to that, the GDE can overcome the highly-detrimental mass-transport limit existing in the RDE configuration, when gaseous reactant must be dissolved in the liquid electrolyte (with a poor solubility and small diffusion coefficient); thus, a GDE enables to properly compare the electrocatalysts kinetics for reactions such as the HER/HOR. Contrary to the hydrogen pump system (which uses a full membrane electrode assemblies), the GDE enables the use of a very small amount of electrocatalyst, and thus facilitates the fast screening of electrocatalysts.

At that stage, I would like to especially thank professor Matthias Arenz and his team for kindly providing me a three-week training session on the GDE in their lab, as well as for offering a physical copy of their GDE setup to the LEPMI. Based on this, the cell was then further optimized, re-designed and fabricated in collaboration with the Centre of Atomic Energy of Grenoble (CEA-Grenoble); the modifications notably aimed to optimize the materials and geometry of the current collecting and reagent-feeding plate.

II.4.4.1 Setup description

As presented in Figure II.8, the GDE is made of an upper part for the reference and counter electrodes (filled with liquid electrolyte), and a lower part for the working electrode (fed by the proper reactant in the gas phase).

The lower body is made of stainless steel. Two channels permit the entry and exit of the gas reactant (here H_2 or CO or a mixture of these, or even N_2 or Ar for baseline characterizations). A current collecting plate made of graphite (to avoid corrosion) is placed is the centre of the body. It is made of multi-linear-canal channels that permit the transport of the gas right below the working electrode.

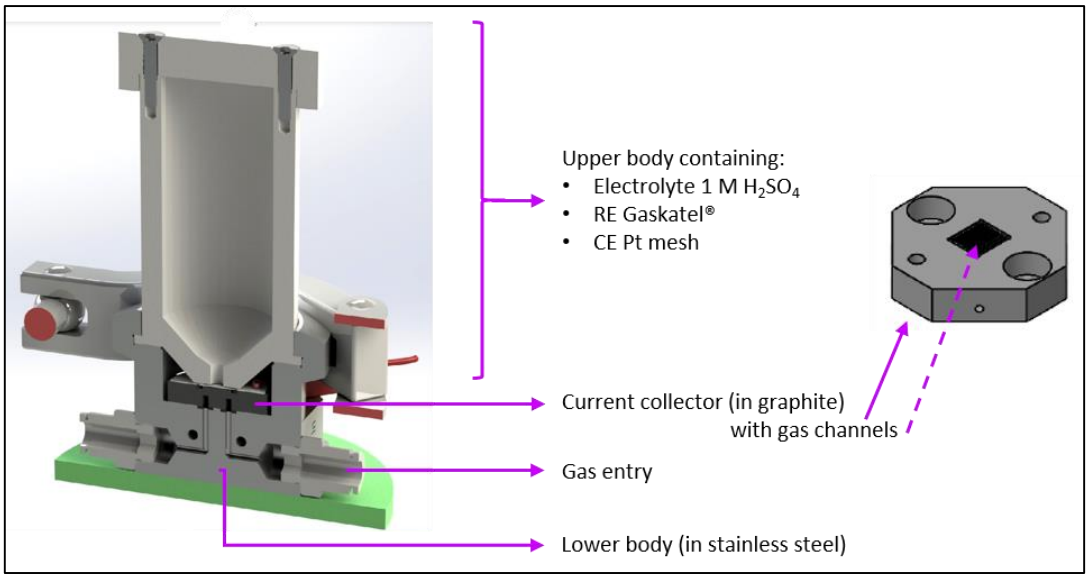

Figure II.8: Gas diffusion electrode schematic drawing in cross-section [214].

The working electrode is made of a carbon GDL (H2315 T10AC1, 241 µm thickness, Freudenberg®) of 6 mm of diameter. It is centred on the current collector plate with a silicon gasket (200 µm thickness). The electrocatalyst ink is made following the same protocol as described in section II.4.1.1. The ink dilution with IPA and ultrapure water is calculated so that 5 µL contains 1.77 µg of platinum, leading to a surface loading of 25 µg cm^{-2}, chosen to be identical as the one used for the RDE characterizations (note that the geometric surface area for the GDE is 0.0707 cm^2). The ink is deposited in the centre of GDL, and left to dry for 5-10 minutes on a hot plate at 60°C.

The upper part of the cell is made of Teflon, and contains the electrolyte, typically (and unless otherwise stated) a 1 M H_2SO_4 solution. This high concentration is necessary to reduce the ohmic drop, as a resistance of only 1 Ω at 0.5 A (a current encountered in GDE, see Chapter V) leads to a 500 mV shift. The reference electrode is a commercial micro-RHE from Gaskatel® (it has a smaller size than common commercial references, more appropriate to the small GDE setup). The counter electrode is made of a very large Pt mesh, necessary to counter very high currents without limiting the reaction.

The stainless steel areas in contact with the upper body are covered by silicon gaskets, to prevent any steel corrosion and gas leaks (or entry). In their work, Inaba *et al.* worked with Nafion® membrane pressed on top of the GDL, to make the junction with the liquid electrolyte [193]. In the present experiment, it was decided to (unless otherwise stated) work without any polymer membrane in between both parts, to further reduce the ohmic drop and permit better water diffusion to/from the active layer. The hydrophobic properties of the GDL were enough to prevent the electrolyte from flooding the working electrode.

Experiments were performed at ambient temperature (around 22°C), and the potential was monitored using a Biologic VMP3 potentiostat. The hydrogen gas flow was controlled using mass flow controllers (Brooks Instrumentation®) calibrated beforehand, and set at 29 mL min^{-1}. The CO dilution was made using a dilution of a 0.1% CO/H_2 mix (Messer) with pure hydrogen (Messer).

II.4.4.2 Experimental protocol

For each electrocatalyst, the following protocol was used in order to ensure proper comparison from one material to the other. All measurements were performed with a dynamic ohmic drop compensation (ZIR). Both cyclic voltammetry and CO-stripping were performed following the same protocol as presented in section II.4.2.

1- Cyclic voltammetry

2- CO-stripping

3- Cyclic voltammetry under H_2

The gas inlet was switched to a feed of 29 mL min^{-1} of pure hydrogen. The potential was cycled three times between -0.02 and 1.23 V for Pt, -0.02 and 0.9 V for Ru-containing materials, and -0.02 and 0.7 V for tungsten-based materials. To ensure proper comparison with RDE, the scan rate was chosen at 20 mV s^{-1}.

A second cyclic voltammetry was then performed, this time in order to measure the exchange current density. The scan rate was then lowered to 5 mV s^{-1}, and the potential scan was performed from -0.2 to 0.3 V.

4- Chronoamperometry (CA) in pure H_2

Three CA were performed in each gas feed. They all lasted 15 minutes (decided because of the very fast current loss) and were fixed respectively at 20 mV, 130 mV and 400 mV. Prior each CA, a cyclic voltammetry was performed between -0.1 and 1.23 V (or 0.9 V with Ru and W), in order to "clean" the surface from any poisoning adsorbates, and regain the initial current.

5- CA in 10 ppm CO/H_2

The electrochemical protocol followed in CO-containing feed is the same as the one presented for pure H_2 feed. For each cleaning CV, the gas was switched back to pure H_2.

6- CA in 50 ppm CO/H_2

The same protocol as for CA in 10 ppm CO/H_2 was followed.

II.5. Conclusion

All the techniques gathered here will permit a better understanding of the studied electrocatalysts and their behaviour towards the HOR reaction in presence of impurities. Electrochemical techniques such as the gas diffusion electrode and the four electrodes cell give information about the electrocatalysts behaviour and reaction kinetics in presence of H_2 and CO, in gas or liquid phase. When associated with a mass spectrometer, more precision on the reactions products and their potential range of production can be gathered.

The techniques related to the physico-chemical characterization of the materials on the other hand, give detailed data on the state of the studied electrocatalysts as their size (TEM, XRD),

morphology (TEM, XPS), crystallographic organisation (XRD), etc. This information can give a better understanding on the electrochemical behaviours of the studied materials, ad can help improve them.

The next chapters will then be presented in the following plan: the physico-chemical studies of the family of electrocatalysts will be first present so as to draw a proper resume of the materials characteristics. Those data will then be used in a second part to assist the analyst of the electrochemical behaviour of those catalysts.

CHAPTER III

Un-alloyed PtRu and their CO tolerance/oxidation properties

Chapter III Un-alloyed PtRu and their CO tolerance/oxidation properties

This chapter will focus on the so-called "Pt+Ru family" of electrocatalysts. The genesis of such composite materials will firstly be introduced. Secondly, after a brief summary of their synthesis method, the chapter will present their physico-chemical properties (composition, structure). Lastly, their electrochemical performance regarding CO tolerance, and structure-activity relationship will be highlighted.

III.1. PtRu alloy: A little state of the art

As developed in Chapter I, platinum-ruthenium (PtRu) alloy is one of the most used electrocatalyst in term of CO-tolerance in low-temperature fuel cells, and in direct alcohol fuel cells, in which CO can be formed as an intermediate of the reaction or trace pollutant [159,166,173,215]. Regarding to CO-tolerance in PEMFC fed with impure H_2, PtRu alloys have been widely studied both in model condition (RDE setup) and in close-to-real application (full PEMFC setup), as a catalyst for the anode side, capable to oxidize hydrogen in the presence of impurities of fuel reformate (in the first line: CO). For both PEMFC and the EHC, this alloy provides many advantages, but several drawbacks can also be put into light.

III.1.1. Advantages

The CO-tolerance of PtRu alloys is frequently ascribed to a combination of electronic [216,217] and bifunctional effects [218–220]. Firstly, by alloying Pt with Ru, the Pt-CO bonding is greatly weakened (electronic effect), as Maillard et al. measured with Fourier transform infrared spectroscopy (FTIRS) [221]. This results in weakened CO adsorption, thereby destabilizing the CO_{ad} adsorbate and facilitating its oxidation [222–224]. Secondly, as explained in Chapter I, Ru can adsorb OH groups at much lower potential than Pt, which could diffuse on the electrocatalyst to participate in CO_{ad} oxidation on Pt [156] (bifunctional effect). According to Gasteiger et al. [157], the best CO performances are achieved with a PtRu 1:1 atomic ratio.

III.1.2. Drawbacks

It was reported however that PtRu alloys can show low stability at high potentials. In particular, dissolution and de-alloying phenomena were brought to evidence by Lee et al. [225] and Hengge et al. [226], as a result of the propensity of Ru to form non-negligibly-soluble hydrous oxides [227]. This preferential dissolution of Ru from PtRu alloyed nanoparticles is known since two decades and was shown to detrimentally affect the cell performances, not only because it compromises the activity of the PtRu anode electrocatalysts, but also because it poisons the cathode electrocatalyst (after crossover of Ru species through the electrolyte membrane) [165,228].

Also, the same alloying process that is said to bring CO resistance thanks to Pt-CO bond weakening, might negatively impact the electrocatalyst activity towards hydrogen reactions. Pt Fermi level being lowered; Pt-H bond can also be weakened [217]. However, as it was previously brought to attention in Chapter I (see section I.2.2), the EHC necessitates a very high current density, above 2 A cm^{-2}, to be competitive versus other hydrogen compression technologies. Thus, despite the well-known high activity towards hydrogen reactions in presence of impurities of PtRu alloys, one may not be able to cope with their possible loss of HOR activity (versus Pt) due electronic structure modification for the very specific EHC anode [217].

III.1.3. Interest to keep Pt and Ru in contact, while in distinct phases

With this last point in mind, one idea would be to keep only the bifunctional effect of PtRu compounds, and avoid the electronic effect found in alloys. In other words, Pt should be kept in its own phase, with its own electronic structure, and beneficiate from the vicinity of Ru site that can provide OH groups for the CO oxidation reaction. In such a configuration, Pt should keep its excellent activity. The main question however will be: will the CO resistance be enough [156] ?

To answer that question, a new electrocatalyst was designed: pure Pt and pure Ru individual nanoparticles, alone in their phase and present in a 1 :1 atomic ratio, both deposited on the same carbon substrate. Such electrocatalyst was already proposed for the direct methanol fuel cell (although in different atomic proportion between Pt and Ru) [161], and will be studied here for the EHC application. This material will be called Pt+Ru/C, in order to differentiate it from the alloyed PtRu/C electrocatalysts. The following sections of the chapter focus on this material conception, physical and electrochemical characterizations.

III.2. Synthesis of the electrocatalysts

III.2.1. Adaptation of the polyol process to Ru nanoparticles

The synthesis of the Pt+Ru/C electrocatalysts follows the polyol synthesis described in Chapter II (section II.2) in which metal colloids are made separately, and then mixed with the substrate, with pH adjustment, before filtration.

Ru colloids were prepared from $RuCl_3$ salt (AlfaAesar, SPEC), in an ethylene glycol/water mix, with a concentration of 0.33 g_{Ru} L^{-1}. As for Pt colloids, Ru colloids were made by basification of the solution and temperature increase [229,230]. The final suspension shade is as dark as for platinum ones.

Pt+Ru/C electrocatalysts were then prepared in separate vials, by addition of Pt colloids, Ru colloids and Vulcan® XC-72 carbon in calculated proportions so that Pt and Ru are in 1:1 atomic ratio. Three metal loadings are targeted, as described in Table III.1. Another electrocatalyst, consisting of pure Ru/C, was also synthetized for later comparison, with a 20 wt.% metal loading on carbon.

Table III.1 : Targeted proportions for Pt+Ru electrocatalysts, presented in % per mass of electrocatalyst.

Electrocatalysts	Targeted wt.% Pt	Targeted wt.% Ru
Pt/C 33%	40	0
Ru/C 9%	0	20
Pt+Ru/C 12%	10	5
Pt+Ru/C 22%	20	10
Pt+Ru/C 42%	40	20

III.2.2. Electrocatalysts studied in this chapter

This chapter will then focus on the comparison of the Pt+Ru/C electrocatalysts, with either homemade or commercial electrocatalysts, all supported on carbon black Vulcan® XC72. To avoid confusion, they are named with the element in presence, with the metal loading in percentage per mass of electrocatalyst, which will be calculated in the forthcoming sections on TGA and ICP-MS.

- Pt/C 33% is a homemade electrocatalyst obtained by polyol synthesis.
- Ru/C 9% is also homemade by polyol synthesis. It was only characterized chemically and physically for comparison with Pt+Ru/C.
- Ru/C 20% is a commercial electrocatalyst from ETEK. It was used for electrochemical characterizations, as its metal loading better fits comparison with the other tested electrocatalysts.
- PtRu/C 29% is a commercial electrocatalyst, from ETEK.
- Pt+Ru/C 12%, 22% and 42% were prepared by the polyol synthesis described above with the same batch of Pt and Ru colloids for all three electrocatalysts. They are named with the loading in Pt and RuO_2.

III.3. Physical and chemical characterizations

In this part, all selected electrocatalysts will be studied both physically and chemically through the use of multiple techniques (as described in Chapter II), in order to determine their morphology and physico-chemical properties. The results will be firstly presented by techniques, prior being discussed.

III.3.1. Metal content in electrocatalyst powder

Despite all care taken during the synthesis, they are many sources of error that can impact the final loading of each metal on the carbon substrate, which can lead to different practical values from the targeted ones. Amongst these sources are the unknown exact hydration of the metal precursor salts, the incomplete adsorption of colloids onto the carbon surface or even possible losses during the weighting, handling and (mainly) filtration processes.

The real metal loading of each element was then properly characterized using the TGA, ICP-MS and AAS techniques described in Chapter II.

III.3.1.1 TGA analysis

TGA experiments were performed on all electrocatalysts, from 20°C to 1000°C, with a ramp of 5°C per minute, under a mixed N_2 and O_2 flux. Thermographs are shown Figure III.1 a) and b): a) featuring common references and their support, the carbon Vulcan® XC72, and b) all three Pt+Ru electrocatalysts.

The carbon Vulcan® thermograph, in black on Figure III.1 a), presents a typical carbon combustion curve. It starts with a very slight mass decrease, until 100°C, which other studies using TGA-MS setups related to moisture removal [231,232]. A clean plateau is then present until 550°C, where the mass starts decreasing until 870°C. This mass variation is due the oxidation of carbon with the oxygen flow. After 870°C, only 1.2% of mass is left in the crucible (ashes), which is low enough to conclude that all the carbon has been oxidized in the process.

Now focusing on the Pt/C curve, in blue on the graph, a very similar curve as for the bare carbon support is found. A first mass decrease is present between 20 and 200°C, related to the vaporization of adsorbed water (adsorbed on the carbon surface or present as capillary water in the porosity); this loss of free water is usually amounting a few wt.% at maximum, typically 3 wt.%.

Then, a slightly declining plateau can be seen until 350°C. This decline was attributed to water by Sellin et al. [231] since only H_2O signal was measured in this area, and no CO_2 or CO reactants could be detected. They suggested that such slow removal could come from adsorbed water on the oven ceramic parts, which seems quite unlikely in the present case, since this mass decline before 350°C only occurs in the presence of metals. Another explanation could be related to the removal of water adsorbates from the nanoparticles metallic surfaces.

Above 350°C, and until 550°C, carbon oxidation into CO_2 is observed. This reaction happens at much lower temperature, nearly 200°C, than on bare carbon Vulcan®. Such a phenomena highlights the well-known catalytic effect of (noble) metal nanoparticles on carbon oxidation, which exists both in the gas phase [233] and in electrochemical environment [141,142,234–237]. In the Pt/C 33% case, the carbon oxidation step of carbon-supported electrocatalysts can be decomposed in 2 steps: the first main loss at 400°C, and the second one, slower, until 700°C. One can ascribe the later to the oxidation of carbon particles which are not in contact with metal nanoparticles.

Ru/C and PtRu/C thermographs present a shape strongly similar to that of Pt/C 33%. For each step, the same explanation can be used. In the Ru/C 9% case however, a non-negligible decrease happens between 250 and 370°C; this could come for an anticipated carbon combustion, though no TGA-MS studies on such material could be found to prove it.

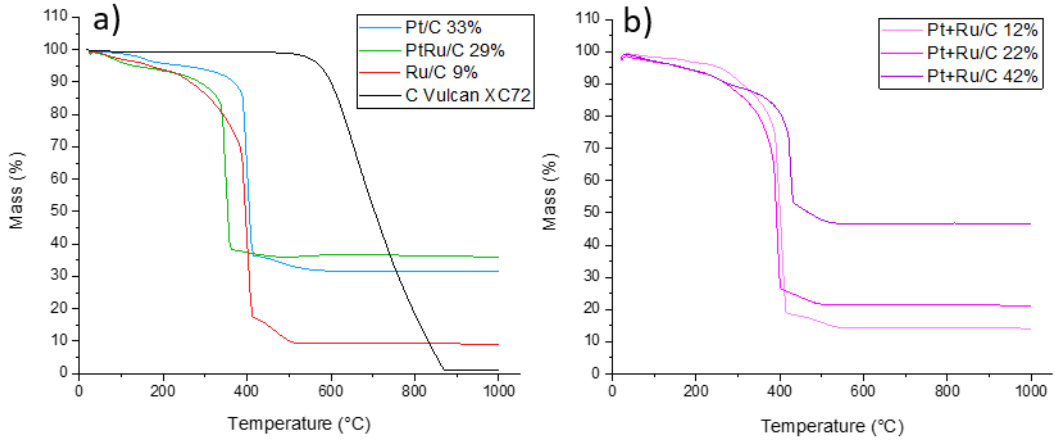

Figure III.1 : TGA curves with sample mass measured from 20 to 1000°C at 5°C.min^{-1} under a flow of mixed O_2+N_2 ; a) Pt/C 33%, PtRu/C 29%, and Ru 20%, b) Pt+Ru/C 12, 22, 42% .

Table III.2 gathers the analytical results of such experiments in terms of mass loading of metal in each electrocatalyst. Considering the uncertainty of the phenomena between 120 and 350°C, it was chosen to measure the water content at 120°C. Although this calculated water content must be read with caution, it will nevertheless be considered to correct the weights of electrocatalysts powders in all quantitative chemical analyses (ICP-MS, AAS), with an average value of 3 wt.%.

In addition, as explained previously, Ru can form RuO_4 volatile compounds starting 108°C in oxidizing conditions [201]. This means that some metal loss can happen during this experiment (for Ru-containing electrocatalysts), despite being far below the fusion temperature of ruthenium, at 1850°C for 1 nm nanoparticles (as it will be measured later) [238]. Ru-metal contents presented here hence correspond to the minima present, keeping in mind the real value could be slightly higher. For Pt/C electrocatalyst, TGA analyses should be more precise.

Table III.2 : Metal, carbon and water estimated from ATG measurement (at 120°C for water), as a function of hydrated or dry powder.

Electrocatalyst	**wt.% with water**			**wt.% without water**
	Metal	*Carbon*	*Estimated H_2O*	*Metal content*
Pt/C 33%	31.6	70.0	1.6	32.5
Ru/C 9%	8.8	94.6	3.4	9.1
PtRu/40% ETEK	35.9	68.8	4.7	37.0
Pt+ Ru/C 12%	14.0	87.9	1.9	14.4
Pt+Ru/C 22%	21.0	82.4	3.4	21.7
Pt+Ru/C 42%	46.4	57.0	3.4	47.8

Keeping in mind the potential issues listed above, the commercial PtRu/C shows 37.0 wt.% metal content, which is in agreement with the expected 40 wt.%. In the case of Pt/C and Ru/C on the other hand, the loss is less negligible with respectively 32.5 wt.% of Pt instead of the theoretical 40 wt.%, and 9.1 wt.% of Ru instead of 20 wt.%.

The metal contents calculated for Pt+Ru/C electrocatalysts also show that discrepancy. Instead of the theoretical 15, 30 and 60 wt.%, the practical values 14.4, 21.7 and 47.8 wt.% were respectively obtained. Even though the lower loading is in agreement with the expected value, the difference increases with the metal content. The error can either come from the synthesis process, or could be related to a Ru loss during the TGA, much higher than expected. The comparison of TGA results to ICP-MS and XPS results might help to resolve that issue.

III.3.1.2 AAS/ICP-MS measurements

Samples of each electrocatalysts were digested in aqua regia, diluted and then analysed with either AAS or ICP-MS. Both ICP-MS and AAS measurements are presented in Table III.3. A correction of 3 wt.% was applied to the measured values, in order to take the electrocatalyst powder hydration into account. This value was chosen following TGA results (see section C.1.a. of this chapter) on water content and used for all electrocatalysts.

Table III.3 : AAS and ICP-MS results for the five studied electrocatalysts, presented in percentage of metal per mass of electrocatalyst.

Electrocatalyst	wt.% Theoretical	ICP-MS values		AAS values
Pt/C 33%	40% Pt 0% Ru	33.3% Pt	0% Ru	31.5% Pt
Ru/C 9%	0% Pt 20% Ru	0% Pt	7.0% Ru	0% Pt
PtRu/C 29% ETEK	26.7% Pt 13.3% Ru	20.4% Pt	8.8% Ru	17.5% Pt
Pt+ Ru/C 12%	10% Pt 5% Ru	7.4% Pt	3.2% Ru	5.5% Pt
Pt+Ru/C 22%	20% Pt 10% Ru	14.3% Pt	5.5% Ru	10.9% Pt
Pt+Ru/C 42%	40% Pt 20% Ru	33.4% Pt	8.3% Ru	29.9% Pt

It can first be noticed that for each of the five Pt-containing electrocatalysts, the platinum loading given by AAS with the classic dissolution protocol is lower than the one measured by ICP-MS with the microwave-assisted dissolution protocol. The microwave dissolution being more effective, such a result is not surprising. Furthermore, despite AAS being a very good technique on its own, ICP-MS presents the benefits of being able to ionize small nanoparticles, which can make the difference in the case of a hard to dissolve material (like Ru). For later discussion, only ICP-MS results will then be taken into account. Table III.4 gathers the calculated values of metal content, and amount of Ru atoms for one Pt atom.

Secondly, the metal content of the commercial electrocatalyst PtRu/C was measured at 29.2 wt.%, instead of the expected 40 wt.%. This is 11 wt.% lower than the value given by the manufacturer, and 8 wt.% lower than the value measured by TGA. It is possible that the electrocatalysts undergoes oxidation during the TGA process, thus leading to an overestimation of the real metal content of the powder. Even more, the Pt:Ru atomic ratio should be of 50:50, and is instead of 55:45. As explained previously, some Ru losses may happen above 108°C and under oxidizing conditions [201], which could at least partially explain that discrepancy.

Table III.4: Metal content as a function of electrocatalyst weight and Pt atomic ratio according to ICP-MS results

	Pt : Ru atomic ratio	Metal content wt.%
Pt/C 33%	100 : 0	33.3
Ru/C 9%	0 : 100	7
PtRu/C 29%	55 : 45	29.2
Pt+Ru/C 12%	55 : 45	10.6
Pt+Ru/C 22%	58 : 42	19.8
Pt+Ru/C 42%	67 : 33	42

It can be noticed that in fact, all electrocatalysts present lower metal loading compared to the targeted values. Homemade Pt/C presents 33.3 wt.% platinum content, in very good agreement with the value measured in TGA, but still below the targeted one. Ru/C however, shows less than half the expected metal content, which leads to wonder which, between the synthesis process or the volatile property, is the most plausible explanation.

In the case of the three Pt+Ru/C electrocatalysts, the loss increases with the metal content. From the lowest to the highest loading, the difference with the aimed metallic amount is respectively 4, 10 and 18 wt.%. These real values however are still arranged in a gradation of loadings, which was the first aim with these three materials. There is however also an impact on the Pt:Ru ratio, as it seems that the lowest loading has, like with the commercial PtRu/C, 45 at.% of Ru in the metallic phase, and the highest loading has 33 at.% of Ru. This could lead to a possible decrease in contact between the two elements. STEM and electrochemical experiments will show that the Ru dispersion being wide and homogenous, the contact deficiency will be very minor.

III.3.2. Structural properties

The electrocatalysts structural and textural properties were then evaluated by XRD and TEM analyses.

III.3.2.1 X-Ray Diffraction

XRD patterns are presented Figure III.2 for all the studied electrocatalysts. They show diffraction peaks obtained for Pt/C and Ru/C electrocatalysts, as well as Pt+Ru/C in its different loadings.

The peak for $2\theta = 22°$ is present on all the samples, and can be ascribed to the (002) reflection of the Vulcan® XC72 carbon substrate; the (004) reflection of carbon is also encountered at $2\theta = 42°$ for the Ru/C electrocatalyst [239,240].

It appeared that Ru/C 9% presented only carbon diffraction features, and no peak related to crystalline ruthenium. Such an absence could be explained by (i) the amorphous state of Ru

nanoparticles or (ii) the size of particles being to small (< 2 nm) to detect any crystalline order. Transmission Electron Microscopy imaging will prove the latter to be true. The same absence of any crystalline Ru phase is obvious for the three Pt+Ru/C electrocatalysts.

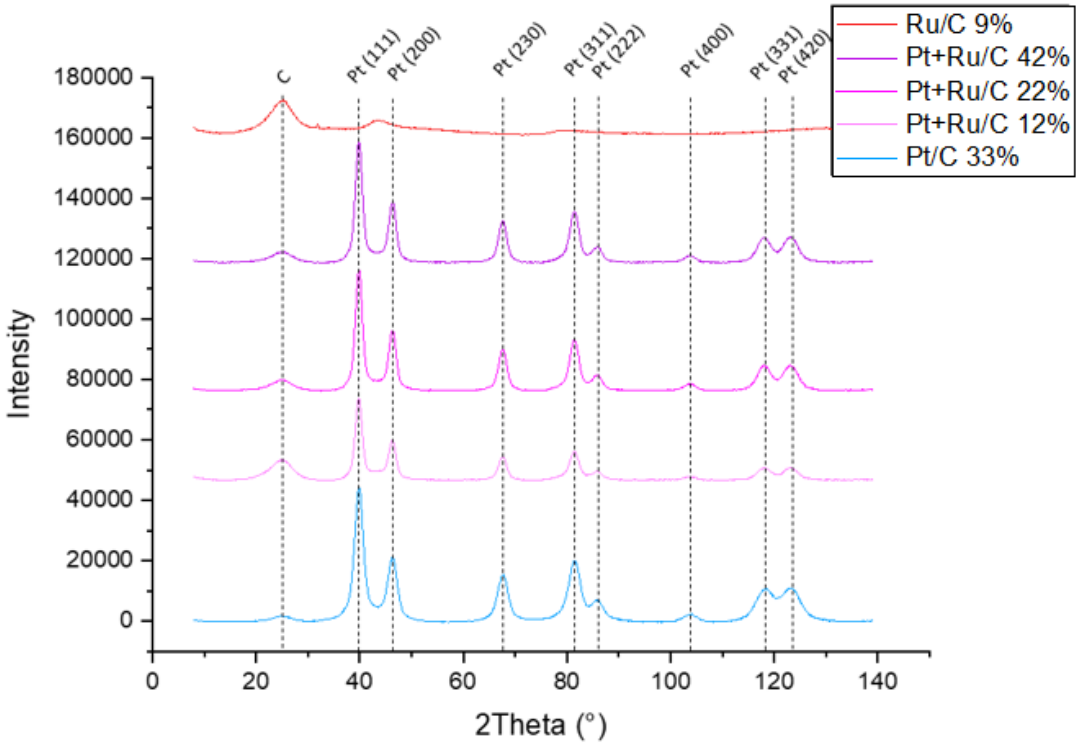

Figure III.2 : X-ray diffraction patterns of the family of Pt+Ru/C electrocatalysts together with the Pt/C and Ru/C benchmarks; the plots are presented with an offset for better lisibility

Pt/C and all three Pt+Ru/C electrocatalysts exhibit the diffraction peaks of the fcc Pt, with, for Pt/C, a lattice parameter of a=3.915 Å. In the case of the three Pt+Ru/C electrocatalysts, irrespective of their metal loadings, none of them presented any shift of the diffraction Pt peaks versus the Pt/C sample, thus proving the total absence of PtRu alloy in these electrocatalysts [241,242].

The diffraction peaks broadness is related to the nanometric size of the crystallites. The Scherrer formula, presented in Chapter II, section II.3.4, explains that relationship, and thus gives the size of coherence of the crystalline domains depending on the peak width, for the various orientations (diffraction peaks) monitored experimentally. Size domains are shown Table III.5. To limit the errors related to the baseline determination, only the most pronounced diffraction peaks were used for the calculation: Pt(111) and Pt(230), observed at 2θ = 40° and 2θ = 68°, respectively.

Table III.5 : Size of the platinum crystallites in the (111) and (230) directions estimated from the XRD patterns of Figure III.2 using the Scherrer formula, compared with the mean volume-average diameter calculated from TEM images.

	(111) crystallite size (nm)	(230) crystallite size (nm)	d_v *(nm)*
Pt/C 33%	5.1	5.0	4.9
Pt+Ru/C 12%	6.4	6.5	5.7
Pt+Ru/C 22%	6.3	6.5	5.9
Pt+Ru/C 42%	6.3	6.6	5.6

For all studied electrocatalysts, both orientations provide very similar results, thus encouraging the idea of isotropic particles (hence of near-spherical morphology). It can also be noticed that all Pt+Ru/C electrocatalysts exhibit nanoparticles of ca. 6.5 nm of diameter, regardless of the metal loading, which was expected since the three composite materials were prepared from the same colloidal Pt suspension (see above). This average is however slightly superior to that of Pt/C 33%, which is around 5 nm. Two possibilities could explain such a difference despite the use of similar Pt-colloids: either the two colloids batches (one used for Pt/C and the other for Pt+Ru/C) presented differences, or the presence of Ru colloids in the same beaker during deposition onto carbon could have affected the Pt nanoparticles size.

The average crystallite size was compared to the volume-averaged particle diameter calculated from TEM nanoparticles distribution histograms (see after).

III.3.2.2 X-Ray Photoelectron Spectroscopy

XPS analyses were performed with the K-alpha ThermoScientific spectrometer (Al-source) and data treated with the ThermoScientific Advanta software. The spectra were calibrated using the main carbon contribution and C, Pt, and Ru local spectra were decomposed in order to determine the nature of the ruthenium in presence, and its atomic ratio with Pt.

Ru can be studied on either Ru3d (*ca.* 280-295 eV) or Ru3p (*ca.* 450-510 eV). The Ru3p peak however presented very low intensity. It was decided to measure Ru content with the Ru3d band, which unfortunately overlaps the C1s spectra. The spectra were decomposed with the three main carbon contributions (C-C, C-H and C-O), and the four ruthenium contributions (Ru3d 5/2 and 3/2, and their satellites). The resulting spectra are presented for Ru/C 9% as well as the three Pt+Ru/C electrocatalysts in Figure III.3.

Ru/C 9% presents a main peak at 284.7 eV, mainly due to carbon contribution. A smaller pre-peak can be seen at 281.7 eV. It is mostly related to RuO_2 contribution [243,244]. No peak however, could be seen at 280 eV, associated to metallic Ru. In fact, the decomposition can be obtained with only RuO_2 contributions. The ruthenium present in this homemade electrocatalyst is therefore mainly oxidized.

Pt+Ru/C 12, 22 and 42% all present similar spectra with the main carbon contribution and the RuO_2 pre-peak. The latter is in fact more and more intense (compared to the carbon peak) as the metal loading increases, which agrees with the estimated ruthenium content. Here again, no contribution was measured for the metallic Ru.

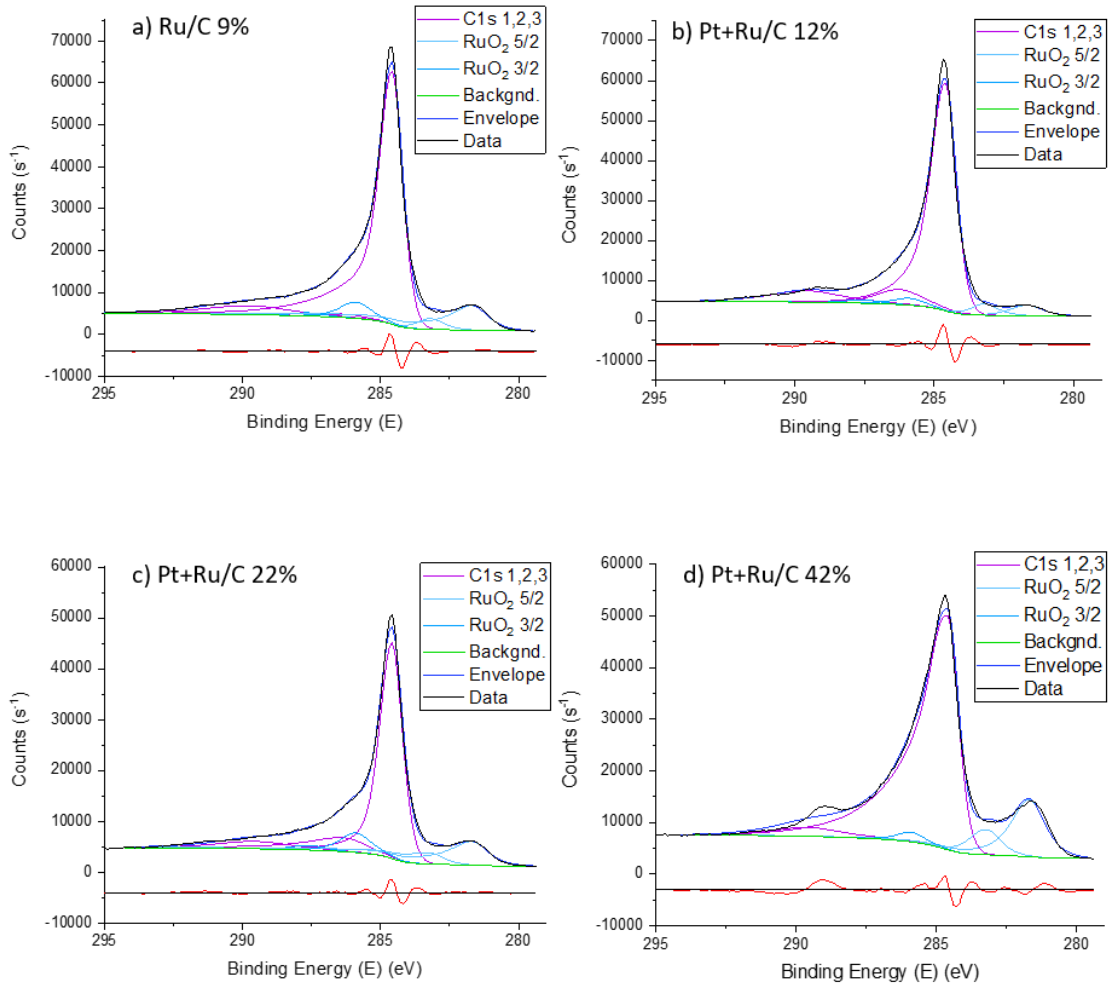

Figure III.3: XPS spectra for Ru3d and C1s deconvolutions for a) Ru/C 9%, b) c) and d), Pt+Ru/C 12, 22 and 42%. The residuals (counts x2) are presented in red below the curves.

Pt4f peaks were also analysed (not shown here), in order to determine the Pt:Ru atomic ratio in each of the composites electrocatalysts. The de-convoluted areas were summed for each elements, and then multiplied by the corresponding atomic sensitivity factor [245]. The atomic ratios are given Table III.6.

Table III.6: Pt:Ru atomic ratios calculated by XPS Ru3d and Pt4f spectra for Pt+Ru/C electrocatalysts compared to ICP results.

	Pt : Ru (at. ratio)	**Pt : Ru ICP (at. ratio)**
Pt+Ru/C 12%	45 : 55	55 : 45
Pt+Ru/C 22%	63 : 37	55 : 45
Pt+Ru/C 42%	63 : 37	58 : 42

It appears that for Pt+Ru/C 12%, the atomic ratio is close to the intended one: 50:50. It however slightly differs from the one measured in ICP-MS (55:45) as Ru seems dominant here.

Pt+Ru/C 22 and 42%, present an opposite result, with 63% of Pt per metallic atom for both of them. The Pt content differs from ICP-MS results by 8 at.% for the former and 5 at.% for the latter;

this means that a good amount of ruthenium is present in the electrocatalyst, in an apparently oxidised state, which was the desired situation.

III.3.3. Microscopy imaging

III.3.3.1 TEM

The morphology and texture of the prepared electrocatalysts was evaluated at the nm scale by TEM imaging. A selection of representative TEM micrographs is shown in Figure III.4, along with the corresponding particle size distribution histograms (per number of counted particles) for each electrocatalyst, based on the counting of ca. three hundred isolated nanoparticles.

All the materials present non-negligible extent of agglomerated nanoparticles and regions with larger density of nanoparticles at the carbon surface than in others; in brief, the materials are not completely homogenous in terms of texture, which was expected considering to the rather high metal loading involved.

For Pt/C 33%, despite some empty areas and small-sized agglomerates of a few 10 individual crystallites, the nanoparticles are of essentially bimodal distribution, with diameters centred on 3 and 5 nm; such nanoparticle size distribution is often encountered in electrocatalysis and appears as a relevant compromise between high surface area and large activity and durability [246]. Ru/C 9% is composed of very small nanoparticles (average diameter < 2 nm), so much that the smallest might not be visible on such TEM images. Also, some empty areas onto the carbon are witnessed (at least at that magnification).

Pt+Ru/C 12%, 22% and 42% all have bimodal distribution of sizes: one around 2 nm, and the other around 6 nm. This could be explained with the presence of very small nanoparticles of Ru, similar of those of Ru/C 9%, but mixed on the carbon surface with nanoparticles of Pt like those in Pt/C 33%. Slight amount of agglomerates is also detected on all three electrocatalysts, which seem to vary in size and numbers as a function of the overall metal loading at the carbon; the most prominent ones are therefore observed in Pt+Ru/C 42%.

Along with XRD results, there seems to be a slight difference between Pt/C et Pt+Ru/C mean volume diameter. Despite the lower figure of ca. 5.8 nm instead of 6.5 nm, Pt+Ru/C nanoparticle sizes also present a similarity in the average volume diameter. This lower number could possibly be explained by the fact that small Ru nanoparticles were also counted in TEM distribution, thus lowering the calculated average.

Additional micrographs were taken with the very high resolution FEI Titan ETEM on the Pt+Ru/C 12% electrocatalyst; they confirm the small size of the Ru nanoparticles (Figure III.5). On the left image, one ruthenium nanoparticle has a diameter of 1.5 nm, while on the right one, a dispersion of ruthenium shows sizes between 1 and 2 nm, with a remarkable lattice diffraction; these small crystallites were likely not visible on the TEM micrographs of Figure 3.

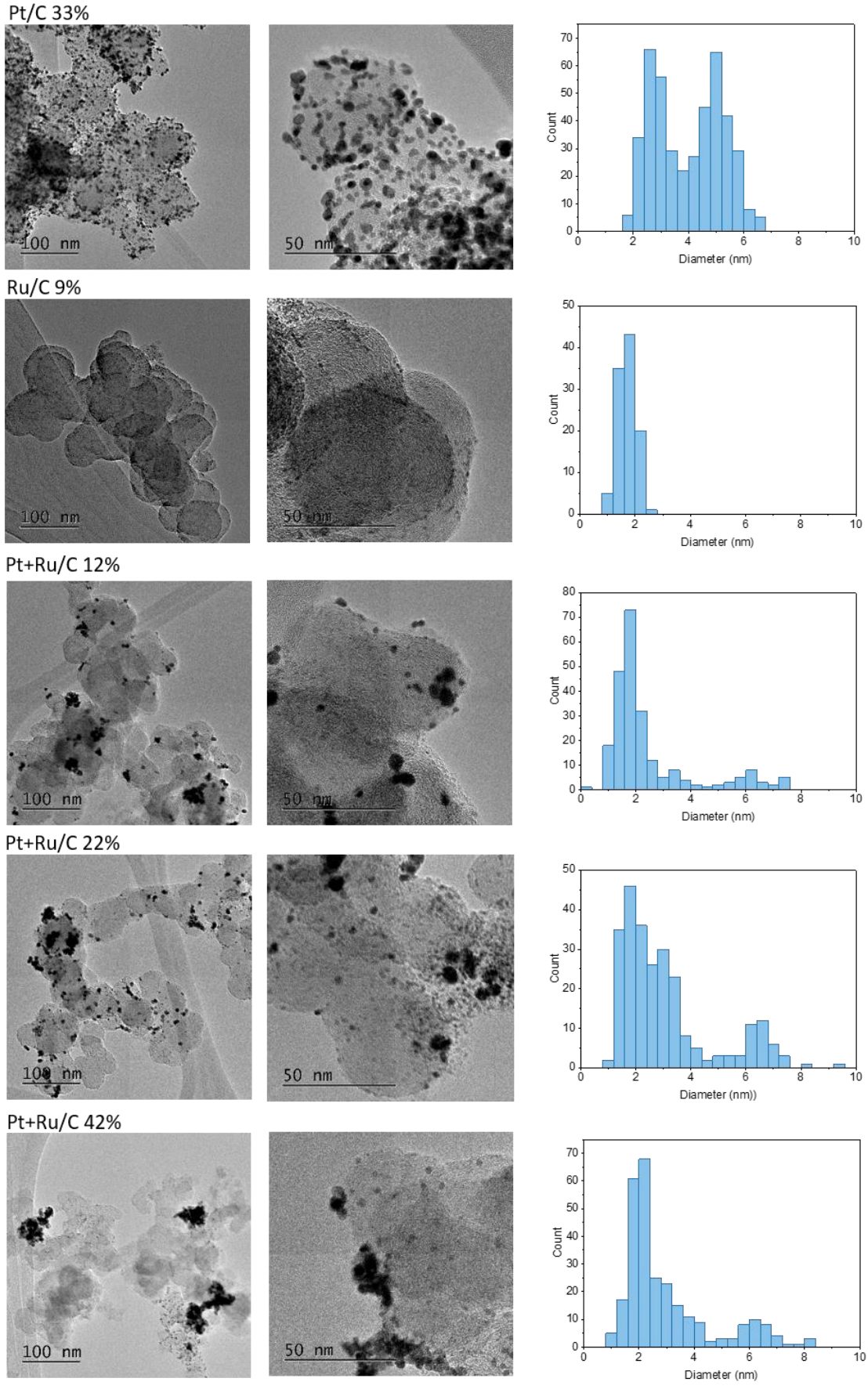

Figure III.4 : TEM images at 50 kX (column 1), 200 kX magnification (column 2) and nanoparticle size distribution (column 3)

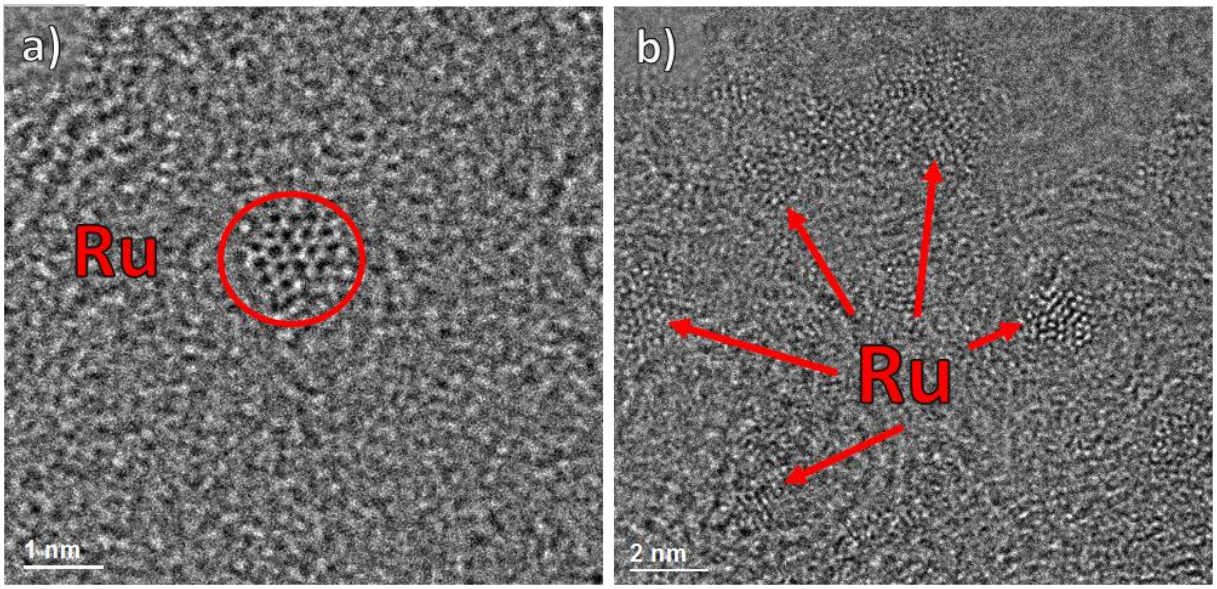

Figure III.5 : Ultra high resolution TEM images (FEI Titan ETEM G2) of Pt+Ru/C 12%, focusing on ruthenium areas: On the left, One ruthenium nanoparticles, on the right, a dispersion of several ruthenium nanoparticles, identified with X-EDS.

III.3.3.2 Elemental mapping

STEM experiments were performed with the FEI Titan ETEM on Pt+Ru/C 12% and with the JEOL 2100 STEM for Pt+Ru/C 22% and 42%. Elemental maps are shown Figure III.6. Experiments having been performed on two different microscopes, the colour legend is different for both of them.

It can first be noticed that on all three samples, Pt nanoparticles are ca. 5 nm in size, but also often present in small agglomerates, which is in accordance with the previous TEM micrographs. Ru nanoparticles on the other hand, are in this case much more visible despite their very small size (< 2 nm). They seem to be homogenously dispersed on the all carbon substrate, as well as on the Pt agglomerates. There is direct contact between Pt and Ru nanoparticles, which was the objective for these materials.

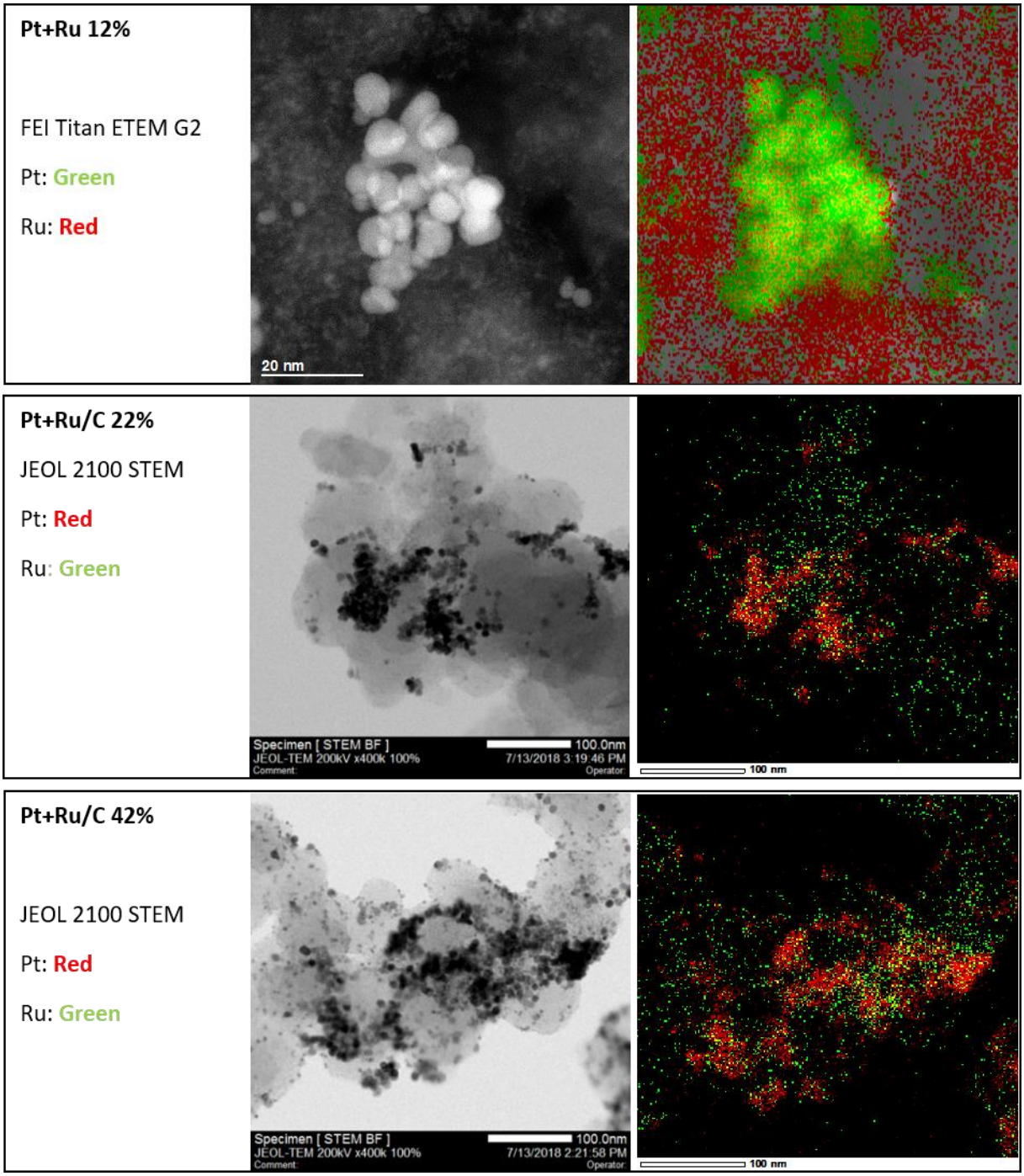

Figure III.6 : Elemental mapping of Pt+Ru/C 12% on Titan (Pt in Green, Ru in Red); Pt+Ru/C 22% and 42% on JEOL (Pt in red, Ru in green)

III.3.3.3 E-TEM

In order to observe the behaviour of Pt+Ru/C electrocatalysts in reducing conditions (*i.e*. those typically experienced by the electrocatalyst when at the anode of the EHC), Pt+Ru/C 12% was studied with the ETEM under H_2 environment, at 0.2 mbar and ambient temperature. An area including both Pt agglomerates and isolated nanoparticles was chosen and images were

successively recorded under the constant electron beam. Images at respectively 0, 40 and 80 seconds are presented on Figure III.7.

It appears that the carbon substrate is degraded at very high rate, and most of carbon particles have disappeared after only one minute. Mostly the metallic components (Pt and Ru) are left; because the support "shrinks" (and the mechanisms at stake are not discussed here), the remaining nanoparticles get progressively agglomerated at the remaining carbon substrate, the surface area of which gets lower and lower versus time in these conditions. In addition, one notices that those nanoparticles seem to keep the same size, and are not impacted severely by the hydrogen atmosphere; for instance, there does not seem to be nanoparticles' growth or coalescence at that stage.

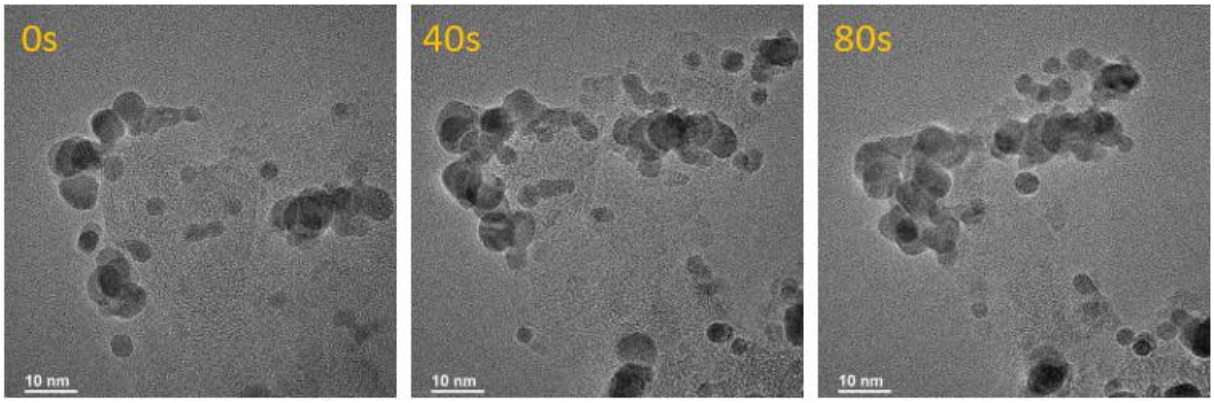

Figure III.7 : Snapshots of a movie of Pt+Ru/C 12% imaged the FEI Titan ETEM under 0.2 mbar H_2 at ambient temperature. Images were taken at 0, 40 and 80 seconds of recording.

III.3.4. Summary of the physicochemical analyses

Electrocatalysts from the "Pt+Ru Family" have been thoroughly studied in terms of their metal content, atomic structure, morphology and texture, and oxidation state. From one technique to another, the results are in agreement and permit a better understanding of each electrocatalyst properties.

Alloyed PtRu/C 29%, the sole commercial catalyst studied in this section, presents surprising results concerning its metal content. ICP-MS measurements gave 29.2 wt.% of total metal content while TGA results gave 37 wt.%, instead of the supposed 40 wt.% announced by the provider (E-TEK). One can put forth that the alloy dissolution necessary for the ICP-MS analyses was incomplete and/or that non-negligible amounts of Ru "vanished" in the process, some Ru-oxides being volatile. On this basis, the ICP-MS results seem the most reliable, and this material will then be referred to as PtRu/C 29%.

Pt/C 33% is a homemade electrocatalyst synthetized by polyol process. It contains 33 wt.% of Pt nanoparticles from 2 to 6 nm of diameter. Those particles are partially agglomerated on the carbon substrate.

Ru/C 9% is also a homemade electrocatalyst. Its metal content reaches at least 7%, bearing in mind the possible loss due to the volatility of ruthenium. It is composed of very small oxidized RuO_2

nanoparticles, less than 2 nm of diameter, which explains why no Ru diffraction signal could be measured with XRD. With such small particles, it is possible that the coulombic charge of Ru colloids during the synthesis was so low that the colloid-carbon attraction was decreased (the author did not find any reference supporting this hypothesis, though), thus also slightly decreasing the proportion of ruthenium onto the carbon substrate (for high metal loadings). This small size also likely favours vaporisation of Ru-oxides upon mild heating in the several steps of the synthesis or analyses.

The three electrocatalysts from the Pt+Ru/C family all consist of composites of very small isolated RuO_2 nanoparticles (diameter < 2 nm) homogeneously dispersed onto the carbon substrate, with larger and sometimes mildly agglomerated Pt nanoparticles (*ca.* 6.5 nm in diameter). XRD measurements also confirmed the fact that despite Pt, and Ru being in close contact on STEM images, there is no alloying between the two of them. Depending on the metal loading, the size and proportion of Pt agglomerates increases. Real metal contents were determined to be respectively 12, 22 and 42 wt.% (instead of the intended 15, 30 and 60 wt.%).

This difference between targeted and true metal content will not be a problem however, since Pt loading in Pt/C is still comparable to the one in Pt+Ru/C 42%. For all Pt+Ru/C electrocatalysts, the expected gradation is still present and will permit the characterization of the metal loading effect on the materials electrocatalytic activities.

For further measurements, it was chosen to replace the homemade Ru/C 9% by a commercial Ru/C 20% from ETEK. The metal loading was too low to properly compare it to the other electrocatalysts.

III.4. Electrochemical characterizations

In order to properly characterize their electrochemical behaviour and activity, electrocatalysts are first electrochemically characterized with the RDE setup, prior any real-scale measurements. The details concerning the electrochemical setup and the different protocols are given in Chapter II, section II.4 : Electrochemical characterizations.

III.4.1. Electrochemical signature

Figure III.8 presents the different electrochemical signatures obtained for each catalyst during the cyclic voltammetry in supporting electrolyte (0.1 M H_2SO_4, T = 25°C). For better visibility, they are divided into three groups: (a) Pt/C, (b) Pt/C, Ru/C and PtRu/C, and (c) the three Pt+Ru/C loadings.

For all electrocatalysts except Pt/C, the maximum potential was chosen at 0.9 V (all potential values being expressed on the RHE scale), to limit ruthenium dissolution. Pt/C maximum potential was kept at 1.23 V to keep its activity by forming and reducing Pt oxides on the surface, which helps to remove impurities from the surface.

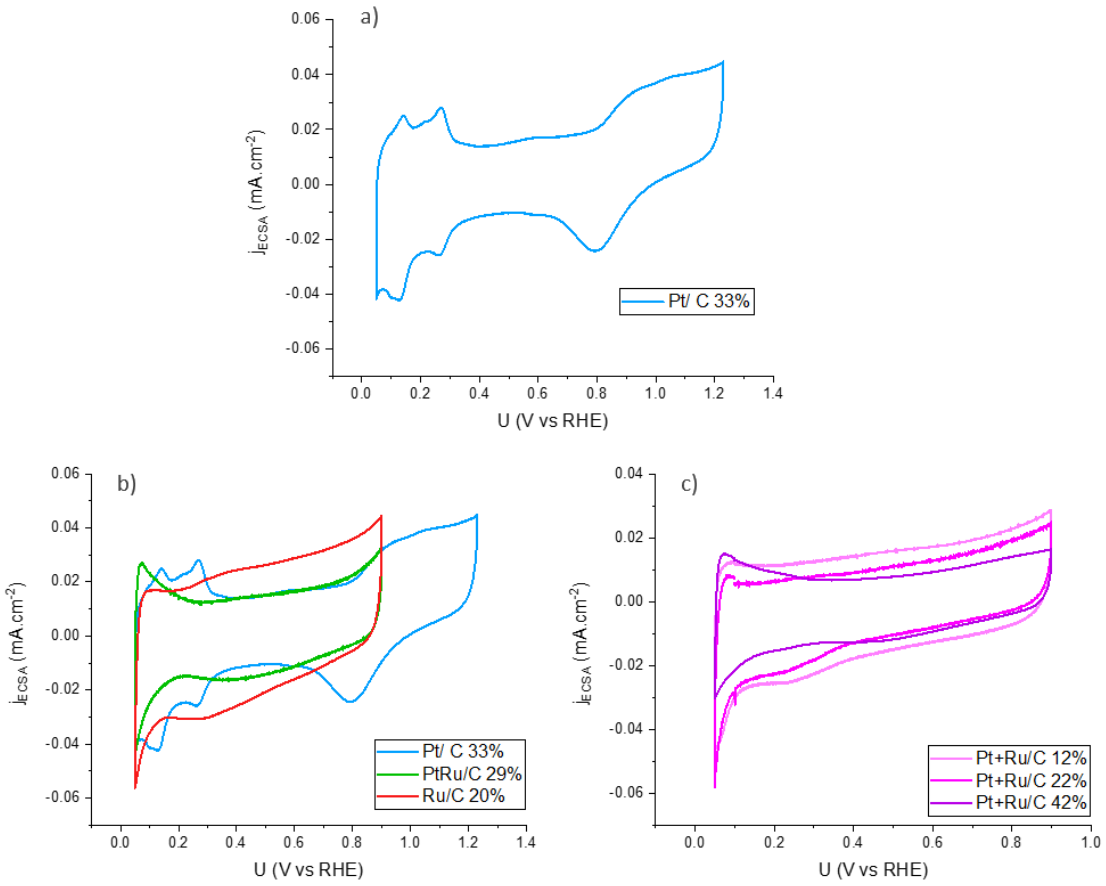

Figure III.8 : Cyclic voltammetries of (a) Pt/C 33%, Ru/C 20%, and PtRu/C 29% ; (b) Pt+Ru/C 12%, 22% and 42% in supporting electrolyte (0.1 M H_2SO_4, T = 25°C). They were performed under Ar flux at 20 mV s^{-1}.

The electrochemical signature of Pt/C presents very distinct areas. On the cathodic scan at low potentials (< 0.4 V), the typical Hydrogen under potential deposition (H_{UPD}) peaks can be seen, often associated to distinct Pt surface orientations [247]. They are followed by the H-desorption peaks, on the same potential range. At high potentials, the Pt oxidation can be witnessed starting 0.8 V. This reaction is reversible, with the corresponding reduction peak centred at 0.8 V. The current plateau in between the H_{UPD} and the Pt oxidation corresponds to the double layer capacitance, and is connected both to the Pt and the carbon surfaces.

PtRu alloy, on Figure III.8 b), displays a broad and poorly-defined H_{UPD} peak. Due to the upper potential limitation, Pt oxide formation/reduction features are also very minored. In the case of Ru/C 20%, a larger double layer capacitance can be seen, probably due to the higher amount of bare carbon substrate due to the lower metal loading, but also to the inherent pseudo-capacitive behaviour of Ru/Ru(oxo)hydroxides. The H_{upd} region, though even less defined than for PtRu, is however discernible as well.

The H_{upd} region is less defined on other Pt+Ru/C electrocatalysts than on Pt/C, presenting one poorly-defined H_{UPD} with only the proton adsorption having more current on the lowest loadings, 12 and 22%. This behaviour corresponds to that of the PtRu alloy, with no specific peak related to platinum. This finding was not anticipated, owing to the fact that these electrocatalysts are indeed composites with pure Pt and pure Ru nanoparticles; the fact that the Pt character is “hidden” can

originate either from masking by the large and broad pseudocapacitive peak of Ru/Ru(oxo)hydroxides in the H_{upd} region, or from the possible electronic effect of the Ru nanoparticles on the Pt nanoparticles they are in contact with, or of both.

III.4.2. CO oxidation behaviour

The CO oxidation is studied on all electrocatalysts by the CO-stripping method, a method fully-described in Chapter II and very convenient to both probe the metal surfaces and provide insights into their resistance to organic poisons. Two types of procedure will be used: a "common" CO-stripping, with an argon purge, or a CO-stripping with a hydrogen purge. The latter, less classical, is more precise to detect the onset potential of the electro oxidation of CO_{ad} species. Finally, the DEMS technique is used to analyse the product gases as a function of the electrode potential.

III.4.2.1 CO-stripping with argon purge

CO-stripping cyclic voltammetries are shown on Figure III.9. To facilitate the analyses, Pt/C is solely presented (a), then compared with Ru/C (b). The best Pt+Ru/C electrocatalyst, Pt+Ru/C 42% is then compared to the commercial alloy PtRu/C (c) and with the two other Pt+Ru/C loadings (d).

On Figure III.9 a), Pt/C displays no current until ca. 0.6 V, the surface is completely blocked by CO_{ads}. A strong current oxidation then appears to form three main peaks, related to the oxidation of CO_{ads} from the Pt surface. Literature has brought many explanations to the multiplicity of peaks in a Pt CO-stripping [248]. In the present case, considering the morphology of homemade Pt/C 33%, the two pre-peaks might be related to the presence of agglomerates [151], and/or to the effect of particle sizes [210,248]. The major peak at 0.81 V is typical for a Pt electrocatalyst exposing ca. 4-5 nm nanoparticles [249,250]. As previously explained in Chapter I, the CO-oxidation on Pt surfaces is a two-step mechanism: the adsorption of OH_{ads} onto the Pt sites (equation (III.12)), and the oxidation of CO_{ads} into CO_2 (Equation (III.13)). The first is the limiting step on Pt, since it is dependent on OH_{ads} adsorption that only happens after 0.6 V on Pt, (and since Pt sites are mainly blocked by CO_{ads}) [148].

$$H_2O + Pt \rightarrow Pt - OH_{ads} + H^+ + e^- \quad \text{(III.12)}$$

$$Pt - CO_{ads} + Pt - OH_{ads} \rightarrow Pt + CO_2 + H^+ + e^- \quad \text{(III.13)}$$

Ru/C 20% presents a different shape on Figure III.9 b). The surface is blocked until the onset potential at 0.4 V, much lower than Pt/C. This is related to the earlier adsorption of OH_{ads} onto the Ru surface, thus helping CO oxidation. The main oxidation peak is broad and less defined on this material also. It happens centred at 0.56 V.

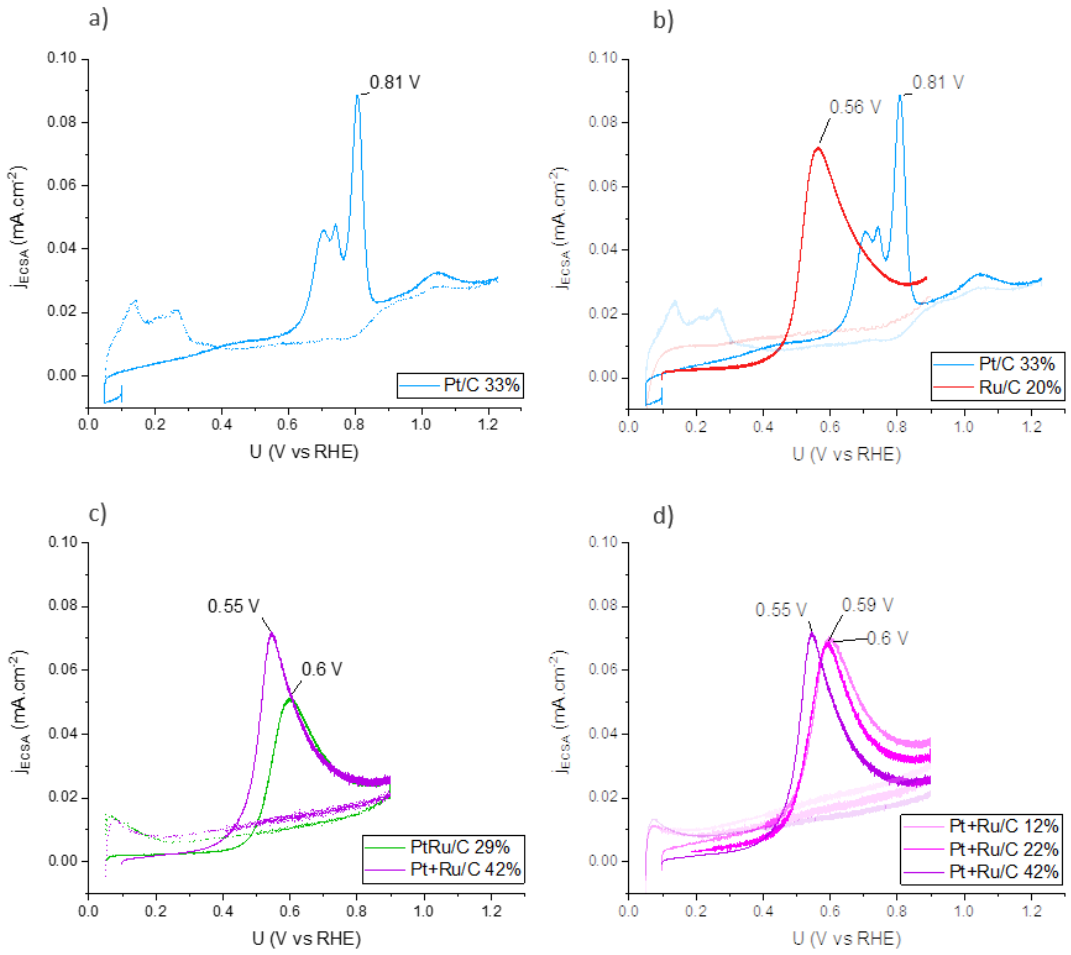

Figure III.9 : CO-stripping with argon purge performed on (a) Pt/C, PtRu/C, Ru/C and Pt+Ru/C 42% ; (b) Pt+Ru/C 12%, 22%, 42%. The potential is held at 0.1 V for 35 minutes then cycled at 20 mV s^{-1} in the potential region [0.05 – 1.23 V] for Pt and [0.05 – 0.9 V] for any Ru-containing material. First cycle is in full line, and second cycle in dotted line.

The commercial alloy, PtRu/C 29%, well-known for its activity towards CO oxidation, presents a shape very similar to Ru/C, with a broad oxidation peak at 0.6 V, and a slightly later oxidation onset, around 0.45 V. This is much lower than pure Pt/C, but slightly higher than Ru/C, showing that the CO-oxidation kinetics are the largest at pure Ru surfaces.

Focusing on Figure III.9 (d), it can be seen that all three composite electrocatalysts present a single oxidation peak, similar to the cases of pure Ru and PtRu alloy. From the lowest to the highest loading, CO-stripping peaks are at 0.6, 0.59 and 0.55 V, respectively, which means that Pt+Ru/C 42% oxidizes CO_{ads} earlier (and that the larger the metal loading is, the better are the CO-stripping kinetics). The onset potential U_{onset}, is calculated to be at 0.45, 0.45, and 0.44 V, nearly unchanged, showing that the initiation of the CO-oxidation reaction is essentially not depending on the metal loading (and hence the density of the nanoparticles on the carbon substrate).

When comparing the CO-oxidation activity of Pt+Ru/C with the three reference electrocatalysts, it can be seen that not only it is better than Pt/C, but also better than the PtRu/C alloy, and competitive towards pure ruthenium, despite the presence of pure Pt in the vicinity of the Ru nanoparticles. This very encouraging result agrees with what was already seen for methanol oxidation on unalloyed PtRu nanoparticles [161,162].

III.4.2.2 CO-stripping with hydrogen purge

CO-stripping with hydrogen purge were performed on all electrocatalysts with the RDE set at 1000 rpm. Results are shown Figure III.10 a) to d), as a function of the geometric surface area of the electrode, so that the mass-transport limiting currents can be directly compared (and are equal) for all the studied materials.

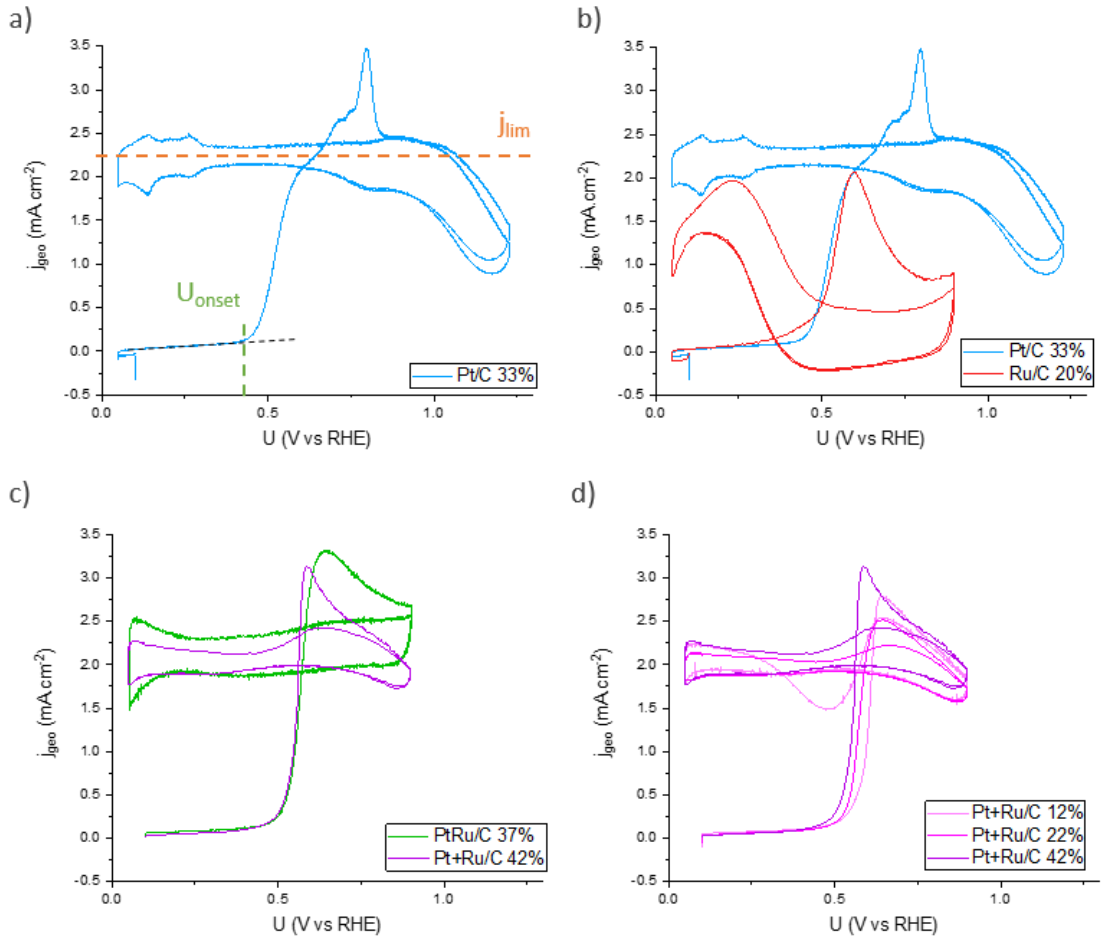

Figure III.10 : CO-stripping with hydrogen purge for (a) Pt/C, Ru/C, PtRu/C and Pt+Ru/C 42% ; (b) Pt+Ru/C 12%, 22% and 42%. The potential was held at 0.1 V during 35 min before cyclic voltammetry at 20 mV s^{-1}. The rotation is set at 1000 rpm. Experiments were done in H_2SO_4 0.1 M at T = 25°C.

Pt/C 33%, on Figure III.10 a), displays a null current until around the start of CO-oxidation, around 0.45 V. At this moment, the first Pt sites are freed from CO poisoning, and can adsorb H_2 to perform the HOR, a very fast reaction on this electrocatalyst. The mass-transport current limit is reached soon after, with 2.3 mA cm^{-2} of current density. The rest of CO_{ads} is oxidized soon after, forming a peak that adds to the HOR limiting current, and the electrode deactivates at potentials where Pt-oxides significantly cover the Pt surface (ca. above 0.9 V), PtOx being much less active towards the HOR than Pt metal. The second cycle being free from CO_{ads}, only the HOR can be witnessed at low potentials, with additional peaks related to the H_{upd} adsorption/desorption. Above 0.9 V, the decrease in current density related to the formation of platinum oxides is also witnessed.

Looking at Figure III.10 (b), which displays the reference electrocatalysts, one can notice that even though Ru/C 20% has the lowest onset potential for CO-oxidation at nearly 0.3 V, its hydrogen oxidation activity is nearly null, and the HOR plateau is not reached, whatever the potential applied and the presence or absence of CO_{ads} on the Ru surface: ruthenium has a negligible activity towards the HOR in these conditions [217].

As for the PtRu alloy presented in Figure III.10 c), its CV shape is very similar to that of Pt/C: they both reach the current transport limit once CO_{ads} has been stripped. The oxidation onset seems similar, around 0.45 V on Pt/C, PtRu/C and Pt+Ru/C. This onset is much earlier than the one measured in CO-stripping with argon purge, in previous section, as the HOR oxidation emphasizes the liberation of electrocatalysis sites.

On Figure III.10 d) are compared all Pt+Ru/C electrocatalysts. It appears that the potential onset is slightly lower for the electrocatalyst with the higher metal content, with Pt+Ru/C 42% presenting the earliest oxidation. The CO_{ads} oxidation peaks (added to the HOR reaction) are respectively at 0.56 V, 0.64 V and 0.65 V from the highest to the lowest metal loading. After the de-poisoning of the surfaces, all three electrocatalysts reach the current transport limit. Pt+Ru/C 12% however, presents a small decrease in current density between 0.3 and 0.5 V during the second cycle, possibly due the presence of very small nanoparticle size, easily oxidized at lower potentials (and thus less active for the HOR). Overall, these materials seem to deactivate at lower potential than Pt/C, which can be ascribed to their larger oxophilicity (detrimental for the HOR).

In the end, Pt+Ru/C 42% is compared to PtRu/C alloy. Both electrocatalysts present a similar CO_{ads} oxidation onset, though much different from the one measured in CO-stripping with argon purge. DEMS experiments presented in the next section will help determine the real potential onset for CO_{ads} oxidation. The hydrogen oxidation activity seems even better on the composite as the mass transport limit is reached a little sooner than on the alloy.

Globally, Pt+Ru/C 42% presents very interesting features. It has a very good hydrogen oxidation rate, far better than pure Ru, and perhaps even better than the alloy itself. This latter point will be detailed in section III.4.4.2. Furthermore, it can oxidize CO much earlier than Pt, being even competitive with Ru and PtRu. The following DEMS experiment will help confirm this latter assumption.

III.4.2.3 DEMS experiments

In order to confirm the potential at which CO_{ads} starts to be oxidized into CO_2, the DEMS technique was used. As for common CO-stripping, the potential is held 35 minutes at 0.1 V before performing a cyclic voltammetry, this time at 10 mV s^{-1}. The results for Pt/C 33%, PtRu/C 37%, Ru/C 20% and Pt+Ru/C 42% are featured on Figure III.11.

For each electrocatalyst, CO_2 formation is detected (m/z = 44 signal in DEMS) with a good intensity during the oxidation measured by potentiostat. In fact, for most of them, both electrochemical and spectrometric currents seem proportional as the same shape is found in both cases.

Pt/C 33% presents a small increase of current compared to the second cycle starting 0.4 V, before a proper CO_{ads}-oxidation peak starting at 0.6 V. The CO_2 detection is presented below with the

second cycle in dashed line, for baseline comparison. A small CO_2 quantity is detected starting 0.4 V, and increases significantly starting at 0.6 V until 0.85 V, in agreement with the electrochemical current. The current peak measured in the first cycle of the CV is thus due to CO_{ads}-oxidation on Pt.

On the ruthenium electrocatalyst, the electrochemical onset is at ca. 0.4 V, with the main oxidation peak being centred at ca. 0.55 V. That same peak can also be seen for CO_2 production, though a small quantity of CO_2 is detected before the electrochemical onset potential, proving that some Ru sites were seemingly liberated before 0.4 V. The CO_2 is however detected in good quantity until 0.9 V, meaning that CO production was spread on a potential range of 450 mV, contrary to Pt with an oxidation range of 250 mV. It is possible some Ru sites necessitate a higher potential in order to oxidize CO or that the CO_{ads} (or the OH_{ads}) mobility at Ru is slow.

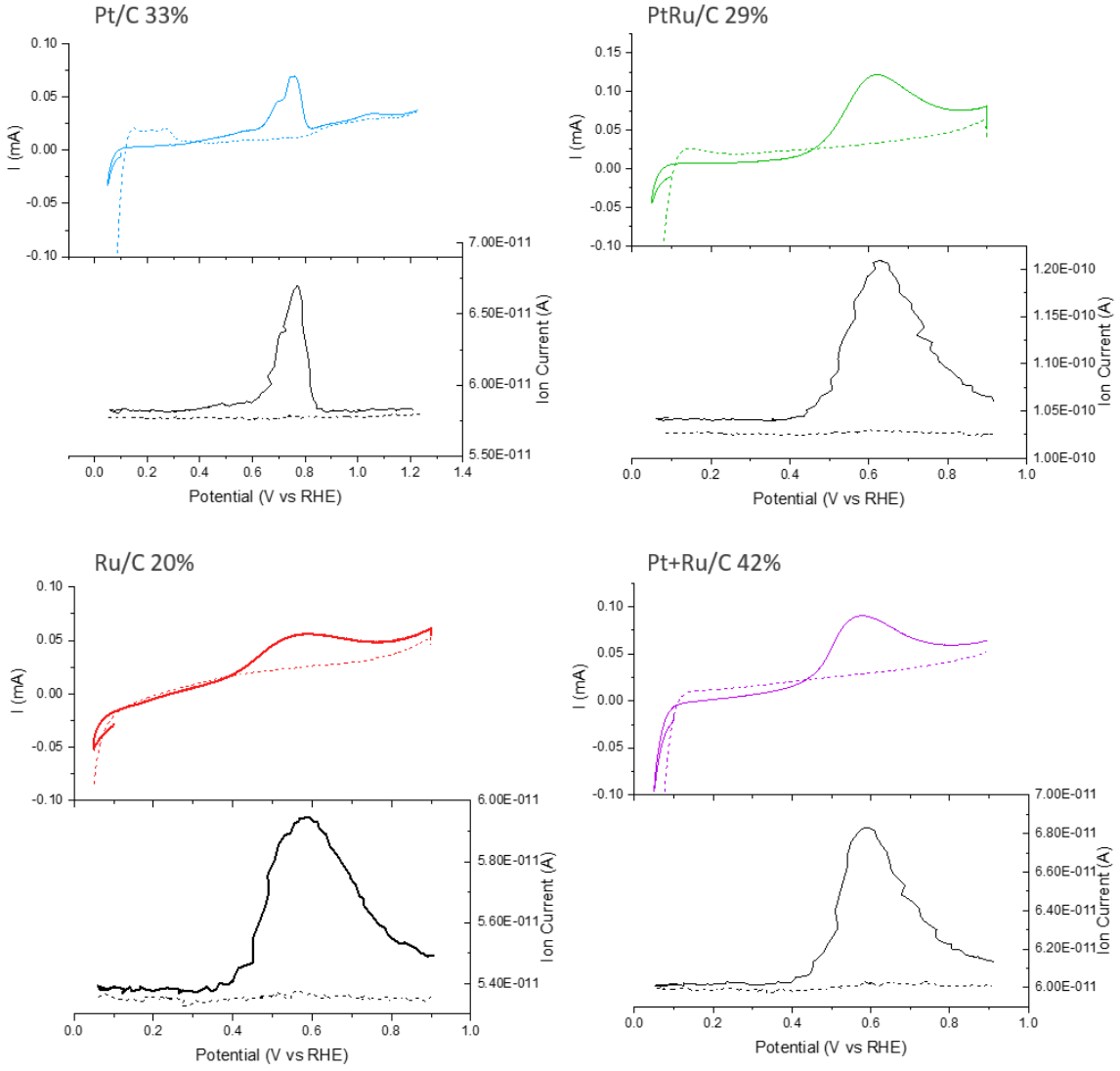

Figure III.11: DEMS analysis presented with two linked graph per electrocatalysts: on top is the CO stripping performed by electrochemistry (0.1 M H_2SO_4 at 23°C); on bottom is the ion current measured by the mass spectrometer on channel m/z = 44, for CO_2.

Again, the PtRu alloy presents a CO_{ads} oxidation behaviour very similar to that of Ru. The onset of oxidation can be seen around 0.45 V for electrochemistry, at the beginning of the main oxidation

peak. Meanwhile the CO_2 current increases slightly after 0.4 V, before reaching the same peak. Here again, a large part of the oxidation happens above 0.8 V.

The most loaded composite electrocatalyst, Pt+Ru/C 42%, also presents a broad and poorly defined electrochemical peak, starting 0.45 V. As for PtRu, some CO_2 content is detected slightly prior the oxidation peak, as soon as 0.4 V.

Pt+Ru/C, PtRu/C and Ru/C can free most of their surfaces much earlier than the common Pt/C, limited at 0.6 V for the onset of the main CO oxidation peak. Those three Ru-containing electrocatalysts, thus, present some very good CO oxidation properties. For the EHC application however, they also need to present a very good HOR activity. This will be addressed in the next section.

III.4.3. HER/HOR activity

In view of the targeted EHC application, one aim of this work is to compare the HOR activity of each studied catalyst. In the RDE setup however, the measurements are made in liquid electrolyte, where the hydrogen solubility (concentration) and diffusivity are much smaller than in the gas phase. The measured current for HOR is thus almost always limited by the mass-transport.

As seen in section III.4.2.2 about CO-stripping with hydrogen purge, the second cycle (performing solely the HOR) reached the current transport limit plateau for almost all electrocatalysts (Ru being the exception) at rather low potential, which forbids any clear comparison between the catalysts intrinsic HOR activities.

It was therefore decided to study the HER instead, making the assumption that if an electrocatalyst presents very good activity for the hydrogen evolution reaction, it will also be active towards the hydrogen oxidation reaction.

Geometrical current densities were extracted at -20 mV and -100 mV from cyclic voltammetries performed at low potential, as presented in Figure III.12. Results based on 3 to 7 measures per electrocatalysts are presented in boxplots graphs, in Figure III.12 a) and b).

At low potential, only small current densities are reached. Despite a poor reproducibility, the PtRu alloy presents the best results in this range, with a current density mean at 21.5 mA cm_{geo}^{-2}. It seems even better that pure Pt/C 33%, that displays a mean current of 15 mA cm_{geo}^{-2}. Far behind, the ruthenium electrocatalyst presents only 4.4 mA cm_{geo}^{-2}, an expected value considering its reported poor activity towards hydrogen [217,218,251]. In agreement with the previously made assumption, Ru/C displays poor performances for both the HOR and the HER.

The Pt+Ru/C 12, 22 and 42% electrocatalysts reach respectively 16.8, 12.8 and 10.3 mA cm_{geo}^{-2}. The current density then increases when the metal content reduces, in this current range. Despite this conclusion, it was decided to choose the highest loading, Pt+Ru/C 42% to perform high current density experiments, in both RDE and GDE, considering its slightly better activity towards CO oxidation.

At higher current densities (in the range of ca. 100 mA cm_{geo}^{-2}) Pt presents better performances than PtRu alloy, thus reversing their behaviour from a lower current density. Ru/C still presents a

very poor HER activity in comparison. As for the Pt+Ru/C composite, its mean geometrical current density is of 60 mA cm_{geo}^{-2}, which, despite being less than for Pt/C and PtRu/C, is still interesting nonetheless.

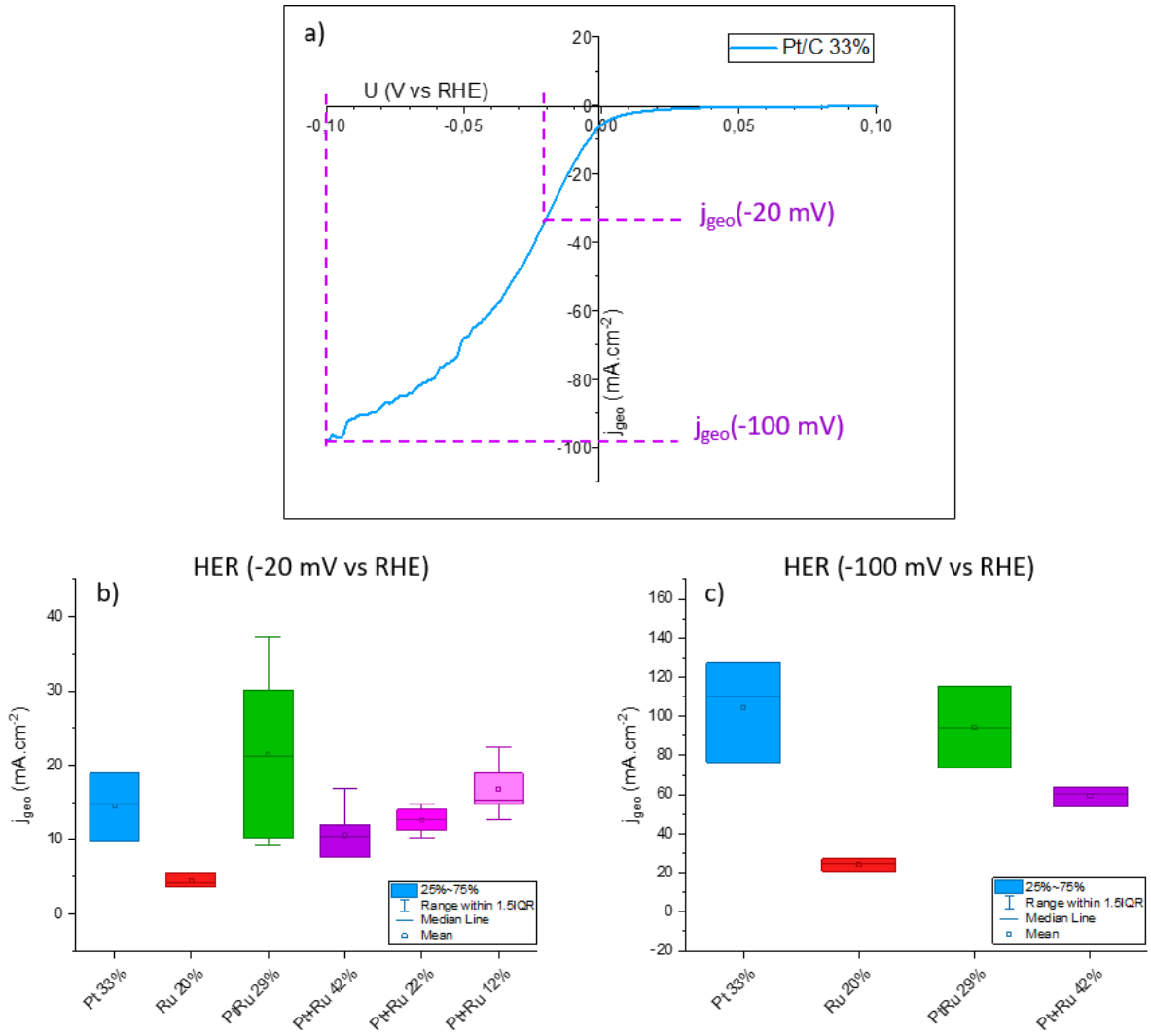

Figure III.12: HER results in geometrical current density calculated as presented for Pt/C 33% in a). Currents at -20 mV (b) and -100 mV (c) are measured in Ar-saturated electrolyte (0.1 M H_2SO_4, T = 25°C) for each electrocatalyst (25 μg_{Pt} cm^{-2}) at a potential sweep of 20 mV s^{-1}.

One can however note that the reproducibility of these experiments seems very disputable. The range of values measured for each electrocatalyst is so large, that despite the qualitative comparison previously attempted, no rigorous discussion can be made concerning the kinetic parameters of the HER, or even HOR activity. As it was preciously pointed out in the literature, a new, more realistic setup is needed in order to rigorously study the hydrogen reactions, the gas diffusion electrode [187,193,252]. It will be used in Chapter V.

III.4.4. Discussion

III.4.4.1 CO oxidation

The new Pt+Ru electrocatalyst was first studied as a function of the metal loading onto the substrate for its CO_{ads} oxidation properties. It was found that, according to the CO-stripping peak and onset potentials, the highest metal content presented the best activity. Two hypotheses (or a mix of both) could explain such a result:

(i) Larger Pt agglomerates were found on Pt+Ru/C 42%. Such formations are known to oxidize Pt more easily than isolated Pt nanoparticles [151], thanks to the presence of concave sites between nanoparticles that strongly adsorb OH groups necessary to CO_{ads} oxidation.

(ii) The loading increase makes the substrate surface more crowded with nanoparticles, thus increasing the amount of contact between Pt and Ru nanoparticles. This means the amount of OH_{ads} provided to the Pt surfaces also increases, this step being the limiting one of the Langmuir-Hinshelwood mechanism (see equation III.1 and III.2).

When comparing the Pt+Ru/C 42% electrocatalyst to other reference materials, it was found that Pt+Ru/C not only presents better CO oxidation than Pt/C 33% but also better than PtRu/C 29%. This last data proves that even without the electronic effect reducing Pt-CO bond in the alloy, ruthenium-platinum contact is enough to enhance CO-oxidation on Pt nanoparticles. This leads to wonder if the so-called synergic effect is instead a simple bifunctional effect, purely related to the presence of OH_{ads} at low potential on Ru particles in the vicinity of the CO_{ads}-covered Pt particles, favouring the de-poisoning.

It also needs to be noticed that this mixed electrocatalysts present identical or better CO oxidation activity than Ru/C, despite the presence of pure Pt. Such a result is very promising. More realistic experiment, in gas phase (e.g. in EHC or PEMFC), would be interesting to assess the real gain brought by this bi-phased morphology. Chapter V will provide preliminary data in this direction.

III.4.4.2 HOR/HER

The cyclic voltammetries at negative potential showed interesting results concerning the HER activity for the studied electrocatalysts. These values have to be read with great care, bearing in mind their great sensibility towards environment impurities, deposition thickness of the active layer, and other experimental variables. It was possible, however, to determine an average behaviour for each type of electrocatalyst, and thus anticipate the possible kinetic behaviour towards the HOR. Pt+Ru/C 42% seemed to display less interesting performances than lower Pt+Ru/C loadings, though the difference was quite light. Compared to reference electrocatalysts, Pt+Ru/C 42% showed interesting results: much better activity than Ru/C for the HER, while almost competing with Pt/C and PtRu/C. Importantly, the reader must keep in mind that these results are valid only in aqueous environment, not in the gas phase, as will be the case in a EHC or a PEMFC anode.

The HOR on the other hand, reaches its maximum in liquid electrolyte due to the low hydrogen gas dissolution in water. This can be seen on Figure III.10, when on the second cycle, all Pt-containing electrocatalysts reach the same geometrical current density.

As for the HER study, the huge difference in current between the liquid and the gas environment is enough to put those results into question, and highlights the necessity to perform electrochemical tests with gaseous reactants. This would be the subject of Chapter V

.

III.4.5. Conclusion

The hypothesis to use only one aspect of PtRu "synergetic effect" by keeping Pt and RuO_2 unalloyed while in contact, and thus keep Pt activity was proven right. Even if the activity towards hydrogen reaction could not be determined precisely, it appeared that such composite electrocatalysts have very close kinetics for hydrogen reaction to Pt and PtRu. This aspect will be further studied in Chapter V, at much higher current densities, using a GDE setup.

Pt+Ru/C also proved to be very active towards CO_{ads} oxidation, presenting a potential onset as low as 0.44 V, which could be very interesting for the EHC application. One can wonder if this behaviour will be enough for that same application, considering the very high rate of CO expected in inlet (> 1%). Its behaviour in a polluted hydrogen flux will also be addressed in Chapter V.

Pt/WO_3 is another electrocatalyst that has shown great result towards CO-oxidation, showing oxidation current as low as 0.1 V [181,183]. The next Chapter will be dedicated to the study and improvement of this electrocatalyst, in the same approach used for the Pt+Ru/C family.

CHAPTER IV

Tungsten-oxide supported Pt electrocatalysts

Chapter IV Tungsten-oxide supported Pt electrocatalysts

IV.1. Why tungsten-oxide supported Pt electrocatalysts?

In Chapter I, the strategies available to design CO-tolerant electrocatalysts were presented. One of them consisted in supporting Pt on a metal-oxide to favour CO oxidation at low potentials. Some metal oxides, provided they can undergo a reversible redox transition in the appropriate potential domain, can adsorb OH groups at lower potential than Pt (which forms Pt-OH at 0.6 V) [211,253,254]. In particular, tungsten presents redox frontiers located in the vicinity of the hydrogen potential (Equation (IV.1) and (IV.2)); WO_3 forms a bronze (HWO_3) by proton insertion at low potentials (in the hydrogen region, Equation IV-3) in acid, which has dual advantages: (i) the surface of WO_3/HWO_3 could play the role of a redox mediator enabling formation of OH species to assist CO-oxidation (Equation (IV.3))[255] and (ii) HWO_3 have increased electron conductivity versus WO_3, poor electron conductivity being the main drawbacks of metal-oxides supports in electrocatalysis .

$$2\ WO_2 + H_2O \leftrightarrow W_2O_5 + 2\ H^+ + 2\ e^- \qquad E° = -0.031\ V\ vs\ SHE \qquad (IV.1)$$

$$W_2O_5 + H_2O \leftrightarrow WO_3 + 2\ H^+ = 2\ e^- \qquad E° = -0.029\ V\ vs\ SHE \qquad (IV.2)$$

$$WO_3 + y\ H^+ + y\ e^- \leftrightarrow H_yWO_3 \leftrightarrow WO_{3-y}(OH)_y \qquad (IV.3)$$

An association of platinum and tungsten oxide supported on carbon was already tested by several teams. Pt/WO_3 synergy was brought to attention by multiple teams, bringing to evidence the spill over effect of adsorbates from WO_3 to Pt [255–258]. In 2006, Maillard et al. found that such a combination presented a new CO oxidation pre-peak at 0.55 V [259]. The same year, Colmenares et al. synthetized surface-modified Pt-W/C electrocatalysts and performed DEMS experiments, finding CO_2 production at the very low potential of 0.2 V, an outstanding result [260]. Experiments were also performed in H_2-CO mix [155] with improved electrocatalytic performances versus Pt/C.

In 2007, Micoud et al. synthetized Pt/WO_3 by Pt salt impregnation and reduction. They added carbon to the mix to enhance the electronic conductivity. This electrocatalyst showed outstanding results in CO-stripping, with a pre-oxidation wave observed at 0.4-0.7 V (Figure IV.1), agreeing with Maillard et al. observations [183]. They also performed a CO-stripping with hydrogen purge, a technique that emphasizes the liberation of the first few Pt sites using Pt very high activity towards the HOR. When the HOR current was null on Pt until ca. 0.4 V, due to the blocked state of the electrocatalyst sites, HOR could be seen as low as 0.1 V on the Pt/WO_3 electrocatalyst, thus proving the very early de-poisoning of several Pt sites at that potential, which had been unachieved with any other electrocatalyst at that stage. A high CO tolerance has also been observed on mesostructured Pt/WO_3 composites by Cui et al. [261]

However, it was also found that Pt/WO_3 presented a poor durability. Prior any experiment, Pt proved to be instable in the ink (made of Nafion®, Water IPA in definite proportions, as described in Chapter II). TEM images presented in Micoud's PhD work [181] show a clear migration of Pt nanoparticles located on the WO_3 towards the carbon additive, thus decreasing all contact between Pt and WO_3 within only a few days of ink storage.

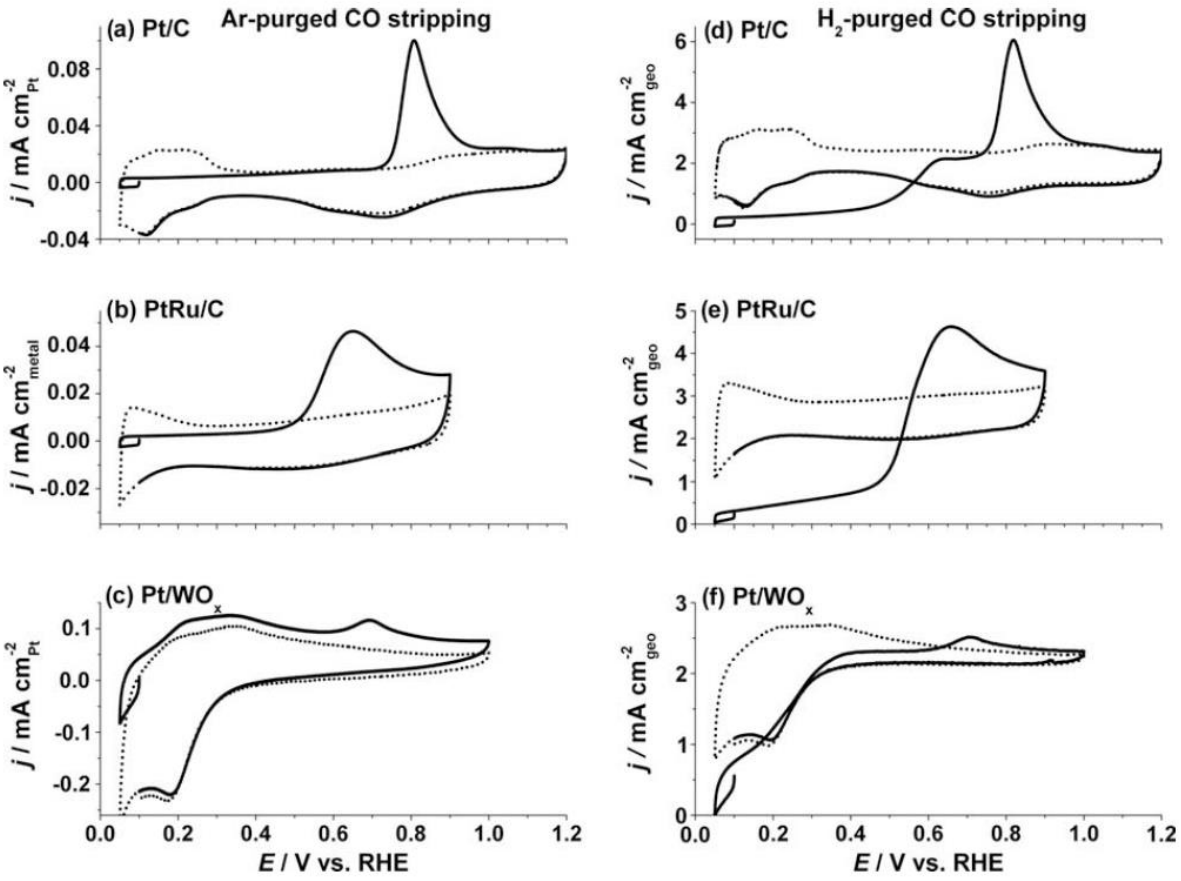

Figure IV.1: CO-stripping cyclic voltammetries 1st cycles (in plain lines) and 2nd cycles (in dotted lines) for (a,d) Pt/C, (b,e) PtRu/C, (c,f) Pt/WO_x/C. Performed in H_2SO_4 0.1 M at T = 25°C at a 20 mV s^{-1} scan rate [183].

In the perspective of the EHC, where H_2 must be oxidized at very high current densities despite the presence of impurities, and especially carbon monoxide, the performance of the Pt/WO_3 system seems very promising, provided the durability of the material can be improved. It was decided to try to improve the material durability by keeping only WO_3 as the support (without carbon addition), along with an increase of Pt loading. The idea was to form Pt "chains" agglomerates around the WO_3 nanoparticles, as presented Figure IV.2; by this morphology, it was hoped to stabilize Pt onto the WO_3 surface (because the Pt crystallites are connected to each-other), but also to create a surface pathway for electron conduction through these interconnected Pt crystallites. This new material was synthetized and both chemically and electrochemically characterized.

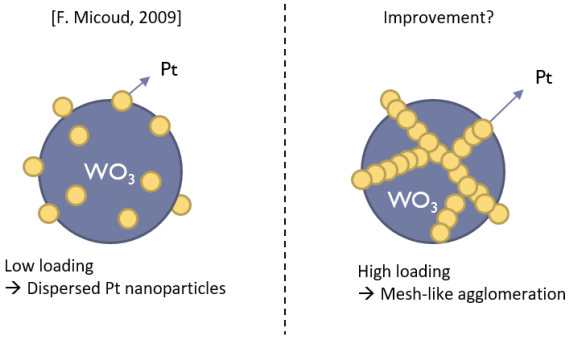

Figure IV.2: Schematic drawing of two possible strategies to disperse Pt nanoparticles onto a tungsten oxide support

IV.2. Synthesis process for Pt/WO_3 electrocatalysts

In order to obtain agglomerated chains of Pt surrounding the WO_3 nanoparticles, a different synthesis pathway was chosen from previous studies, compatible with larger Pt loading at the WO_3 support: the colloidal polyol synthesis.

IV.2.1. Adaptation of the polyol process

The so-called polyol process was used for the Pt/WO_3 electrocatalysts synthesis, and the Pt loading was deliberately chosen sufficiently high to trigger Pt nanoparticles agglomeration. The protocol introduced in details in Chapter II was generally followed here, from the production of Pt colloids to the filtration and drying process. The only change was the replacement of the carbon Vulcan® XC-72 support with WO_3 nanoparticles from Nanostructures & Amorphous Materials® (30-70 nm, 99%, 8 $m^2\ g^{-1}$).

The Pt colloids were prepared in ethylene glycol/water mix (2:1) by increasing both the pH and the temperature. Then, they were mixed with WO_3 nanoparticles and the pH was decreased to 0.5 by adding drops of H_2SO_4 96%. When carbon black nanoparticles were used as support of the Pt colloids, the pH only had to be decreased below ca. 3; the very low pH of 0.5 chosen here permits a proper deposition of the Pt colloids, charged negatively (as shown on Figure II.1, Chapter II), on the tungsten oxide, charged positively below its zero point charge ZPC = 2.6 [262]. After stirring overnight and filtration, the filtrate solution was fully transparent, thus proving a good Pt deposition on tungsten oxides (contrary to the first synthesis test, done at a pH of 2-3, were the filtrate solution was entirely black, the colour of the Pt colloids solution – which shows how important it is to adapt the colloid deposition pH to the ZPC of the chosen support).

For Ru-containing electrocatalysts, Ru colloids were simply added in proportion with Pt colloids to obtain a Pt:Ru atomic proportion of 1:1. The aimed proportions for each of the four studied electrocatalysts are presented Table IV.1.

Table IV.1: Targeted proportions of tungsten oxide-supported electrocatalysts, presented in % per mass of electrocatalyst.

Electrocatalysts	Targeted wt.% Pt	Targeted wt.% Ru
Pt/WO_3 6%	7	0
Pt/WO_3 25%	25	0
$Pt+Ru/WO_3$ 24%	16	8
$Pt+Ru/WO_3$ 36%	24	12

IV.2.2. Electrocatalysts studied in this chapter

This chapter will feature the comparison of homemade tungsten-supported electrocatalysts. For reference purposes, electrochemical results will also be compared to Pt/C and PtRu/C electrocatalysts. To avoid confusion, all electrocatalysts are named with the elements in presence,

with the Pt+Ru loading in percentage per mass of electrocatalyst which will be determined in the following ICP section.

- Pt/WO_3 6% and 25% are homemade electrocatalysts made by polyol synthesis.
- $Pt+Ru/WO_3$ 24 and 36 % are homemade catalysts made by polyol synthesis.
- Pt/C 33% is a homemade electrocatalyst made by polyol synthesis. Its physical-chemical properties were thoroughly presented in Chapter III.
- Pt+Ru/C 42% is the homemade Pt+Ru composite electrocatalyst presented in Chapter III.

IV.3. Physical and chemical characterizations

This sections will focus on the physical and chemical properties of all tungsten-oxide-supported electrocatalysts with the use of multiple techniques (detailed in Chapter II). Results will firstly be presented by techniques, and will then be discussed as a whole.

IV.3.1. Metal content in electrocatalyst powder

As explained in Chapter III, many sources of error can impact the final loading of each element in the electrocatalyst, which can lead to different practical loading values from the targeted ones. Such errors can come from the incomplete adsorption of colloids onto the tungsten support, the unknown exact amount of hydration in the precursor salts used for colloids synthesis, or also possible losses during the handling of materials, from weighing to the filtration process.

The practical loading in each element was then properly characterized using ICP-MS technique as described in Chapter II. The combustion temperature of each element is however too high to obtain any result from TGA experiments, which explains the absence of this technique from this chapter.

IV.3.1.1 ICP and AAS analysis

ICP-MS and AAS measurement are presented Table IV.2 for Pt/WO_3 6% and 25%. $Pt+Ru/WO_3$ 24% and 36% have not been measured. After dissolution of the electrocatalysts in aqua regia, the samples were diluted for AAS measurements, then diluted again for ICP-MS measurement. As it was done in Chapter III, results are corrected by taking into account the same estimation of 3% H_2O in weighted content of the electrocatalyst (prior the dissolution).

Table IV.2: AAS and ICP-MS results for the five studied electrocatalysts, presented in percentage of metal per mass of electrocatalyst.

Electrocatalyst	wt.% Theoretical	ICP-MS values	AAS values
Pt/WO_3 6%	6% Pt 93% WO_3	5.5% Pt	5.5% Pt
Pt/WO_3 25%	25% Pt 75% WO_3	23.3% Pt	24.5% Pt

The platinum contents in both electrocatalysts are very close to what was expected. The loss is exceptionally small, especially in Pt/WO_3 25%. After those synthesis, the filtrate was also analysed by ICP-MS, finding less than 0.01% loss of Pt mass. In can also be noticed that ICP-MS and AAS results are in very good agreement with each other.

WO_3 was also measured with ICP-MS, with near to no signal as a result. Such an absence can be explained by the very difficult dissolution of WO_3 in aqua regia (as in many solvents). It appears that the best solution for tungsten oxide dissolution would have been to use a mix of hydrofluoric acid and nitric acid [263], which for safety purposes and because it was not of primary importance, was not done here.

IV.3.2. Structural and surface properties

The electrocatalyst crystallographic structure and its oxidation state (especially for ruthenium) were surveyed by XRD, XPS and even Fast Fourier transform (FFT) analyses.

IV.3.2.1 X-ray diffraction patterns analysis

XRD analyses were performed on all electrocatalysts, as well as on the WO_3 support. Patterns are presented Figure IV.3.

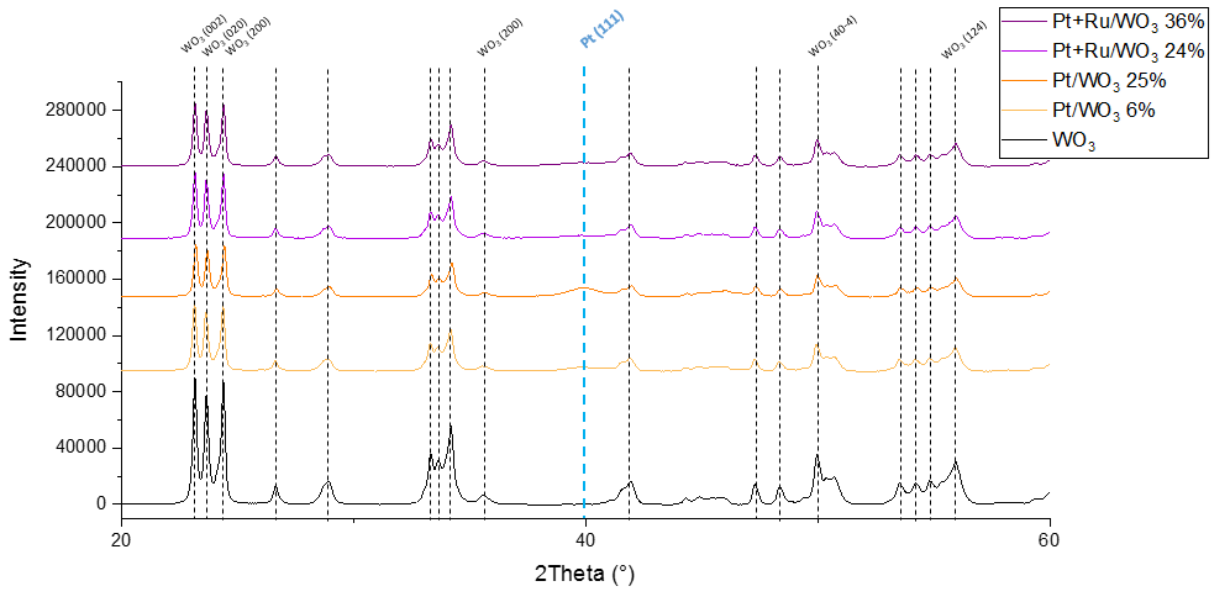

Figure IV.3: XRD Pattern for WO_3, Pt/WO_3 6% and 25% and Pt+Ru/WO_3 24% and 36%

In accordance with the provider data, the tungsten oxide structure is found to be mainly monoclinic (space group $P2_I/n$) with lattice parameters a, b and c being respectively: 7.30030, 7.53161, and 7.68978 Å, with a β-angle (between vectors a and C) of 90.9° [264]. Some peaks (too weak to be visible on the diffractograms), were related to the tungsten oxide bronze $H_{0.23}WO_3$.

Their contribution (for the as-synthesized samples) is however so weak that the tungsten-oxide will still be addressed as WO_3 – the author admitting that in electrochemical operation, the materials structure could be very different.

At $2\theta = 40°$, the specific Pt (111) pic can be slightly seen on both Pt/WO_3 6% and 25%. Its definition is yet insufficient to perform a proper estimation of the nanoparticles size in that orientation. This peak however seems absent on the XRD patterns of both $Pt+Ru/WO_3$ 24% and 36%. Such a result is quite surprising, especially considering the amount of Pt nanoparticles witnessed on those electrocatalysts with TEM observation (see section IV.3.3.1). Two hypothesis could explain such a discrepancy: either Pt nanoparticles are amorphous in those electrocatalysts, or they are too small to detect any atomic organization. Later TEM results will point the latter as most probable explanation.

As for Pt+Ru/C electrocatalysts, no Ru contribution could be seen on XRD diffractograms. This is related to the very small size of those particles (< 2nm), as it was explained in Chapter III.

IV.3.2.2 ETEM- images FFT analysis

Pt/WO_3 6% was observed with an ultrahigh resolution microscope, the ETEM Titan, under environmental conditions in order to determine its behaviour in different conditions. The following Figure IV.4 a) shows the WO_3 support under low-pressure hydrogen environment, at high temperature (100°C). The HR-TEM permits an atomic resolution of the tungsten oxide structure, local FFT confirms the monoclinic structure (the observations were performed by Mimoun Aouine, IRCELYON).

a)

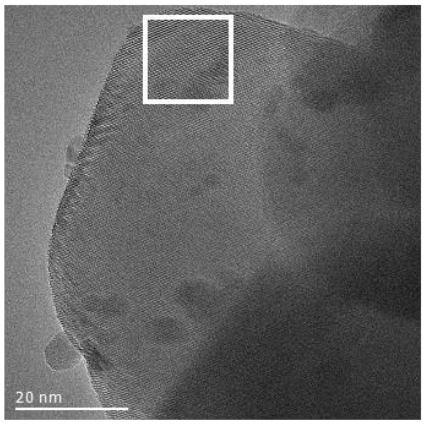

b)

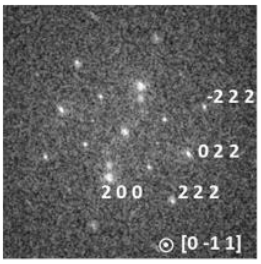

WO3
PDF : 43-1735
S.G. : 14
System : Monoclinic
a = 0.7297 nm, b = 0.7539, c = 0.7688
β = 90.91

c)

h k l	d (exp.) nm	α (exp.)	d (théo.) nm	α (théo.)
2 0 0	0.371	0.00	0.3648	0.00
2 2 2	0.218	53.10	0.2154	53.17
0 2 2	0.273	89.26	0.2691	89.36
-2 2 2	0.221	125.75	0.2177	126.00

Figure IV.4: a) Pt/WO_3 6% observed with an HR-TEM under 12 mbar H_2, at 100°C ; b) FFT performed on WO_3 structure from image a) ; crystallographic determination from FFT

Though the results are presented in H_2 environment, it has to be specified that from the observations in ultra-high vacuum at room temperature to that point, no changes, both in WO_3 structure and morphology, could be witnessed (as it will be detailed in section IV.3.3.2)

WO_3 presents a monoclinic structure, without any bronze formation, this results thus confirms XRD analysis on the nature of the tungsten oxide.

IV.3.2.3 X-ray photon spectroscopy analysis

XPS analyses were performed with the K-alpha ThermoScientific spectrometer (Al-source) and data treated with the ThermoScientific Advanta software. All spectra were calibrated with the carbon contamination contribution, and the local background modelled with the Smart algorithm. The decomposed spectra for both tungsten and ruthenium element are presented here, for Pt+Ru/WO_3 24% and 36%.

Tungsten oxidation state was analysed on the W4f ray, between 30 et 45 eV, as presented on Figure IV.5. Two convoluted peaks can be seen for both electrocatalysts. Those peaks are attributed to WO_3 4f7/2 et 4f 5/2 at 36 eV and 38.2 eV [265–267]. Only WO_3 oxide is present here, which is in accordance with the technical data sheet of the provider.

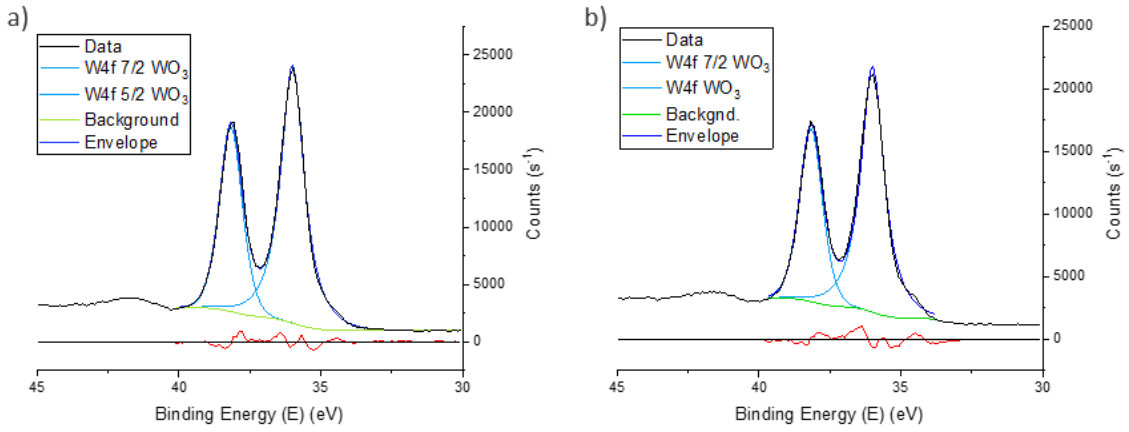

Figure IV.5: W4f XPS spectra on a) Pt+Ru/WO_3 24% and b) Pt+Ru/WO_3 36%. Experiments performed with an Al-ay X-ray source. Residuals are presented in red line (counts x2).

The main goal for XPS analysis was to determine the oxidation state of ruthenium on this support (which explains why only Pt+Ru electrocatalysts where studied here). As explained in Chapter III, The Ru signal was found more intense on its Ru 3d spectra, and it was thus decided to study this region[243,244]. For these electrocatalysts however, the combination of carbon and Ru on the same spectra rendered the decomposition more difficult. However, the absence of any signal at 280 eV is proof of the absence of Ru metallic contribution. Ru from the Pt+Ru/WO_3 electrocatalyst is then mainly in its RuO_2 oxidation state.

The Pt4f energy band was also fitted (curves no presented here) in order to compare its contribution to the other elements. It was found to be a combination of metallic Pt and PtO. The areas associated to each element were summed and then multiplied by the atomic sensitivity

factor [245] with respective values of 1.75 for $Pt4f_{7/2}$, and 2.0 for W4f. The Pt/WO3 weigh ratio can then be compared to the theoric one (see Table IV.3).

Table IV.3: Pt : WO3 weight determined by XPS analysis for Pt+Ru/WO_3 24% and 36%.

	Theory	**XPS**
	Pt : WO_3 (wt.% ratio)	Pt : WO_3 (wt.% ratio)
Pt+Ru/WO_3 24%	17 : 83	59 : 41
Pt+Ru/WO_3 36%	27 : 73	46 : 54

It can first be noticed that the Pt : WO_3 ratio is far higher than expected, for both electrocatalysts. One explanation could come from the strong presence of agglomerates onto the surface of those two electrocatalysts (as it will be detailed in section IV.3.3), thus covering WO_3 surface and reducing its signal (as XPS is limited to surface analysis of 9 nm at maximum).

IV.3.3. Microscopy analysis

IV.3.3.1 Transmission electronic microscopy analysis

All four WO_3-based electrocatalysts were observed with transmission electron microscopy imaging to determine their morphology, shape, and the dispersion and size of Pt and Ru nanoparticles. TEM images are presented on Figure IV.10, along with the size distribution for Pt nanoparticles, counted from ca. 70-120 nanoparticles per sample. Only the clearly distinct particles were measured, which, considering the high amount of agglomerates in those samples, explains the low number of counted nanoparticles. Table IV.4 presents the standard mean particle size d_n for each electrocatalyst, along with its mean surface size d_s and mean volume size d_v. Their explicit formula can be found in chapter II.

Table IV.4: Standard, surface and volume mean particle sizes calculated from TEM images.

	d_n /nm	d_s /nm	d_v /nm
Pt/WO_3 6%	3.0	4.2	4.9
Pt/WO_3 25%	2.5	3.7	4.2
Pt+Ru/WO_3 24%	2.4	2.9	3.1
Pt+Ru/WO_3 36%	1.9	2.3	2.4

On all TEM images the WO_3 support can be clearly distinguished; it is constituted of particles of around 30-70 nm diameter, in agreement with the manufacturer information. Contrary to carbon support, the shape of WO_3 is angular, certainly due to its high crystallinity (see XRD).

Pt/WO_3 6% displays a highly heterogeneous dispersion of Pt nanoparticles onto the tungsten oxide surface: some oxides are filled with Pt agglomerates, while some others are void of any Pt. A third part of WO_3, the main one, presents a good Pt nanoparticle dispersion onto its surface with several isolated nanoparticles, quite similar to what can be seen with a carbon substrate. The mean nanoparticle size is of 3 nm, which confirms the fact that despite several bigger particles (> 6 nm), the agglomeration of particles did not seem to impact their size (which was expected for a colloidal synthesis method).

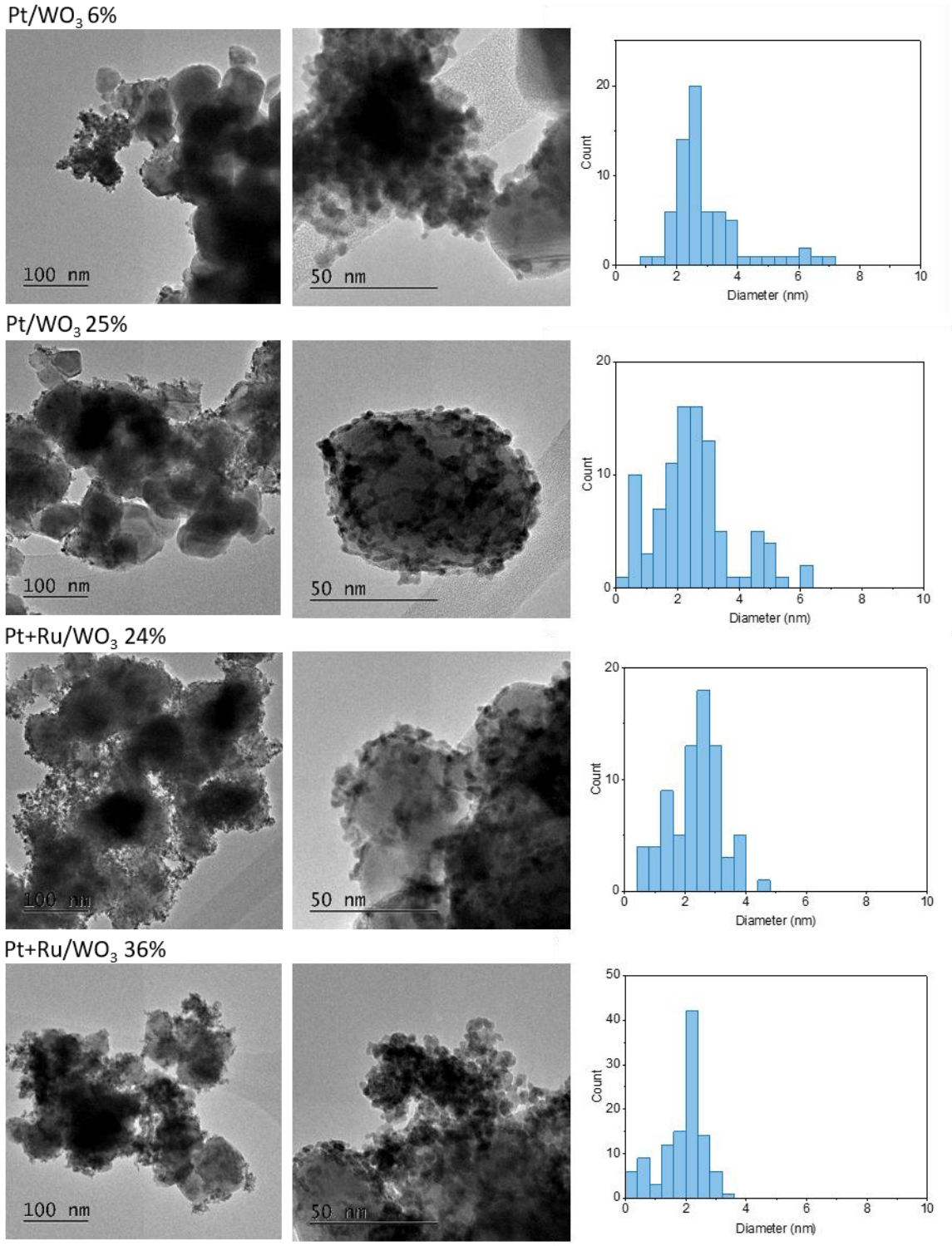

Figure IV.6: TEM imaging for Pt/WO_3 6%, 25% and Pt+Ru/WO_3 24% and 36%. The particle size distribution is given on a population of 100-150 counted nanoparticles.

Pt/WO_3 25% presents a much higher Pt loading onto the oxide; as expected. Despite the small surface area of WO_3 (8 $m^2\ g^{-1}$, far lower than that of carbon Vulcan XC72: 254 $m^2\ g^{-1}$) [181,268], the Pt nanoparticle dispersion presents a more homogenous aspect than with Pt/WO_3 6%. In fact, as it can particularly be seen on the second micrograph, the nanoparticles are arranged in a mesh-like manner, forming long chains rather than volumetric agglomerates. Such a dispersion could be

explained by a stabilization of the Pt onto the oxide and this morphology perfectly corresponds to the targeted material described in section 1. The nanoparticle mean size is of 2.5 nm, even lower than with Pt/WO_3 6%, some very small nanoparticles being also measured in occasion.

Pt+Ru/WO_3 24% presents a very high metal loading on its surface, resulting in the absence of any isolated Pt nanoparticle. Many agglomerated areas can be seen on the WO_3 surface, a lot of them being present in-between the WO_3 nanoparticles rather than on their surface. Those agglomerations are organised in nanoparticles chains, quite similar though denser, than on Pt/WO_3 25%. Visually, no distinction could be made between Pt and Ru nanoparticles. The mean particle size is of 2.4 nm, similar to what was found for Pt/WO_3 25%. The surface and volume sizes however put in evidence the dispersion of smaller nanoparticles, certainly due to the presence of Ru nanoparticles, that were found to be around 1-2 nm in Chapter III (the same colloidal method was used in both cases, which permits this comparison).

Pt+Ru/WO_3 36% displays a high heterogeneous nanoparticle dispersion, with most of metallic nanoparticles present in agglomerates at the WO_3 rims, while the middle surface of WO_3 is nearly void of any particles. In fact, some agglomerates seem only connected to WO_3 by the rim, most of the Pt nanoparticles being without any connection to the oxide surface. Such a phenomenon could be due to both Pt low stability on tungsten oxide, and the very high metal loading, superior to what WO_3 can sustain.

In fact, the maximum Pt loading as a monolayer onto WO_3 can be approximated by a rough calculation. Let's consider an average Pt nanoparticle of 3 nm diameter, with $S_{Pt,3nm}$ being the maximum surface section of that particle, the mass-normalized surface area $A_{Pt,3nm}$ is given by:

$$A_{\mathrm{Pt,3nm}} = \frac{S_{\mathrm{Pt,3nm}}}{m_{\mathrm{Pt,3nm}}} = \frac{4 * \pi * r_{\mathrm{Pt,3nm}}^2}{\rho_{\mathrm{Pt}} * \frac{4}{3} * \pi * {r_{\mathrm{Pt,3nm}}}^3} \quad \text{(IV.4)}$$

Where $m_{\mathrm{Pt,3nm}}$ is the mass of one 3 nm- Pt nanoparticle and ρ_{Pt} the density of Pt (21.45 g cm^{-3}, density of bulk Pt, taken for this approximation but larger than the expected density of a nanoparticle). Assuming $A_{\mathrm{WO_3}} = 8\ m^2 g^{-1}$ and $A_{\mathrm{C}} = 254\ m^2 g^{-1}$, this yields:

$$A_{\mathrm{Pt,3nm}} = 93\ m^2 g^{-1} \quad \text{(IV.5)}$$

If one considers a maximum Pt loading onto the oxide surface being roughly defined by $S_{\mathrm{WO_3}} = S_{\mathrm{Pt}}$, with S_{Pt} the total surface covered by Pt nanoparticles, one obtains:

$$A_{\mathrm{WO_3}}\, m_{\mathrm{WO_3}} = A_{\mathrm{Pt}}\, m_{\mathrm{Pt}} \quad \text{(IV.6)}$$

$$m_{\mathrm{Pt}} = \frac{A_{\mathrm{WO_3}}\, m_{\mathrm{WO_3}}}{A_{\mathrm{Pt}}} \quad \text{(IV.7)}$$

Let's define R, the ratio between the mass of Pt and the total mass of electrocatalyst:

$$R = \frac{m_{\mathrm{Pt}}}{m_{\mathrm{Pt}} + m_{\mathrm{WO_3}}} \quad \text{(IV.8)}$$

Using the previous equation (IV.7), R can be calculated with Pt and WO_3 respective surface areas:

$$R = \left(1 + \frac{m_{WO_3}}{m_{Pt}}\right)^{-1} = \left(1 + \frac{A_{Pt}}{A_{WO_3}}\right)^{-1} \quad \text{(IV.9)}$$

The results of this approximation can be found in Table IV.5. For comparison purposes, the value for carbon Vulcan XC-72 used in the previous chapter was also calculated. It is first important to precise that these values are merely approximations made by overlooking the real density of a Pt nanoparticle as well as the real dispersion of nanoparticles onto a surface (they cannot geometrically take 100% of the surface area. Considering those two points, the real value should actually be lower.

Table IV.5: Approximated maximum Pt mass loading on two supports, considering an average nanoparticle size of 3 nm

	Approximated maximum Pt loading (3 nm particles)
WO_3	8 wt.%
Vulcan® XC 72	73 wt.%

It is found that the tungsten oxide can in fact only withstand a mass ratio of 8% of Pt in the powder, which is much lower than the present loading of 25wt.% of Pt. This explains the very high amount of agglomeration and the presence of 3D agglomerates.

IV.3.3.2 Environmental microscopy

One electrocatalyst, Pt/WO_3 6%, was analysed with environmental microscopy. The aim was to witness the behaviour of WO_3 and of the Pt nanoparticles on its surface, while changing the operating conditions, oxidant or reductive).

Starting from vacuum, the hydrogen partial pressure was slowly increased in the chamber, from 0 to 12 mbar along with the temperature, from ambient to 100°C to 300°C. As shown on Figure IV.7, neither the oxide shape nor that of Pt nanoparticle were impacted. Except for one nanoparticle at the bottom of images a) and b), no nanoparticle mobility could be witnessed. The presence of isolated Pt nanoparticles on image c), despite the very high temperature, demonstrates the very high stability of the electrocatalyst in those conditions.

Pt/WO_3 6% was also studied under oxidizing conditions, by repeating the same process as with hydrogen, this time with a low oxygen pressure. As for the previous conditions, no change was witnessed, in the tungsten oxide as in the Pt nanoparticles dispersion. Figure IV.7 d) shows isolated Pt nanoparticles on the oxide, without any visible agglomeration.

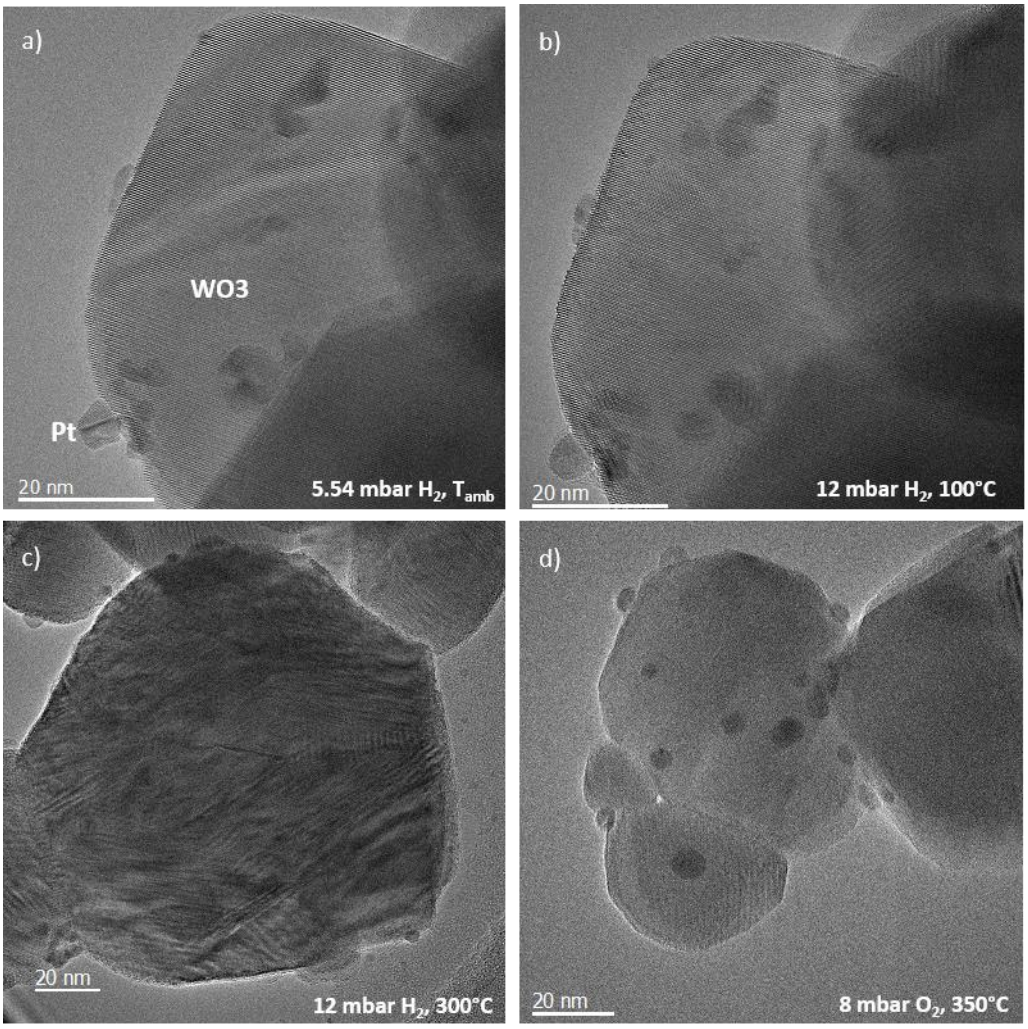

Figure IV.7: E-TEM imaging of Pt/WO_3 6% under low pressure hydrogen or oxygen atmosphere, from a) 5.54 mbar H_2 at ambient temperature to b) 12 mbar H_2 at 100°C and c) 12 mbar H_2, 300°C. d) 8 mbar O_2, 350°C

One can compare this experiment to the one that was presented in Chapter III, in section III.3.3.3., with Pt+Ru/C 11%. Under less than 1 mbar of hydrogen, the carbon support was strongly damaged, thus producing an agglomeration of nanoparticles. Here, WO_3 seems extremely stable, even in the most extreme conditions. It could be interesting to see if such a stability is kept during electrochemical experiments.

IV.3.4. Discussion on physico-chemical characterizations

In this section all tungsten-based electrocatalysts were thoroughly analysed in their morphology, their composition and their atomic structure.

The tungsten support WO_3 has a monoclinic structure which can accommodate protons to form a tungsten bronze H_xWO_3. E-TEM experiments showed a very high stability of the material under high temperature conditions (300°C) in hydrogen or even oxygen environment. Despite the strong electron beam, no surface or crystallographic change was reported, which highly differs from the carbon support in Chapter III. Though those conditions are not representative of electrochemical

environments, such stability could prove interesting in strong reducing conditions, as at the anode of an EHC for instance.

Pt/WO_3 6% was synthetized through the adaptation of the common polyol process. A proper pH adaptation taking the pzc of WO_3 into account, permitted reaching a very good Pt dispersion onto its surface. In fact, the final Pt content are in very good agreement with the synthesis goal., which completely validates this new technique. TEM microscopy showed a somewhat heterogeneous nanoparticle dispersion however, with isolated nanoparticles, local agglomerates of Pt nanoparticles and even WO_3 areas without any Pt supported. This contrasts with the electrocatalysts synthesized by Micoud with a similar loading, which was designed to present very good dispersion after a impregnation and reduction process and for which the morphology was homogeneous on the whole support [181]. This heterogeneous distribution for sure originates from the polyol colloidal synthesis and the high weight metal loadings used in the present work.

The higher loaded electrocatalysts, Pt/WO_3 25%, also presents a very good agreement between the Pt content and the measured one in the electrocatalyst. This result seems even surprising in this case considering the calculated maximum loading onto the low-developed surface of WO_3, which is three times inferior the actual value. TEM images showed a very different nanoparticle dispersion on this electrocatalyst compared to Pt/WO_3 6%. Pt nanoparticles were found agglomerated in chain-shapes, arranged as a mesh around WO_3 nanoparticles. Such an organisation could permit a better electronic conductivity of the overall electrocatalyst, while maybe increasing the stability of Pt onto the tungsten oxide support. These properties could greatly increase the electrochemical performances of the electrocatalyst, which will be discussed in later section.

After the encouraging results of the Pt+Ru/C electrocatalysts, it was decided to test the same metallic configuration onto a different support. The lower loading of those electrocatalysts, $Pt+Ru/WO_3$ 24% seems however to present only a small Ru proportion (<10% atomic). This element was found to be entirely oxidised in RuO_2. The nanoparticle size, even smaller in this electrocatalyst than on the Pt/WO_3 ones, lead to a decrease of the Pt response in XRD experiments. The very high loading was distinctively visible in TEM, and leads to a very strong extent of agglomeration, agglomerates being heterogeneously distributed on some WO_3 nanoparticles. The weak WO_3 response in XPS analysis is related to the coverage of Pt aggregates that thick nanoparticle layer in some areas, thus “hiding” a portion of the tungsten oxide surface.

$Pt+Ru/WO_3$ 36% presents very similar results to $Pt+Ru/WO_3$ 24%. Its higher loading leads to an “external” agglomeration phenomenon, where nanoparticles would agglomerate with close to no contact with WO_3 nanoparticles. This leaves large surfaces of WO_3 void of any metallic nanoparticles. For both 24% and 36%, this strong agglomeration outside of the support could lead to a loss of electronic contact with some nanoparticles, which could decrease the bifunctional character of the obtained materials, which could detrimentally impact their electrochemical activity.

IV.4. Electrochemical characterizations

Electrochemical characterizations were performed on all electrocatalysts (as well as the tungsten-oxide support) in order to define their behaviour and activity towards reactants such as CO or H_2. To that goal, the RDE setup was used. The details about electrochemical setup and protocol are given in Chapter II.

IV.4.1. Ink stability

All inks used in this Chapter were done following the protocol described in Chapter II. Early results however presented a certain irreproducibility that required more thorough investigations. Figure IV.8 show TEM images taken for the dry Pt/WO_3 25% electrocatalyst powder, and for two inks made with that same electrocatalyst, respectively after one hour and after one month. On the dry powder, Pt nanoparticles are well dispersed on the tungsten-oxide surface forming both small agglomerations and lone particles. An ink is then prepared by mixing 5 mg of electrocatalyst with Nafion® ionomer, IPA and ultrapure water in fixed proportions (given in Chapter II). After 15 min stirring in the ultrasonic bath, to properly disperse particles in the solution, and 45 minutes of cool down, a TEM grid is made by casting a drop of ink.

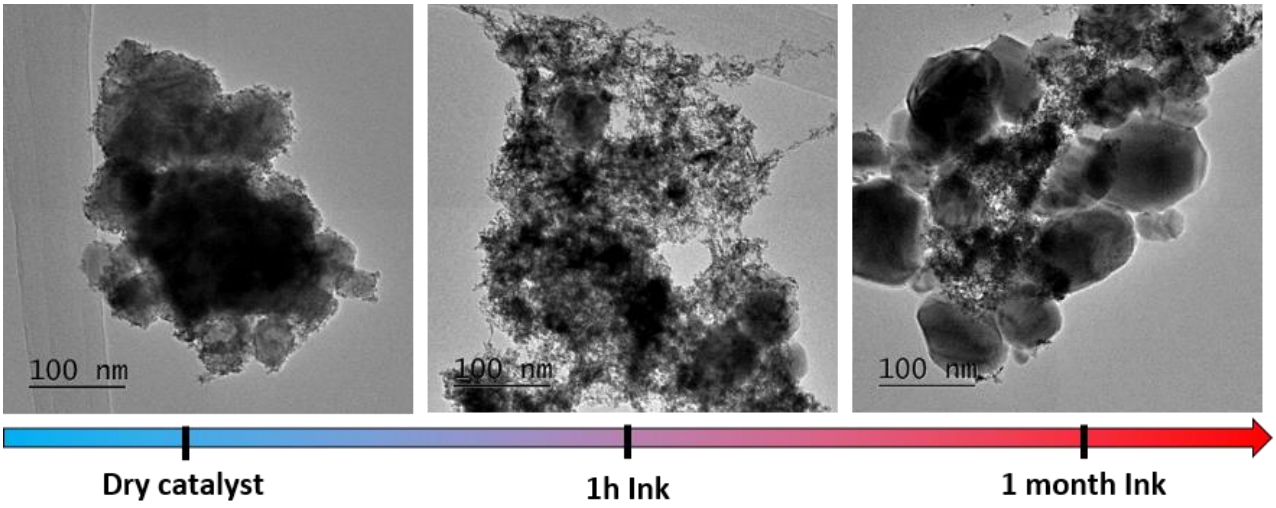

Figure IV.8: Pt/WO_3 25% ink aging via TEM microscopy.

One can notice the different aspect of the TEM image, in Figure IV.8, related to the presence of Nafion®. The ionomer seems homogeneously dispersed onto the tungsten oxide surface, which is highly favourable for ionic conductivity. However, several Pt nanoparticles, recognisable from their size and shape, seem to have diffused from the support surface to the Nafion®, thus losing all electronic contact with the support. The third TEM grid was made from an ink aged for one month. It features an aggregation of WO_3 nanoparticles, supporting a central, large agglomeration of small Pt nanoparticles. Most of the WO_3 nanoparticles surface seems void of any Pt nanoparticles at that stage, except for that central agglomeration, in great contrast with the dispersion presented for the dry electrocatalyst powder. Such a change of particle dispersion comes from the instability of Pt onto the WO_3 surface.

Micoud witnessed similar behaviour when observing the aging of a Pt/C-WO_3 electrocatalyst in a ink, as shown Figure IV.9 [181]. When carbon was also added to the ink (for electronic conductivity), the Pt nanoparticles diffused towards the carbon support, while forming agglomerates. All electrochemical benefits related to the close contact between Pt and tungsten oxide was then lost.

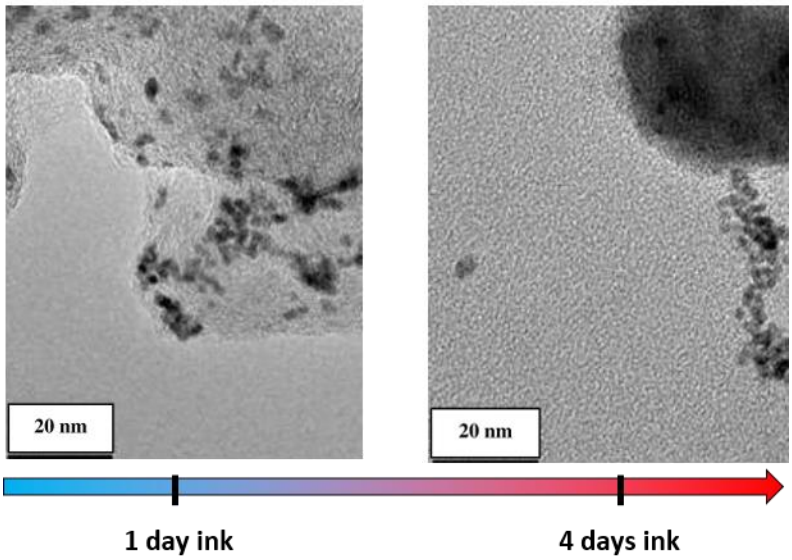

Figure IV.9: Aging of a Pt/C/ WO_3 ink observed by TEM microscopy [181]

With the present Pt/WO_3 ink, a test was made to replace the ultrapure water of the ink by 0.1 M H_2SO_4 acid. Pt being known for its instability in basic environment, a supposition was made that the ink pH was too high, and thus needed to be reduced (so to maintain the ink pH at a proper value versus the pH of zero charge of the support). Figure IV.10 shows the state of one neutral ink (made with H_2O) and one acid ink (made with H_2SO_4) in acidic environment. Contrary to the neutral ink, were Pt nanoparticles are still dispersed onto the WO_3 surface, the acidic ink presents far more heterogeneities. Pt nanoparticles have mostly left the WO_3 support to agglomerate in the Nafion ink, thus reaching the state of the one-month neutral ink presented in Figure IV.8.

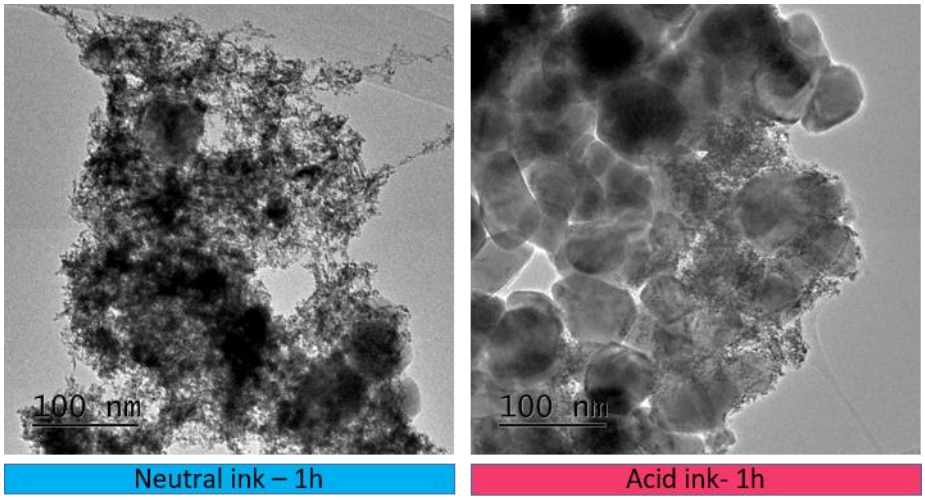

Figure IV.10: TEM images of two Pt/WO_3 25% inks, aged one hour. The neutral ink was made with water; the acid ink was made with 0.1 M H_2SO_4.

Considering all those results, it was chosen to keep the same neutral ink protocol with ultrapure water. The inks however, were prepared each time right before the deposition onto the RDE electrodes tips, keeping the 15 minutes stirring for particle dispersion.

IV.4.2. Electrochemical signature

Cyclic voltammetries were performed on the four WO_3-supported electrocatalyst, as well as the bare WO_3 support, in order to define their behaviour in the studied potential range (from 0.05 to 0.7 V), in acidic conditions. All cyclic voltammetries are presented Figure IV.11, normalized per geometric area.

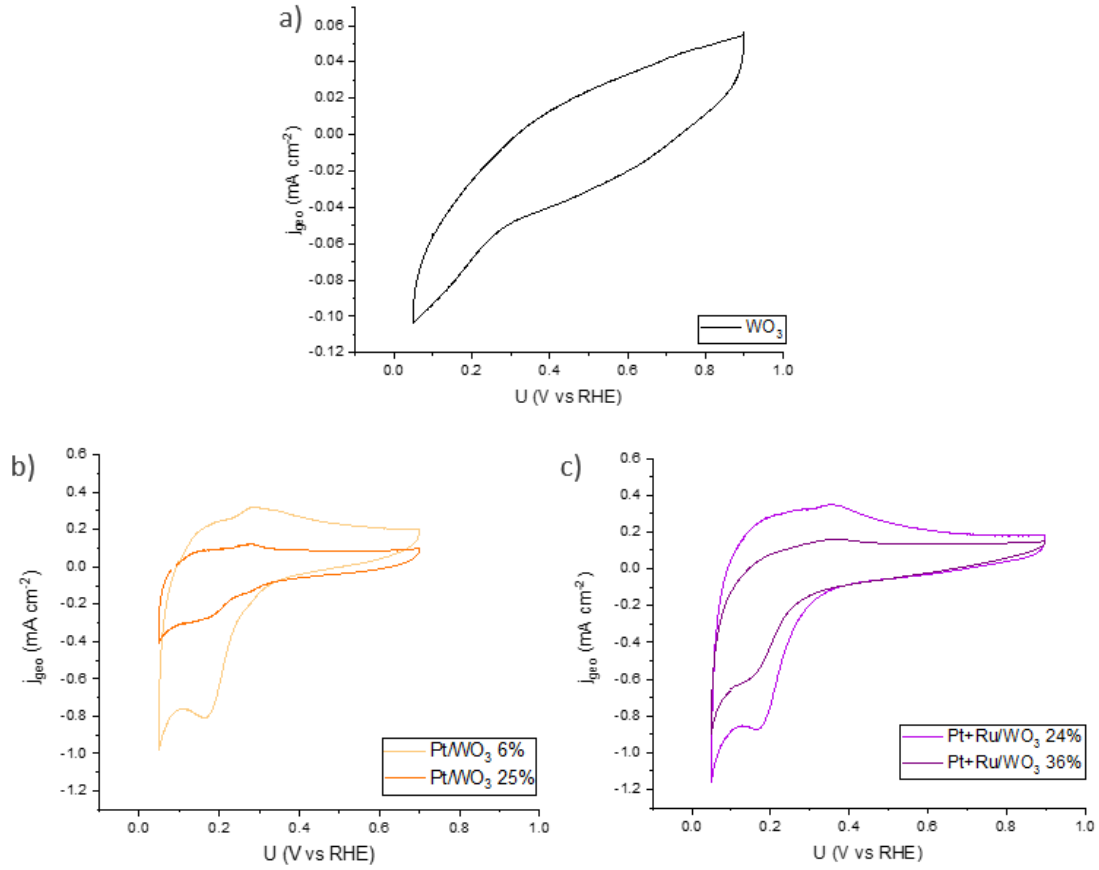

Figure IV.11: Cyclic voltammetries of a) bare WO_3 support, b) Pt/WO_3 6% and 25% and c) Pt+Ru/WO_3 24% and 36%. They were performed at a potential sweep of 20 mV s^{-1}, in a 0.1 M H_2SO_4 Argon-saturated electrolyte, at T° = 25°C.

The electrochemical signature of tungsten-oxide is strongly capacitive. Below ca. 0.25 V vs RHE, a small reduction can be witnessed, possibly due to the insertion of proton into the oxide, forming tungsten oxide bronze H_xWO_3 (equation (IV.3)). A large ohmic drop can be noticed on the voltammetry, proof of the low electronic-conductivity of the oxide.

Pt/WO_3 6%, in clear orange in Figure IV.11 a), presents a very distinct shape of voltammetry from the bare tungsten-oxide. A noticeable negative current is observed in the anodic scan, below 0.3 V, related to the insertion of protons into the first layers of tungsten oxide. A current much higher

than on WO_3 is measured, which demonstrates that the presence of Pt onto the surface catalyses the insertion of protons. This agrees with the literature that explains such catalysis by the diffusion of adsorbed-protons from the Pt surface to WO_3 (see equation (IV.10)) [269–271]. Focusing now on the low potentials of the anodic scan, where H_{UPD} is known to happen on Pt/C, two undefined peaks can be witnessed. Such peaks could be attributed to the de-insertion of protons from both Pt and WO_3. H de-insertion on Pt usually ends at 0.4 V, when it is stretched until at least 0.7 V on WO_3. As tungsten returns to its full oxide shape, it loses electronic conductivity, which explains the positive thinner shaper of the scan at high potentials.

$$x\,Pt - H_{ad} + WO_3 \rightarrow x\,Pt + H_xWO_3 \qquad \text{(IV.10)}$$

Pt/WO_3 25%, presented on the same graph, has a much lower capacitive signature than Pt/WO_3 6%. Both H-insertion and de-insertion are less defined and present less current. Since the Pt loading is very high on that electrocatalyst, the Pt nanoparticles might be covering the tungsten-oxide surface, thus reducing the surface for proton insertion. As for the lower loading, proton de-insertion provokes a diminution of the electronic conductivity of the material above 0.4 V

On Figure IV.11 c), $Pt+Ru/WO_3$ 24% and 36% have an electrochemical signature very similar to that of Pt/WO_3. Proton insertion is well defined, even more than Pt/WO_3 25%, despite the very high metal loadings. This discrepancy can be explained by the dispersion of metallic nanoparticles onto the tungsten-oxide surface for those two catalysts. As it could be seen in section IV.3.3.1), the high loading leads to very strong agglomeration of nanoparticles, sometimes even “out” of the oxide surface. A large area of WO_3 is then uncovered, and free to adsorb and insert protons. It can also be noticed that as for Pt/WO_3, the higher loading presents the lesser the capacitive signature.

IV.4.3. CO oxidation behaviour

As in Chapter III, the CO stripping method is used to study the oxidation of CO onto the four studied electrocatalysts. CO-stripping CVs are first performed with Argon-purge, to determine the materials’ ECSA and oxidation peak; then, an H_2-purge is adopted, to rigorously determine the onset of CO oxidation. The DEMS technique is finally used to analyse the gas produced as a function of the electrode potential.

IV.4.3.1 CO-stripping with argon purge

CO stripping CVs with Argon purge are presented for each electrocatalyst in Figure IV.12.

Figure IV.12 a) displays the behaviour of bare WO_3 under a CO-stripping. The first cycle, in plain line presents a small over-oxidation compared to the second cycle. This is related to the de-insertion of protons, all inserted during the potential hold at 0.1 V. Then, the second cycle shape is similar to a common cyclic voltammetry.

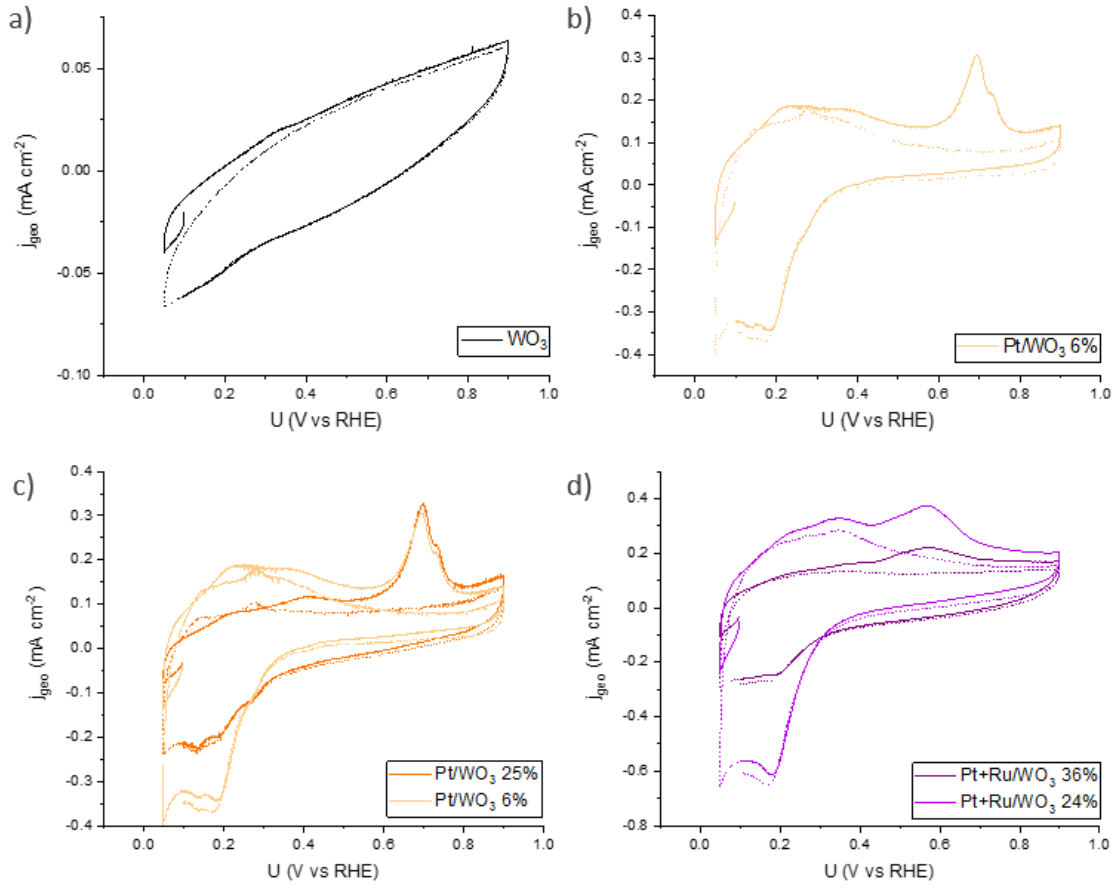

Figure IV.12: CO-stripping CVs with Ar purge for a) WO_3, b) Pt/WO_3 %, c) Pt/WO_3 6 and 25%, and d) Pt+Ru/WO_3 24 and 36%. First cycles are presented in plain lines, and second cycles in dashed lines. The potential was held for 35 min at 0.1 V and then cycled at 20 mV s^{-1}. Experiments were performed in 0.1 M H_2SO_4, at T = 25°C.

On Figure IV.12 b), the CO-stripping for Pt/WO_3 6% is presented. The first cycle starts at 0.1 V and goes to 0.05 V to begin the anodic scan. Instead of the null current witnessed for a common Pt/C catalyst (which is fully-blocked by CO_{ad} in these conditions), an oxidation current can be seen here until ca. 0.5 V, certainly related to H-de-insertion from the WO_3 support (H_xWO_3 bronze). At 0.55 V starts another oxidation contribution, with two noticeable peaks, at 0.69 and 0.73 V. This peak can mainly be attributed to CO oxidation, as it will be discussed in section IV.4.3.3. The cathodic scan is then similar to a cyclic voltammetry in supporting electrolyte. It can be noticed that the difference between the first and second cycle during the anodic scan is small (below 0.4 V), which makes it difficult to attribute the supplementary current to proton de-insertion or to CO oxidation. This is all the more problematic for electrocatalysts known to oxidize CO at potentials as low as 0.1 V. This issue will be addressed later in this section.

Pt/WO_3 25% CO-stripping voltammetry can be seen on Figure IV.12 a). Despite a smaller capacitive current than Pt/WO_3 6% explained in section IV.4.2, its shape is very similar to the one with a lower Pt loading. The H-de-insertion from H_xWO_3 is also present, with a very small current difference between the first and second cycles. In fact, both cycles display distinct shapes. The first one slowly increases in two waves at 0.2 and 0.4 V, while the second one has two peaks at respectively 0.1 and 0.25 V. This discrepancy is also present in the current values, sometimes higher at the second

cycle than at the first one. The CO oxidation peak however, is very similar for the two loadings, presenting the same potential peaks in identical proportions.

Pt+Ru/WO_3 24% CO stripping voltammetry is presented in Figure IV.12 d). Below 0.4 V, the first cycle shape seems less defined than for Pt/WO_3: no distinct peaks or waves can be noticed. The attributed CO-oxidation peak happens at 0.57 V: an even lower potential than Pt/WO_3. Its current is also much smaller, and broader, certainly related to a diversity of distribution of catalytic sites.

The higher loading, Pt+Ru/WO_3 36%, displays the same shape as Pt+Ru/WO_3 24%, with a reduced capacitive current. In fact, the proton insertion current is the lowest of all WO_3-based electrocatalysts.

For all four electrocatalysts, the proper CO oxidation onset cannot be determined because of the proton deinsertion from H_xWO_3 taking place around the same potential region. In order to properly separate both contributions, a pseudo-CO-stripping was performed on Pt/WO_3 25%. This experiment consists in following the same protocol as for CO-stripping (35 min at 0.1 V followed by cyclic voltammetry at 20 mV s^{-1}), while staying in Argon environment, without any CO. The resulting curve is shown Figure IV.13.

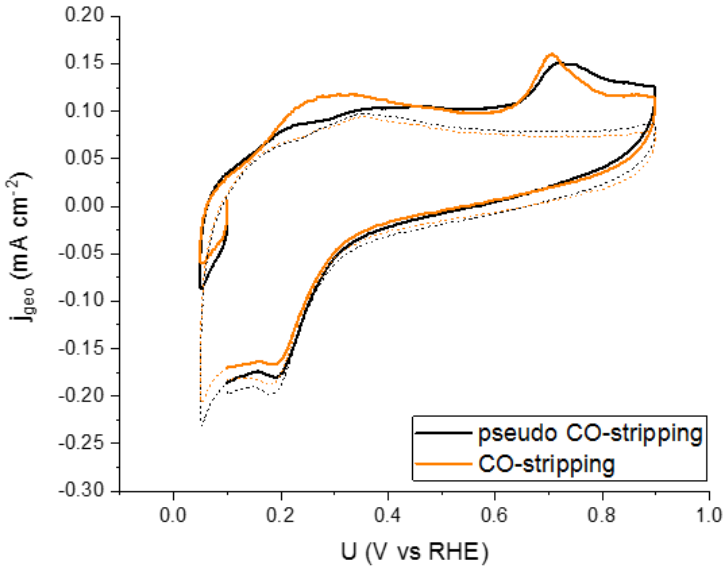

Figure IV.13: Pseudo-CO-stripping performed on Pt/WO_3 25%. The potential is held for 35 minutes at 0.1 V before cycling at 20 mV s^{-1}. Experiment is done in 0.1M H_2SO_4, at T = 25°C.

The pseudo CO stripping curve, in black in the graph, presents a first cycle very similar to a plain cyclic voltammetry at potentials below 0.5 V. In that potential range, both the first and second cycle present very comparable shapes, with a little more current for the first cycle, due to the larger insertion of protons (the Pt surface is not poisoned by CO, hence can assist better proton insertion in the WO_3 lattice). At high potentials however, a surprising new peak is found at 0.73 V, overlapping the CO oxidation peak present on the common CO-stripping curve. At this point, it is important to clarify that no CO was put into the cell prior the pseudo-stripping. A common cyclic voltammetry was performed right before, without any CO trace. This high potential peak thus

cannot be related to any CO oxidation. Considering its potential, one possibility could be the de-insertion of deeply -inserted protons from Pt/WO_3. In those conditions, Pt surface is not blocked, and can then actively participate in the bronze formation by adsorbing H_{ads}, as described in previous section. Another possibility could be that WO_3 assists Pt oxidation, thus producing a larger oxidation peak than on common cyclic voltammetry.

It must be noticed however that despite this unknown peak, the CO-stripping curve presents a higher current than the pseudo-CO-stripping between 0.2 and 0.4 V. Such current could be related to the oxidation of weakly adsorbed CO, though this will have to be further studied by CO_2 measurement with DEMS experiment, in IV.4.3.3.

Despite prior assumptions, the pseudo-CO-stripping was not of any help to separate both contributions. Other techniques could however lift this confusion: CO stripping with H_2 purge and DEMS.

IV.4.3.2 CO-stripping with hydrogen purge

In order to properly determine the onset of CO oxidation, the cell is purged with hydrogen right after CO poisoning. As explained in Chapter II, this permits a better visualisation of the liberation of the first Pt sites, thanks to the very high HOR activity on platinum. The related curves are presented Figure IV.14 with a rotation speed of 1000 rpm.

Bare WO_3 shows almost no change compared to the CO-stripping with Ar purge performed in previous section. The usual ohmic drop is present, as well as the supplementary H-deinsertion from H_xWO_3 present in first cycle. Above 0.8 V however, a small oxidation current can be witnessed, and seems purely related to the presence of hydrogen in the electrolyte (as that contribution is also present in the 2nd cycle). No definite conclusion can be however given whether this small oxidation is related or not to hydrogen oxidation.

Pt/WO_3 6% is presented on Figure IV.14 b). The electrode current is nearly null until 0.3 V, where the Pt surface is slowly freed from CO poisoning. The maximum current is reached at 0.67 V though no proper peak can be seen. The current then reaches a plateau for hydrogen oxidation, around 1.4 mA cm^{-2}. Pt/WO_3 25% displays an even earlier CO oxidation, with an onset as low as 0.24 V, a very promising result. The CO peak is reached at 0.7 V, higher than with Ar-purged CO stripping.

$Pt+Ru/WO_3$ 24% and 36% both show very different behaviours than Pt/WO_3 6 and 25%. As with the previously presented electrocatalysts, $Pt+Ru/WO_3$ 36% has a blocked surface until 0.37 V, where it slowly increases before reaching its maximum current at 0.9 V. The current density then decreases during the cathodic cycle, without forming a plateau. Pt/WO_3 24% presents an even lower maximum current density (0.42 mA cm^{-2}), with a CO onset also happening much later, at 0.46 V. This very low HOR activity compared to Pt/WO_3, despite the presence of the same mass of platinum, could be related to lack of proper electronic contact between metallic agglomerates and the support surface, as it was witnessed on TEM images (c.f. IV.3.3).

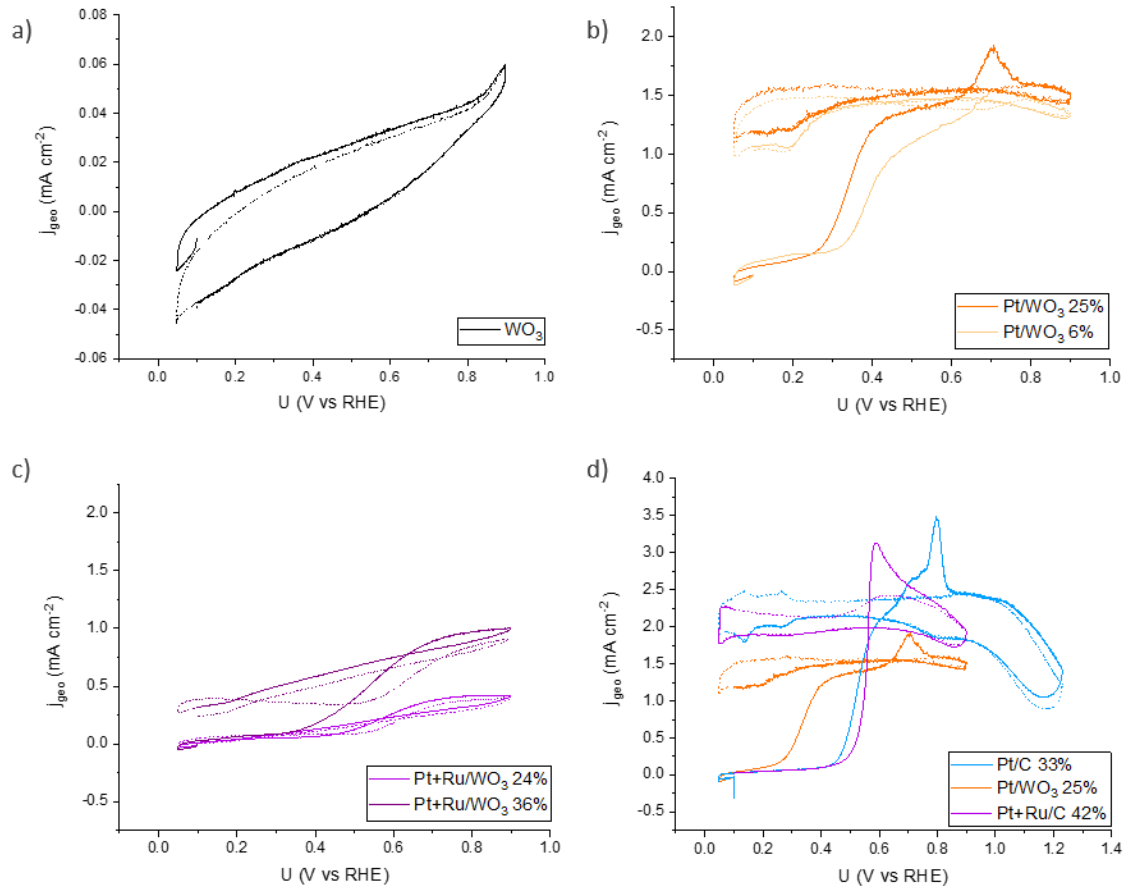

Figure IV.14: CO-stripping with hydrogen purge performed on a) WO_3, b) Pt/WO_3 6 and 25%, c) Pt+Ru/WO_3 24 and 36% and d) Pt/C 33%, Pt+Ru/C 42% and Pt/WO_3 25%. The potential is held for 35 minutes at 0.1 V before cycling at 20 mV s^{-1}. Experiment is done in 0.1 M H_2SO_4, at T = 25°C.

The best tungsten oxide supported electrocatalyst, Pt/WO_3, was then compared in Figure IV.14 d) to Pt/C 33% and the best electrocatalyst of the previous chapter, Pt+Ru/C 42%. It can first be noticed that despite the plateau-like shape of its HOR, Pt/WO_3 25% does not reach the current transport limit reached by Pt/C and Pt+Ru/C, as defined by the Levich law. This issue will be further approached in IV.4.4. When comparing the onset potentials however, Pt/WO_3 25% starts oxidizing CO 300 mV prior Pt, an outstanding result that confirms what was witnessed by Micoud et al. in 2007 [272].

IV.4.3.3 DEMS

Differential electrochemical mass spectrometry experiments were then performed on both Pt/WO_3 6% and 25% electrocatalysts in order to determine the onset potential for CO_2 production. As described in Chapter II, the setup was globally similar to the one used in RDE experiments. The anodic scan of the first and second cycles of a CO stripping (performed at 10 mV s^{-1}) are shown on Figure IV.15, along with the ion current related to carbon dioxide (m/z = 44).

The current of the Pt/WO_3 6% electrode presents the same shape than with the CO stripping described in section IV.4.3.1. Below 0.5 V, the first and second cycles overlap, before a clear oxidation peak at 0.7 V on the first cycle. Focusing on the related ion current measured by the mass spectrometer, a large amount a CO_2 was measured between 0.6 and 0.8 V, related to the main peak of CO oxidation on the CVs. A small amount of CO_2 was also detected for this electrocatalyst between 0.3 and 0.6 V, the region of the first wave of CO + H_2 oxidation noticed in Figure IV-14. This product could be related to the partial electro oxidation of CO from the Pt/WO_3 surface. The superposition of the first and second cycles could then be explained by the CO oxidation in the first cycle, and the de-insertion of protons in the second cycle, which was blocked in the first cycle due to the poisoning of the Pt sites.

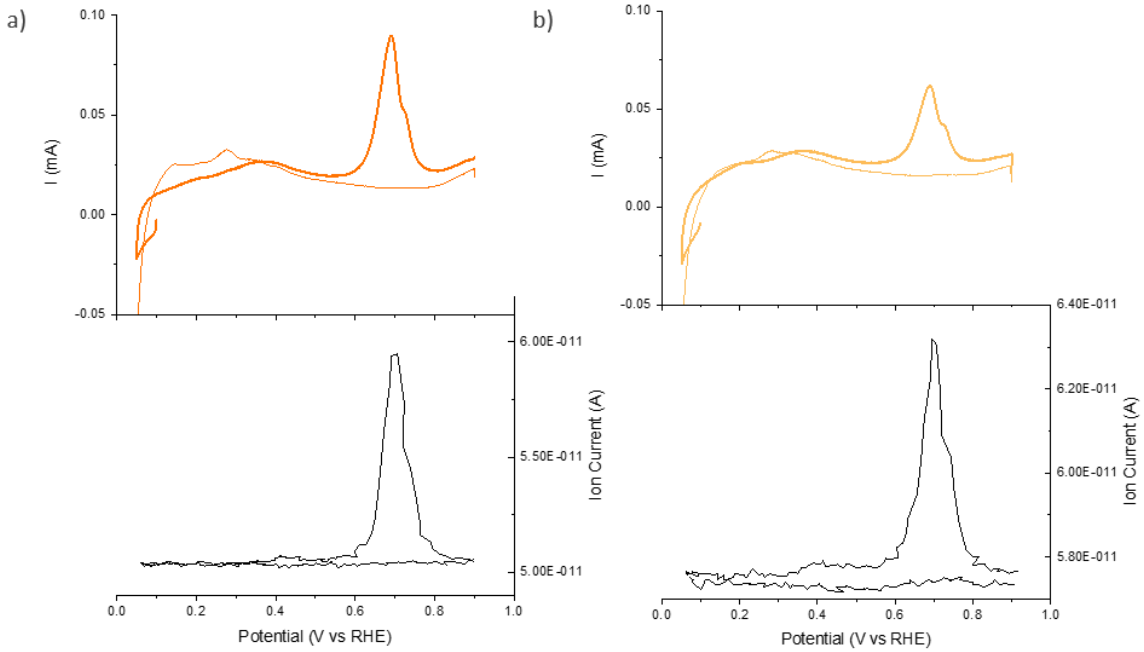

Figure IV.15: DEMS experiments on Pt WO_3 a) 6% and b) 25%. The current measured by potentiostat, and the CO_2 ion current (m/z = 44) measured by the mass spectrometer are presented as a function of the potential. Cyclic voltammetries were done at 10 mV s^{-1}, in 0.1 M H_2SO_4, at T = T_{amb}.. Only the anodic scan of 1st cycle (thick lines) and 2nd cycle (thin lines) are presented.

Pt/WO_3 25%, presents a higher current at low potentials on the second cycle of the cyclic voltammetry than on the first one, related to the H_{upd} region of the Pt nanoparticles. This tendency in reversed around 0.5 V; a clear oxidation peak is present at ca. 0.7 V. As for Pt/WO_3 6%, the ion current confirms the presence of carbon dioxide in this potential range, with an intensity peak synchronised with the oxidation peak. This confirms the assumption that the electrochemical peak at 0.7 V is (mainly) related to CO oxidation. However, this does not exclude the possible combination with another reaction such as proton de-insertion. Since the mass spectrometer could not be calibrated in those conditions, no relationship can be drawn between the CO_2 production faradic current and ionic current, unfortunately. A small quantity of CO_2 was also measured between 0.4 and 0.6 V, related to the oxidation of either weakly adsorbed CO molecules, or molecules closer to WO_3 sites (in this case, the principal peak would be related to the oxidation of further CO_{ads} that have diffused to those contact sites) [211].

IV.4.4. Activity for the hydrogen reactions

As it was presented in section IV.4.3.2, the hydrogen oxidation reactions present diverse and surprising results from the tungsten-based electrocatalysts. HOR curves at 1000 rpm rotating are presented again in Figure IV.16.

Both Pt+Ru/WO_3 composites showed very poor performance towards the HOR reaction with a maximum geometrical current of less than 1 mA cm^{-2}. This is two times less than the current mass transport limit of 2.2 mA cm^{-2} reached by Pt/C 33%. Pt/WO_3 6 and 25% display better performances then the composites for the HOR, though do not reach the mass transport limit either. It is possible that for this electrocatalyst, the charge transfer is also limiting, especially considering the poorer electronic conductivity of the metal oxide.

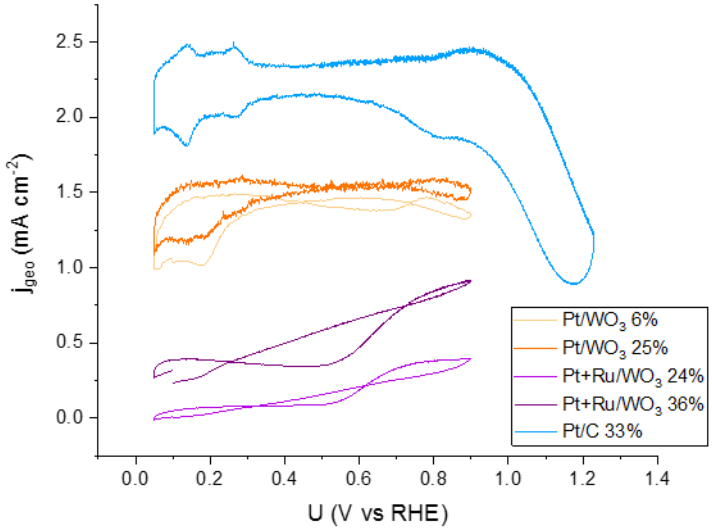

Figure IV.16: HOR geometrical current densities for tungsten-supported electrocatalysts, compared to Pt/C 33%. Experiments were performed at 1000 rpm at 20 mV s^{-1}, in a 0.1 M H_2SO_4 electrolyte. T = 25°C.

The HOR is however strongly limited the RDE setup, due to the low solubility of hydrogen in the liquid electrolyte. As for Chapter III, it was therefore decided to study the HER instead, making the assumption that if an electrocatalyst presents very good activity for the hydrogen evolution reaction, it will also be active towards the hydrogen oxidation reaction. Geometrical current densities were extracted at -20 mV and -100 mV from cyclic voltammetries performed at low potential, and their results (based on 3 to 7 measures per electrocatalysts) are presented in boxplots graphs, in Figure IV.17. Pt/C and PtRu/C were added as a comparison.

Despite the poor reproducibility of the experiment, it is still possible to draw a qualitative comparison of the respective behaviours of each electrocatalyst towards the HER. At -20 mV, Pt/WO_3 6 and 25% present a large difference. Pt/WO_3 6% exhibits a very poor reproducibility compared to Pt/WO_3 25%. It seems also more active than the lower loading, and displays a mean value in the range of Pt and PtRu, a very good result that was not excepted (considering the low HOR activity presented earlier). On the other hand, both Pt+Ru/WO_3 loadings exhibit very low current densities, with the lower loading presenting only 2 mA cm^{-2}.

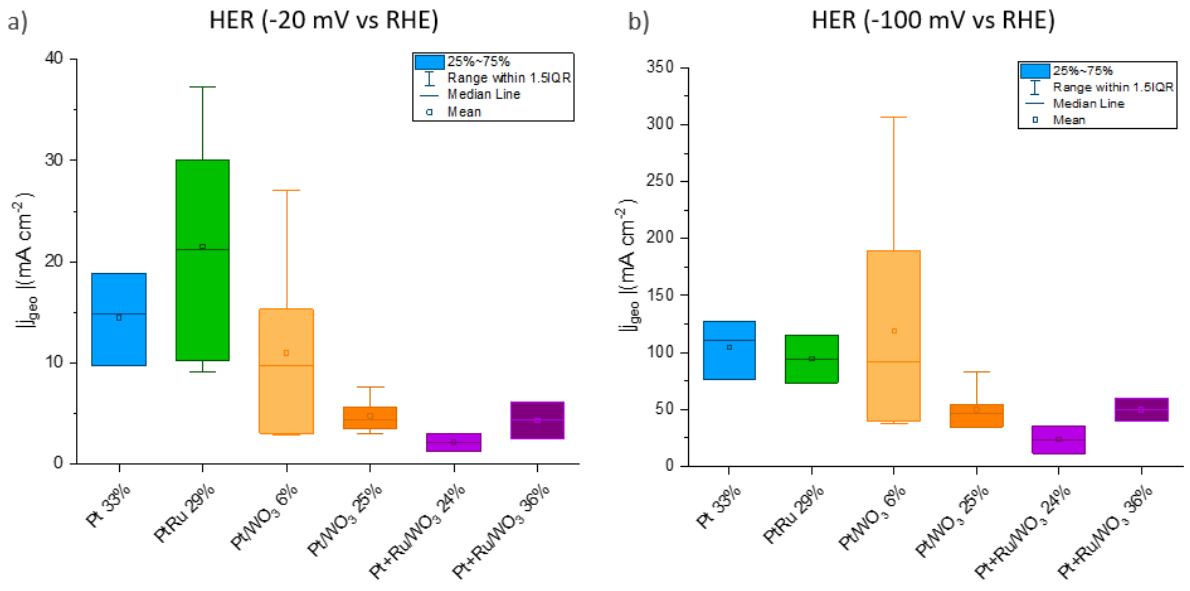

Figure IV.17: HER currents (in geometrical current density) at -20 mV (b) and -100 mV (c) are measured in Ar-saturated electrolyte (0.1 M H_2SO_4, T = 25°C) for each electrocatalyst (25 μg_{Pt} cm^{-2}) at a potential sweep of 20 mV s^{-1}.

At -100 mV, Pt+Ru/WO_3 electrocatalysts as well as Pt/WO_3 25% present a similar behaviour then at -20 mV. Pt+Ru/WO_3 24% presents the lowest current density mean, closely followed by Pt+Ru/WO_3 36% and Pt/WO_3 25%. Pt/WO_3 6% still displays a very poor reproducibility. It however seems to present some very high current densities for the HER, even higher than the ones measured for Pt/C.

As in Chapter II, one can note that the reproducibility of these experiments seems however very disputable. Despite the qualitative comparison previously attempted, the range of values measurements is too high to present any rigorous discussion on the kinetics of the HER, or even HOR activity. Chapter V will present a new and more rigorous setup, the GDE, in order to draw a proper comparison between the electrocatalysts' kinetics towards the hydrogen reactions.

IV.4.5. Discussion

The tungsten-supported electrocatalysts are divided in two categories: The Pt/WO_3 electrocatalysts at 6 and 24% of Pt loadings and Pt+Ru/WO_3 electrocatalysts at 24 and 36% metallic loadings (respectively 16 and 24% of Pt intended mass loading).

Both Pt+Ru/WO_3 electrocatalysts presented a very heterogeneous dispersion of nanoparticles with strong agglomeration areas, with sometimes contact loss with the support and on the contrary, tungsten oxide surfaces empty of any metallic nanoparticles. These materials showed very poor performances in electrochemistry. For the HOR in particular, the current is so low that it is more limited by charge transfer limitations than transport limitations. Even with a low-potential CO-oxidation, an absence of proper HOR activity will reduce EHC performances. It is not suitable for this application and thus, will not be discussed further here.

For Pt/WO_3 6% and 24%, the CO tolerance was tested with the CO stripping technique with both argon and hydrogen purges. As reported previously, Pt/WO_3 6% presents very good CO-tolerance, and Pt/WO_3 25% seems even better when looking at CO-stripping in hydrogen, with an oxidation onset at 0.36 V compared to 0.47 V for Pt/WO_3. Contrary to the same experiments performed with Pt/C however, the recorded current at very low potential (< 0.3 V) was not null. DEMS experiments showed no carbon dioxide production below 0.3 V, which lead to think that CO-oxidation in that range remains small (it had been detected in in situ FTIR by Micoud on similar materials [182,183]). Some of the positive current in that region must then be ascribed to the proton-de-insertion from the WO_3 matrix, which insertion was catalysed by the presence of Pt (and the potential held for 35 min at 0.1 V). Contrary to what was reported previously, Pt/WO_3 do not present any CO oxidation onset at 0.1 V. Still, the oxidation starts at 0.3 V, which overwhelms the previously measured Ru and Pt+Ru/C electrocatalysts.

Looking at the HOR activity of Pt/WO_3 electrocatalysts, it is found that even mass transport limitation current (though low in RDE), could not be reached with these WO_3 supported materials. It can however be noticed that despite a similar Pt loading onto the electrode surface (25 μg_{Pt} cm^{-2}), Pt/WO_3 25% presents better results than the lower loading sample. This could be due to the presence of the Pt mesh on the WO_3 surface, that should help increasing overall electronic conductivity of the material.
The formation of H_xWO_3 was though to help with this limitation, though no H insertion was reported by the mere presence of hydrogen in the environment (as seen in E-TEM experiments). This insertion seems to only happen in electrochemical environment at low potential, and is enhanced in the presence of Pt nanoparticles [211].
The HER activity study permitted only qualitative comparison, presenting Pt/WO_3 6% as the most active tungsten supported material for the HER, but the least reproducible. All three other electrocatalysts presented poor current densities towards the HOR.

The aim of this work is however to find electrocatalysts capable of performing HOR in a polluted environment. It will then be interesting to see if the CO-tolerance reported for Pt/WO_3 can also be present under a H_2/CO mix, and thus counterbalance its lower activity towards hydrogen. This will be addressed in Chapter V.

IV.5. Conclusion on tungsten-supported electrocatalysts

Pt/WO_3 electrocatalysts, and in particular Pt/WO_3 25%, present outstanding CO-tolerance compared to Pt/C and even Ru electrocatalysts. Its HOR activity is however limited by its poor electron-conduction, leading to a severe loss compared to more common electrocatalysts (as much as can be measured in RDE setup). As stated previously, the main idea is however to perform HOR at high current activities under strong pollution. It will thus be interesting to see if despite the poor HOR activity of Pt/WO_3, its CO-tolerance is enough to make it competitive to other electrocatalysts in a CO/H_2 flux.

$Pt+Ru/WO_3$ presented very poor performances due to its morphology. The metal loading was certainly far too high compared to the developed surface area of WO_3 and thus, these results

cannot be attributed to the Pt+Ru/WO_3 association. It is still an interesting material that should maybe be synthetized at lower metal contents, in the order of 10% for instance, to maximize the interface between the metal nanoparticles and the WO_3 support.

The next chapter will then present data obtained using a gas diffusion electrode setup, which feeds the reactant to the working electrode surface in the gas phase; this system enables to avoid the strong mass-transport limitations faced in RDE. The best materials studied so far will be compared in that setup, in pure hydrogen as well as in CO/ H_2 mix.

CHAPTER V

Hydrogen oxidation in pure/impure environment

Chapter V Hydrogen oxidation in pure/impure environment

In Chapters III and IV, the physico-chemical properties, CO-tolerance and hydrogen oxidation (evolution) activity of two electrocatalyst families were thoroughly studied and discussed. In particular, those materials were tested towards the HER in a RDE setup, the HOR being severely limited by mass-transport in liquid electrolyte, hence making any charge transfer kinetics measurement awkward. Even by studying the less mass-transport limited HER (and hoping the results could be extrapolated to the HOR) the results showed very poor reproducibility, and the comparison between the various materials could not be more than qualitative. To go beyond these limitations, this Chapter will make use of an alternative setup, the gas diffusion electrode, in order to present a more realistic and pragmatic comparison of the electrocatalysts. Although using GDE in fundamental electrocatalysis is not new [273], GDE setups have recently been optimized by adopting current collection plates engraved to provide channel/lands for the gas flows, which enables convective fluxes and hence mitigate the GDE flooding [274]. The group of M. Arenz at the University of Bern (Switzerland) is amongst the pioneers in such renewed GDE cells [193,275], and they gently provided to me (i) a 3-week training session to test the cell and (ii) a complete setup to be used at LEPMI. Based on this, the cell used for electrochemical experiments was redesigned in collaboration with the Centre of Atomic Energy of Grenoble (CEA-Grenoble), notably to optimize the current collecting plate in terms of materials (graphite was used instead of stainless steel) and of geometry. Complete details about the experimental setup and operation protocol are given in the dedicated section of Chapter II.

For the present chapter, the six most representative and interesting electrocatalysts of the previous chapters III and IV were chosen: benchmarks: Pt/C 33%, Ru/C 20%, PtRu/C 29%, and the home-made Pt+Ru/C 42%, Pt/WO_3 6% and Pt/WO_3 25%. After a brief presentation of the influence of several parameters on GDE results (which can severely affect the conclusions with this technique), the hydrogen oxidation reaction activity in pure hydrogen will then be assessed for these six electrocatalysts. Finally, the behaviour of these materials in two CO/H_2 mix will then be addressed, to unveil the relevance of (some of) these materials for the EHC anode.

V.1. Basic experiments in GDE

The gas diffusion electrode is a setup presenting both a gas phase (for the working electrode) and a liquid phase (for the reference and counter electrodes). Contrary to RDE, the electrocatalyst is deposited on a porous gas diffusion layer, differing from the mirror-polished glassy carbon by the presented volume. Its interest is that the reactant (here H_2) is fed to the active layer in the gas phase, *i.e*. at a partial pressure (concentration) much higher than in liquid electrolyte (e.g. 1 bar = activity of 1, versus ca. 1 mM L^{-1} = activity of 10^{-3} when dissolved in the electrolyte), and with a diffusion coefficient orders of magnitude larger in the gas phase than in water-based electrolytes, resulting in extremely efficient mass-transport. Added to the channel/land pattern of the current collector (monopolar) plate enabling gas fluxes to the active layer and removal of possible liquid water droplets, the system is compatible with measurements at very high current densities without mass-transport limitation, for which one hopes that the reaction will be only limited by

the charge-transfer kinetics (especially if low aerial loading of electrocatalyst are used – which was adopted herein), hence enabling to unveil true HOR kinetics parameters [193,274,276].

In order to draw a proper comparison between the RDE and GDE setup, the ink recipe was kept identical, as well as the platinum surface loading of 25 μg_{Pt} cm^{-2}. The electrolyte is still H_2SO_4, though used at 1 mol L^{-1} instead, 10 times the prior concentration; this larger concentration was adopted in order to reduce the ohmic drop in the electrolyte (much larger current densities being experienced). For the same reason (as well as to ease H_2O transport), no polymer membrane was added between the GDL and the electrolyte [274]. All presented results are corrected from 100% of the measured ohmic drop.

This section is focused on the study of the influence of several parameters on the GDE setup, as the electrolyte the presence or absence of Nafion®.

V.1.1. Electrochemical signature of Pt/C

A cyclic voltammetry was made for the Pt/C 33% electrocatalyst in the GDE setup, in order to first compare its electrochemical signature to the one priory obtained in RDE. The resulting curve is presented in light blue on Figure V.1.

It can first be noted that the GDE voltammogram is slightly shifted towards negative currents, compared to the RDE curve. This shift is typical of the ORR, and proves the very high sensitivity of this new setup to the impurities present in the gas network. However, despite many improvements, the oxygen content could not be lowered further (this is the same in other studies using GDE).

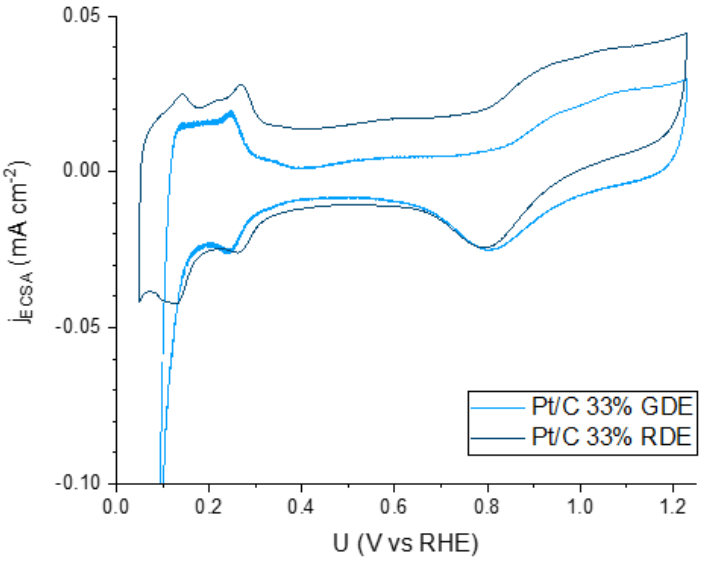

Figure V.1: Cyclic voltammetry of Pt/C 33% electrocatalyst performed in GDE setup at 20 mV s^{-1} in acid electrolyte (1 M H_2SO_4 , T = T_{amb}) and compared to RDE setup.

The general shape of the cyclic voltammogram is similar in both setups, with the H_{UPD} present at low potentials, the double layer capacitance forming a plateau between 0.4 and 0.8 V and the oxidation of Pt and reduction of Pt-oxides at high potentials. Taking a closer look, some differences can however be seen. If one looks at the cathodic section, the first peak of H_{upd} (proton adsorption + sulphates desorption), starting at 0.3 V for the RDE, is slightly negative by ca. 20 mV in GDE. Furthermore, at 0.15 V, the current then decreases drastically, yielding hydrogen evolution reaction at 0.1 V, when it has almost not initiated in RDE at 0.05 V. This phenomenon, though very surprising, was also witnessed by other teams with setups including gas reactants supply [187,193,252,277,278], with shifts ranging from 50 to 100 mV. Carter *et al.* attributed this effect to a low H_2 partial pressure on the cathode side, thus leading to a thermodynamic shift of the HER towards higher potentials. It seems however unlikely is the present case, considering the absence of any polymer separator between the upper (electrolyte) and lower (gas phase) compartments of the GDE. One hypothesis could be that the sulphates adsorption/desorption (very likely in fully flooded-RDE active layers, much less in partially-flooded GDE active layers) could be incriminated (strongly adsorbed sulphates could inhibit hydrogen adsorption and evolution in the RDE case), though more work would be desirable to assert so.

As a result of this, the H_{UPD} region is greatly reduced in the GDE configuration due to the higher HER onset and lower H_{upd} onset. It is also less defined that in RDE setup, as only one clear peak is witnessed at 0.25 V, but not at 0.14 V or 0.2 V. This could non-negligibly alter the active area determination, if attempted by H_{upd} coulometry, and this is why CO-stripping was preferentially used. The Pt oxide reduction, at ca. 0.8 V, is also shifted, but this time it is a positive shift of 20 mV for the GDE with respect to the RDE; here again, the best explanation from the literature (still tentative) would be the effect of sulphates, much more pronounced in RDE than in GDE (in that case, Carter's explanation cited above, makes no sense).

V.1.2. CO-stripping and influence of parameters for Pt/C

In order to measure the ECSA of each electrocatalyst, a CO-stripping voltammetry with argon purge was performed at the beginning of each experiment. Here, the influence of several parameters the CO-stripping of a Pt/C 33% is presented.

V.1.2.1 Influence of the setup

Two CO-stripping of the Pt/C 33% electrocatalyst are presented Figure V.2. The one made in RDE setup (in dark blue) presents a null potential until ca. 0.6 V, where the first CO_{ads} oxidation peaks (pre-peaks, related to CO_{ads} oxidation on Pt agglomerates (see Chapter III)), are witnessed; then the main CO_{ads} oxidation peak is centred at 0.81 V, attributed to the oxidation of CO_{ads} on isolated Pt nanoparticles. With the GDE (in light blue), the same absence of current is seen at low potentials. The CO_{ads} oxidation peak however, is composed of one single peak centred at 0.81 V. The absence of pre-peaks in GDE configuration cannot be related to the imperfect initial CO_{ads} coverage (that would leave Pt agglomerates unblocked by CO), since no current was measured in the H_{UPD} potential range (which means full Pt blockage was achieved at low potential). One can

assume that the lack of water in the hydrophobic carbon pores of the GDL impacts the CO oxidation mechanism by reducing the amount of adsorbed OH_{ads}, or (again) that strongly adsorbing sulphates ease the desorption/stripping of CO_{ads} from some Pt sites.

On both curves, a later, broader peak can be seen (at 1.05 V in RDE), related to the oxidation of CO_{ads} on very small (and isolated) Pt nanoparticles. This peak is shifted positive by 40 mV with the GDE.

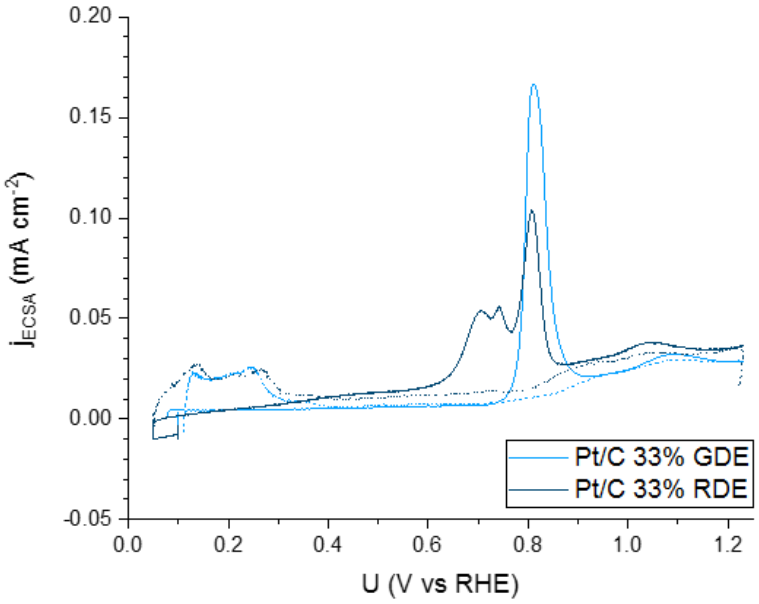

Figure V.2: CO-stripping of Pt/C 33% performed in GDE (light blue) and RDE (dark blue) setup, at 20 mV s^{-1} after 35 min of holding the potential at 0.1 V. 1st cycle is in plain line, 2nd cycle in dashed line.

Despite the differences of CO-oxidation behaviour in the GDE and RDE setups, ECSA measurements for GDE active layers have been performed following the same process given in Chapter II for RDE experiments.

V.1.2.2 Influence of the electrolyte

The influence of the electrolyte was studied by replacing the 1 M H_2SO_4 by 1 M $HClO_4$ in the upper compartment of the GDE (this experiment was first done in order to see the impact of sulphuric acid presence on the CV and HOR). The comparison between both configurations is given Figure V.3.

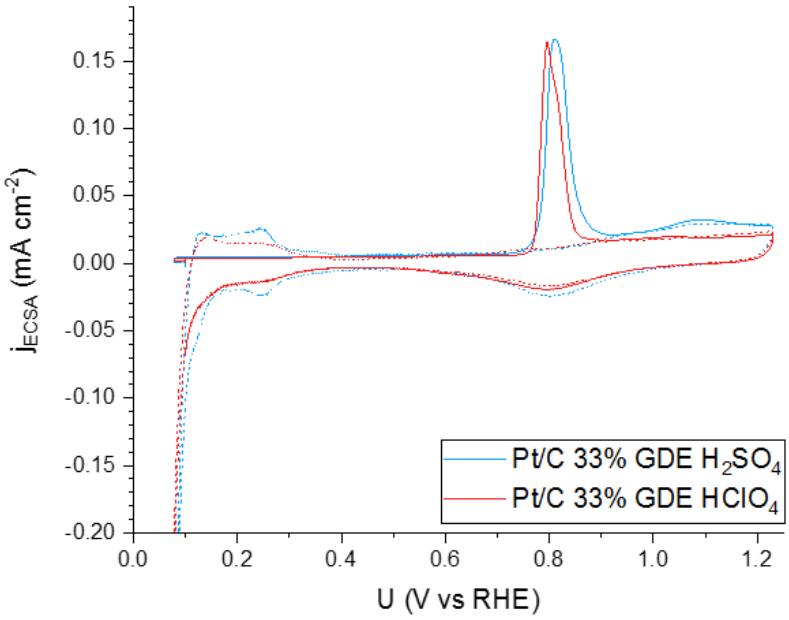

Figure V.3: CO-stripping of Pt/C 33% performed in 1 M H_2SO_4 (blue) and 1 M $HClO_4$ (red) electrolyte, at T = T_{amb},, at 20 mV s^{-1} after 35 min of holding the potential at 0.1 V. 1st cycle is in plain line, 2nd cycle in dashed line.

As previously detailed, the CO-stripping in sulphuric acid presents one very defined peak at 0.81 V, with another broad, less defined peak at higher potentials. The shape of the CO-stripping in perchloric acid is quite similar, with the same defined peak around 0.8 V. The shape of the main peak is however slightly different, asymmetric with a small shoulder at high potential values: the main peak is shifted negative by 20 mV in perchloric acid. According to Maillard *et al.* [250], this could be related to the presence of strongly-adsorbing sulphates on Pt nanoparticles in the sulphuric acid configuration, whereas perchlorates are poorly-adsorbing species.

The H_{UPD} region visible on the second cycle also presents marked differences: the hydrogen (and sulphates, in sulphuric acid) adsorption and desorption peaks are less defined in perchloric acid, which confirms that the set of high potential peaks (nearly absent in perchloric acid) are indeed to some extent connected to the adsorption/desorption of sulphates. The HER onset is however globally the same for both configurations, proving its shift is not related to the nature of the anion of the liquid electrolyte.

V.1.2.3 Presence of a polymer membrane

In their work, Inaba *et al.* used a Nafion® polymer membrane between the GDL-supported GDE (where the electrocatalyst is deposited) and the liquid electrolyte [193]. This configuration presents the advantage of being very close to the one used in PEMFC, and thus contributes to the realism of the measured data. However, the poorer proton conductivity and much poorer water diffusivity in polymer membranes versus concentrated liquid acids can lead to the incomplete utilisation of the catalytic layer, and large ohmic drop/mass-transport hindrance can affect reactions studied at high current densities [274,276] . In order to properly study the intrinsic kinetics of electrocatalysts, it was thus decided to work without polymer membrane, as suggested

by Pinaud and Ehelebe [274,276]. For comparison purposes, the CO-stripping obtained in both cases are nevertheless presented Figure V.4.

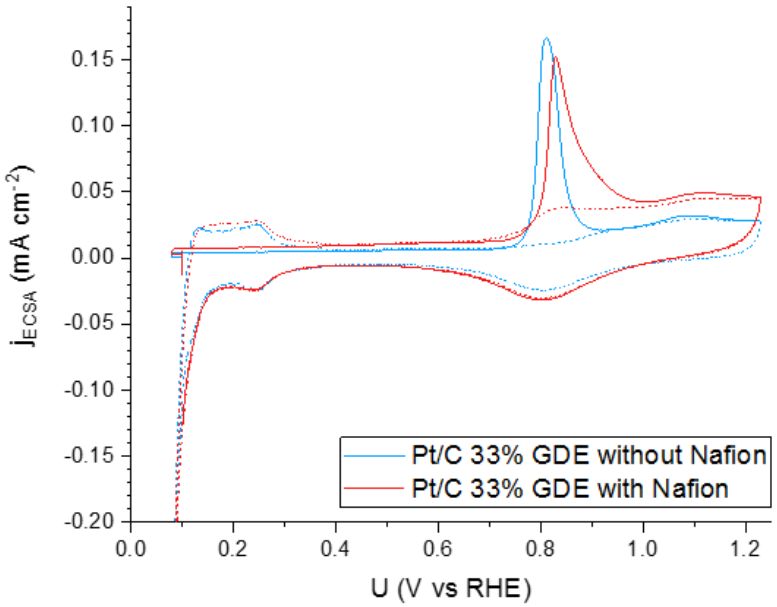

Figure V.4: CO stripping of Pt/C 33% performed with (in red) and without (in blue) a Nafion® polymer membrane in-between the GDL and the liquid electrolyte. Experiments were done at T = T_{amb}, at 20 mV s^{-1} after 35 min of holding the potential at 0.1 V. 1st cycle is in plain line, 2nd cycle in dashed line.

The main oxidation peak, at 0.81 V in the absence of Nafion®, is slightly shifted positive in its presence. The peak shape is also broadened towards high potential values. Those shifts could come from the limited presence of protons, water and thus OH_{ads} groups on the GDL side of the setup (inside the active layer), thus limiting the first step of the CO-oxidation mechanism. The major change however lies in the presence of a larger baseline at high potentials. Above 0.75 V on the second cycle, a larger oxidation current that could be attributed to Pt oxidation can be seen. The oxidation of Pt seems enhanced in the presence of a polymer membrane, which the author cannot explain, to date (this observation is reproducible).

In Figure V.4, the current is presented in current per measured surface area of platinum, in order to properly compare the two CO_{ads} oxidations shapes. The actual measured ECSA is however quite different between the two electrodes (made from the same ink, with the same protocol), with 0.59 cm² measured without Nafion, and 0.30 cm² in the presence of Nafion. This really low active surface value in the second configuration could come from the lack of proper ionic contact for some Pt nanoparticles in the GDE active layer, resulting in “Pt utilization” well below 100% in this configuration. It might however be possible to increase the ionic contact in the presence of Nafion with the hot pressing techniques used in the PEMFC industry [279].

Those results comforted the decision taken to remove the Nafion membrane, as no major inconvenient could be seen from this configuration.

V.2. Electrocatalyst behaviour in pure H_2

After the determination of the ECSA, the cell inlet was connected to a pure hydrogen flux. The behaviour and performances of all six studied electrocatalysts were studied in that media, by the means of cyclic voltammetry at 20 and 5 mV s^{-1} and chronoamperometry at the potentials of 20, 130 and 400 mV.

V.2.1. HOR in mass-transport-free setup

Figure V.5 presents the cyclic voltammetry of the Pt/C 33% in hydrogen environment, in a GDE setup, with a current normalized with the geometrical surface of the electrode. For comparison purposes, the geometrical transport limit previously obtained with RDE (2.4 mA cm^{-2}) is indicated on the same graph (purple dotted line). The huge difference between the maximum currents reached with the same loading of 25 µg cm^{-2} of platinum is an evidence of the limits of the RDE setup. In fact, Pt/C performances in RDE were only representing 0.02% of its possibilities (considering the maximum value attained in GDE). This difference explains the recent enthusiasm in the electrochemistry community for GDE setup, in which gas reactant are supplied to the working electrode.

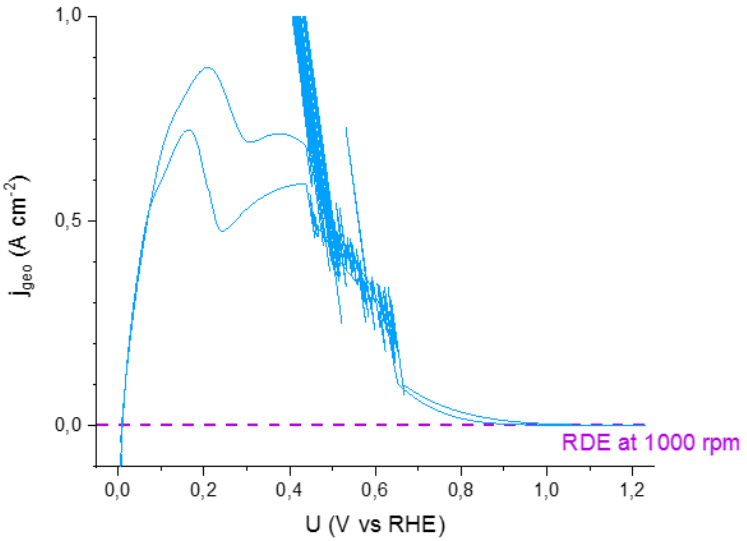

Figure V.5: Cyclic voltammetry of Pt/C 33% performed in GDE under H_2 feed at 20 mV s^{-1}, presented in current density per geometrical surface area. Experiments were performed in 1 M H_2SO_4, at T = T_{amb}. The loading is of 25 µg_{Pt} cm^{-2}. RDE value at 2.4 mA cm^{-2} for 1000 rpm.

Without those mass-transport limitations, it is now possible to visualize the real shape of the HOR voltammogram on Pt (Figure V.5). Starting from 0 V, the potential first greatly increases, before reaching a region where several peaks are observed; these peaks show a pronounced hysteresis from ca. 0.08 to 0.6 V, also observed by other groups working in gas-reactants setups [187,189,190,278]. In the anodic scan, that lies above the cathodic scan, two main HOR peaks are observed at 0.21 and 0.38 V, the second being with a smaller current versus the first one. Zalitis *et al.* attributed this peak to the presence sulphate anions that, starting from the Pt point of zero

total charge (PZTC) measured at 0.24 V in their case, start adsorbing preferentially onto Pt sites, thus partially blocking the active surface [189]. Between 0.4 and 0.7 V, a large noise effect can then be seen (the angled lines are due to the ohmic drop correction on the noise). This noise was often seen during our experiments in this potential range, and was attributed to a competition between hydrogen oxidation and platinum oxide formation, which could result in sustained oscillations (often witnessed when such activation/inhibition processes compete) [280–283]. Pt oxide presenting poor activity towards the HOR, the overall current slowly decreases until 0.9 V, were it forms a plateau, at almost zero current. Starting from 1.23 V, the cathodic scan follows the anodic one until ca. 0.5 V, going through the same plateau and region of large noise in the Pt oxides reduction area. In the HOR peaks region, the cathodic scan is below the anodic scan (possibly due to the late desorption of sulphate anions), but shows essentially the same HOR peaks as observed on the anodic scan.

The cyclic voltammograms in hydrogen of all studied electrocatalysts are then presented Figure V.6, in separate graphs for better visibility. The current density is this time presented normalised per active surface area, to ensure proper comparison on the basis of the total amount of catalytic sites.

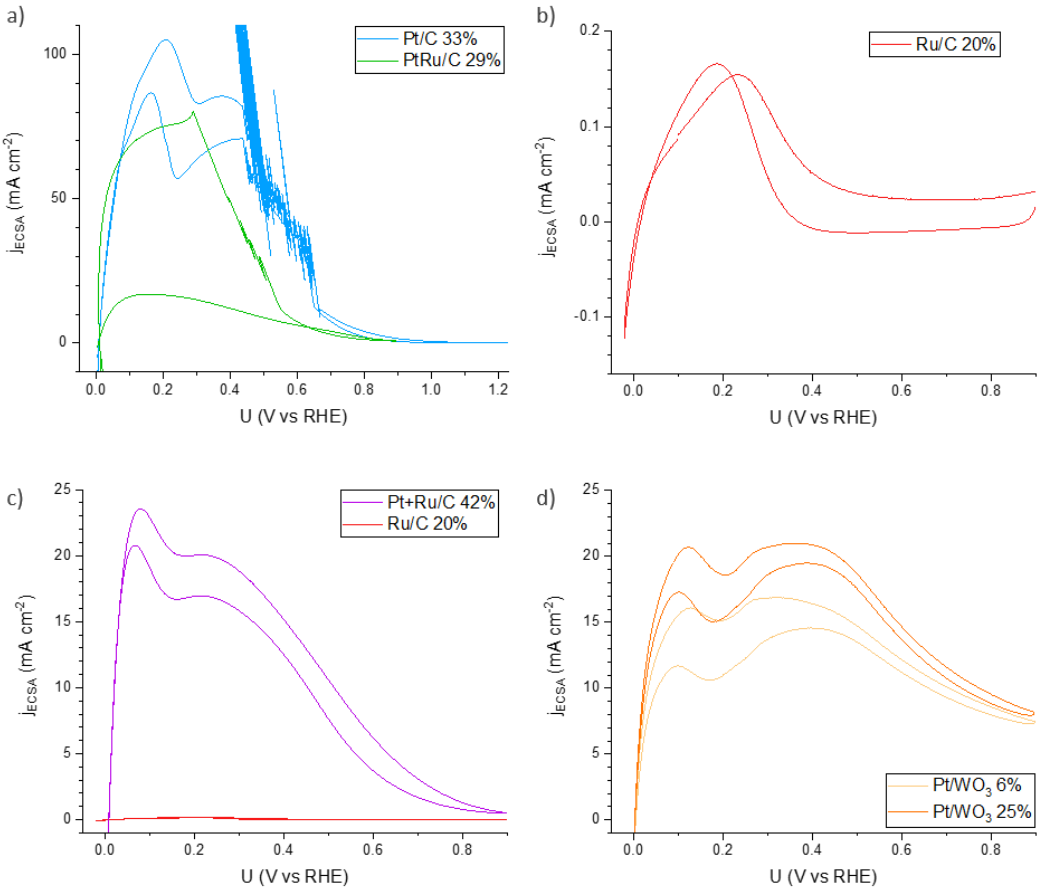

Figure V.6: Cyclic voltammetries of a) Pt/C 33% and PtRu/C 29%, b) Ru/C 20%, c) Pt+Ru/C 42% and Ru/C 20%, and d) Pt/WO_3 6 and 25%, performed in GDE under H_2 feed at 20 mV s^{-1}, presented in current density per active surface area. Experiments were performed in 1 M H_2SO_4, at T = T_{amb}. The loading is of 25 μg_{Pt} cm^{-2}.

PtRu/C 29% presents a very fast current increase on the anodic scan, even faster than Pt at very low potentials, going as high as 80 mA cm_{ECSA}^{-2}, very close to Pt with 105 mA cm^{-2} at its highest point. The PtRu alloy presents an even larger hysteresis than the Pt, with a cathodic current nearly divided per 4 compared to the anodic one. Contrary to Pt (and all other Pt-containing electrocatalysts), no peak can be seen in the low potential range, a similarity to the absence of any defined peaks in the H_{UPD} area during a more classical cyclic voltammetry in argon. The current rapidly decreases from 0.3 V, marking the beginning of the Pt oxidation. The PtRu alloy, more oxophilic than Pt is therefore not capable to sustain large HOR current above ca. 0.3 V, where Ru-Ox starts to form significantly, detrimentally affecting the overall HOR kinetics.

On a different level, Ru/C stays constant versus the prior results: it is very poorly active towards the HOR. Its current represents less than 0.2% of the Pt one, thus not interesting towards the HOR. The shape of its curve under hydrogen can however bring some information on the behaviour of ruthenium nanoparticles in this media. As for the other electrocatalysts, the maximum current is found in the low potential region, prior a fast decrease around 0.4 V. This decrease could be attributed to both Ru oxidation and sulphate adsorption, though more investigations would be needed to determine in which proportions.

In Figure V.6 b), Pt+Ru/C presents a shape very similar to that of Pt, with low potentials marked by high currents and an hysteresis, and a decrease in HOR activity starting 0.25 V. At low potentials, the first peak at 0.08 V is clearly defined, while the second is more wave-shaped. It can be seen however, that the hysteresis continues down to 0.9 V, with the cathode and anode scan always distinct from one another. The very fast decrease observed from the second wave is probably due to the contribution of both Pt and Ru oxidation, as well as anion adsorption on both surfaces. In any case, the HOR current densities reached are ca. 4 times lower than on Pt/C.

Pt/WO_3 6 and 25% samples, in opposition to previously presented electrocatalysts, do not lose as much HOR activity at high potentials. In fact, both the low potential peak and the following wave at 0.35 V present similar maximum current prior a slow decrease at 0.5 V. This particularity implies that the poisoning phenomena occurring on other electrocatalysts as soon as 0.25 V (related to sulphate adsorption and Pt-oxides formation) do not occur as much on tungsten-oxide-supported platinum nanoparticles, at least until 0.5 V. One can suggest that the presence of the WO_3 support (almost) suppresses the Pt-oxides formation [182](which is classical for metal oxides supports [284]) and could also affect sulphates' adsorption, a clear advantage for high-potential HOR activity. For the same ECSA, Pt/WO_3 25% presents slightly better activity than the lower loading, following what was measured in RDE. It can however be pointed out that both display approximatively the same current at 0.9 V.

Globally, Pt and PtRu both present very high activity, in the order of 100 mV cm_{ECSA}^{-2}, in the low potential region (E < 0.3 V for PtRu or E < 0.5 V for Pt). This value is however several times inferior to the ones measured in other gas-phase setups, which reached current densities from 200 to 600 mA cm_{Pt}^{-2} on Pt/C [187,189,208]. For instance, Durst *et al.* reached 500 mA cm_{Pt}^{-2} in hydrogen pump at 40°C, and Zalitis also reached that value, at 25°C in a floating electrode setup.

Surprisingly, Pt+Ru/C does not reach these values, despite its apparent good activity in HOR in the RDE setup. It is however very close to both Pt/WO_3 6 and 25% electrocatalysts, with ca. 20 mA cm_{ECSA}^{-2} of maximum current.

V.2.2. Exchange current density

The electrocatalysts intrinsic activity towards the hydrogen reactions is better assessed by the determination of kinetics parameters, e.g. the Tafel slope or exchange current densities. As presented Figure V.7 a), a cyclic voltammetry is performed, with Pt/C 33% sample, under hydrogen at the slow rate of 5 mV s^{-1}, then plotted in log*i* as a function of the potential. The current exchange density, intrinsic activity marker of a given material, can be measured by the intersection between the equilibrium potential and the so called "Tafel slope" of the reaction. That slope was fitted between +50 mV and +100 mV for the HOR and between -50 mV and -100 mV for the HER. Results for each electrocatalysts for both the HER and HOR are presented in Figure V.7 b).

One can first notice that the values of exchange current density for the HER are much higher than for the HOR, which was also reported by Durst *et al.* [187]; they attributed the H_{ads} adsorption as the rate determining step of the HOR. It could also be that the HER (leading to H_2 gas bubbles formation) is less mass-transport limited than the HOR (that necessitates diffusion of H_2 to the catalytic sites – through the gas phase, the ionomer and/or the liquid electrolyte film ionically connecting each Pt site), even in the GDE configuration.

Looking at the HOR current densities, Pt/C unsurprisingly presents the best value, with j_0 = 17 mA cm^{-2}. It must however be noticed that this value is far below the ones measured in hydrogen pump or FET setups, reaching 600-200 mA cm_{Pt}^{-2} [187]. PtRu/C 29%, despite very high currents measured in the previous section, displays only 4.7 mA cm_{Pt}^{-2}, even lower than Pt/WO_3 6 and 25% at respectively 5.9 and 8.4 mA cm^{-2}. The Pt+Ru/C 42% composite on the other hand, presents a much higher current density of 11.5 mA cm^{-2}, though still lower than pure platinum. The close values for exchange current density for Pt+Ru and Pt (and larger than for PtRu alloy), somewhat validates the initial hypothesis of this PhD: to use a composite between Pt and Ru versus an alloy to obtain a better compromise between CO-tolerance and HO activity.

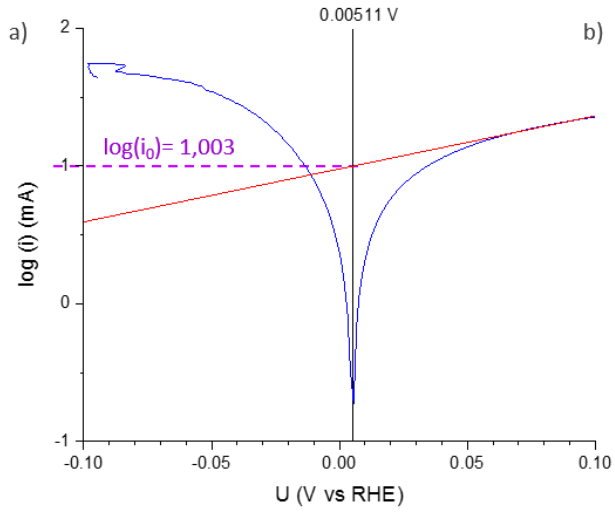

b)

Electrocatalyst	$j_{0,\ HOR}$ (mA cm^{-2})	$j_{0,HER}$ (mA cm^{-2})
Pt/C 33%	17.1	35.6
PtRu/C 29%	4.7	7.5
Ru/C 20%	0.02	0.03
Pt+Ru/C 42%	11.5	16.4
Pt/WO3 6%	5.9	62.5
Pt/WO3 25%	8.4	58.3

Figure V.7: a) Tafel slope measurement presented in a Pt/C 33% in GDE configuration, at 5 mV s^{-1} in 1 M H_2SO_4 at T = $T_{amb,}$. b) Table of measured exchanged current values normalized per active surface area of electrocatalyst.

Concerning the HER, Pt/WO_3 6 and 25% respectively present the first and second best activities towards the HER activity. This result is even more astounding when looking at the values: Pt/WO_3 presents values nearly twice larger current density than Pt. This could perhaps be explained by the possibility for WO_3 to "store" protons when forming a H_xWO_3 bronze, though this is only an assumption. Behind, both PtRu and Pt+Ru present values similar to the ones measured in HOR, Pt+Ru/C still presenting higher values than the alloy. Ru, on the other hand, does not present any consequent activity in both HER and HOR.

The author would like to point out that, despite being more convincing than the RDE measurements, these experiments performed in more realistic GDE conditions are still not equivalent to those in real system (H_2 pump of EHC), and could for sure be improved (the GDE setup is only operational since a few months); such tests could not be performed in the frame of this PhD, though.

V.2.3. Chronoamperometry in pure hydrogen

Prior any experiments with carbon monoxide, the behaviour of each electrocatalyst at fixed potential under a set hydrogen flux of 29 mL min^{-1} was measured. To recover the lost surface, cyclic voltammetries at fast rate (500 mV s^{-1}) were performed between each chronoamperometry (CA). The result obtained for Pt/C 33% is presented in Figure V.8. The large noise present on the 130 mV curve was very often present on curves with high absolute current.

To ease the data understanding, all initial and final current densities were extracted and plotted in the bar chart presented on Figure V.9. Lighter colours represent the initial measured values (immediately upon application of the desired potential), and darker colour the final value after 15 minutes of experiment.

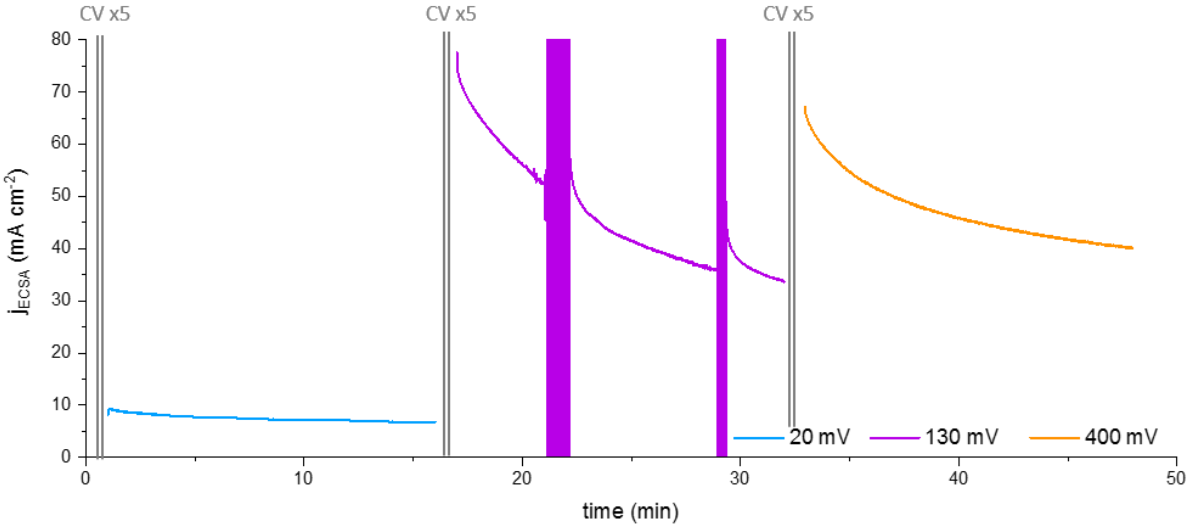

Figure V.8: Pt/C 33% chronoamperometries measured at 20, 130 and 400 mV under pure hydrogen in GDE setup in 1 M H_2SO_4 at $T = T_{amb}$.

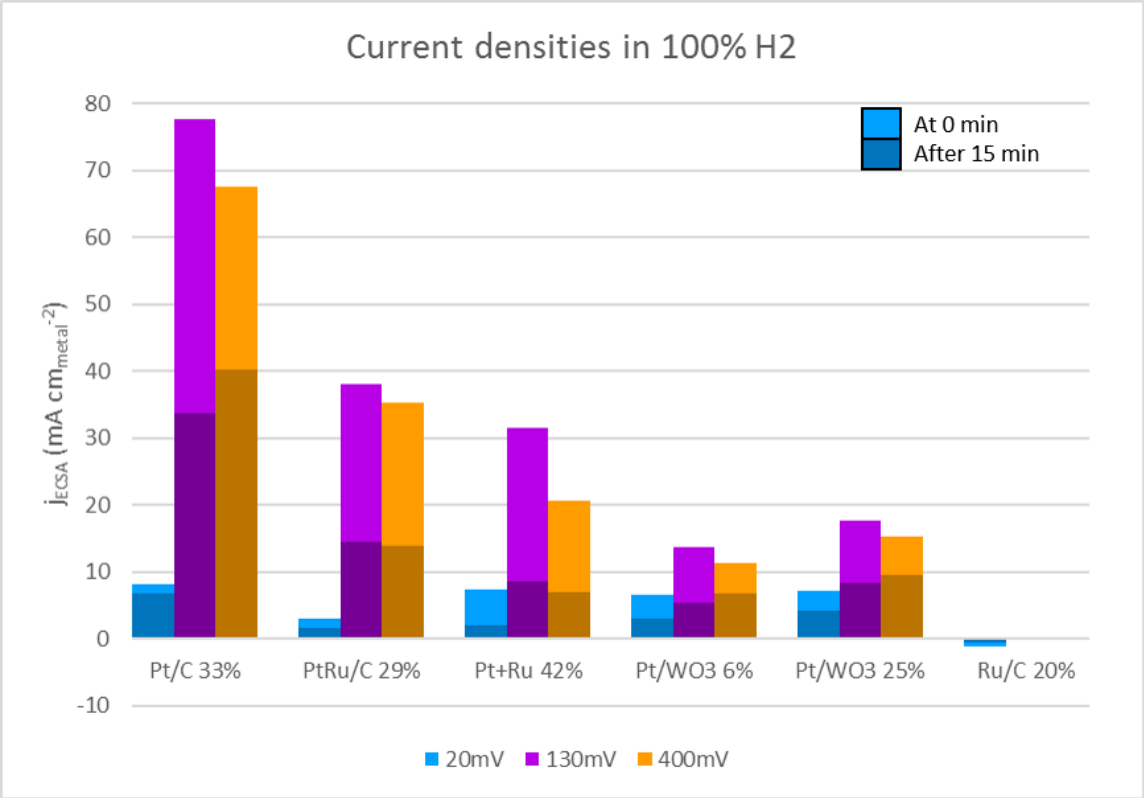

Figure V.9: Bar chart presenting the initial (in lighter colour) and final (in darker colour) values obtained for 20, 130 and 400 mV for the studied electrocatalysts in pure hydrogen.

As seen on Figure V.8, Pt presents a large loss of current in only 15 minutes of potential hold. This loss is weak on the small value obtained at 20 mV, but for 130 and 400 mV, the loss is respectively of 57 and 40%, clearly non negligible. Up to now, only a tentative explanation can be given to justify such an important drop: the most obvious is a detrimental and gradual adsorption of sulphates (which would explain why this effect is not so mentioned for experiments performed in polymer electrolyte environment: PEFC or EHC); another reason is connected to the presence of impurities (despite the experimental care adopted, the low-loaded GDE uses a commercial GDL that is very hard to clean prior the experiment). The same experiment was attempted in perchloric acid or with a Pt loading three times higher (75 $\mu g_{Pt}\,cm^{-2}$) or even in the presence of a polymer, with no improvement. Each configuration also presented a large drop of more than 50% the initial value at large HOR potential values. The current seems to however be regained after performing cyclic voltammetries, which hints at the hypothesis of a poisoning by trace components in the electrolyte or impurities contained in the gas (even though it is a N5 hydrogen gas), or even gradual oxides formation. Since this issue was reproducible and concerned all electrocatalysts, it was decided to pursue the experiment is order to compare the different electrocatalysts' behaviour.

The PtRu alloy presented two times less HOR current than Pt, at any potential. Unlike Pt, the loss at low potential reaches 50%, despite the low current density. At 130 and 400 mV, 75 and 60% of the initial current is lost, even more than for Pt. Because PtRu alloy is more oxophilic than Pt (hence more prone to assist the oxidation of organic impurities, but also more prone to form surface oxides), it is possible that the noted deactivation of the HOR activity is (at least somewhat) connected to Pt-oxides formation.

Pt+Ru/C 42% showed similar current losses, of 42, 62 and 60% for 20, 130 and 400 mV. The maximum initial current was also slightly inferior to the one measured for PtRu.

As for Pt/WO_3 electrocatalysts, they both presented losses in the order of 50% of the initial value, whatever the holding potential. It can be remarked that as for cyclic voltammetries in hydrogen, the higher loading presents the highest current values.

Despite its very low current density, barely visible on the bar chart scale, Ru also presented some losses in the order of 60-70% of its initial value.

Despite the unexpected issue of current losses in pure hydrogen feed, a gradation of electrocatalyst in pure hydrogen environment could be achieved. Pt present the best HOR activity in pure hydrogen, then follows the PtRu alloy, and shortly behind, the Pt+Ru composite. Finally, Pt+WO_3 25 and 6% present some HOR activity, even though it is not high enough to compete against the Ru-based electrocatalyst in pure hydrogen. One question is, will this gradation stay the same with an impure hydrogen feed?

V.3. Electrocatalyst behaviour in polluted H_2

The behaviour and current density evolution of each electrocatalyst were compared in an impure H_2 feed, firstly consisting of hydrogen mixed with 10 ppm of carbon monoxide.

V.3.1. H_2 + 10 ppm CO

As in the previous section with the pure hydrogen chronoamperometries, results are first presented in raw graph for Pt on Figure V.10, and then in bar chart summing up all initial and final current density values in Figure V.11

The chronoamperometries of Pt/C 33% displays a very fast drop in current for both 130 and 400 mV of potential (much faster than in pure H_2). Most of the loss happens in less than 5 minutes, before the current decays with a smaller slope. This time, the loss is in the order of 93% of the initial value after 15 min, with Pt ending with a current density of 2 mA cm_{Pt}^{-2} only. This loss is very significant, but also quite surprising, especially owing to the low CO content of the feed. Other publication presented less than 30% loss of current in fuel cell, due to the presence of 10 ppm CO in the gas inlet feed at the anode [124,130,285]. One major difference between the “somewhat “good” behaviour noted in PEMFC and the present case comes from the fact that in PEMFC, the performances are significantly limited by the cathode (even in pure H_2 feed) and the ohmic drop and mass-transport, when here, only the intrinsic charge-transfer performance of the HOR catalyst is measured instead. The author also points out that the fast decay observed here could also result from the combination of both CO poisoning and from the unknown decay observed in pure hydrogen.

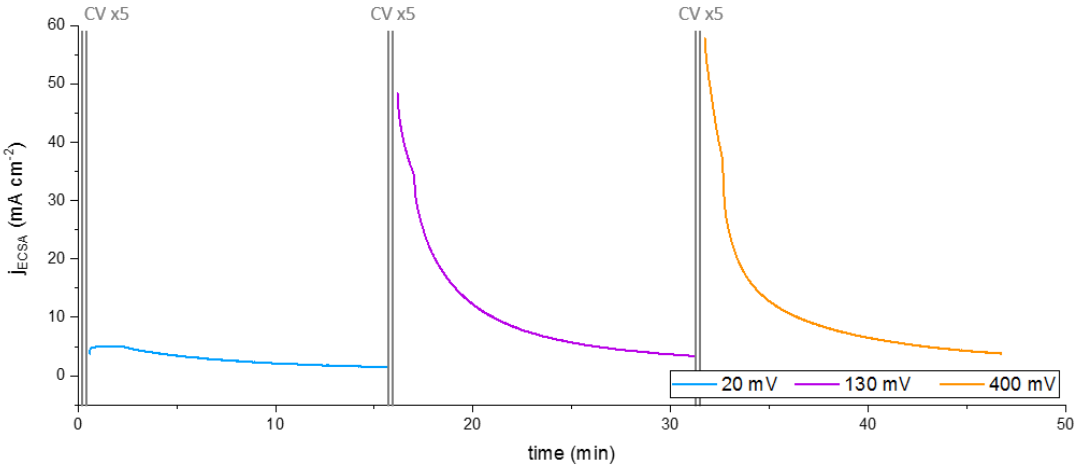

Figure V.10: Pt/C 33% chronoamperometries measured at 20, 130 and 400 mV under 10 ppm CO/H_2 in GDE setup in 1 M H_2SO_4 at T = Tamb.

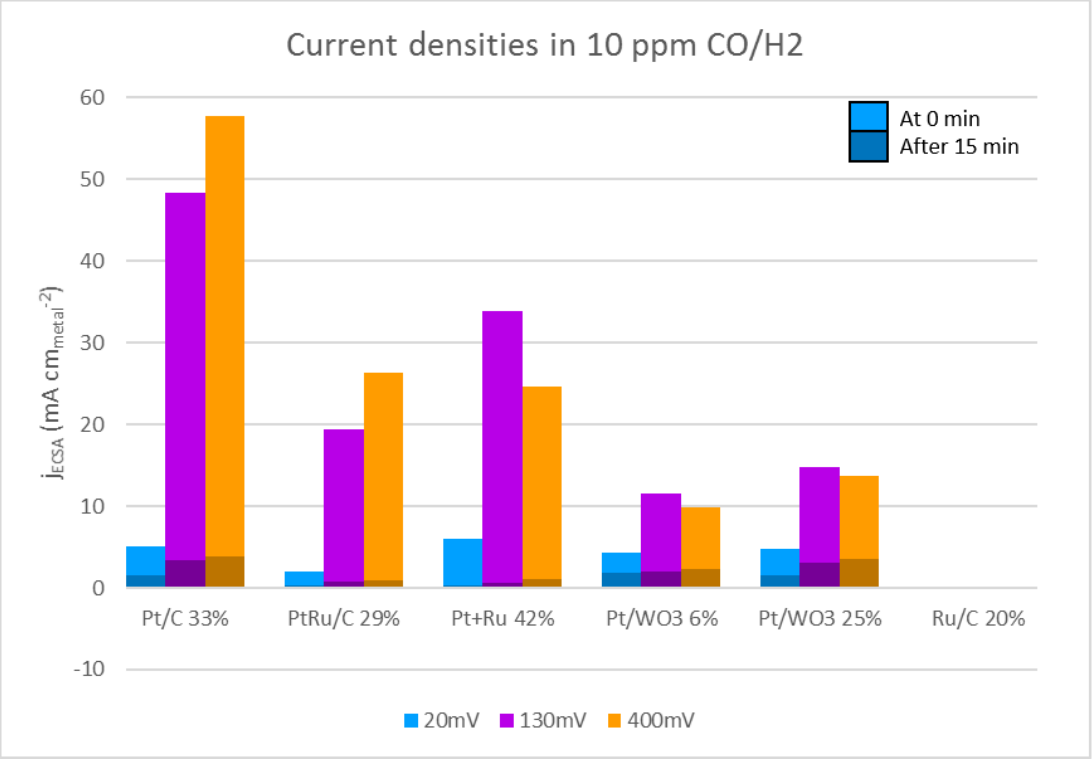

Figure V.11: Bar chart presenting the initial (in lighter colour) and final (in darker colour) values obtained for 20, 130 and 400 mV for studied electrocatalysts in 10 ppm CO/H_2 flux.

In opposition with previous graph, Pt+Ru seems to present more initial current at 20 and 130 mV than the PtRu alloy this time. It however did not so much improve the tolerance to CO poisoning, as both electrocatalysts lost more than 96% of their initial current density after a mere 15 minutes at a given potential.

Pt/WO_3 still presents lower initial current densities than the other electrocatalysts. If only the percentage of retained current is taken into account however, this material presents more interesting performance. In fact, 56 and 67% of current were respectively lost at 20 mV for Pt/WO_3

6 and 25%. For higher potentials, the loss goes up to 82% maximum, which is lower than Ru-containing materials, supposed to be the state-of-the-art CO-tolerant electrocatalyst.

Finally, the addition of 10 ppm CO barely changed the gradation of the electrocatalysts from the previous section in pure hydrogen. Pt/C still present the best current densities even in the final values, despite the competition of Pt/WO_3 25% after 15 minutes. Both Pt and Pt+Ru have lost nearly all their activity after 15 minutes of operation in these conditions.

V.3.2. H_2 + 50 ppm CO

After adding 10 ppm of CO into the hydrogen feed, it was chosen to test the influence of a slightly higher CO percentage: 50 ppm CO in the hydrogen feed.

In Figure V.12 the chronoamperometries measured on Pt/C 33% presented the same angular shape as described with 10 ppm CO/H_2 can be clearly seen, with the first slope presenting an even more drastic loss in the range of 3 minutes. The second slope is afterwards so slow than it is not far from a plateau. These final current values for Pt are from lower to higher potential of 0.33, 0.66 and 0.75 mA cm^{-2}.

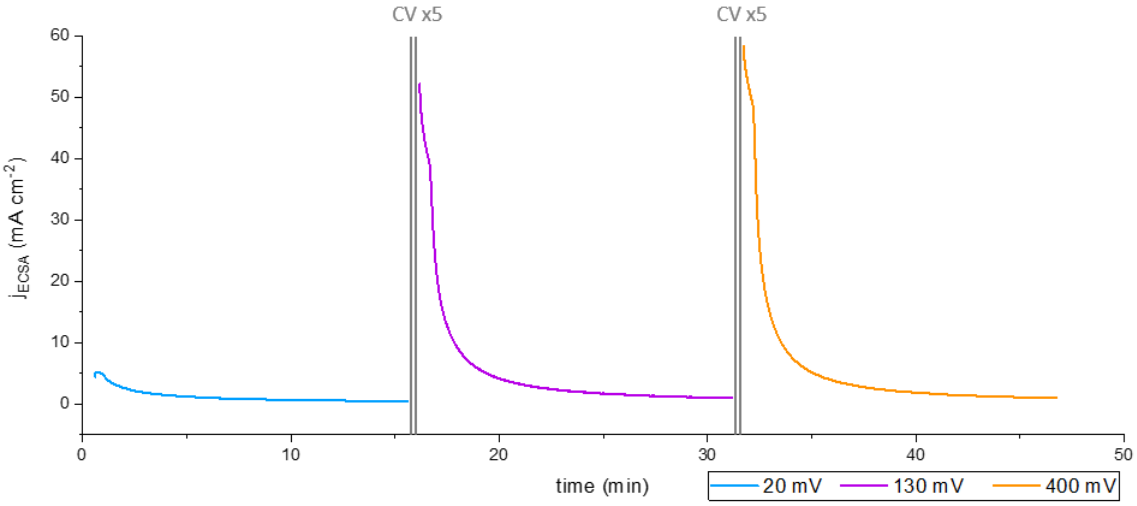

Figure V.12: Pt/C 33% chronoamperometries measured at 20, 130 and 400 mV under 50 ppm CO/H_2 in GDE setup in 1 M H_2SO_4 at T = Tamb.

Figure V.13 gathers the initial and final current values for all chronoamperometries performed in 50 ppm CO + H_2.

Pt/C 33% still presents the best initial values (measured after "reconditioning of the electrocatalysts surface), though the surface seems to have been irreversibly damaged: the maximum current value went from 80 mA cm_{Pt}^{-2} to 60 mA cm_{Pt}^{-2} (measured at 400 mV). This long term loss could come from a combination of irreversible poisoning and degradations during the fast rate potential cycling at high potentials [137,237,286,287], very classical and documented for such electrocatalysts .

In second place is the Pt+Ru composite, this time presenting higher values than the alloy for all three potentials. In fact, the maximum current density value of this material went from 32 to 34

to 35 mA cm_{Pt}^{-2} at 130 mV in consecutive H_2, 10 ppm CO/H_2 and 50 ppm CO/H_2 experiments. Considering the presence of isolated Ru nanoparticles that are known to dissolve at high potential, this results is quite surprising.

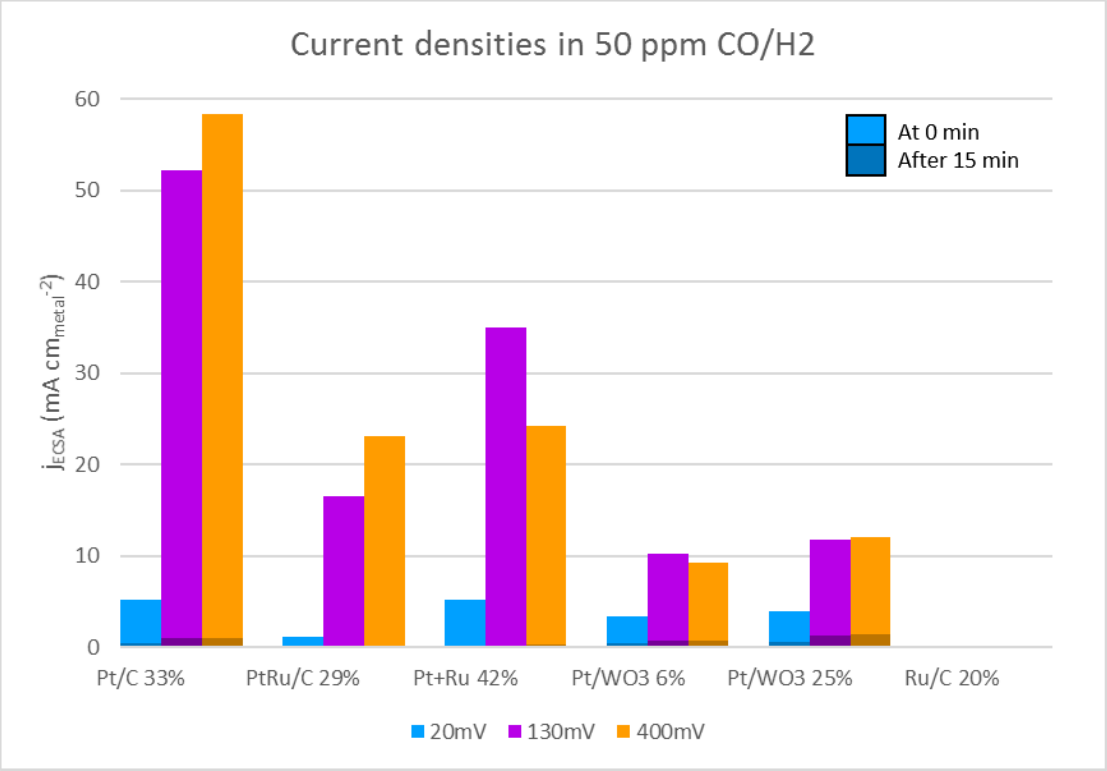

Figure V.13: Bar chart presenting the initial (in lighter colour) and final (in darker colour) values obtained for 20, 130 and 400 mV for studied electrocatalysts in 50 ppm CO/H_2 flux.

Pt/WO_3 6 and 25% still present the lowest initial current densities (with the exception of Ru). They however also present the highest final current densities, with respectively 0.80 and 1.43 mA cm_{Pt}^{-2} at 400 mV. Their overall loss is of ca. 90% (still extremely high), but nevertheless lower than the 98% loss undergone by all other electrocatalysts.

After experiments done in the presence of CO impurities in the hydrogen feed, one can conclude that Pt, PtRu and Pt+Ru all present very poor CO-tolerance in these conditions and should not be capable to withstand prolonged HOR activity at high current density and low overpotential with consequent impurity content (e.g. CO) in a EHC anode, which is very disappointing. Despite its weaker initial activity towards the HOR, Pt/WO_3 25% (and 6%, even if it initial activity is lower), presents the best CO-tolerance in terms of maintained current density at a given potential under a poisoned hydrogen flux. It however also loses 90% of its active sites, a value far too large if the final application, the EHC, is considered.

V.4. Conclusion

As predicted, the new configuration provided by the GDE permitted to drastically reduce mass-transport limitations, that were pointed out in the RDE setup and prevented any relevant HOR kinetics measurement in fully-flooded active layer configuration. Hence, the GDE enabled to measure more reliable HOR kinetics parameters, even though it seems that the intrinsic kinetics parameters of Pt for hydrogen reactions were not reached, considering the literature data sometimes 4 to 10 times higher. The author believes that the used GDE setup and operating conditions can still be optimized, which could not be done in the timeframe of this PhD.

Whatever these biases, six chosen electrocatalysts were tested towards the HOR and HER in pure hydrogen feed. Without surprise, Pt/C was found to present the best activity towards the HOR, followed by the PtRu alloy, and the Pt+Ru composite. Tungsten-based electrocatalysts were more ambiguous, showing low activity towards the HOR both in CA and CV, but presenting very high HER activity (ca. 2-3 times larger than Pt); it is postulated that this follows the propensity of WO_3 to form bronzes following proton insertion.

In order to determine the behaviour of each material in fixed potential conditions with different gas feeds, CA were performed. CA in pure hydrogen showed surprisingly fast current decrease for all six electrocatalysts, though no definitive explanation could be given to explain such a result. The electrocatalysts were then tested in 10 ppm and 50 ppm CO environments. All materials lost nearly all of their HOR activity after a few 10 minutes in these conditions (at 20, 130 or 400 mV potential hold), with the exception of tungsten-based electrocatalysts, which still presented a small oxidation current at the end of the experiments.

However, when considering the requirements of the EHC application of maintaining high oxidation current densities under an impure inlet with as much as 1% CO, no electrocatalysts studied in this thesis seems to fulfill the conditions. This disappointing result shows how much work the research community has to perform to make EHC operating under impure H_2 a practical reality.

General Conclusion

General Conclusion

The electrochemical hydrogen compressor is a promising technology, that could help reducing the cost of hydrogen processing (and this would aid the development of the hydrogen economy) by combining both the purification and compression steps necessary to its use in PEMFCs, into one. An EHC uses the concepts of a PEMFC (for its anode) and a PEMWE (for its cathode); like in these systems, the two electrodes are separated by a PEM; impure hydrogen is oxidized at the anode and the protons generated, after migration in the PEM, are reduced into pure hydrogen at the cathode (at a high pressure).

Such system however needs to hold currents above 2 A cm^{-2} to be competitive versus other purification and compression systems; this makes the challenge high, because oxidizing hydrogen in presence of a large amount of impurities, the main one being CO, is not granted. To this ambitious goal, the electrocatalysts used in the EHC will have to present:

(i) A very high activity towards the HOR;

(ii) A very high CO-tolerance and/or CO oxidation activity;

not speaking from the need to implement them in properly designed/operated electrodes/systems. To that goal, this thesis studied two very promising electrocatalysts, the design of which was inspired from the literature: Pt+Ru/C and Pt/WO_3.

Pt+Ru/C was synthetized with the polyol process in three different loadings: 12%, 22%, and 42%. Despite the absence of any alloying between Pt and Ru, this material presented an electrochemical signature very similar to the one of the PtRu alloy. The CO-tolerance of Pt+Ru was tested by CO-stripping, and it was found the "synergetic effect" indeed took place, by keeping Pt and RuO_2 in contact: the CO oxidation onset potential observed on CO-stripping was as low as 0.44 V, better than the common Pt/C reference, and similar, if not better than the PtRu alloy. This demonstrated the bifunctional mechanism of CO oxidation is at stake on such materials: Ru has the capacity to adsorb OH groups at a lower potential than Pt, that will participate in the oxidation of CO_{ads} on Pt sites in the well-known Langmuir Hinshelwood mechanism. This result was also in part related to the morphology of the Pt+Ru/C electrocatalysts, which presented large extent of Pt agglomerates on TEM images, such agglomerates being known to facilitate the adsorption of OH groups at low potentials. In consequence, it was found that the highest loading presented the most promising CO-tolerance, certainly due to the combination of a larger amount of agglomerates and the multiplicity of contacts between Pt and Ru nanoparticles.

Tungsten-oxide-supported electrocatalysts were synthetized in two chemistries with two loadings each: Pt/WO_3 6 and 25%, and $Pt+Ru/WO_3$ 24 and 36%; the latter was studied to evaluate if the results obtained with Pt+Ru/C could be even improved by changing the support. Those materials were synthesized by an adaptation of the polyol method to the tungsten support, and coherent results were found for the Pt/WO_3 electrocatalysts. The $Pt+Ru/WO_3$ materials, however, presented a very significant extent of agglomeration, many 3D-overstructured of Pt (and Ru),

poorly in contact with the WO_3 support, being observed in TEM. This material presented very poor results in electrochemistry, especially towards the HOR, despite the slow mass-transport conditions of the RDE, and was not studied further. All the Pt/WO_3 materials on the other hand, presented very good dispersions, both for Pt/WO_3 6% and 25%. The former showed small, isolated Pt nanoparticles with small extent of agglomeration, and the latter presented the expected mesh-like agglomerates of Pt, that could help stabilize the nanoparticles onto the tungsten oxide surface. Electrochemical results in the RDE configuration showed a very good CO oxidation activity, and DEMS experiments confirmed the oxidation of CO at potentials as low as 0.3 V. The HOR activity of the WO_3-supported electrocatalysts, however, appeared to be lower than for their carbon-supported counterparts in the RDE setup.

The RDE being associated with very detrimental mass-transport limitation, related to the necessary gas dissolution and diffusion in the liquid electrolyte, no proper HOR activity comparison could be done in that setup in conditions mimicking that of the EHC anode. Another setup, the gas diffusion electrode, was then used in order to test the six best electrocatalysts in a gas phase environment more compatible with the application.

The GDE presented many specific points:

(i) The HER potential is shifted nearly 100 mV positive for all electrocatalyst, in H_2SO_4 as in $HClO_4$.

(ii) The presence of Nafion reduces the protonic conductivity (versus liquid electrolytes), and the contact is thus lost with some electrocatalysis sites.

(iii) The pre-peaks of a CO-stripping, typical of an agglomerated electrocatalyst in RDE, are not present in GDE.

(iv) The HOR can reach currents of nearly 1 A cm^{-2}_{geo}, outperforming the 2.4 mA cm^{-2} mass-transport limitation experienced in the RDE.

(v) These currents, as well as the current exchange current measured by Tafel plots, are still below that can be achieved in other gas phase setup.

(vi) A strong poisoning phenomena occurred in pure H_2 setup, for all electrocatalysts.

The possible adsorption of sulphuric anions to electrocatalysis surfaces could explain some those specificities, though this point remains to be proven. Many experiments are still needed in order to properly understand and improve the functioning of the GDE, which does not appear to be as “routine” as expected (at least, to date).

Despite all that, the electrocatalysts were tested towards pure hydrogen first, and then towards a poisoned hydrogen feed. In pure hydrogen, Pt proved to be the most active electrocatalysts for the HOR (though Pt/WO_3 6% and 25% both showed current exchange densities for the HER 2-3 times higher than Pt, a surprising result attributed to the proton insertion of WO_3 at low potentials). PtRu and Pt+Ru presented lower currents than Pt/C, but with interesting activities nonetheless. Pt/WO_3 showed low activity towards the HOR (at medium to high reaction potential) in pure hydrogen, but was found to retain the most current under 50 ppm of CO. All other electrocatalysts were severely poisoned, at 20 mV as well as 400 mV.

Whatever their interest, these results, however, are not enough to propose any of those electrocatalysts as a possible electrocatalyst for the EHC. Despite interesting HOR current for some of them, their behaviour in only 10 ppm CO proved a very poor CO-tolerance at low potential, at least when operation at high current density is targeted. Considering the high impurity concentration values (of 1% CO) excepted in the real setup, such tolerance will not be enough.

It could however be possible to improve some of those electrocatalysts, like Pt/WO_3, to improve their tolerance. New syntheses of Pt-Ru/WO_3 for instance, in a lower loading, could be of interest. The GDE can be improved has well, and prove to be a useful and effective setup, in between the RDE and the full PEMFC. To go further, it could also be interesting to perform durability tests on the materials, and see if they can hold high current densities in pure as in impure environment, long enough to be used in an industrial system such as the EHC. Concerning the tolerance towards impurities, it was chosen to focus the present work on the study of the carbon monoxide-tolerance. Further experiments could also be performed with the GDE, in the presence of carbon dioxide, or even methane, to study the behaviour of electrocatalysts towards these impurities, at high current densities.

References

References

[1] D.H. Meadows, D.L. Meadows, J. Randers, W.W. Behrens III, Limits to Growth a Rep. Club Rome's Proj. Predicament Mank. **1972**, 515–530.

[2] A. Millward, https://www.guinnessworldrecords.Com/News/2018/7/Omani-Town-Sets-Temperature-Record-after-One-of-the-Hottest-Days-Ever-Monitored-531904 **2018**,.

[3] Meteofrance,https://meteofrance.Com/Changement-Climatique/Observer/Changement-Climatique-et-Vagues-de-Chaleur **2020**,.

[4] NASA/GISS, https://Climate.Nasa.Gov/Vital-Signs/Global-Temperature/**.**,.

[5] V. Masson-Delmotte, P. Zhai, H.-O. Pörtner, D. Roberts, J. Skea, P.R. Shukla, A. Pirani, Ipcc - Sr15 **2018**, 2, 17–20.

[6] P.R. Shukla, J. Skea, R. Slade, R. van Diemen, E. Haughey, J. Malley, M. Pathak, J.P. Pereira, Clim. Chang. L. an IPCC Spec. Rep. Clim. Chang. Desertif. L. Degrad. Sustain. L. Manag. Food Secur. Greenh. Gas Fluxes Terr. Ecosyst. **2019**, 35–74.

[7] M.-V. Guarino, L.C. Sime, D. Schröeder, I. Malmierca-Vallet, E. Rosenblum, M. Ringer, J. Ridley, D. Feltham, C. Bitz, E.J. Steig, E. Wolff, J. Stroeve, A. Sellar, Nat. Clim. Chang. **2020**, 10, 928–932.

[8] IPCC, Clim. Chang. L. an IPCC Spec. Rep. Clim. Chang. Desertif. L. Degrad. Sustain. L. Manag. Food Secur. Greenh. Gas Fluxes Terr. Ecosyst. **2019**, 1–864.

[9] GIEC, Changements Climatiques 2014, **2014**.

[10] ONU, https://www.un.org/fr/sections/issues-depth/climate-change/index.Html,.

[11] OurWorldInData, https://ourworldindata.org/Greenhouse-Gas-Emissions **2021**,.

[12] OurWorldInData,https://ourworldindata.org/Co2-and-other-Greenhouse-Gas-Emissions,.

[13] Center for Climate and Energy Solution, https://www.c2es.Org/Content/International-Emissions/.

[14] ONU, https://unfccc.Int/Process-and-Meetings/the-Paris-Agreement/the-Paris-Agreement.

[15] European Commission, Com(2018) 773 **2018**, 114.

[16] S. Denyer, Washington Post **2021**,.

[17] IEA, https://www.iea.org/Data-and-Statistics/Charts/Total-Primary-Energy-Supply-by-Fuel-1971-and-2018.

[18] ADEME, **2019**, 2019,.

[19] Olivier Danielo, Tech. l'ingénieur **2014**,.

[20] P.C.K. Vesborg, T.F. Jaramillo, RSC Adv. **2012**, 2, 7933.

[21] A.F. Ghoniem, Prog. Energy Combust. Sci. **2011**, 37, 15–51.

[22] Ministère de l'économie des Finances et de la Relance, **2020**,.

[23] Fuel Cell and Hydrogen Joint Undertaking, Fuel Cell and Hydrogen Technology: Europe's Journey to a Greener World, **2017**.

[24] Ministère de la transition écologique, Chiffres Clés Du Climat. France, Europe et Monde, **2021**.

[25] M. Benoit, L. Chauveau, F. Nicot, S. Rouat, Sci. Avenir- La Rech. **2021**, 28–38.

[26] AFHYPAC, L'Hydrogène En France, **2019**.

[27] Toyota Europe Newsroom, https://newsroom.toyota.eu/the-new-Toyota-Mirai/ **2021**,.

[28] https://www.symbio.one/ ,.

[29] https://www.fuelcellbuses.eu/,.

[30] L. Beach, I. Empire, Fuel Cells Bull. **2019**, 2019, 4–5.

[31] ALSTOM, https://www.Alstom.Com/Solutions/Rolling-Stock/Coradia-Ilint-Worlds-1st-Hydrogen-Powered-Train **n.d.**,.

[32] Fuel Cells Bull. **2016**, 2016, 1.

[33] https://Www.energy-observer.org/fr/.

[34] W.R. Grove, London, Edinburgh, Dublin Philos. Mag. J. Sci. **1842**, 21, 417–420.

[35] F.T. Bacon, Electrochim. Acta **1969**, 14, 569–585.

[36] P. Stevens, F. Novel-cattin, A. Hammou, C. Lamy, M. Cassir, P. Stevens, Tech. l'Ingénieur **2000**,.

[37] T. da Silva Veras, T.S. Mozer, D. da Costa Rubim Messeder dos Santos, A. da Silva César, Int. J. Hydrogen Energy **2017**, 42, 2018–2033.

[38] D. Hotza, J.C. Diniz da Costa, Int. J. Hydrogen Energy **2008**, 33, 4915–4935.

[39] T. Alleau, P. Malbrunot, J. Staint-Just, Mémento de l ' Hydrogène PRODUCTION D ' HYDROGENE A PARTIR DES COMBUSTIBLES FOSSILES, **2019**.

[40] IEA, Futur. Hydrog. **2019**,.

[41] B. Parkinson, P. Balcombe, J.F. Speirs, A.D. Hawkes, K. Hellgardt, Energy Environ. Sci. **2019**, 12, 19–40.

[42] H. Nazir, C. Louis, S. Jose, J. Prakash, N. Muthuswamy, M.E.M. Buan, C. Flox, S. Chavan, X. Shi, P. Kauranen, T. Kallio, G. Maia, K. Tammeveski, N. Lymperopoulos, E. Carcadea, E. Veziroglu, A. Iranzo, A.M. Kannan, Int. J. Hydrogen Energy **2020**, 45, 13777–13788.

[43] S. Karekezi, K. Lata, S. Teixeira Coelho, **2004**, 53, 1689–1699.

[44] T. Guan, P. Alvfors, Energy Procedia **2015**, 75, 2003–2008.

[45] H. Balat, E. Kirtay, Int. J. Hydrogen Energy **2010**, 35, 7416–7426.

[46] J. Charlou, **2010**,.

[47] J.-L. Charlou, J.P. Donval, Y. Fouquet, P. Jean-Baptiste, N. Holm, Chem. Geol. **2002**, 345–359.

[48] C. Marcaillou, M. Muñoz, O. Vidal, T. Parra, M. Harfouche, Earth Planet. Sci. Lett. **2011**, 303, 281–290.

[49] A. Prinzhofer, C.S. Tahara Cissé, A.B. Diallo, Int. J. Hydrogen Energy **2018**, 43, 19315–19326.

[50] R.M. Coveney, E.D. Goebel, E.J. Zeller, G.A.M. Dreschhoff, E.E. Angino, Am. Assoc. Pet. Geol. Bull. **1987**, 71, 39–48.

[51] I. Moretti, Actual. Chim. **2019**, 15–16.

[52] H. Toulhoat, Actual. Chim. **2019**, 9–10.

[53] N. Kelly, T. Gibson, D. Ouwerkerk, Int. J. Hydrogen Energy **2008**, 33, 2747–2764.

[54] Z. Du, C. Liu, J. Zhai, X. Guo, Y. Xiong, W. Su, G. He, Catalysts **2021**, 11, 1–19.

[55] ISO 14687-2:2012, **2012**,.

[56] ISO 14687-3:2014,**2014**, 6.

[57] G. Sdanghi, G. Maranzana, A. Celzard, V. Fierro, Renew. Sustain. Energy Rev. **2019**, 102, 150–170.

[58] S. Sircar, T.C. Golden, Sep. Sci. Technol. **2000**, 35, 667–687.

[59] M. Mondal, A. Datta, Int. J. Energy Res. **2017**, 41, 448–458.

[60] J. Bonjour, J.-B. Chalfen, F. Meunier, Ind. \& Eng. Chem. Res. **2002**, 41, 5802–5811.

[61] F.D. Rossini, Pure Appl. Chem. **1970**, 22, 555–570.

[62] N.A. Al-Mufachi, N. V Rees, R. Steinberger-Wilkens, Renew. Sustain. Energy Rev. **2015**, 47, 540–551.

[63] R.C. Agrawal, G.P. Pandey, J. Phys. D. Appl. Phys. **2008**, 41, 223001.

[64] M. Rhandi, M. Trégaro, F. Druart, J. Deseure, M. Chatenet, Chinese J. Catal. **2020**, 41, 756–769.

[65] W. Vielstich, H. Yokokawa, H. Gasteiger, eds., Advances in Electrocatalysis, Materials, Diagnostics and Durability ; Part 2, Wiley, Chichester, **2009**.

[66] W. Vielstich, Fuel Cell Technology and Applications: Pt. 1, Wiley: Chichester, **2007**.

[67] K. Liang, R. Stone, M. Dadd, P. Bailey, Int. J. Refrig. **2014**, 40, 450–459.

[68] K. Liang, Int. J. Refrig. **2017**, 84, 253–273.

[69] N.A. Kermani, I. Petrushina, A. Nikiforov, J.O. Jensen, M. Rokni, Int. J. Hydrogen Energy **2016**, 41, 16688–16695.

[70] J.D. de Ven, P.Y. Li, Appl. Energy **2009**, 86, 2183–2191.

[71] M. V Lototskyy, V.A. Yartys, B.G. Pollet, R.C. Bowman, Int. J. Hydrogen Energy **2014**, 39, 5818–5851.

[72] V.A. Yartys, M. Lototskyy, V. Linkov, D. Grant, A. Stuart, J. Eriksen, R. Denys, R.C. Bowman, Appl. Phys. A **2016**, 122,.

[73] F. Laurencelle, Z. Dehouche, F. Morin, J. Goyette, J. Alloys Compd. **2009**, 475, 810–816.

[74] M. Bampaou, K.D. Panopoulos, A.I. Papadopoulos, P. Seferlis, S. Voutetakis, B. Michael, P.K. D, P.A. I, S. Panos, V. Spyros, M. Bampaou, K.D. Panopoulos, A.I. Papadopoulos, P. Seferlis, S. Voutetakis, Chem. Eng. Trans. **2018**, 70, 1213–1218.

[75] R. Ströbel, M. Oszcipok, M. Fasil, B. Rohland, L. Jörissen, J. Garche, J. Power Sources **2002**, 105, 208–215.

[76] P.J. Bouwman, J. Konink, D. Semerel, L. Raymakers, M. Koeman, W. Kout, W. Dalhuijsen, E. Milacic, M.J.J. Mulder, ECS Trans. **2014**, 64, 1009–1018.

[77] P. Bouwman, Fundamentals of Electrochemical Hydrogen Compression, **2015**.

[78] H. Monjid, **2018**,.

[79] B.M. Besancon, V. Hasanov, R. Imbault-Lastapis, R. Benesch, M. Barrio, M.J. Mølnvik, Int. J. Hydrogen Energy **2009**, 34, 2350–2360.

[80] S. Abbou, J. Dillet, D. Spernjak, R. Mukundan, R.L. Borup, G. Maranzana, O. Lottin, J. Electrochem. Soc. **2015**, 162, 1212–1220.

[81] S. Abbou, J. Dillet, G. Maranzana, S. Didierjean, O. Lottin, J. Power Sources **2017**, 340, 419–427.

[82] S. Um, C.-Y. Wang, K.S. Chen, J. Electrochem. Soc. **2000**, 147, 4485.

[83] X. Cheng, Z. Shi, N. Glass, L. Zhang, J. Zhang, D. Song, Z.S. Liu, H. Wang, J. Shen, J. Power Sources **2007**, 165, 739–756.

[84] C.Y.C.C. Chen, W.H. Lai, W.M. Yan, C.Y.C.C. Chen, S.W. Hsu, J. Power Sources **2013**, 243, 138–146.

[85] T. Tingelöf, L. Hedström, N. Holmström, P. Alvfors, G. Lindbergh, Int. J. Hydrogen Energy **2008**, 33, 2064–2072.

[86] M. Trégaro, M. Rhandi, F. Druart, J. Deseure, M. Chatenet, Chinese J. Catal. **2020**, 41, 770–782.

[87] M. Rhandi, Modélisation de Procédés Électrochimiques de Type PEM (Proton Electrolyte Membrane) Pour Le Développement Du Vecteur Hydrogène, **2021**.

[88] B. Ibeh, C.L. Gardner, M. Ternan, Int. J. Hydrogen Energy **2007**, 32, 908–914.

[89] J. Giner, Electrochim. Acta **1963**, 8, 857–865.

[90] T. Gu, W.-K. Lee, J.W. Van Zee, M. Murthy, J. Electrochem. Soc. **2004**, 151, A2100.

[91] F.A. de Bruijn, D.C. Papageorgopoulos, E.F. Sitters, G.J.M. Janssen, J. Power Sources **2002**, 110, 117–124.

[92] T. Gu, W.K. Lee, J.W. Van Zee, Appl. Catal. B Environ. **2005**, 56, 43–49.

[93] M.A. Díaz, A. Iranzo, F. Rosa, F. Isorna, E. López, J.P. Bolivar, Energy **2015**, 90, 299–309.

[94] W.M. Yan, H. Sen Chu, M.X. Lu, F.B. Weng, G. Bin Jung, C.Y. Lee, J. Power Sources **2009**, 188, 141–147.

[95] D.C. Papageorgopoulos, F.A. de Bruijn, J. Electrochem. Soc. **2002**, 149, A140.

[96] R. Halseid, R. Tunold, J. Electrochem. Soc. **2006**, 153, A2319.

[97] N. Zamel, X. Li, Progess Energy Combust. Sci. **2018**, 37, 292–329.

[98] J.J. Baschuk, X. Li, Int. J. Energy Res. **2001**, 25, 695–713.

[99] S. Gilman, J. Phys. Chem. **1964**, 68, 70–80.

[100] G. Karimi, X. Li, J. Power Sources **2006**, 159, 943–950.

[101] R. Benesch, S. Salman, T. Jacksier, **2006**, 1–11.

[102] R. Halseid, P.J.S. Vie, R. Tunold, J. Electrochem. Soc. **2004**, 151, A381.

[103] F.A. Uribe, S. Gottesfeld, T.A. Zawodzinski, J. Electrochem. Soc. **2002**, 149, A293.

[104] H.J. Soto, W. Lee, J.W. Van Zee, M. Murthy, Electrochem. Solid-State Lett. **2003**, 6, A133.

[105] D. Imamura, Y. Matsuda, Y. Hashimasa, M. Akai, ECS Trans. **2011**, 41(1), 2083–2089.

[106] V. Rosca, M.T.M. Koper, Phys. Chem. Chem. Phys. **2006**, 8, 2513.

[107] Y.A. Gomez, A. Oyarce, G. Lindbergh, C. Lagergren, J. Electrochem. Soc. **2018**, 165, F189–F197.

[108] T.E. Springer, T. Rockward, T.A. Zawodzinksi, S. Gottesfeld, J. Electrochem. Soc. **2001**, 148, L9.

[109] W. Vogel, L. Lundquist, P. Ross, P. Stonehart, Electrochim. Acta **1975**, 20, 79–93.

[110] M. Murthy, M. Esayian, W. Lee, J.W. Van Zee, J. Electrochem. Soc. **2002**, 150, A29.

[111] L. Dubau, F. Maillard, Electrochem. Commun. **2016**, 63, 65–69.

[112] W.H. Scholz, Gas Sep. Purif. **1993**, 7, 131–139.

[113] Y. Wang, H. Yan, E. Wang, W. Yourong, Y. Heqing, W. E'feng, Y. Wang, H. Yan, E. Wang, J. Electroanal. Chem. **2001**, 497, 163–167.

[114] R. Jayaram, A.Q. Contractor, H. Lal, J. Electroanal. Chem. **1978**, 87, 225–237.

[115] T.E. Fischer, S.R. Kelemen, J. Catal. **1978**, 53, 24–34.

[116] G.A. Somorjai, Catal. Rev. **1972**,.

[117] E. Najdeker, E. Bishop, Electroanal. Chem. Interfacial Electrochem. **1973**, 79–87.

[118] T. Loucka, Electroanal. Chem. Interfacial Electrochem. **1971**, 319–332.

[119] W. Shi, B. Yi, M. Hou, F. Jing, P. Ming, J. Power Sources **2007**, 165, 814–818.

[120] V.A. Sethuraman, J.W. Weidner, Electrochim. Acta **2010**, 55, 5683–5694.

[121] R. Mohtadi, W.K. Lee, J.W. Van Zee, Appl. Catal. B Environ. **2005**, 56, 37–42.

[122] I.G. Urdampilleta, F.A. Uribe, T. Rockward, E.L. Brosha, B.S. Pivovar, F.H. Garzon, ECS Trans. **2007**, 11, 831–842.

[123] A.A. Shah, F.C. Walsh, J. Power Sources **2008**, 185, 287–301.

[124] K.K. Bhatia, C.Y. Wang, Electrochim. Acta **2004**, 49, 2333–2341.

[125] G.J.M. Janssen, J. Power Sources **2004**, 136, 45–54.

[126] W. Shi, B. Yi, M. Hou, Z. Shao, Int. J. Hydrogen Energy **2007**, 32, 4412–4417.

[127] X. Wang, P. Baker, X. Zhang, H.F. Garces, L.J. Bonville, U. Pasaogullari, T.M. Molter, Int. J. Hydrogen Energy **2014**, 39, 19701–19713.

[128] D. Imamura, Y. Hashimasa, ECS Trans. **2007**, 11, 853–862.

[129] M.S. Wilson, C.R. Derouin, J. Valerio, S. Gottesfeld, in: Proc. 28th Intersoc. Energy Convers. Eng. Conf. Atlanta, Georg., **1993**.

[130] S. Gottesfeld, J. Electrochem. Soc. **1988**, 135, 2651.

[131] P.A. Adcock, S. V. Pacheco, K.M. Norman, F.A. Uribe, J. Electrochem. Soc. **2005**, 152, A459.

[132] J.J. Baschuk, X. Li, Int. J. Energy Res. **2003**, 27, 1095–1116.

[133] T. Lopes, V.A. Paganin, E.R. Gonzalez, J. Power Sources **2011**, 196, 6256–6263.

[134] C.L. Gardner, M. Ternan, J. Power Sources **2007**, 171, 835–841.

[135] A. Hassan, V.A. Paganin, E.A. Ticianelli, Electrocatalysis **2015**, 6, 512–520.

[136] F.R. Nikkuni, B. Vion-Dury, L. Dubau, F. Maillard, E.A. Ticianelli, M. Chatenet, Appl. Catal. B Environ. **2014**, 156–157, 301–306.

[137] F.R. Nikkuni, L. Dubau, E.A. Ticianelli, M. Chatenet, Appl. Catal. B Environ. **2015**, 176–177, 486–499.

[138] S. Cherevko, A.R. Zeradjanin, G.P. Keeley, K.J.J. Mayrhofer, J. Electrochem. Soc. **2014**, 161, H822--H830.

[139] A.A. Topalov, S. Cherevko, A.R. Zeradjanin, J.C. Meier, I. Katsounaros, K.J.J. Mayrhofer, Chem. Sci. **2014**, 5, 631–638.

[140] S. Cherevko, G.P. Keeley, S. Geiger, A.R. Zeradjanin, N. Hodnik, N. Kulyk, K.J.J. Mayrhofer, ChemElectroChem **2015**, 2, 1471–1478.

[141] A. Zadick, L. Dubau, N. Sergent, G. Berthomé, M. Chatenet, ACS Catal. **2015**, 5, 4819–4824.

[142] C. Lafforgue, F. Maillard, V. Martin, L. Dubau, M. Chatenet, ACS Catal. **2019**, 5613–5622.

[143] C. Yang, J. Wang, H. Fan, Y. Hu, J. Shen, J. Shangguan, B. Wang, Energy \& Fuels **2018**, 32, 6064–6072.

[144] C. Babé, M. Tayakout-Fayolle, C. Geantet, M. Vrinat, G. Bergeret, T. Huard, D. Bazer-Bachi, Chem. Eng. Sci. **2012**, 82, 73–83.

[145] H.A. Aleksandrov, P. St. Petkov, G.N. Vayssilov, Energy \& Environ. Sci. **2011**, 4, 1879.

[146] A. Golmakani, S. Fatemi, J. Tamnanloo, Sep. Purif. Technol. **2017**, 176, 73–91.

[147] T. Yamamoto, M. Tayakout-Fayolle, C. Geantet, Chem. Eng. J. **2015**, 262, 702–709.

[148] A.B. Anderson, E. Grantscharova, J. Phys. Chem. **1995**, 99, 9143–9148.

[149] D.A. Tryk, G. Shi, H. Yano, J. Inukai, H. Uchida, A. Iiyama, M. Matsumoto, H. Tanida, M. Arao, H. Imai, ECS Trans. **2018**, 85, 41–46.

[150] F. Maillard, M. Eikerling, O. V. Cherstiouk, S. Schreier, E.R. Savinova, U. Stimming, Faraday Discuss. **2004**, 125, 357.

[151] F. Maillard, S. Schreier, M. Hanzlik, E.R. Savinova, S. Weinkauf, U. Stimming, Phys. Chem. Chem. Phys. **2005**, 7, 385–393.

[152] G. García, J.A. Silva-Chong, O. Guillén-Villafuerte, J.L. Rodríguez, E.R. González, E. Pastor, Catal. Today **2006**, 116, 415–421.

[153] S. Iwase, M., Kawatsu, Proc. First Int. Symp. Prot. Conduct. Membr. Fuel Cells **1995**, 1, 12–18.

[154] S. Carenco, Chem. - A Eur. J. **2014**, 20, 10616–10625.

[155] L.G.S. Pereira, V.A. Paganin, E.A. Ticianelli, Electrochim. Acta **2009**, 54, 1992–1998.

[156] M. Watanabe, S. Motoo, Electroanal. Chem. Interfacial Electrochem. **1975**, 60, 275–293.

[157] H.A. Gasteiger, N.M. Markovic, P.N. Ross, E.J. Cairns, J. Phys. Chem. **1994**, 98, 617–625.

[158] H.A. Gasteiger, N.M. Markovic, P.N. Ross, J. Phys. Chem. **1995**, 99, 16757–16767.

[159] H.A. Gasteiger, N.M. Markovic, P.N. Ross, E.J. Cairns, J. Phys. Chem. **1993**, 97, 12020–12029.

[160] T. Kawaguchi, W. Sugimoto, Y. Murakami, Y. Takasu, Electrochem. Commun. **2004**, 6, 480–483.

[161] L. Dubau, Electrocatalyseurs Platine-Ruthénium Nanodispersés Pour Une Pile à Combustion Directe de Méthanol, Université de Poitiers, **2002**.

[162] F. Maillard, Influence de La Structure d'électrocatalyseurs Nanodispersés Sur Les Réactions Impliquées Dans Une Pile à Combustion Directe de Méthanol, Université de Poitiers, **2002**.

[163] L. Dubau, F. Hahn, C. Coutanceau, J.-M. Léger, C. Lamy, J. Electroanal. Chem. **2003**, 554–

555, 407–415.

[164] R. Mohtadi, W. -k. Lee, S. Cowan, J.W. Van Zee, M. Murthy, Electrochem. Solid-State Lett. **2003**, 6, A272.

[165] L. Gancs, B.N. Hult, N. Hakim, S. Mukerjee, Electrochem. Solid-State Lett. **2007**, 10, 150–154.

[166] K. Wang, H.A. Gasteiger, N.M. Markovic, P.N. Ross, Electrochim. Acta **1996**, 41, 2587–2593.

[167] D. Lee, S. Hwang, I. Lee, J. Power Sources **2005**, 145, 147–153.

[168] E.I. Santiago, G.A. Camara, E.A. Ticianelli, Electrochim. Acta **2003**, 48, 3527–3534.

[169] R.C. Urian, A.F. Gullá, S. Mukerjee, J. Electroanal. Chem. **2003**, 554–555, 307–324.

[170] E.I. Santiago, M.S. Batista, E.M. Assaf, E.A. Ticianelli, J. Electrochem. Soc. **2004**, 151, A944.

[171] S. Mukerjee, R.C. Urian, S.J. Lee, E.A. Ticianelli, J. McBreen, J. Electrochem. Soc. **2004**, 151, A1094.

[172] T.C.M. Nepel, P.P. Lopes, V.A. Paganin, E.A. Ticianelli, Electrochim. Acta **2013**, 88, 217–224.

[173] S. Mukerjee, R.C. Urian, Electrochim. Acta **2002**, 47, 3219–3231.

[174] A. Hassan, E.A. Ticianelli, An. Acad. Bras. Cienc. **2018**, 90, 697–718.

[175] M. Götz, H. Wendt, Electrochim. Acta **1998**, 43, 3637–3644.

[176] T. Ioroi, Z. Siroma, S. Yamazaki, K. Yasuda, Adv. Energy Mater. **2018**, 1801284, 1801284.

[177] T. Ioroi, T. Akita, S. ichi Yamazaki, Z. Siroma, N. Fujiwara, K. Yasuda, Electrochim. Acta **2006**, 52, 491–498.

[178] L. Liu, F. Zhou, R. Kodiyath, S. Ueda, H. Abe, D. Wang, Y. Deng, J. Ye, Phys. Chem. Chem. Phys. **2016**, 18, 29607–29615.

[179] K. Kwon, Y. Jung, H. Ku, K. Lee, S. Kim, J. Sohn, C. Pak, Catalysts **2016**, 6, 68.

[180] D. Takimoto, T. Ohnishi, Y. Ayato, D. Mochizuki, W. Sugimoto, J. Electrochem. Soc. **2016**, 163, F367–F371.

[181] F. Micoud, Influence d'un Support {MOx} ({M} = {W}, {Ti}) Sur Les Propriétés Électrocatalytiques de Nanoparticules de Platine, **2009**.

[182] F. Micoud, F. Maillard, A. Bonnefont, N. Job, M. Chatenet, Phys. Chem. Chem. Phys. **2010**, 12, 1182–1193.

[183] F. Micoud, F. Maillard, A. Gourgaud, M. Chatenet, Electrochem. Commun. **2009**, 11, 651–654.

[184] S.I. Yamazaki, Y. Yamada, S. Takeda, M. Goto, T. Ioroi, Z. Siroma, K. Yasuda, Phys. Chem. Chem. Phys. **2010**, 12, 8968–8976.

[185] S. Yamazaki, M. Yao, S. Takeda, Z. Siroma, T. Ioroi, K. Yasuda, Electrochem. Solid-State Lett. **2011**, 14, B23.

[186] F. Gloaguen, F. Andolfatto, R. Durand, P. Ozil, J. Appl. Electrochem. **1994**, 24, 863–869.

[187] J. Durst, C. Simon, F. Hasché, H.A. Gasteiger, J. Electrochem. Soc. **2015**, 162, F190--F203.

[188] C.M. Zalitis, D. Kramer, A.R. Kucernak, Phys. Chem. Chem. Phys. **2013**, 15, 4329–4340.

[189] C.M. Zalitis, J. Sharman, E. Wright, A.R. Kucernak, Electrochim. Acta **2015**, 176, 763–776.

[190] A.R. Kucernak, C.M. Zalitis, J. Phys. Chem. C **2016**, 120,.

[191] Y. Bultel, L. Genies, O. Antoine, P. Ozil, R. Durand, J. Electroanal. Chem. **2002**, 527, 143–155.

[192] V. Paganin, E. Ticianelli, E.R. Gonzalez, J. Appl. Electrochem. **1996**, 26, 297–304.

[193] M. Inaba, A.W. Jensen, G.W. Sievers, M. Escudero-Escribano, A. Zana, M. Arenz, Energy Environ. Sci. **2018**, 11, 988–994.

[194] J. Durst, A. Siebel, C. Simon, F. Hasché, J. Herranz, H.A. Gasteiger, Energy Environ. Sci. **2014**, 7, 2255–2260.

[195] K.C. Neyerlin, W. Gu, J. Jorne, H.A. Gasteiger, J. Electrochem. Soc. **2007**, 154, B631.

[196] F. Fievet, J.P. Lagier, M. Figlarz, MRS Bull. **1989**, 14, 29–34.

[197] H.S. Oh, J.G. Oh, H. Kim, J. Power Sources **2008**, 183, 600–603.

[198] M. Chatenet, L. Guetaz, F. Maillard, in: W. Vielstich, A. Lamm, H.A. Gasteiger, H. Yokokawa (Eds.), Handb. Fuel Cells, **2010**.

[199] P. Gravereau, in: Diffr. Des Rayons X Par Les Poudres, Université de Bordeaux 1, France, **2011**, p. 209.

[200] E. Wirth, F. Guitteny, E. Wirth, K.E.P.T. Setaram, K.E.P.T. Setaram, **2019**, 33,.

[201] M. Hoashi, R. R. Brooks, R. D. Reeves, Anal. Chim. Acta **1990**, 232, 317–321.

[202] J. Vandegans, M. Hoenig, A. De Kersabiec, Tech. l'ingénieur **1997**, 33,.

[203] U.A. Paulus, T.J. Schmidt, H.A. Gasteiger, R.J. Behm, J. Electroanal. Chem. **2001**, 495, 134–145.

[204] A. Gamez, D. Richard, P. Gallezot, F. Gloaguen, R. Faure, R. Durand, Electrochim. Acta **1996**, 41, 307–314.

[205] Y. Garsany, I.L. Singer, K.E. Swider-Lyons, J. Electroanal. Chem. **2011**, 662, 396–406.

[206] C.C. Herrmann, G.G. Perrault, A.A. Pilla, Anal. Chem. **1968**, 40, 1173–1174.

[207] S. Trasatti, O.A. Petrii, J. Electroanal. Chem. **1992**, 327, 353–376.

[208] W. Sheng, H.A. Gasteiger, Y. Shao-Horn, J. Electrochem. Soc. **2010**, 157, B1529.

[209] M. Lukaszewski, M. Soszko, A. Czerwinski, A. Czerwiński, Int. J. Electrochem. Sci. **2016**,

11, 4442–4469.

[210] F. Maillard, E.R. Savinova, U. Stimming, J. Electroanal. Chem. **2007**, 599, 221–232.

[211] F. Micoud, Influence d'un Support MOx (M = W, Ti) Sur Les Propriétés Électrocatalytiques de Nanoparticules de Platine, Université de Grenoble, **2009**.

[212] Z. Jusys, J. Kaiser, R.J. Behm, **2001**,.

[213] G. Braesch, Electrocatalyseurs Pour La Réaction d'Oxydation Des Borohydrures : Des Surfaces Modèles Aux Électrodes Non-Nobles de Piles à Combustible Electrocatalysts for the Borohydride Oxidation Reaction : From Model Surfaces to Non-Noble Fuel Cell Electrodes, Université Grenoble-Alpes, **2020**.

[214] C. Lafforgue, F. Vandenberghe, R. Riasse, M. Tregaro, M. Heitzmann, P. Schott, J.-F. Blachot, F. Micoud, M. Chatenet, in: ECS Meet. Abstr., **2020**, p. 2319.

[215] M. Watanabe, M. Uchida, S. Motoo, J. Electroanal. Chem. **1987**, 229, 395–406.

[216] P.K. Babu, H.S. Kim, E. Oldfield, A. Wieckowski, J. Phys. Chem. B **2003**, 107, 7595–7600.

[217] L. Giorgi, A. Pozio, C. Bracchini, R. Giorgi, S. Turtù, J. Appl. Electrochem. **2001**, 31, 325–334.

[218] H.A. Gasteiger, N.M. Markovic, P.N. Ross, J. Phys. Chem. **1995**, 99, 8290–8301.

[219] A. Kabbabi, R. Faure, R. Durand, B. Beden, F. Hahn, J.M. Leger, C. Lamy, J. Electroanal. Chem. **1998**, 444, 41–53.

[220] P. Liu, A. Logadottir, J.K. Nørskov, Electrochim. Acta **2003**, 48, 3731–3742.

[221] F. Maillard, A. Bonnefont, M. Chatenet, L. Guétaz, B. Doisneau-Cottignies, H. Roussel, U. Stimming, Electrochim. Acta **2007**, 53, 811–822.

[222] M. Krausa, W. Vielstich, J. Electroanal. Chem. **1994**, 379, 307–314.

[223] T. Frelink, W. Visscher, J.A.R. van Veen, Surf. Sci. **1995**, 335, 353–360.

[224] Y.Y. Tong, S.K. Hee, P.K. Babu, P. Waszczuk, A. Wieckowski, E. Oldfield, J. Am. Chem. Soc. **2002**, 124, 468–473.

[225] C.H. Lee, C.W. Lee, D. Il Kim, S.E. Bae, Int. J. Hydrogen Energy **2002**, 27, 445–450.

[226] K. Hengge, T. Gänsler, E. Pizzutilo, C. Heinzl, M. Beetz, K.J.J. Mayrhofer, C. Scheu, Int. J. Hydrogen Energy **2017**, 42, 25359–25371.

[227] D. Marijan, D. Cukman, M. Vukovic, M. Milun, J. Mater. Sci. **1995**, 30, 3045–3049.

[228] L. Gancs, N. Hakim, B. Hult, S. Mukerjee, in: ECS Meet. Abstr., **2006**, p. 555.

[229] X. Yan, K. Yong, Ournal Mater. Chem. **2001**, 11, 3387–3391.

[230] F. Bonet, V. Delmas, S. Grugeon, R. Herrera Urbina, P.Y. Silvert, K. Tekaia-Elhsissen, Nanostructured Mater. **1999**, 11, 1277–1284.

[231] R. Sellin, J.M. Clacens, C. Coutanceau, Carbon N. Y. **2010**, 48, 2244–2254.

[232] R. Sellin, C. Grolleau, S. Arrii-Clacens, S. Pronier, J.M. Clacens, C. Coutanceau, J.M. Léger, J. Phys. Chem. C **2009**, 113, 21735–21744.

[233] A. Zubiaur, M. Chatenet, F. Maillard, S.D. Lambert, J.P. Pirard, N. Job, in: Fuel Cells, **2014**.

[234] L.M. Roen, C.H. Paik, T.D. Jarvi, Electrochem. Solid-State Lett. **2004**, 7, A19.

[235] K.J.J. Mayrhofer, J.C. Meier, S.J. Ashton, G.K.H. Wiberg, F. Kraus, M. Hanzlik, M. Arenz, Electrochem. Commun. **2008**, 10, 1144–1147.

[236] Z.Y. Liu, J.L. Zhang, P.T. Yu, J.X. Zhang, R. Makharia, K.L. More, E.A. Stach, J. Electrochem. Soc. **2010**, 157, B906.

[237] L. Castanheira, L. Dubau, M. Mermoux, G. Berthomé, N. Caqué, E. Rossinot, M. Chatenet, F. Maillard, ACS Catal. **2014**, 4, 2258–2267.

[238] R. Defay, A. Bellemans, I. Prigogine, Surface Tension and Adsorption, Longmans, **1966**.

[239] J. Biscoe, B.E. Warren, J. Appl. Phys. **1942**, 364,.

[240] A.H. White, L.H. Germer, J. Chem. Phys. **1941**, 9, 492–497.

[241] H.A. Gasteiger, P.N. Ross, E.J. Cairns, Surf. Sci. **1993**, 293, 67–80.

[242] J. Hutchinson, Platin. Met. Rev. **1972**, 16, 88–90.

[243] D.J. Morgan, Surf. Interface Anal. **2015**, 47, 1072–1079.

[244] S. Carenco, C. Sassoye, M. Faustini, P. Eloy, D.P. Debecker, H. Bluhm, M. Salmeron, J. Phys. Chem. C **2016**, 120, 15354–15361.

[245] D. Briggs, M.P. Seah, eds., Pratical Surface Analysis by Auger and X-Ray Photoelectron Spectroscopy, John Wiley & Sons, **1983**.

[246] K. Wikander, H. Ekström, A.E.C. Palmqvist, G. Lindbergh, Electrochim. Acta **2007**, 52, 6848–6855.

[247] R. Woods, **1976**,.

[248] E.G. Ciapina, S.F. Santos, E.R. Gonzalez, J. Electroanal. Chem. **2018**, 815,.

[249] R. Ianniello, V.M. Schmidt, U. Stimming, J. Stumper, A. Wallau, Electrochim. Acta **1994**, 39, 1863–1869.

[250] F. Maillard, E.R. Savinova, P.A. Simonov, V.I. Zaikovskii, U. Stimming, J. Phys. Chem. B **2004**, 108, 17893–17904.

[251] H.A. Gasteiger, N.M. Markovic, P.N. Ross, J. Phys. Chem. **1995**, 99, 8945–8949.

[252] S. Martens, L. Asen, G. Ercolano, F. Dionigi, C.M. Zalitis, A. Hawkins, A. Martinez Bonastre, L. Seidl, A.C. Knoll, J. Sharman, P. Strasser, D. Jones, O. Schneider, J. Power Sources **2018**, 392, 274–284.

[253] L.W. Niedrach, I.B. Weinstock Electrochem. Technol. **1965**, 3, 270.

[254] G. Cognard, Electrocatalyseurs à Base d'oxydes Métalliques Poreux Pour Pile à Combustible à Membrane Échangeuse de Protons, Université de Grenoble, **2017**.

[255] B.S. Hobbs, A.C.C. Tseung, Nature **1969**, 222, 556–558.

[256] P.J. Kulesza, L.R. Faulkner, J. Electroanal. Chem. **1989**, 259, 81–98.

[257] A.C.C. Tseung, K.Y. Chen, Catal. Today **1997**, 38, 439–443.

[258] R. Ganesan, J.S. Lee, J. Power Sources **2006**, 157, 217–221.

[259] F. Maillard, E. Peyrelade, Y. Soldo-Olivier, M. Chatenet, E. Chaînet, R. Faure, Electrochim. Acta **2007**, 52, 1958–1967.

[260] L. Colmenares, Z. Jusys, S. Kinge, H. Bönnemann, R.J. Behm, J. New Mater. Electrochem. Syst. **2006**, 9, 107–120.

[261] X. Cui, J. Shi, L. Guo, L. Zhang, H. Chen, J. Li, J. Gao, J. Phys. Chem. B **2008**, 112, 12024–12031.

[262] S. Adhikari, S. Mandal, D. Sarkar, D.H. Kim, G. Madras, Appl. Surf. Sci. **2017**, 420, 472–482.

[263] In: Compr. Anal. Chem. Vol. 30, **1996**, pp. 223–260.

[264] JCSP-43-10035-WO3, **2003**.

[265] M. Köppen, Condens. Matter **2019**, 4, 82.

[266] O.Y. Khyzhun, J. Alloys Compd. **2000**, 305, 1–6.

[267] F. Bussolotti, L. Lozzi, M. Passacantando, S. La Rosa, S. Santucci, L. Ottaviano, Surf. Sci. **2003**, 538, 113–123.

[268] M. Bevilacqua, C. Bianchini, A. Marchionni, J. Filippi, A. Lavacchi, H. Miller, W. Oberhauser, F. Vizza, G. Granozzi, L. Artiglia, S.P. Annen, F. Krumeich, H. Grützmacher, Energy Environ. Sci. **2012**, 5, 8608–8620.

[269] B.S. Hobbs, A.C.C. Tseung, J. Electrochem. Soc. **1972**, 119, 580.

[270] B.S. Hobbs, A.C.C. Tseung, J. Electrochem. Soc. **1973**, 120, 766.

[271] S.A. Abbaro, A.C.C. Tseung, D.B. Hibbert, J. Electrochem. Soc. **1980**, 127, 1106.

[272] F. Micoud, F. Maillard, A. Gourgaud, M. Chatenet, Electrochem. Commun. **2009**, 11, 651–654.

[273] O. Antoine, Y. Bultel, R. Durand, P. Ozil, Electrochim. Acta **1998**, 43, 3681–3691.

[274] B.A. Pinaud, A. Bonakdarpour, L. Daniel, J. Sharman, D.P. Wilkinson, J. Electrochem. Soc. **2017**, 164, F321.

[275] G.W. Sievers, A.W. Jensen, V. Brüser, M. Arenz, M. Escudero-Escribano, Surfaces **2019**, 2, 336–348.

[276] K. Ehelebe, D. Seeberger, M.T.Y. Paul, S. Thiele, K.J.J. Mayrhofer, S. Cherevko, J. Electrochem. Soc. **2019**, 166, F1259–F1268.

[277] R.N. Carter, S.S. Kocha, F. Wagner, M. Fay, H.A. Gasteiger, ECS Trans. **2019**, 11, 403–410.

[278] M. Wesselmark, B. Wickman, C. Lagergren, G. Lindbergh, Electrochem. Commun. **2010**, 12, 1585–1588.

[279] S.S. Kocha, Principles of MEA Preparation,From: Handbook of Fuel Cells: Fundamentals Technology and Applications. Volume 3: Fuel Cell Technology and Applications, Chichester: W. Vielstich, A. Lamm, HA Gasteiger, John Wiley \& Sons Inc, **2003**.

[280] S. Malkhandi, A. Bonnefont, K. Krischer, Electrochem. Commun. **2005**, 7, 710–716.

[281] J. Zhang, R. Datta, J. Electrochem. Soc. **2002**, 149, A1423.

[282] V.P. Zhdanov, Surf. Sci. Rep. **2002**, 45, 231–326.

[283] F. Berthier, J.P. Diard, S. Nugues, J. Electroanal. Chem. **1997**, 436, 35–42.

[284] G. Cognard, G. Ozouf, C. Beauger, G. Berthomé, D. Riassetto, L. Dubau, R. Chattot, M. Chatenet, F. Maillard, Appl. Catal. B Environ. **2017**, 201, 381–390.

[285] H. Igarashi, T. Fujino, M. Watanabe, J. Electroanal. Chem. **1995**, 391, 119–123.

[286] L. Castanheira, W.O. Silva, F.H.B. Lima, A. Crisci, L. Dubau, F. Maillard, ACS Catal. **2015**, 5, 2184–2194.

[287] F.R. Nikkuni, E.A. Ticianelli, L. Dubau, M. Chatenet, Electrocatalysis **2013**, 4, 104–116.

Annexes

Annex I: Tafel slopes in GDE

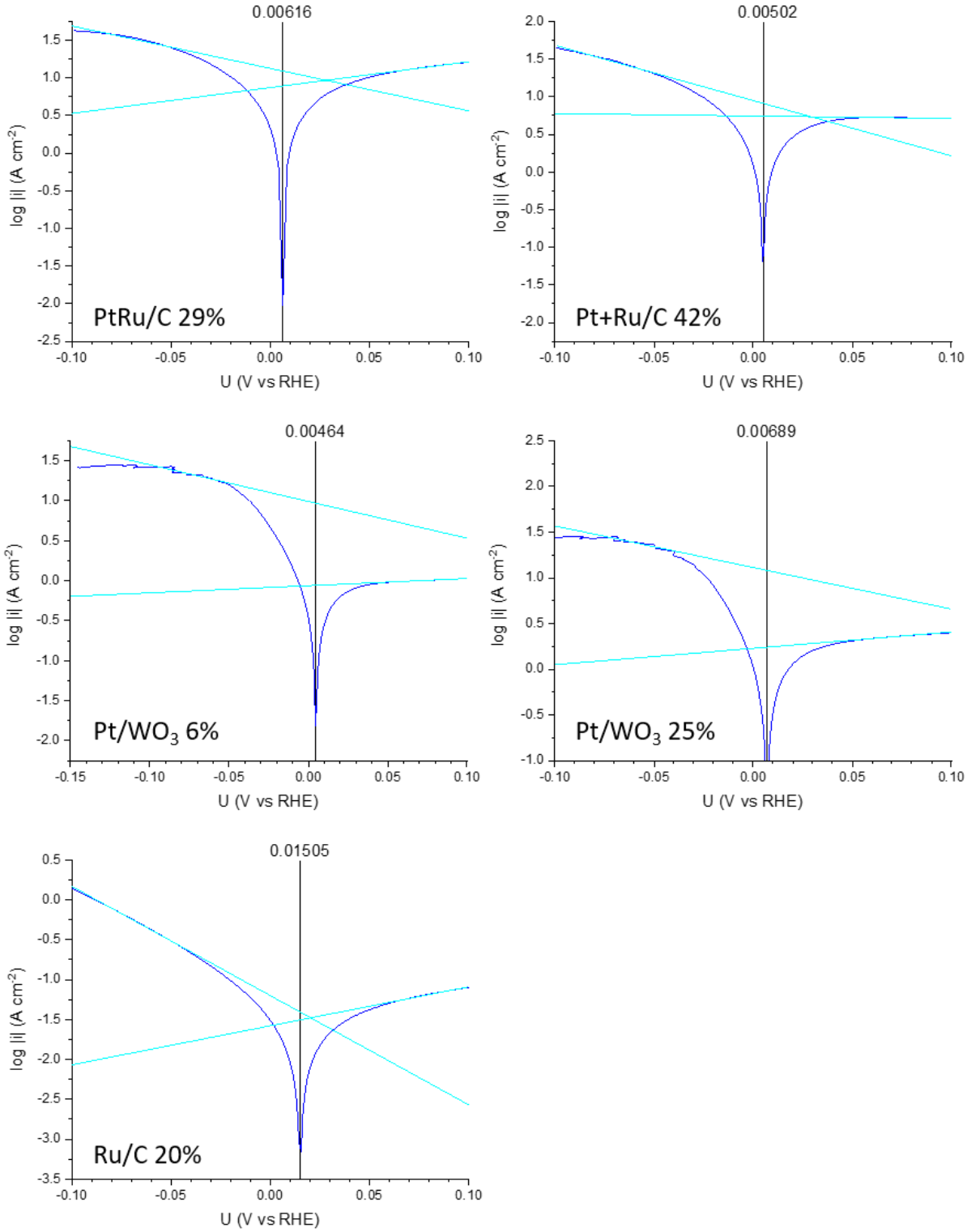

Figure A. 1: Tafel slopes measured in a pure H_2 feed in GDE configuration, at 5 mV s^{-1} in 1 M H_2SO_4 at T = $T_{amb,}$.

Annex II: Chronoamperometries in H_2, and CO/H_2 environments in GDE

II.1. Pure H_2

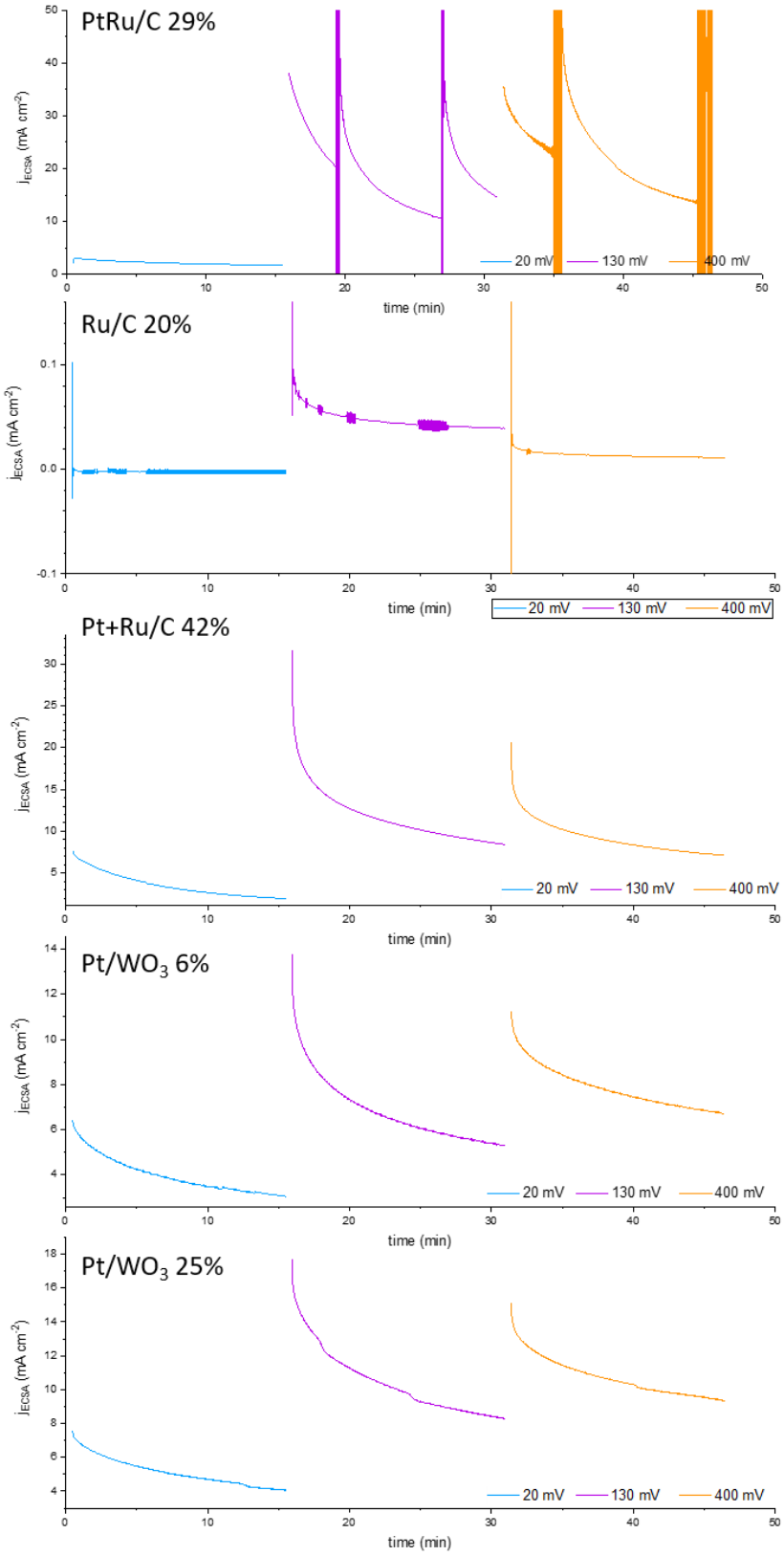

Figure A. 2: Chronoamperometries performed with a pure H_2 feed in GDE at 20, 130 and 400 mV vs RHE, in 1 M H_2SO_4 at T = $T_{amb.}$

II.2 10 ppm CO/H_2

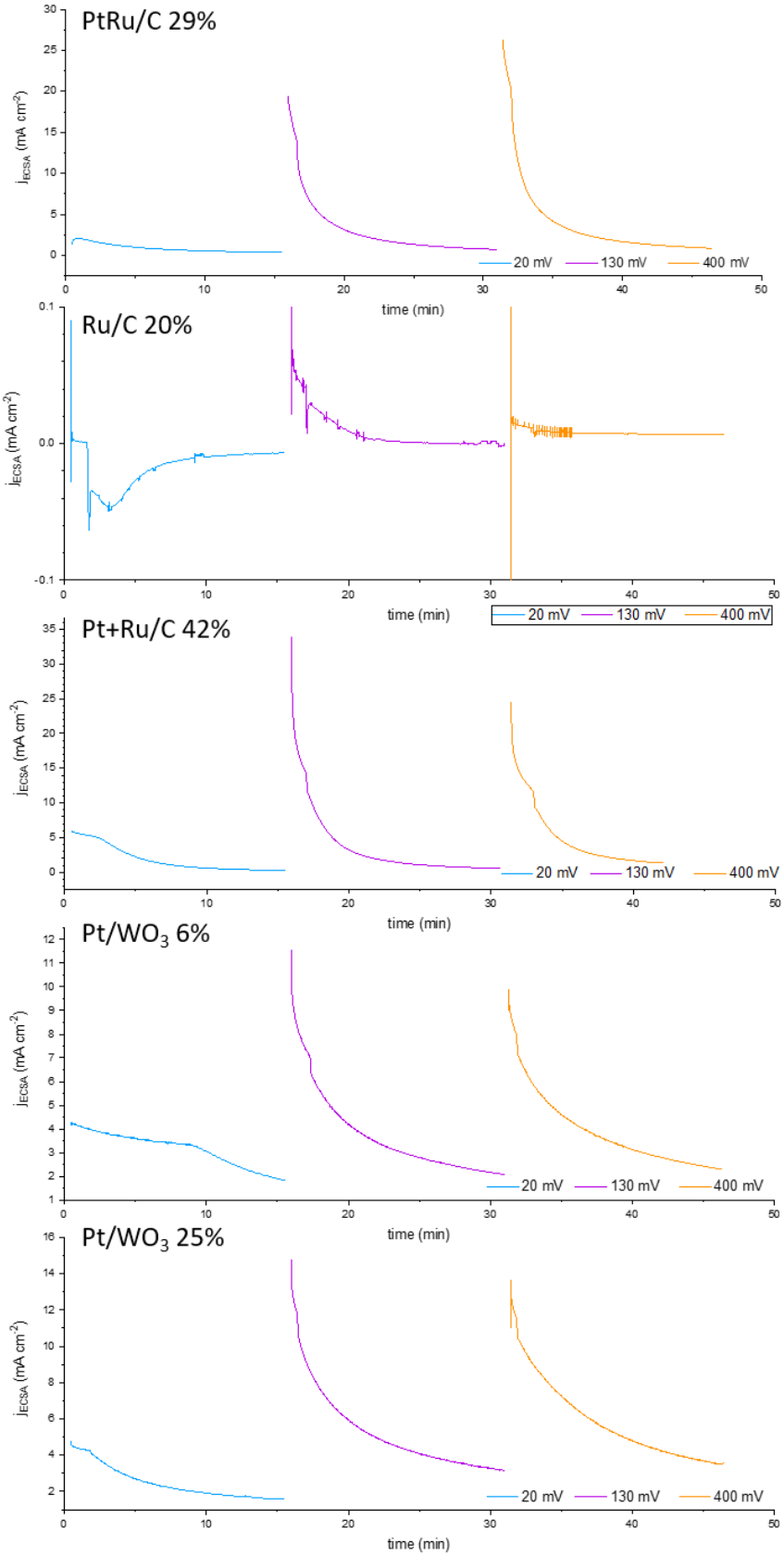

Figure A. 3: Chronoamperometries performed in GDE with a 10 ppm CO/H_2 feed at 20, 130 and 400 mV vs RHE, in 1 M H_2SO_4 at $T = T_{amb.}$

II.3 50 ppm CO/H_2

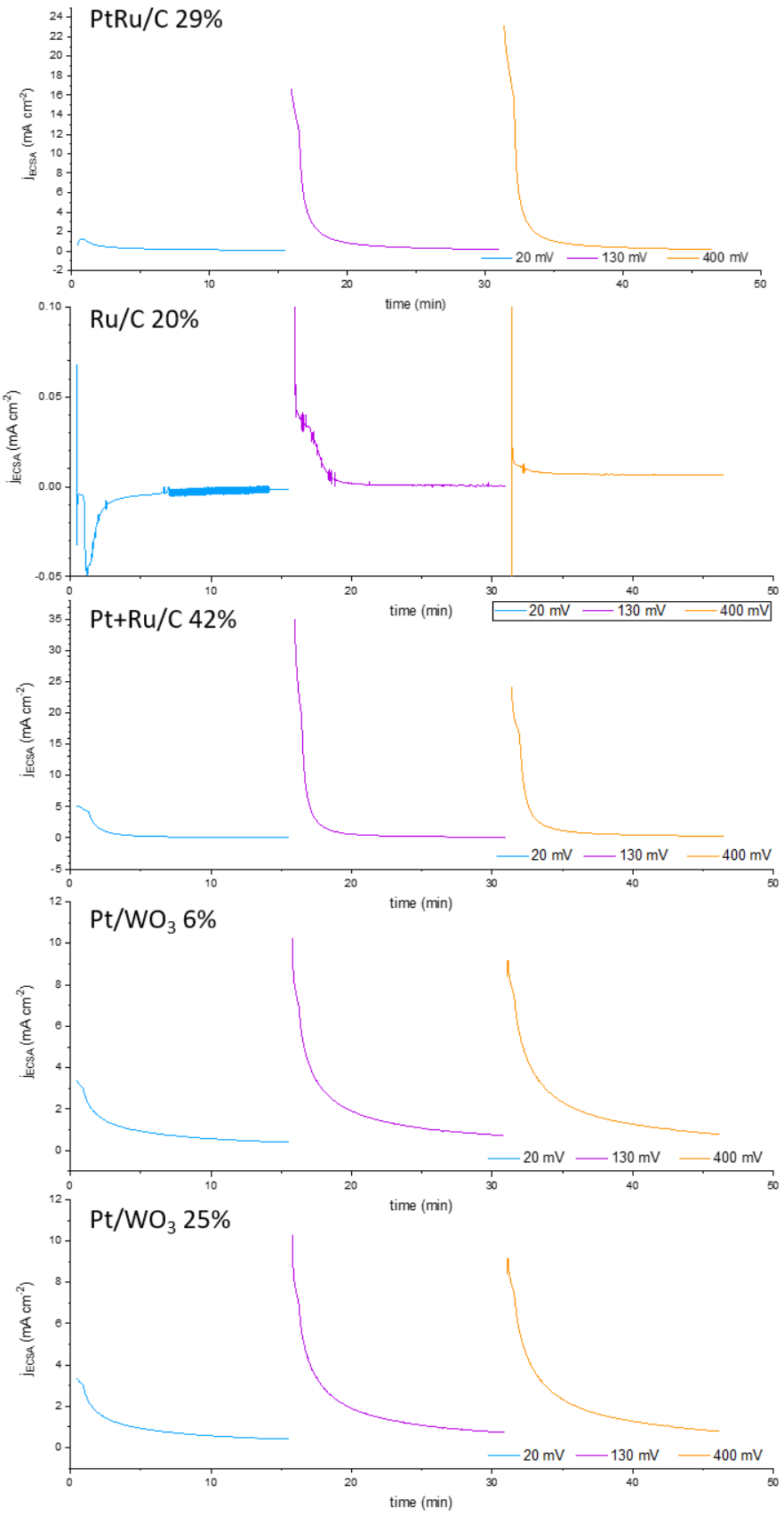

Figure A. 4: Chronoamperometries performed with a 50 ppm CO/H_2 feed in GDE at 20, 130 and 400 mV vs RHE, in 1 M H_2SO_4 at $T = T_{amb}$

Résumé

La pompe électrochimique à hydrogène (EHC en anglais) est un système prometteur combinant à la fois les étapes de purification et de compression nécessaires à l'utilisation de l'hydrogène dans des dispositifs tels que la pile à combustible à membrane échangeuse de protons. Son utilisation pourrait permettre de réduire le coût de l'hydrogène, facilitant ainsi l'essor des technologies de l'hydrogène. Cependant, l'EHC doit fonctionner à grande densité de courant (de l'ordre de 2 A cm^{-2}) pour être compétitif, un objectif ambitieux si l'on prend en compte la présence de polluants à l'anode, où la réaction d'oxydation de l'hydrogène (HOR en anglais) a lieu. Les électrocatalyseurs à l'anode doivent donc présenter une grande tolérance aux impuretés comme le CO ou le CO_2, ainsi qu'une excellente activité pour l'HOR.

Ce travail s'intéresse à l'étude de deux familles d'électrocatalyseurs présentant des propriétés intéressantes pour ces aspects. D'un côté, la famille Pt+Ru est composée de nanoparticules non-alliées de Pt et Ru, déposées sur un même substrat carbone. Elles présentent des courants d'oxydation de CO à un potentiel aussi bas que celui de Ru, tout en gardant une bonne activité HOR (mesurée en électrode à disque-tournant), contrairement à Ru, qui exhibe une faible activité pour l'HOR. De l'autre côté, les électrocatalyseurs de Pt et Pt+Ru supportés sur WO_3 affichent un très bon début d'oxydation de CO, malgré une faible activité HOR et une mauvaise stabilité. Les meilleurs électrocatalyseurs sont comparés avec une électrode à gaz (GDE), qui permet la réduction des limitations de transports de matière. Ce montage permet une comparaison plus rigoureuse des électrocatalyseurs à grande densité de courant, plus représentative de leur usage en EHC.

Mots-clefs : Compresseur électrochimique à hydrogène, Purification de l'hydrogène, Tolérance au CO, Electrocatalyseurs Pt-Ru, Electrocatalyseurs supportés sur WO_3, Electrode à gaz.

Abstract

The electrochemical hydrogen compressor (EHC) is a promising system combining both the purification and compression steps required for the use of hydrogen in devices such as proton exchange membrane fuel cells. Its usage could enable to reduce the price of hydrogen, thus facilitating the popularization of hydrogen-powered devices. However, to be competitive, EHC must sustain large current densities (in the range of 2 A cm^{-2}), an ambitious goal considering the presence of pollutants gases at the anode, where the hydrogen oxidation reaction (HOR) is performed. Therefore, it is essential for the anode electrocatalysts to present a high tolerance towards poisoning impurities such as CO or CO_2, as well as very good activity towards the HOR.

The present work investigates two families of electrocatalysts with promising properties in those aspects. On the one hand, the Pt+Ru family, composed of unalloyed Pt and Ru nanoparticles deposited on carbon support, presented CO-oxidation current at potential values as low as for pure Ru, while keeping a good activity for the HOR when measured in rotating disk electrode (contrary to Ru, that displays poor HOR activity). On the other hand, the WO_3-supported Pt and Pt+Ru electrocatalysts displayed good CO-oxidation onset, despite a lower HOR activity and a very poor stability. The most promising electrocatalysts were compared in a gas diffusion electrode (GDE) test cell, in which mass transport limitations are lowered. This enabled the proper comparison of all the electrocatalysts at high current densities, an endeavour to their use in EHC.

Keywords: Hydrogen electrochemical compressor, Hydrogen purification, CO-tolerance, Pt-Ru electrocatalysts, WO_3-supported electrocatalysts, Gas diffusion electrode.